FIBRIN STRUCTURE AND MECHANICS

A JOURNEY ACROSS SCALES

Bart Eduard Vos

This thesis was reviewed by:

Prof. dr. M. de Groot	Vrije Universiteit
Prof. dr. R.A.S. Ariëns	University of Leeds
Prof. dr. C. Storm	Technische Universiteit Eindhoven
dr. P.H.J. Kouwer	Radboud Universiteit Nijmegen
Prof. dr. P. Schall	Universiteit van Amsterdam

The work described in this thesis was performed at AMOLF, Science Park 104, 1098 XG Amsterdam, The Netherlands. This work is part of the research program of the Foundation for Fundamental Research on Matter (FOM), which is financially supported by the Netherlands Organisation for Scientific Research (NWO).

© B.E. Vos, 2018

Cover The great journey depicted on the cover contains a range of length scales, whose ratio spans the same range as the ratio of the smallest to the largest length scale found in this Thesis.
Cover design Linda Brouwer
Printed by Ipskamp, Amsterdam, The Netherlands

ISBN 978-94-92323-21-7

A digital version of this thesis can be obtained from `http://www.amolf.nl` and from `www.ub.vu.nl`. Printed copies can be obtained by request via `library@amolf.nl`.

VRIJE UNIVERSITEIT

FIBRIN STRUCTURE AND MECHANICS

A JOURNEY ACROSS SCALES

ACADEMISCH PROEFSCHRIFT

ter verkrijging van de graad Doctor
aan de Vrije Universiteit Amsterdam,
op gezag van de rector magnificus
prof.dr. V. Subramaniam,
in het openbaar te verdedigen
ten overstaan van de promotiecommissie
van de Faculteit der Bètawetenschappen
op vrijdag 5 oktober 2018 om 9.45 uur
in de aula van de universiteit,
De Boelelaan 1105

door

Bart Eduard Vos

geboren te Purmerend

promotor: prof.dr. G.H. Koenderink

Aan mijn muze

CONTENTS

1

Introduction

Telephones! Holidays!
First-world necessities.
Are these the topics
this Thesis will face?

No! It's a key to our
survivability.
Blood clots are strong; but why
is this the case?

1

FIBROUS networks are everywhere. They form the structural framework of cells, connective tissues and living systems [1], and they are also utilized in many man-made materials [2]. Figure 1.1 shows a small selection of examples of both naturally occurring and man-made fibrous structures, from the microscopic (paper) to the macroscopic (Zwinger palace, Dresden, Germany) level. A striking feature is how little space is occupied by the fibers in fibrous materials, be it concrete beams in a building or calcified collagen fibers in bone, yet they form a mechanically robust entity.

In living systems, which are very crowded places [3, 4], high rigidity at a low volume fraction is a welcome feature. For instance, the fibrous cytoskeleton of the cell, consisting of actin, septin, intermediate filaments and microtubules, accommodates organelles and regulate cellular growth, mechanical integrity, shape change, division and transport [5, 6]. Likewise, the fibrous extracellular matrix, mainly collagen, which is the most abundant protein in our bodies [7], accommodates cells, and allows for nutrient transport. It is then no surprise that fibrous networks are the mechanical scaffold for life, both within the cell and outside.

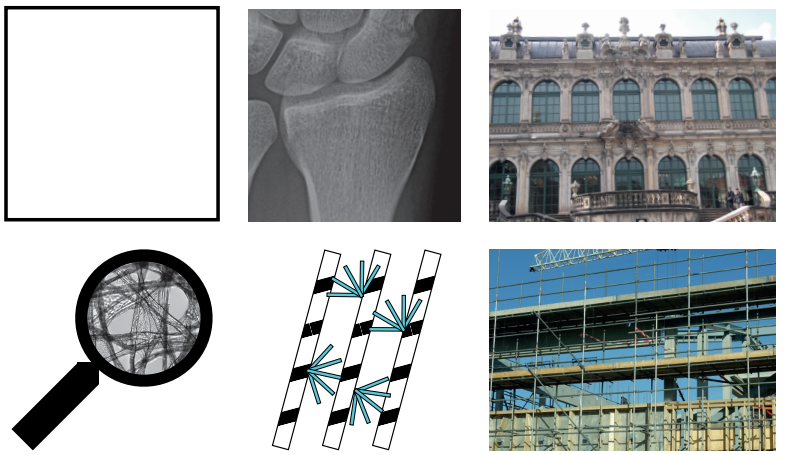

Figure 1.1: Three examples of natural and man-made structures where a fibrous material acts as the mechanical scaffold, on the scale of micrometers, millimeters, and meters. Paper is a meshwork of cellulose fibers; the wrist bones are porous networks of collagen fibers reinforced with calcium phosphate crystals [8–10]; and buildings gain their strength from a stone (or metal reinforced concrete) skeleton. All pictures are owned by B.E. Vos.

1.1. FIBRIN

In this thesis we will focus on another type of extracellular matrix that is found in our body. After damage of a blood vessel, a cascade of biological events takes place that is the blood clotting process. This is schematically illustrated in Figure 1.2. In brief, a damaged blood vessel initiates an enzymatic cascade that results in the activation of prothrombin, the precursor of thrombin. This enzyme cleaves two peptides from the

fibrinogen monomer that is dissolved in our blood. The fibrinogen monomers start to assemble into thin, double-stranded protofibrils, which in turn form thick fibers. The result is that a provisional network of fibrin is formed, to temporarily seal off the wound site.

The discovery of fibrin dates back to 1666, when Malpighi's *De Polypo cordis*, literally translated as 'On the cardiac polyp', was published [11]. Since then, fibrin matrices have been studied extensively in the context of their biological function in haemostasis [12]. Moreover, fibrin has gained a wide range of applications, from medical sealant to 3D scaffold for cell culture. For these applications, but also in the light of obstructive intravascular clots [13], an understanding of the mechanical behaviour of fibrin is very relevant.

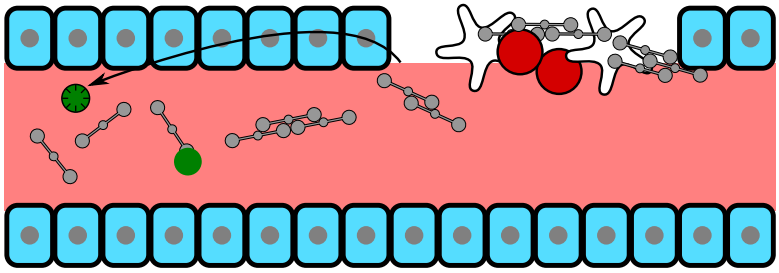

Figure 1.2: Formation of a blood clot in a damaged blood vessel. From left to right: Prothrombin (green) is activated through a cascade of enzymatic reactions (black arrow), upon which it cleaves fibrinopeptides A and B from fibrinogen (grey). This causes fibrinogen to assemble into fibrils, which, together with platelets (white) and red blood cells (red) seal off the wound site.

1.2. POLYMER THEORY

The mechanical behaviour of the fibrin network, both at small and large deformations, is relatively well understood on a coarse-grained level, by describing the network as an elastic fibrous material [14, 15]. In this model, the constituent filaments are described as continuum elastic beams with a certain bending and stretching modulus, that is, an energy penalty to bend or stretch a filament when the network is deformed. Upon deformation of these simulated networks, an energy will be required to accommodate the deformation, and by minimizing the energy of the whole network, the (elastic) response of the network is simulated.

A large variety of physical networks can be simulated by the right choice of these bending and stretching moduli. In Figure 1.3 we schematically present three different kinds of networks. By choosing a large bending modulus, i.e. a large energy requirement to bend a filament, the typical length over which correlations in the direction of the tangent are lost due to thermal fluctuations, the persistence length l_p, is large. Examples include macroscopic structures such as buildings, but also collagen networks. Synthetic polymers typically have a very small persistence length, and in between these limiting cases we find semiflexible polymers, a broad category that contains e.g. DNA

and actin filaments, but also the double-stranded protofibrils that are formed from fibrin monomers [16]. Interestingly, fibrin fibers, which are cross-linked bundles of these protofibrils [17–21], are on the boundary between semiflexible and rod-like. Since the fiber thickness can be tuned by changing the assembly conditions [22], fibrin can be directed into either of the categories.

Another parameter that characterizes a network is the architecture by which the filaments are connected. Simple spring networks require a connectivity, the number of filaments that meet at a node, of at least 6 for a mechanically stable network [23], while due to the stabilizing effects of stress and the large bending resistance of fibers, fibrous networks can form stable networks at lower connectivity [24–27], up to the point where removal of a single bond would reduce the network from stable to floppy, the so-called marginal point [28–30].

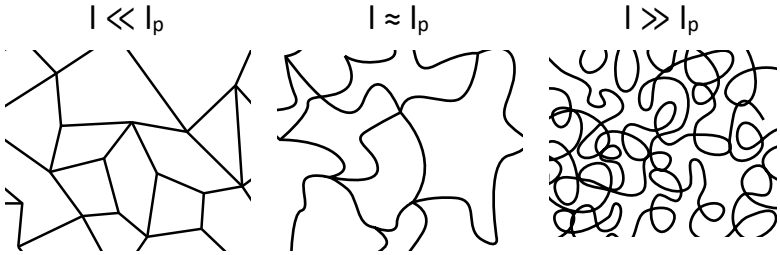

Figure 1.3: Three examples of polymer networks where the constituent fibers have different persistence lengths l_p. The fibers in the leftmost network have a large persistence length compared to their length l, such that the filaments behave as stiff, rod-like elements. The fibers in the middle network have a persistence length on the order of the filament length, acquiring the classification "semiflexible". In this case, the network elasticity is entropic in origin. The fibers in the rightmost network have a small persistence length, such that the filaments are flexible. In the latter two cases, the fibers are susceptible to thermal fluctuations.

1.3. A JOURNEY ACROSS SCALES

An understanding of the mechanical behaviour of fibrin gels based on a model of semiflexible filaments ignores three important aspects, that we address in this Thesis. These aspects are illustrated in Figure 1.4. Firstly, the fibrin clot is a hydrogel, consisting of an elastic network of protein, and a viscous solvent. Although the solvent phase accounts for more than 99% of the mass of the gel, it is not taken into account in existing models. Indeed, the elastic properties of the static gel purely originate from the network, but during deformation of the clot, solvent movement is induced and its role can no longer be neglected. Secondly, current models ignore the internal structure of the fibrin fibers, which consist of cross-linked bundles of protofibrils, and the molecular packing structure of the protofibrils themselves. There are indications that the extreme stretchiness of fibrin [31] originates from the molecular scale, and propagates toward the network level through a complex interplay between monomers, protofibrils, and fibers [32]. Finally, filaments in the semiflexible fiber model are purely elastic. However, in the real world,

inelasticity is ubiquitous in biology [33]. Also the fibrin network has the ability to change its morphology in response to mechanical loading, both on the level of the network and of the individual fibers [34, 35].

1.4. THESIS OUTLINE

In this Thesis, we study the structure and mechanical behaviour of fibrin networks by taking a reductionist approach. We use reconstituted fibrin networks, out of their biological context, since the assembly of fibrin into a mature network is a complex biological process. This approach removes the influence of mechanical stimuli from contracting platelets [36, 37], steric interactions from high densities of red blood cells [38], or chemical stimuli from the complex cascade pathway of coagulation factors [39].

We start this Thesis by implementing and advancing three light scattering models, to reliably determine the radius and mass density of fibrin fibers (Chapter 2). We then ask how the complex structure of fibrin and its constituent fibers, protofibrils and monomers relate to the network's complex mechanical properties. In particular, we split this question in three parts (not entirely coincidentally at three different length scales), which we summarize graphically in Figure 1.4.

We start in Chapter 3 on the network scale, schematically illustrated in the bottom left. Although fibrin is a hydrogel, consisting almost entirely of water, the solvent has until now been ignored in literature in the description of the mechanical behaviour of the network. We show, both experimentally and theoretically, that solvent-network interactions govern the mechanical behaviour of fibrin networks on time scales that are comparable to the time scale of solvent flow through the network. In Chapter 4, top-right in the schematic, we correlate, through *in situ* structural measurements by X-ray scattering and microscopy in conjunction with mechanical deformation, structural changes of the fibrin network and its constituents to the mechanical properties. More specifically, we see fiber alignment consistent with an affine deformation field, and at higher strains changes in the packing structure of the fibers, indicating that flexible, unstructured domains of the fibrin monomer are stretched. Thirdly, in Chapter 5, we show, in a combination of experimental work and network simulations, that fibrin networks exhibit plasticity arising from fiber-fiber interactions, mediated by the flexible, unstructured domains of the fibrin monomer that spontaneously bond when brought in contact. Stresses on these newly formed bonds in turn strongly enhance the network's stiffness.

In Chapter 6 we present the development of a light sheet microscope, in combination with a device that can stretch fibrin gels. This setup allows us to perform both rapid and long-term microscopy measurements of fibrin network remodeling in response to tensile loading. Finally, in Chapter 7 we summarize our findings, and present some further thoughts on the work presented in this Thesis.

1.5. OLLEKEBOLLEKE

It is my firm belief that Art and Science are not two unrelated institutions. In our educational system, and consequential, to a certain extend also in our society, there is a tendency to classify subjects either as Art *or* as Science. However, one can be found in

1

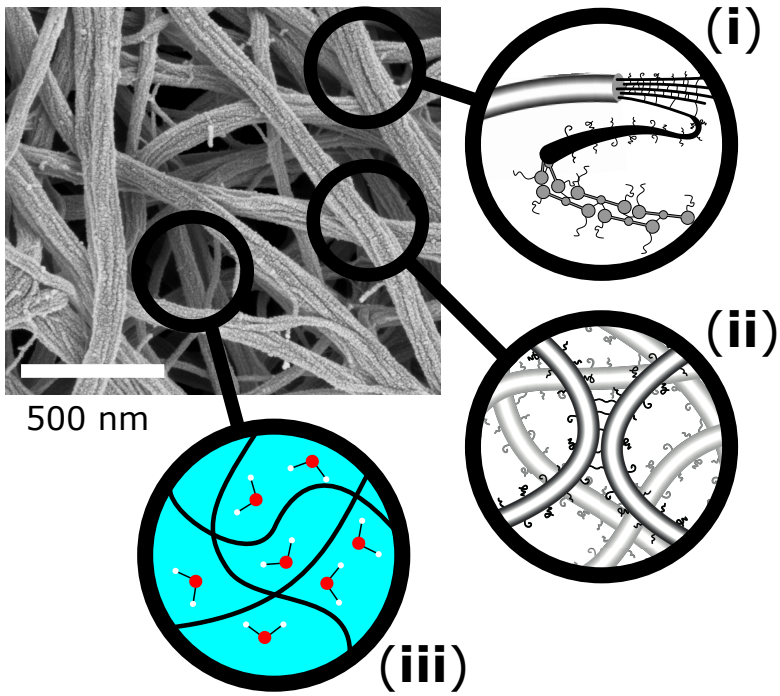

Figure 1.4: A scanning electron microscope image of a fibrin gel (see Chapter 5 for details on sample preparation and imaging settings). The three focal points of this Thesis are encircled: **(i)** the internal structure of fibrin filaments; **(ii)** the interaction between fibrin fibers; and **(iii)** the role of the solvent and filament-solvent interactions in the mechanical properties of the fibrin network.

the other and vice versa, mutually strengthening the conveyed message. Bearing this in mind, combined with my desire to convey the messages of this Thesis to a public as broad as possible, all Chapters in this Thesis are introduced with a brief summary of the Chapter by a small poem, in the style of the Ollekebolleke.

This verse form is known in English as Higgledy-piggledy, and was introduced into the Dutch language by Heinz Polzer [40]. Since I will use the Dutch adaptation of the rules for writing this form of poetry, I will also refer to the poems by their Dutch name (for a detailed account on the differences between the English and Dutch definition, see Ref. [40]). An Ollekebolleke is strictly defined with mathematical precision. It consists of eight lines, divided in two groups of four. Each line has six syllables with emphasis on the first and fourth syllable (a dactylic hexameter), except the fourth and last line, which have four syllables (still with emphasis on the first and fourth syllable). The fourth and eight line are in rhyme. The sixth line has to consist of a single word (which poses a challenge in the English language, since six-syllable words are relatively rare[1]). An example is shown here:

Dactylus! Dactylus!
Ollekebolleke
Two times four lines that should
rhyme at their end.

One word containing
Six-syllabicity
Joy for the poet
When effort is spent.

I hope the reader finds reading the Ollekebolleke's in this Thesis informative, and as enjoyable as it was to write them.

[1] In e.g. Dutch, merging of two nouns is allowed, allowing a much greater variety in six-syllable words. This might have contributed to the popularity of the Ollekebolleke in the Dutch language.

2

QUANTITATIVE ANALYSIS OF THE STRUCTURE OF FIBROUS NETWORKS BY LIGHT SCATTERING

"Miss, what's your weight today?
Is that size forty-four?"
Asking this question:
not decent, nor wise.

Yet with the aid of a
Spectrophotometer
Fibers will tell us
their mass and their size.

Fibrous structures are ubiquitous in nature, being found in both unicellular and multicellular organisms, on a wide variety of length scales. They are also present in many man-made materials, made from both natural and synthetic matter. Hence, there is a strong need for quantitative characterization of the structure of fibrous networks to understand the physical basis of their functions and tailor the structure-function relation for applications. However, many commonly used techniques for determining the structure of fibrous networks, such as light and electron microscopy, require invasive sample preparation such as fluorescent labeling or drying, potentially disrupting the network in its natural state. To overcome this challenge, light scattering is commonly used, as it is a non-invasive, bulk-averaging technique, that provides quantitative structural information encoded in the wavelength dependence of scattered light. Here we use light scattering to extract the fiber diameter and mass per unit fiber length of fibrin, a fibrous biopolymer

acting as the mechanical scaffold of a blood clot. To obtain these structural parameters from the scattering spectra we implement three different light scattering models proposed in literature, and enhance their accuracy by implementing a correction on the wavelength dependence of the refractive index and the differential refractive index. We show that this correction significantly improves the accuracy of the light scattering models. Furthermore, we test various methods to obtain the fractal dimension of the fibrin network, a parameter that characterizes the spatial arrangement of fibers and lies at the basis of one of the light scattering models.

2.1. INTRODUCTION

In many fields of research, techniques based on the scattering of light are being used to study molecular weight, size, shape and interactions of small particles and macromolecules [41–43]. The advantages of such methods are that they are non-invasive and provide an ensemble average. Unlike fluorescence microscopy, light scattering techniques do not require labelling, which can perturb the properties of the particles of interest. And unlike electron microscopy and atomic force microscopy, light scattering can be performed *in situ*, while the particles remain dispersed in solvent, which is particularly relevant for biological samples and hydrogels that tend to be highly hydrated.

There are two alternative methods to determine structural information from the scattered light of a solution of particles. The first method, commonly denoted as *static light scattering*, is to determine the scattered intensity at a single wavelength while varying the angle of detection. The second method, commonly denoted as *turbidimetry*, is to determine the loss of transmitted light through a solution due to scattering, as a function of wavelength (the turbidity $\tau(\lambda)$ is defined as the shape of the extinction spectrum) [44]. Although in principle both methods carry the same information [45], the turbidimetry method can be used to quantify interactions in suspensions subject to multiple scattering over a wide range of particle sizes and concentrations [46, 47] whilst static light scattering is limited to less opaque samples where light is only scattered a single time. Using appropriate theoretical models, structural parameters of the particles of interest can be extracted from the measured extinction spectrum, such as the size, shape and polydispersity of the scattering objects [48], while the absolute extinction magnitude is determined by their density, size and difference in refractive index with the surrounding solvent [49, 50].

Light scattering is particularly useful for fibrous biopolymers such as fibrin, a biopolymer that acts as the mechanical scaffold of a blood clot. Several models have been proposed that relate the extinction spectrum of fibrous structures such as fibrin gels to structural parameters [51–53]. The assembly of fibrinogen monomers into the final network is a hierarchical process, where fibrinogen monomers first form double-stranded protofibrils, which then laterally aggregate to form fibers. This process is strongly influenced by the assembly conditions, where the final protein content per filament cross-section spans two orders of magnitude [54]. Hence, the structural information provided by light scattering is essential for characterization of the network. However, each model necessarily relies on certain assumptions, which limit the accuracy of the extracted parameters.

In this Chapter we study the structure of a fibrin network by analysis of the wavelength-dependent extinction of light. We start with the analysis using two existing scattering models valid for non-interacting fibers [51, 52] based on the Rayleigh-Gans scattering theory, and increase the accuracy of the extracted parameters by considering a more advanced model including the fibrin network structure [53]. We improve these models by including a correction factor for wavelength dispersion in the refractive index of the solvent and the differential refractive index following an approach proposed in Ref. [55]. Furthermore, in order to implement the fibrin network structure in the scattering model, we use two independent methods to determine the network fractal dimension. The techniques developed and implemented in this Chapter provide a useful tool for

further studies of the structural properties of fibrous networks and suspensions, including natural systems such as fibrin and collagen, and synthetic systems such as carbon nanotubes [56, 57].

2

2.2. MATERIALS AND METHODS

2.2.1. FIBRIN

Human plasma fibrinogen (Plasminogen, von Willebrand Factor and Fibronectin depleted) and human α-thrombin were obtained in lyophilized form from Enzyme Research Laboratories (Swansea, United Kingdom). All chemicals were obtained from Sigma Aldrich (Zwijndrecht, The Netherlands). Fibrinogen (lyophilized in 20 mM sodium citrate-HCl buffer at pH 7.4) was dissolved in water at 37°C for 15 min to its original concentration (approximately 13 mg/ml) and dialysed against fibrin buffer containing 20 mM HEPES and 150 mM NaCl at a pH of 7.4 in order to remove citrate, which complexes with Ca^{2+} ions that are required for FXIII and thrombin activity. A dialysis membrane with a Molecular Weight Cut-Off (MWCO) of 10 kD was used. 50 ml of sample was dialysed against 1 L of buffer, under continuous stirring. After one hour of dialysis at room temperature, the buffer was replaced, and after another hour, the buffer was replaced again. The third dialysis step was performed at 4°C overnight. After dialysis, the fibrinogen solution was aliquotted, snap-frozen in liquid nitrogen and stored at -80°C. The monomer concentration was checked by spectrophotometric measurements of the absorbance at 280 and 320 nm using a Nanodrop 2000 spectrophotometer (Thermo Scientific) and using an extinction coefficient of 16.0 mg/(ml cm) [51] at 280 nm. The absence of absorption at 320 nm indicates that no aggregates are present. The final fibrinogen concentration was typically around 10 mg/ml. Prior to use, the fibrinogen was quickly thawed at 37°C, and then diluted and mixed with 500 mM $CaCl_2$ at room temperature to a final assembly buffer containing 20 mM HEPES, 150 mM NaCl and 5 mM $CaCl_2$ ("coarse clots"). Dense networks ("fine clots") with an average pore size of 0.08 μm were obtained in fine-clot assembly buffer (400 mM NaCl, 3.2 mM $CaCl_2$ and 50 mM Tris-HCl) at a pH of 8.5 [54].

Thrombin (lyophilized in 50 mM sodium citrate and 0.2 M NaCl) was, on ice, reconstituted in water to its original concentration (approximately 10,000 U/ml), and quickly aliquotted, snap-frozen in liquid nitrogen and stored at -80°C. Assembly was initiated by the addition and quick mixing of 0.5 U/ml of thrombin from a 20 U/ml thrombin stock, kept on ice for a maximum of 24 hours. After addition of thrombin, the mixture was quickly transferred by pipetting to a cuvette to allow *in situ* polymerization.

2.2.2. TURBIDIMETRY

Turbidimetry measurements were carried out using a Lambda 35 spectrophotometer (Perkin Elmer, Groningen, The Netherlands). A schematic representation of the setup is shown in Figure 2.1. Light from a white light source, emitting between $\lambda = 350$ nm and $\lambda = 900$ nm, is reflected on a grating with 1053 lines/mm to obtain a monochromatic beam, which is split by a beamsplitter to a reference sample and the sample itself. The transmitted light intensities are measured and the extinction of the sample relative to the

reference is reported to the user. Colloid samples were loaded in disposable plastic cuvettes (Plastibrand, Wertheim, Germany), requiring approximately 550 μl, while quartz cuvettes from Hellma (Kruibeke, Belgium) with a sample volume of 400 μl were used for fibrin samples, both having a 10.0 mm optical path length. For fibrin samples with a high optical density (exceeding approximately 2.5 cm^{-1}), we used quartz cuvettes suitable for fluorescence measurements (Hellma, Kruibeke, Belgium), which can be used either with a 10.0 mm path length or a 2.0 mm path length. Prior to measurements, a baseline correction was performed by placing a cuvette containing only the assembly buffer in both the measurement and reference position. Measurements were performed at room temperature, although when necessary the temperature can be controlled using a Peltier system. Wavelength scans were taken from 450 nm to 900 nm, unless otherwise noted. Extinction values were taken at 1 nm intervals at a scanning rate of 480 nm/s, and a slit width of 2 nm. With this slit width, the beam dimensions are approximately 2×7.5 mm (width $\times$ height).

To test the sensitivity of the device we performed wavelength scans on a suspension of 100 nm beads of increasing concentration. As shown in Figure 2.2, we find that the sensitivity of the device ranges from an optical density of approximately 0.01 to 3.0; below that range too few photons scatter to measure accurately the difference between the sample and the reference beam, while above that range too few photons are passing through the sample. For the suspension with the highest bead concentration, the extinction spectrum shows saturation in the blue half of the spectrum due to a too high optical density at these wavelengths. This problem can be addressed either by a switching to a cuvette with a shorter path length, or by only using the red part of the spectrum for analysis.

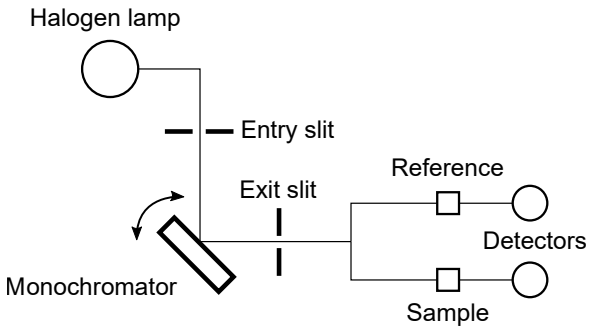

Figure 2.1: Schematic representation of the spectrophotometer setup. The schematic is based on the user manual [58]. White light from a halogen lamp is reflected on a monochromator and split into two pathways. One beam passes through the sample while the other passes through a reference. Afterwards, the intensity of both beams is measured by two detectors, from which the attenuation of the sample beam is determined.

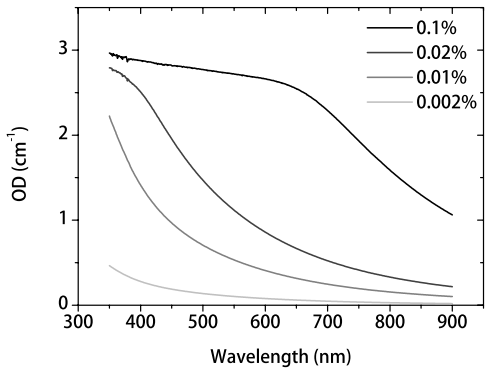

Figure 2.2: An assay to determine the range over which the optical density (OD) can be reliably measured using our spectrophotometer. The sample is a suspension of polystyrene beads (r = 100 nm) in water, at various weight concentrations. The optical density is expected to increase with shorter wavelengths ($I \propto \lambda^{-4}$, see Eq. 2.1), which is indeed observed for the samples with a bead concentration of 0.002% and 0.01%. Instead, the curves taken at bead concentrations of 0.1% and 0.02% saturate at short wavelengths since too little light reaches the detector. The optical density of the bead suspension at a concentration of 0.002% is close to the sensitivity limit of the spectrophotometer.

2.2.3. CONFOCAL MICROSCOPY

Confocal microscopy was performed on a Nikon Eclipse Ti inverted microscope equipped with a 100x oil-immersion objective (NA = 1.40). Fibrinogen labeled with Alexa Fluor 488 (Life Technologies, Bleiswijk, The Netherlands) was mixed with unlabeled fibrinogen in a 1:19 molar ratio. Samples were prepared in glass chambers made of a microscope coverslip and slide with Parafilm spacers. Polymerization occurred at room temperature for at least 12 hours.

2.3. LIGHT SCATTERING MODELS

In this Chapter, it is important to note the crucial difference between the terms *scattering, absorption* and *extinction*. The *extinction* of a beam of light is the sum of *scattered* and *absorbed* light. Scattering refers to light being deviated from a straight path, with no energy transfer to the scattering object[1], while absorption refers to photons being taken up by matter[2]. Provided that the specimen of interest does not absorb light in the exper-

[1] Strictly speaking, conservation of momentum dictates that a tiny fraction of the photon energy must be lost: as the photon changes direction, the object it scattered on must also gain some momentum, and thereby energy, such that the total momentum is conserved. However, due to the huge mass of scattering objects compared to the photon energy, this contribution can be easily neglected.

[2] Absorption followed by re-emission (fluorescence) is fundamentally different from scattering: the former creates an excited energy state in the fluorophore, while the latter only interacts with matter through an exchange in momentum.

imental wavelength range, scattering can be determined directly from the extinction of light from a difference in light transmission compared to a reference sample (extinction). This is the case for the samples we study here.

In the remainder of this Section, we will first shortly review the basics of light scattering, and continue with several models that predict structural parameters of a suspension of particles based on the shape of the extinction spectrum. In particular, we consider three models designed to provide structural information of suspensions of rods, which are an approximation of our fibrin network [51–53]. Finally, we consider several methods to obtain the network fractal dimension D_m, a number that characterizes network structure and serves as an input parameter in one of the models [53, 59].

That light can be scattered by particles can be verified every instance when one observes that the sky is blue [60], rather than the complete blackness one would expect to see when not directly looking into the sun. The explanation why we do not stare into the darkness of outer space comes from the fact that particles scatter light, including the molecules that we find in air, mainly nitrogen and oxygen. That the sky is blue rather than a copy of the solar spectrum is a consequence of a wavelength dependence of scattering from the small particles that make up the atmosphere. This wavelength dependence is described by Rayleigh's law [61] and can be understood on ground of a simple dimensional analysis (Chapter 3 in [43]). Energy conservation requires that the scattering intensity I scales with r^{-2}, where r is the distance from the observer to the scattering particle; and with the square of the dipole field (scaling with the volume V of the particle), introducing a V^2 term. Any refractive indices or numerical constants involved in the scattering process are dimensionless, indicating that, in order to match units, there must a $length^{-4}$-term. Next to the distance to the source and the particle volume, the third relevant parameter with units of length is the wavelength of the scattered light: we expect a λ^{-4}-term that depends on the wavelength λ of the scattered light, such that the scattered intensity I is of the form

$$I = I_0 f(n_1, n_2)(V^2/r^2\lambda^4) \tag{2.1}$$

where I_0 is the incident radiation and $f(n_1, n_2)$ is some unitless function that contains all numerical constants and depends on the refractive indices of the medium of propagation n_1 and of the scattering particle itself n_2. Finally, the λ^{-4}-term indicates that light with shorter wavelengths scatters more strongly than long wavelengths, hence the explanation that the sky (except the celestial area that spans the sun; being a source of non-scattered light) appears blue (during day, given non-cloudy conditions).

Rayleigh scattering theory holds under the assumption that the particle radius r is small compared to λ. The range of validity in terms of particle size is improved by the Rayleigh-Gans-Debye approximation [42] as long as the ratio of the refractive index of the scattering object and its environment, $\frac{n}{n_s}$, is close to unity, and $\frac{r}{\lambda}|\frac{n}{n_s} - 1| \ll 1$. However, as shown in Ref. [62], for particles large compared to the wavelength of light the validity is uncertain. Solutions of the scattering problem for particles of arbitrary shape and size exist, and can be found in e.g. Refs. [41, 43]. Named after Gustav Mie, this is commonly coined Mie scattering and predicts to high accuracy the scattering spectra of colloidal particles (e.g. Ref. [63, 64]). A downside of Mie theory is that it requires the scattering object to have certain symmetries in its shape and composition, which are found

in spherical particles or rods of infinite length. Nevertheless, in practice, the theory can be applied to many filamentous systems including biopolymers, which tend to have a high length to width (aspect) ratio.

When the particle density is raised to a level where the particles are interacting, the wavelength dependence of the scattered light intensity becomes sensitive not only to the individual scattering particles, but also to the higher-order structure formed by these particles. Hence, in the analysis of light scattering spectra, scattering models characterize the sample with two factors [53, 65]: the form factor describing the internal structure of the scattering object (denoted by $P(q)$), and the structure factor, taking into account the effect of the collective structure (denoted by $S(q)$). In a dilute system of scattering particles that are non-correlated, $S = 1$, while $S < 1$ at higher densities [66]. Here q is the wavevector, that is proportional to the scattering angle θ and inversely proportional to λ:

$$q = \frac{4\pi n \sin(\theta)}{\lambda} \tag{2.2}$$

2.3.1. MIE SCATTERING ON SPHERICAL AND ROD-SHAPED PARTICLES

In order to demonstrate the accuracy of Mie scattering theory, and also to illustrate some concerns that should be considered during light scattering experiments, we calculate angle-resolved radiation patterns and extinction cross-sections in a home-written Python script based on Mie scattering theory for the radiation patterns of spherical particles [41], assuming the suspension is sufficiently dilute such that the structure factor $S = 1$. We verified that the extinction cross-section vanishes in the following limits: the particle radius $r \to 0$, the relative refractive index between the solvent and the scattering particle $\frac{n}{n_s} = 1$, and $\lambda \gg r$. We confirmed that the shape of the scattering curves agrees with textbook results [42].

We experimentally validate the accuracy of Mie scattering by applying the theory to an experimental measurement of the optical density of a suspension of spherical particles. In Figure 2.3 we show the turbidity of a dilute suspension (volume fraction $\phi = 10^{-5}$) of latex beads ($n = 1.6$, diameter of 300 nm, Polysciences, Hirschberg an der Bergstrasse, Germany) in water ($n = 1.33$) over a wavelength range from $\lambda = 350$ nm to $\lambda = 900$ nm with 1 nm scanning intervals, together with a fit to Mie scattering theory. For comparison, we also show the fits to Rayleigh and Rayleigh-Debye scattering models. The only free fitting parameter in the models is the radius of the beads; fitting the data to the model gives an optimum at $d = 298.0$ nm for Mie, $d = 200.2$ nm for Rayleigh, and $d = 194.6$ nm for Rayleigh-Debye scattering theory. The close agreement of the Mie scattering result with the diameter specified by the manufacturer illustrates the strength of Mie scattering theory, even when the particle dimension is comparable to the wavelength of the scattered light.

We now use Mie scattering to calculate the radiation patterns of individual particles. Figure 2.4a shows the radiation pattern for a spherical particle with a radius of 50 nm, illuminated by light with $\lambda = 500$ nm and a relative refractive index of $1.6/1.33 = 1.203$, where 1.6 and 1.33 are the refractive indices of polystyrene and water, respectively. The extinction cross-section of the particle is $0.0064\times$ the geometrical cross-section. In Figure 2.4b the scattering pattern is shown for a particle with $r = 500$ nm in otherwise sim-

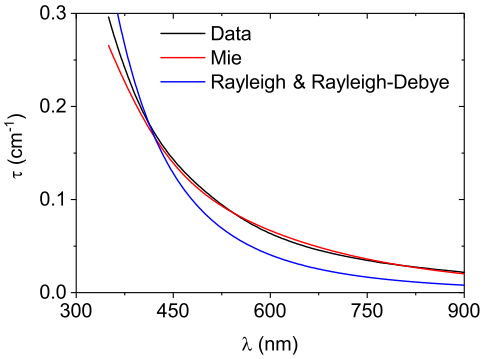

Figure 2.3: Fitting of Mie, Rayleigh and Rayleigh-Debye scattering models to an experimental measurement of the optical density of a 0.001%-suspension in water of spherical particles of 300 μm diameter. The graph shows the experimental data (black), and fits using Mie scattering (red) and Rayleigh and Rayleigh-Debye scattering (blue). As the latter two scattering models have the same wavelength dependence ($y(\lambda) \propto \lambda^{-4}$), their functional form is identical; the difference lies in the parameter extraction. In all models, the only free parameter in the fits is the particle diameter. The obtained particle radii are 149.0 nm, 100.1 nm and 97.3 nm, respectively.

ilar conditions, where the scattering efficiency (the ratio of the scattering cross-section to the geometrical cross-section) is 2.57[3]. Apart from an increase in scattering amplitude, the directionality of the scattered light is more in the forward direction than for the smaller particle. This demonstrates two experimental challenges: for large particles, a relatively large part of the scattered light propagates in the same direction as the non-scattered light beam. The cross-section of the incident beam and the pinhole in front of the detector should therefore be as small as possible to reduce the effect of scattered light still reaching the detector. Secondly, in a polydisperse system with a range of particle sizes, the scattering from particles with a larger radius will have a disproportionally high contribution.

Using Mie scattering theory, we demonstrate a final experimental point of concern in the analysis of scattering experiments on rod-like particles. In Figure 2.5 we show the scattering cross-section, calculated for an infinitely long cylinder with a 100 nm radius and $n = 1.6$ in a solvent with $n_s = 1.33$, as a function of the angle θ of the cylinder orientation with respect to the incident light. For $\theta = 0$ the scattering cross-section vanishes, increasing to a maximum value for $\theta \approx 7°$ and converging to an intermediate value for higher values of θ. In the calculation of the radiation pattern for an ensemble of cylinders, the scattering cross-section is averaged over the entire range of θ. This is done under the implicit assumption that rods are isotropically oriented. If there is an alignment of rods, it needs to be taken into account that the preferential rod orientation affects the magnitude of light scattering [69, 70].

[3]Although seemingly counter-intuitive, the extinction cross-section can be larger than the geometrical cross-section ([67, 68]); a phenomenon that is for example used in the design of solar cells, to optimize light capturing efficiency.

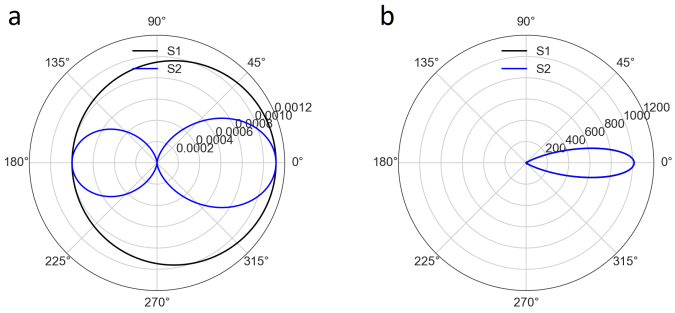

Figure 2.4: Scattering patterns (intensity versus scattering angle, where 0° is the forward direction) calculated using Mie theory for a spherical particle, for both polarizations (S1 and S2) of the incoming light. The radiation pattern is symmetric around the horizontal axis. The wavelength of the incident light $\lambda = 500$ nm, and the particle has a relative refractive index n/n_s of 1.203. **(a)** A sphere with $r = 50$ nm, and **(b)** a sphere with $r = 500$ nm. With increasing particle diameter both the shape and the intensity of the scattering pattern change.

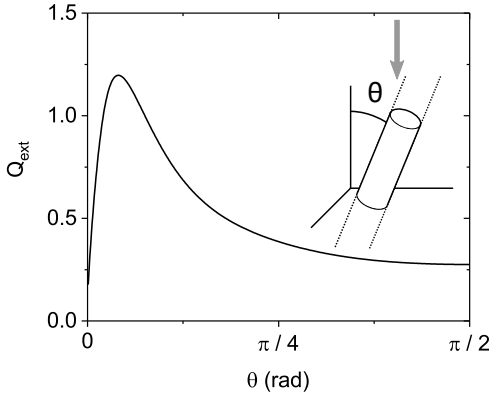

Figure 2.5: Light scattering ($\lambda = 500$ nm) on an infinitely long cylinder with radius 100 nm. The calculated extinction cross-section Q_{ext} for the particle is plotted as a function of the angle of incidence θ. The inset shows a schematic of a (finite) cylinder, with the orientation θ of the cylinder axis with respect to the incident light (grey arrow).

2.3.2. LIGHT SCATTERING MODELS FOR FIBROUS NETWORKS

Several studies have proposed light scattering models valid for solutions of fibers or networks of fibers [51, 52, 71–73]. These models assume an isotropic ensemble of rods, which have a uniform mass density and an aspect ratio $\gg 1$. Moreover, the fiber refractive index n is assumed to differ little from the surrounding medium with n_s, such that $1-\frac{n}{n_s}$ multiplied by the rods' radius r is small ($\ll 1$). This is a simplification with respect to the Mie scattering discussed above, in the sense that here the difference in optical path length is assumed to be small for light travelling outside versus within the scattering medium. Furthermore, the fibers are assumed to be non-interacting such that the structure factor $S = 1$. The form factor $P(q) \approx 1$ in the Rayleigh limit where the scattering particle is much smaller than the wavelength of the incident light, while $P(q)$ becomes q-dependent (i.e., smaller than 1) for increasing q-values or increasing particle size.

In order to describe light scattering experiments on fibrin gels, we start with the implementation of the Carr-Hermans-derived form factor [51]:

$$\frac{c}{\tau\lambda^3} = \frac{1}{\mu}\frac{15\,\mathrm{n_A}}{88\pi^3 n(dn/dc)^2}(1+\frac{23}{77}\pi^2 n_s^2(2a)^2\lambda^{-2}) \tag{2.3}$$

where τ is the measured turbidity in units of cm^{-1}, obtained by multiplying the extinction coefficient by $\ln(10)$, $\mathrm{n_A}$ is Avogadro's constant, dn/dc is the differential refractive index, c is the protein concentration, n_s is the solvent index of refraction, and the fitting parameters are fiber mass-per-length μ and radius a. This formula states that there is a linear relation between $\frac{c}{\tau\lambda^3}$ and λ^{-2}.

A later paper re-evaluating the Carr-Hermans approach [52] commented that the Taylor expansion used to obtain Eq. 2.3 is invalid, and proposed the following equation (where an erroneous prefactor was corrected in Ref. [74]):

$$\tau\lambda^5 = 2\pi^3 C\, n_s\, \mu(\frac{dn}{dc})^2\frac{44}{15}(\lambda^2 - \frac{2}{3}\frac{184}{154}\pi^2 a^2 n s^2) \tag{2.4}$$

According to this model, there is a linear relation between $\tau\lambda^5$ and λ^2, where the slope of this curve relates to the mass-per-length ratio and the intercept to the fiber radius. Interestingly, later work [53] claims that Eq. 2.4 is inaccurate, and Eq. 2.3 is more robust.

Fibrous networks generally have a fractal structure due to branching and cross-linking of the fibers [75–77]. It is therefore more accurate to account for a contribution of the structure of the network to the total scattering intensity by including the structure factor $S(q)$ [59]:

$$R(q) = K * c_F * M * S(q) * A(q) * P(q) \tag{2.5}$$

where $R(q)$ is the scattered intensity distribution, such that $R(q)$ integrated over the solid angle $d\Omega$ gives the scattered intensity $I_{scat} = \int_0^{max} R(q)\sin(\theta)d\theta d\phi$. K is an optical constant, $K = 4\pi^2 n^2(\frac{dn}{dc})^2\frac{1}{N_A\lambda^4}$, and M the blob molecular weight, $M \approx \mathrm{n_A}\rho\pi\xi^{D_m}a^{3-D_M}$, ρ the fiber mass density, ξ the blob size (Figure 2.6 and Refs. [59, 65]), and D_m the 3D network mass fractal dimension. The rationale for the addition of the fractal dimension in the structure factor is to take into account that networks have a fractal structure. In the case of isolated fibers, where $D_m = 1$ and ξ is the length of the fiber segment, M reduces to the mass of a straight cylinder. The structure factor $S(q)$ describes the spatial

correlations among blobs:

$$S(q) = 1 - \beta \exp(-\frac{q^2 \xi^2}{4\pi\eta^2}) \tag{2.6}$$

where β is a parameter describing the amplitude of spatial correlations between the blobs, and η the level of overlap between the blobs, where $\beta \approx 1$, $\eta \approx 1$ [53]. $A(q)$ is the blob form factor, describing the internal structure of the blob:

$$A(q) = \frac{1}{(1 + (\frac{q\xi}{\delta(D_m)})^2)^{D_m/2}} - \frac{(2a/\xi)^{D_m}}{(1 + (q * d/\delta(D_m))^2)^{D_m/2}} + (\frac{2a}{\xi})^{D_m} \tag{2.7}$$

where δ is a function that adopts a sigmoid shape between $\delta(D_m = 1) \approx \pi$ and $\delta(D_m = 2) \approx 2.76$:

$$\delta(D_m) = \pi - 0.38 * (\frac{\tanh(D_m - 1.44)/0.1 + 1}{2})^{0.5} \tag{2.8}$$

$P(q)$ is finally the form factor of the cylindrical rod-shaped segments:

$$P(q) = (\frac{2 * J_1(q * a)}{q * a})^2 * (\frac{2 * Si(q * 2a)}{q * 2a} - \frac{\sin(q * a)}{q * a})^2 \tag{2.9}$$

where $J_1(x)$ is the first order Bessel function and $Si(x)$ the sine integral. Note that the form of $P(q)$ slightly differs from the formula given in [53], the latter containing an error that is corrected in [78]. To obtain the turbidity τ, we integrate $R(q)$ over a solid angle $d\Omega$:

$$\tau = \int_0^{2\pi} \int_0^{\pi} R(q(\theta)) \frac{1 + \cos(\theta)^2}{2} d\Omega \tag{2.10}$$

We then replace $q(\theta)$ by $\sin(\theta/2)$, and using that $\cos(\theta) = 1 - 2\sin(\theta/2)$, we can substitute:

$$\frac{1 + \cos(\theta)^2}{2} = \frac{1 - (1 - 2x^2)^2}{2} = 1 - 2x^2 + 2x^4 \tag{2.11}$$

Furthermore, the azimuthal integration $\int_0^{2\pi} d\phi = 2\pi$ and the integration limits of the θ-integral change from $0, \pi$ to $0, 1$.

To determine ξ, we make the approximation that the blob size is equal to the pore size. To determine the pore size of our fibrin networks, consisting of bundles of protofibrils of *a priori* unknown thickness, we multiply the mass-per-length ratio μ of a single protofibril by the number of protofibrils per fiber N_p, and divide by the protein concentration c. This ratio is essentially the area in the network that is belonging to a single fiber. We take the square root to obtain ξ (in units of length):

$$\xi = \sqrt{\frac{\mu\, N_p}{c}} \tag{2.12}$$

We use this value of ξ as input in Eq. 2.5 - 2.9 to obtain a new value of N_p, and iterate until N_p and ξ remain constant. A similar form of self-similarity is also applied in [53], where the fractal dimension is iteratively determined in a polymerizing fibrin network.

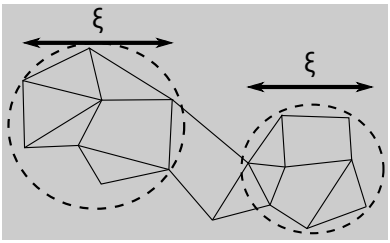

Figure 2.6: Schematic representation of the blob size ξ, inspired by Ref. [59]. The blob size ξ is the size of a region where fibers are correlated.

Finally, we take into account the wavelength dispersion in the values of n and $\frac{dn}{dc}$ by using Cauchy's empirical relations:

$$n(\lambda) = A_1 + \frac{A_2}{\lambda^2} + \mathcal{O}(\lambda^4) \tag{2.13}$$

$$\frac{dn}{dc}(\lambda) = B_1 + \frac{B_2}{\lambda^2} + \mathcal{O}(\lambda^4) \tag{2.14}$$

where we use the values for A_1, A_2, B_1 and B_2 as shown in Table 2.1, obtained from earlier experiments [51, 53, 55].

Name	value	unit
A_1	1.3270	-
A_2	3.0595×10^{-3}	μm^2
B_1	0.1846	cm^3/g
B_2	2.550×10^{-3}	$cm^3 \mu m^2/g$

Table 2.1: Values for Cauchy's wavelength dispersion for a fibrin gel in an aqueous solution, obtained from Ref. [53].

2.3.3. FRACTAL DIMENSION

The (mass) fractal dimension, used in the light scattering model described above, is a dimensionless number that quantifies the fractality, the degree to which a structure repeats itself on smaller or larger length scales. A straight line has a fractal dimension $D_m = 1$, while D_m increases for systems with a more fractal structure, to a maximum of $D_m = 2$ and $D_m = 3$ for a two- and three-dimensional system, respectively.

One way to experimentally determine D_m is through a combination of static and dynamic light scattering [53, 79]. However, as the setup required for this kind of analysis is not commonplace in most labs, and requires samples to have a low optical density to ensure that no multiple scattering occurs, we will instead determine D_m through analysis of images obtained by fluorescence microscopy. There are multiple methods to determine the fractal dimension from images [80–82], two of which we discuss here. The first

method involves computing the power spectral density by Fourier transforming the images [59, 83, 84], while the second method involves a box counting method [83, 85, 86]. As detailed in Appendix 2.A, we found that the box counting method generates artefacts. In the remainder of this Chapter, we therefore use the power spectral density method.

To get an intuition for the behaviour of D_m for random fibrous networks in both 2D and 3D, we benchmark the image analysis methods by applying them on *in silico* generated networks. The *in silico* networks are the networks generated and analysed in Ref. [59], which were generated by randomly picking points in a 3D-volume. Every point was then connected to its two nearest neighbours, and also to the third nearest neighbour if the sum of the two largest angles between the three newly created filaments exceeded 240°. This procedure was repeated for every nodal point, regardless of the number of filaments already connected to the neighbouring nodal points. The density of the network was varied by increasing or decreasing the number of generated points. In this way, a network is generated with a minimum connectivity of $z = 3$, yet an average connectivity $z > 3$. The topology of the networks generated in this way was shown to closely resemble that of actual fibrin networks [59].

To make a comparison between the PSD analysis in two and three dimensions, we extract a 2D slice from the 3D *in silico* network. To this end, we took the maximum projection of slices with a thickness of 1 μm, resembling the actual thickness of a single confocal slice, which is set by the diffraction limit [87]. Two examples of 2D slices from networks of different densities, together with a 3D stack, are shown in Figure 2.7.

The power spectral density $P(q_x, q_y)$ of two-dimensional computational or experimental fiber images with an intensity distribution $I(x, y)$ is given by

$$P(q_x, q_y) = \int |I(x, y) e^{-2\pi i (q_x x + q_y y)}|^2 dx\, dy \tag{2.15}$$

where q_x and q_y are the spatial frequencies in x and y, respectively. In words, this is the square of a two-dimensional Fourier transform, with the absolute value to obtain a real value of $P(q_x, q_y)$. Radial integration then gives the power spectral density $P(q_x, q_y)$. This is easily extended to three dimensions:

$$P(q_x, q_y, q_z) = \int |I(x, y, z) e^{-2\pi i (q_x x + q_y y + q_z z)}|^2 dx\, dy\, dz \tag{2.16}$$

The slope of the power spectrum provides the network fractal dimension [88]:

$$I(q) \propto q^{-D_m} \tag{2.17}$$

When we perform a power spectrum analysis, we obtain, after radial integration, an intensity as a function of q. We use a fitting routine where we first take the logarithm of the radially integrated intensity, to prevent that the large intensities (at low q-values) contribute disproportionally to the fit. For our *in silico* generated networks, we use a fitting regime between $q = 0.53$ pixel^{-1} and $q = 2.09$ pixel^{-1}, corresponding to spatial lengths between 3 and 12 pixels. The lower limit of this regime was chosen to avoid single-pixel artefacts, while the upper limit was chosen to stay below the average fiber length.

An example of the power spectral density with a fit of the fractal regime is shown in Figure 2.8a, together with the fractal dimensions obtained for a series of networks with varying fiber density in Figure 2.8b. We find that D_m increases with increasing network density. We furthermore find that D_m is almost the same when calculated from the PSD of 2D slices or from the PSD of the 3D stack. This finding is in contrast to a reported empirical relation $D_{M,3D} = D_{m,2D} + 0.9$ obtained from confocal image stacks of collagen networks [89, 90].

In Figure 2.9 we show a single slice and a 3D-view from a confocal fluorescence stack of a 1 mg/ml fibrin network. The radially integrated power spectral density is shown in panel a and b for 2D and 3D, respectively. In the radially integrated curves we can identify several features on different length scales [91]. The largest q values, corresponding to the smallest spatial features, contain limited information, as the pixel size (64 nm) is smaller than the diffraction limit in the imaging plane ($\frac{\lambda}{2NA} = \frac{540}{2*1.4} = 193$ nm [87]). On the other side, q is limited by the size of the image, 127 μm. In between these limits, we can obtain the fractal dimension of the network from the slope of the curve using Eq. 2.17. Here we chose a fractal region with a q-range between 0.6 μm (three times the diffraction limit) and 10 μm. From the slope of the power spectral density we find $D_m = 1.51$ and $D_m = 1.54$ for two and three dimensions, respectively. Again, we find that analysis of 2D projections or 3D stacks results in the same value of D_m.

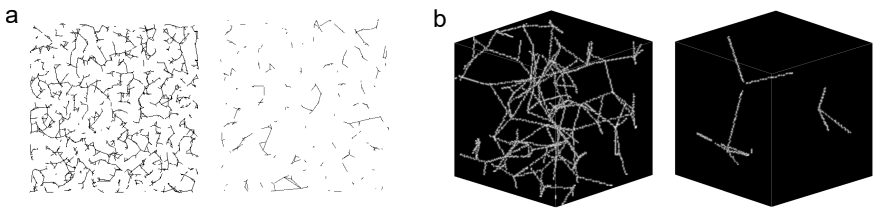

Figure 2.7: (a) Examples of $50\times50\times1$ μm slices of the *in silico* networks [59], at the highest (left) and lowest (right) network concentration, with a network mass of $M = 2.7\times10^{-3}$ and $M = 1.1*10^{-3}$, respectively. The mass is the fraction of the pixels containing a filament (with a width of 1 pixel) in the 3D *in silico* network (see also Figure 2.8b). **(b)** The corresponding 3D view of $5\times5\times5$ μm cubic sections.

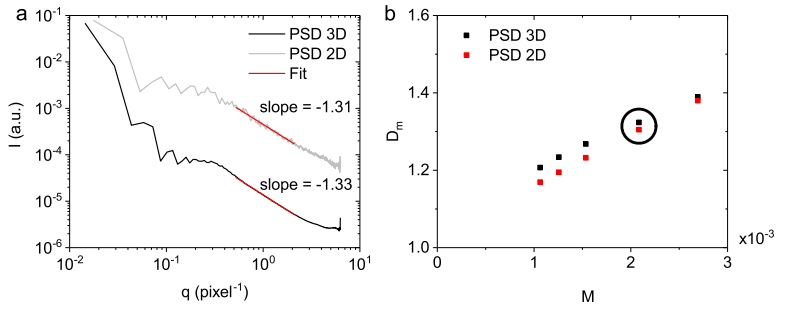

Figure 2.8: (a) The intensity I of the power spectral density (PSD) as a function of q for a 2D and 3D *in silico* network (encircled in panel b). The fractal regime (between 3 and 12 pixels) has been fitted (red line), the fractal dimension is obtained from the slope. The PSD of the 2D slice is more noisy since the input image is smaller than the 3D stack. To overcome this, the average D_m is taken of multiple slices from the same stack. For clarity, the curves have been shifted along the y-axis. **(b)** The fractal dimension D_m as a function of network mass M (the fraction of all pixels containing a filament) of the *in silico* networks, obtained from the PSD in three and two dimensions, resulting in a nearly identical D_m.

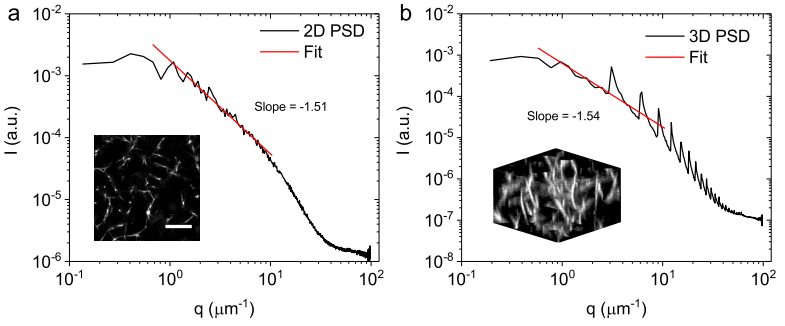

Figure 2.9: Power spectrum analysis of a confocal fluorescence image stack of a 1 mg/ml fibrin network, taken 20 μm above the microscopy coverslip. **(a)** The radially integrated power spectral density of a 2D slice (black curve), with a power law fitted to the fractal region, between 0.60 μm and 9.3 μm (red line). The slope of the fitted power law is -1.51. The inset shows a single slice from the 3D stack shown in **(b)**. The scale bar is 10 μm. **(b)** The radially integrated power spectral density of a 3D stack (black curve), with a power law fitted to the fractal region, between 0.59 μm and 10.8 μm (red line). The slope of the fitted power law is -1.54. The separation in z between slices (1 μm) shows up as spikes in the 3D-power spectrum. The inset shows a 3D view of a 1 mg/ml fibrin network, with dimensions $20 \times 20 \times 10$ μm.

2.4. RESULTS AND DISCUSSION

To test the performance of the light scattering models described in Section 2.3.2, we performed turbidimetry measurements on fibrin gels prepared at three different concentrations, 1, 2 and 4 mg/ml. We perform fits to all the models (the dilute colloidal rod model (Carr-Hermans) [51], the dilute colloidal rod model (Yeromonahos et al.) [52], and the fractal network model (Ferri et al.) [53]), both with and without a correction for wavelength dispersion. We perform the fits over a wavelength range between $\lambda = 450$ nm and $\lambda = 900$ nm. In Figure 2.10 we show the raw data and the fits for the 1 mg/ml fibrin gel for the three different models, including a correction for wavelength dispersion. As Eq. 2.3 and Eq. 2.4 predict a linear relation between $\frac{c}{\tau\lambda^3}$ and λ^{-2}, and $\tau\lambda^5$ and λ^2, respectively, we changed the axes in Figure 2.10a and b to reflect this. We show the best-fit values for the fiber radius and the number of protofibril per cross-section for the different scattering models and experimental conditions in Table 2.2.

Since the fractal dimension significantly deviates from unity (Table 2.2), we cannot assume that $S = 1$, and therefore the dilute colloidal rod model (Carr-Hermans) and the dilute colloidal rod model (Yeromonahos et al.) should be used very cautiously. This is reflected by the observation that the fractal network model (Ferri et al.) describes the experimental data over the entire wavelength regime, while panel a and b in Figure 2.10 show that the linear relations for the rescaled turbidity data predicted by the two models assuming $S = 1$ are not entirely attained. In that light, it is perhaps surprising that especially the values for the number of protofibrils per fiber, and to a lesser extent also the fiber radius, show little variation between the different scattering models. The differences between the dilute colloidal rod model (Carr-Hermans) and the dilute colloidal rod model (Yeromonahos et al.) are less than 5%, which could be expected since the difference between those models is just a Taylor expansion. The correction for the wavelength dispersion on the values of n and dn/dc is substantial in all three cases: the difference is on average 24% in the fiber radius and 3% in the mass-per-length ratio.

The absolute values of the difference between the data and the fitted functions are shown in Supplementary Figure 2.3. Overall, the fractal network model (Ferri et al.) with a correction for wavelength dispersion has the lowest residual, indicating that the experimental data is best described by this model.

A drawback of the fractal network model (Ferri et al.) is that the fitting routine is more complex than for the dilute colloidal rod models (Carr-Hermans and Yeromonahos et al.). When fibrin is polymerized in the presence of a high salt concentration and at a high pH (400 mM NaCl and a pH of 8.5 versus 150 mM NaCl and a pH of 7.4 for our regular fibrin buffer, see Section 2.2.1), the fibers that comprise the network are only several protofibrils thick [54]. We observed that for these gels, the fit of the fractal network model did not converge, as illustrated in Figure 2.11. Here we show the residual square values of the turbidity data of a coarse and fine fibrin gel minus the Ferri light scattering model (Eq. 2.5 - 2.9) with a correction for wavelength dispersion, for a range of fiber radii and mass density. This is essentially an energy landscape, where a minimum indicates that the optimal values for the fit are found. In panel a, for a coarse clot fibrin gel, there is a clear minimum for a particular set of parameters. In panel b, for a fine clot fibrin gel, there is not a single minimum, but rather a band of low residuals. This graphically illustrates why in the fitting routine an optimum combination of parameters was not

found.

A further complication for fine clot fibrin is that the fractal dimension cannot be determined from confocal microscopy images, as the pore size is smaller than the diffraction limit (inset in Figure 2.11b). Hence, for fine fibrin gels, we suggest that alternative methods are used to determine structural properties of single fibers, such as atomic force microscopy (AFM) [92–94] or mass mapping using scanning transmission electron microscopy (STEM) [95]. Furthermore, these techniques can also serve as an independent benchmark for the light scattering analysis.

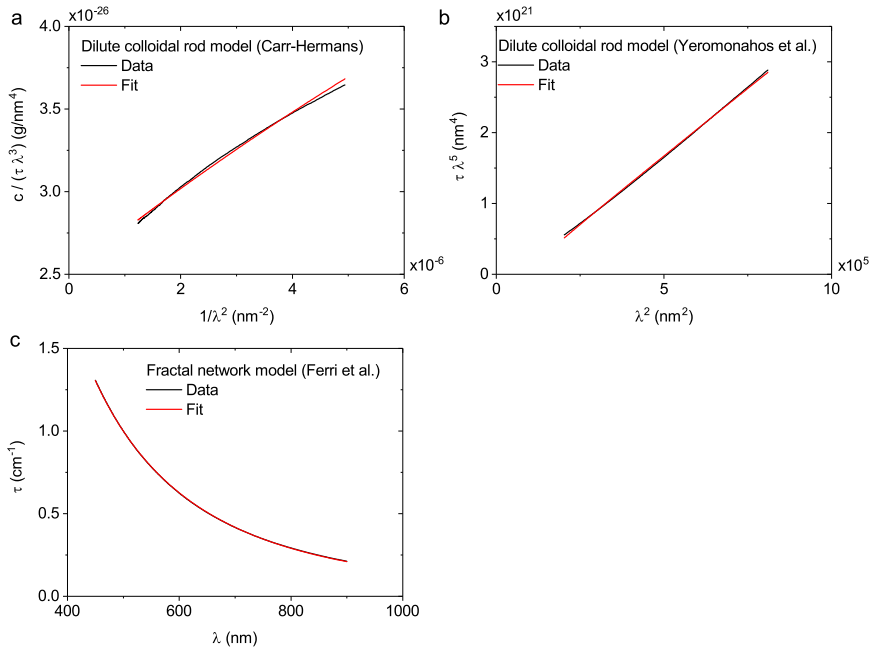

Figure 2.10: Fitting of turbidimetry data of a 1 mg/ml fibrin gel using **(a)** the dilute colloidal rod model (Carr-Hermans) (Eq. 2.3), **(b)** the dilute colloidal rod model (Yeromonahos et al.) (Eq. 2.4), and **(c)** fractal network model (Ferri et al.) (Eqs. 2.5 - 2.9), all including a correction for wavelength dispersion. In **(a)** and **(b)** the axes are changed to illustrate the supposed linear relation between $\frac{c}{\tau\lambda^3}$ and λ^{-2} (Eq. 2.3), and $\tau\lambda^5$ and λ^2 (Eq. 2.4), respectively.

Method	r (nm)	N_p	r (nm)	N_p	r (nm)	N_p
colloidal rod model (Carr-Hermans)	66.2	190	76.0	182	75.6	200
+ wavelength dispersion	81.5	193	91.5	187	90.9	205
colloidal rod model (Yeromonahos et al.)	69.3	186	79.9	181	76.5	194
+ wavelength dispersion	77.6	183	85.9	177	83.3	191
fractal network model (Ferri et al.)	55.2	166	68.0	192	78.8	261
+ wavelength dispersion	80.2	174	97.6	210	109.4	288
Fibrin concentration (mg/ml)	1		2		4	
Pore size (μm)	2.10		1.62		1.35	
Fractal dimension D_m	1.5 ± 0.1		1.5 ± 0.1		1.5 ± 0.1	

Table 2.2: Best-fit values for the fiber radius r (nm) and the number of protofibrils N_p per fiber, obtained from fitting turbidity data of a 1, 2 and 4 mg/ml fibrin gel to the dilute colloidal rod model (Carr-Hermans) [51], the dilute colloidal rod model (Yeromonahos et al.) [52] and the fractal network model (Ferri et al.) [53], both with and without a correction for wavelength dispersion. The pore size is iteratively determined using N_p and Eq. 2.12, D_m is obtained from PSD analysis on 2D fluorescence microscopy slices. Data shown is for $N = 1$ experiment.

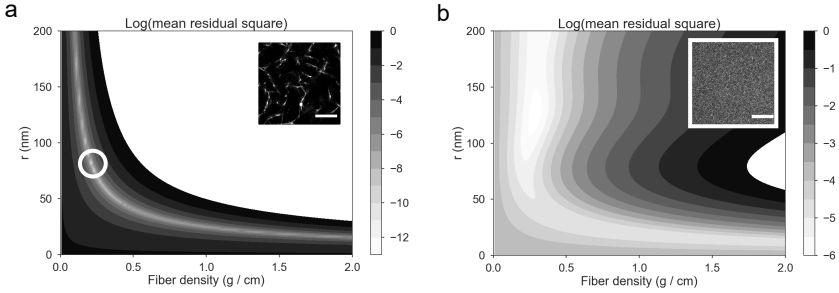

Figure 2.11: Residual squares from the scattering data, subtracted from a fit using the fractal network model (Ferri et al.) with a correction for wavelength dispersion, for **(a)** a fibrin gel polymerized under coarse clot conditions, and **(b)** a fibrin gel polymerized under fine clot conditions. In **(a)** a single minimum is detected (encircled in white), while in **(b)** a broader band of low mean residual squares is found. The insets show a 2D slice from a confocal fluorescence image stack. The scale bar is 10 μm. The fixed parameters in the model were a fractal dimension of $D_m = 1.5$, and $\xi = 2.1$ μm and $\xi = 0.1$ μm for the coarse and fine clot, respectively.

2.5. CONCLUSION

In many fields of science, light scattering is a quantitative, non-invasive technique used in the determination of structural parameters of colloidal particles, including rigid biopolymers. For fibrin, a biopolymer that acts as the mechanical scaffold of blood clots, reliable determination of the filament diameter is an important tool for quantitative modeling of the networks [16], to understand the mechanism of self-assembly of monomeric building blocks into mature fibers [65, 96–101], but also to identify regulatory factors [20, 94, 102, 103] and disease-related abnormalities [92, 104, 105].

In this Chapter, three different models to quantitatively obtain information from light scattering data have been implemented [51–53]. We have shown that the network fractal dimension D_m is larger than unity, and therefore that the structure factor $S < 1$, where $S = 1$ corresponds to the dilute limit. Furthermore, we showed that the wavelength dispersion of light should not be neglected over the wavelength regime that spans our measurements (450 to 900 nm). When the equations describing the turbidity of our samples are complemented with a term correcting for wavelength dispersion, we find that the fiber radius is systematically increased by an average of 24%.

Considering the dilute rod models, we find that the predicted linear relations in Refs. [51, 52] are not fully observed in our experimental data. We indeed only satisfy one of three criteria for applying these models, as mentioned in Ref. [52]: a dilute system such that the structure factor $S = 1$ (with $D_m > 1$, we have $S < 1$), a small fiber diameter compared to the wavelength of the scattered light (with fiber radii $\sim$ 80 nm, the fiber diameter is of the same order as the wavelength of the scattered light), and a small difference between the refractive index of the fiber and solvent (which is indeed the case). We find that the fractal network model (Ferri et al.) with a correction for wavelength dispersion best describes the experimental data.

Note that all three models assume that the particle diameter is much smaller than the wavelength of the scattered light ($\frac{r}{\lambda} \cdot (n_s - n) \ll 1$) (the Rayleigh-Debye criterium). For fibrin fibers, this is criterium is satisfied by only a small margin. A future improvement would be to use Mie scattering theory as the basis of light scattering models, since this holds for cylinders of arbitrary radius.

Furthermore, all scattering models discussed in this Chapter assume that filaments themselves are homogeneous in cross-section. However, it has been shown that fibrin fibers have a dense core and a more open periphery [96, 106, 107]. We propose that an improved scattering model includes non-homogeneity in the fiber cross-section. We note a final caveat in the analysis of turbidity data. The fact that light scattering is a technique that averages over a (relatively) large volume of of the studied material has the obvious disadvantage that information on single scattering objects is lost. Ref. [108] demonstrates a problem with the assumption of homogeneity in fiber radii, using an example of a fibrin network model with a bi-disperse size distribution where the thick fibers are ten-fold thicker than the thin fibers. The thin fibers contribute negligibly to the scattering spectrum, although their effect on other network parameters, such as the permeability to liquid, are significant.

I gratefully thank Fabio Ferri (Università dell'Insubria, Italy) and Mattia Rocco (IRCCS AOU San Martino-IST, Italy) for discussions on the fractal dimension, for their help with analysing the data with their light scattering model and providing the 3D

in silico networks. I also thank Francois Caton (University Joseph Fourier, France), Nicholas Kurniawan (Technical University Eindhoven) and Federica Burla (AMOLF) for discussions on methods to analyse light scattering measurements on fibrin, and Mathijs Vermeulen (Technical University Eindhoven) for discussions on Mikado networks. Finally, I thank the AMOLF workshop for their help in adapting the quartz cuvettes to fit our spectrophotometer.

APPENDIX

2.A. FRACTAL DIMENSION: MIKADO NETWORKS AND BOX COUNTING

There are multiple methods to determine D_m through analysis of images obtained by fluorescence microscopy. Here we use the box counting method, which we apply to two different kinds of *in silico* generated networks.

MIKADO NETWORKS

In Section 2.3.3 we introduced *in silico* networks generated by connecting randomly placed nodal points [59]. Another type of *in silico*-generated networks are Mikado networks [109–111]: 2D networks of randomly placed rigid filaments ("Mikado"). We generated the Mikado networks in an area with size 1, with number density N and a segment length L that is defined in terms of the area size. Every segment is furthermore characterized by a random x and y-coordinate of one of its end points, and a random orientation θ. Periodic boundary conditions are implemented such that every fiber leaving the box on the right will re-enter on the left, and similarly for top-bottom. Unlike Mikado networks used in mechanical simulations of fibrous materials (e.g. [27]), in our simple implementation there is no detection of crossing points, or removal of dangling ends: filament segments that are situated between the filament end and the last crossing point, that do not contribute to the mechanical properties of the simulated network. Four examples of Mikado networks are shown in Supplementary Figure 2.1, where $N = \{100, 500\}$ and $L = \{0.1, 0.3\}$.

BOX COUNTING

A method to determine the fractal dimension from images is the box counting method [83, 85, 86]. The principle is to detect any self-similarity in a structure by counting the number of boxes with a certain size ϵ required to cover the structure. This is repeated for boxes with decreasing ϵ, to obtain a relation between the number of boxes as a function of the box size. When this is plotted on a double-logarithmical scale, D_m can be extracted from the slope.

To determine the fractal dimension, we use the ImageJ plugin FracLac. We set the minimum box size to 5 pixels, to avoid single-pixel artefacts. The maximum box size is 50% of the system size, larger than any of the filaments we consider. The box size increases linearly between the minimum and maximum box sizes in 100 steps. Every image is analysed with 25 different initial positions, to avoid any bias from the initial position.

In Supplementary Figure 2.2a we show the apparent fractal dimension for the Mikado networks obtained from box counting. There is initially a strong growth of the fractal di-

mension with increasing mass (the sum of all pixels containing a filament normalized to the total surface area), starting from 1.0 and saturating at approximately 1.8. We observe that the network mass is sufficient to describe the apparent fractal behaviour of Mikado networks, as different combinations of number density and length with the same mass result in the same fractal dimension. Moreover, when we generate Mikado networks with filament lengths normally distributed around a mean value with a standard deviation $\sigma = 0.05$ and $\sigma = 0.2$ (setting filaments with a negative length to $L = 0$), we find that, irrespective of the width of the distribution, the same relation between mass and fractal dimension holds as for Mikado networks consisting of filaments with a uniform length.

However, using the PSD-analysis, we find that all Mikado networks have a D_m of around 1, independent of network mass. Hence, they are not truly fractal, which could be expected since the fibers are placed randomly and there is no branching. When we apply the box counting method on the networks generated by connecting randomly placed nodal points, using the same parameters as for the Mikado networks, we also find a substantial deviation between the apparent fractal dimension obtained by box counting and the PSD result (Supplementary Figure 2.2b).

Hence, from the PSD-analysis we learn that, although the Mikado networks have overlapping filaments that are detected by the box counting analysis as an apparent fractal structure, they are not truly fractal. Hence, we choose the networks generated by connecting randomly placed nodal points as benchmark for the fractal dimension analysis opposed to the Mikado networks as the former is a fractal structure while the latter is not; and the PSD as analysis tool opposed to the box counting method as the latter generates artefacts.

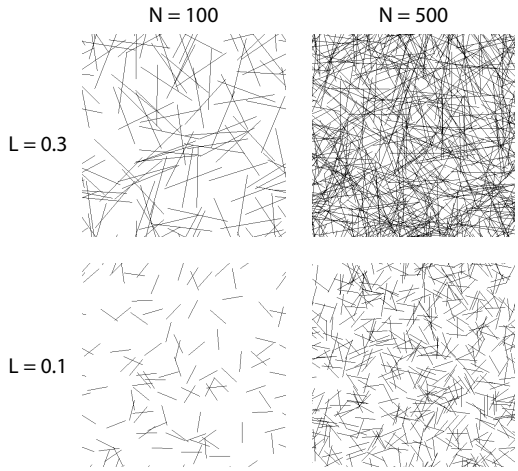

Supplementary Figure 2.1: Examples of Mikado networks, with $N = 100$ and $N = 500$ filaments, and filament length $L = 0.1$ and $L = 0.3$.

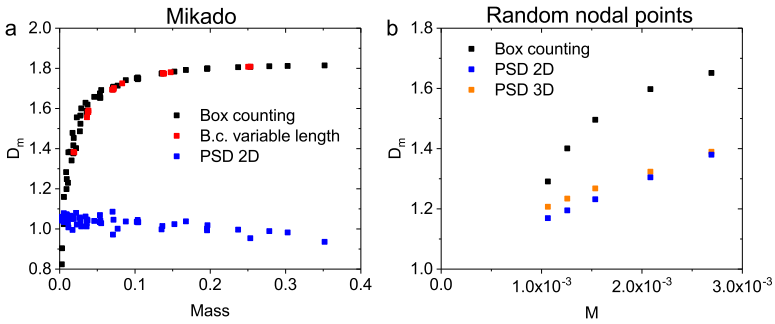

Supplementary Figure 2.2: Fractal dimension D_m as a function of network density for both the Mikado networks and the networks generated by connecting randomly placed nodal points, obtained through box counting (b.c.) and the power spectral density (PSD). **(a)** D_m as a function of mass (the normalized intensity of all pixels containing a filament) of a Mikado network. We observe that different combinations of number density and length with the same mass produce approximately the same fractal dimension. Moreover, we find that Mikado networks generated with filament lengths normally distributed ($\sigma = 0.05$ and $\sigma = 0.2$) around a mean value of $L = 0.2$, follow the same relation between mass and fractal dimension. The fractal dimension obtained from the power spectral density (PSD) shows qualitatively different behaviour, retaining a slope of approximately 1, independent of the network density. **(b)** D_m as a function of network mass for the networks generated by connecting randomly placed nodal points. The PSD analysis consistently show a trend of increasing D_m with increasing network density. The PSD analysis results in a nearly identical D_m, regardless whether the analysis was performed in two or three dimensions. However, the values obtained by box counting differ substantially from those obtained by the PSD analysis.

2.B. RESIDUALS OF TURBIDIMETRY FITTING

In Figure 2.10 we fitted the turbidity spectra to Eq. 2.3, Eq. 2.4, and Eqs. 2.5 - 2.9. In Supplementary Figure 2.3 we show the absolute value of the difference between the fit and the experimental data, normalized by the scattering intensity at each wavelength. In Table 2.3 we show the root mean square values of the residuals in Supplementary Figure 2.3. Overall, the fractal network model (Ferri et al.) with a correction for wavelength dispersion has the lowest residual, indicating that the experimental data is best described by this model.

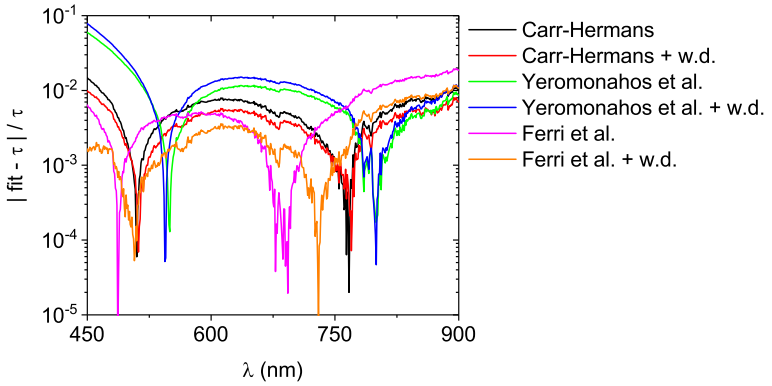

Supplementary Figure 2.3: Residual values when best fit is subtracted from the scattering data (1 mg/ml fibrin gel) for the fractal network model (Ferri et al.) [53], the dilute colloidal rod model (Yeromonahos et al.) [52] and the dilute colloidal rod model (Carr-Hermans) [51], both without and with a correction for wavelength dispersion ("w.d."). Absolute values of the differences were taken and normalized by the turbidity at the corresponding wavelength. The dips in the curves indicate the crossing of the fitted curves with the experimental data.

Method	RMS ($\times 10^{-3}$)
colloidal rod model (Carr-Hermans)	4.3
+ wavelength dispersion	3.0
colloidal rod model (Yeromonahos et al.)	16.5
+ wavelength dispersion	21.1
fractal network model (Ferri et al.)	4.1
+ wavelength dispersion	2.0

Table 2.3: Root-mean-square values of the fits shown in Supplementary Figure 2.3.

3

ELASTICITY AND HYDRAULIC PERMEABILITY GOVERN NORMAL FORCE IN FIBRIN NETWORKS

Positive! Negative!
Always that minus sign
Bio or manmade, what
makes them contrast?

Now please consider the
permeability!
Liquid won't flow when one
measures too fast.

Fibrin, the principal protein responsible for the mechanical integrity of blood clots, is a member of a broad class of materials called "hydrogels". As their name suggests, hydrogels are composed mainly of water, while only a small fraction of the hydrogel mass comprises the polymer network that is responsible for the gel's solid-like behaviour. In previous mechanical studies on fibrin hydrogels, only the influence of the protein network on the mechanical response to external stresses was considered, while the role of the solvent was ignored. In this Chapter, we present data on the poroelastic behaviour of fibrin hydrogels, probed by measuring the normal (axial) force that the gels develop when sheared or compressed between the parallel plates of a shear rheometer. Under compressive deformation, we observe an instantaneous network response, accompanied by a slow, dynamic response of the normal force due to solvent flow, consistent with expectations for fluid-filled elastic networks. Interestingly, we also observe effects of fluid flow in response to shear, despite

the volume-conserving nature of shear deformations. We show that the fibrin hydrogels exhibit a time-dependent normal stress response to an applied shear that is positive at short times, but decreases to negative values with a characteristic time scale set by pore size, which we associate with solvent relaxation. We use a new two-fluid model to interpret the response in terms of a combination of network elasticity and fluid permeation. We find that the model correctly predicts a transient behaviour of the normal stress, which is in excellent agreement with the full time-dependent normal stress we measure. Our results highlight the important role of poroelastic effects in tissue and extracellular matrix mechanics. Our findings suggest a new route to tailor the sign and magnitude of the normal stresses for polymer materials by tuning the pore size, solvent viscosity, and nonlinear shear elasticity.

3.1. INTRODUCTION

GIVEN that water is the main component of the human body (around 70%, depending on sex, age and body mass[1]), it is of little surprise that it is also the main component of most tissues. A mechanical description of tissues and its components should therefore include not only solid components, but also the liquid phase. To describe the mechanical behaviour of biphasic materials composed of an elastic, solid phase permeated by a liquid phase, the theory of poroelasticity was developed [113–115]. In short, this theory constructs a stress field in a poroelastic material, whose physical origin is twofold: stresses originating from an elastic skeleton, and hydrostatic stresses. Elastic and hydrostatic stresses are thus tightly coupled: when a deformation is applied, stresses are induced in the elastic material, and, by equilibrium conditions on the stress field, also in the fluid, inducing liquid flow through the porous material.

The theory of poroelasticity has important applications in the description of living systems. One example is the flow of interstitial fluid through (mineralized) bone tissue [116–119]. Interstitial fluid plays a role in the distribution of nutrients and disposal of waste products, and acts as a medium for mechanotransduction and cellular excitation [120]. It also plays an important mechanical role, as it has been shown that interstitial fluid pressure supports over 90% of the total applied stress during confined compression of cartilage [121–123].

Also in wound repair, where a provisional matrix of fibrin fibers seals off the wound site, water is a major constituent [124]. Nevertheless, at rest the mechanical properties of fibrin gel are dominated by the protein network: the storage modulus G', associated with elastic, reversible deformation, is typically one to two orders of magnitude larger than the loss modulus G'', associated with inelastic flow [125]. In addition, the loss modulus associated with the fibrin network strongly dominates over the loss modulus associated with the solvent.

However, under mechanical deformation, the role of the solvent can no longer be neglected. Upon compression or extension, the volume of the fibrin network changes [31, 126], which, due to the incompressibility of water, induces a flow of liquid through the fibrin network. In turn, this introduces a time-dependency to the force exerted in the direction of compression or extension. Yet also during shear deformation, which is inherently volume-conserving, a normal stress (orthogonal to the applied shear stress) is measured [127].

Although this seems counter-intuitive, materials can shrink (shear contraction) or expand (shear dilatancy) when subjected to a shear stress, as shown by Poynting more than a century ago [128]. Similar behaviour has since been observed in more complex viscoelastic systems, such as granular materials, rubbers and polymer glasses [129, 130]. The tendency of such (synthetic) materials to dilate can be measured as a positive (outward) normal stress or pressure that develops when the material is sheared between two plates with a fixed gap (Figure 3.1a). In case of polymer materials, shear dilatancy is usually described by the classical Mooney-Rivlin model [131, 132], which predicts a normal stress difference $N_1 \sim G\gamma^2$, where γ is the shear strain and G the network shear modu-

[1] However, there is much controversy around the claim that, to keep a right fluid balance, one should drink at least 8 glasses of water a day. An extensive review debunks the urban myth [112].

lus. Unlike the normal stress response to compressive deformations, the normal stress response in shear is fundamentally nonlinear, since its sign cannot reverse when the direction of shear strain γ is reversed. Thus, to lowest order, normal stress is expected to increase as γ^2, even while the shear stress remains linear in γ. An example of this behaviour is illustrated in Figure 3.1a, showing the normal stress of polyacrylamide hydrogels.

Surprisingly, biopolymer networks have been reported to exhibit the opposite response compared to classical polymer materials in normal stress: they contract when sheared [127, 133–136]. This contractile behaviour is illustrated in Figure 3.1b, which shows that fibrin gels develop a negative normal stress under shear. The magnitude of the normal stress increases quadratically with strain, but it reaches values comparable to the shear modulus at significantly lower shear strain ($\gamma \simeq 0.1$) than for classic polymeric materials ($\gamma \simeq 1$). This threshold coincides with the onset strain γ_0 of nonlinear stiffening in the shear stress (Chapter 4). Specifically, semiflexible polymer theories predict [127, 135] that

$$\left|\frac{\sigma_{zz}}{\sigma_{xz}}\right| \sim \frac{\gamma}{\gamma_0} \tag{3.1}$$

where this ratio saturates to a value of order 1 for $\gamma \gtrsim \gamma_0$.

Hence, there is a striking difference in the mechanical response of synthetic and biopolymer hydrogels. Yet also structurally there is a profound difference between synthetic and biopolymer hydrogels: while synthetic gels have a pore size of order 10 nanometers [137], fibrin networks have pore sizes that can be in the micrometer range [138–140].

In this Chapter, we measure the response of fibrin hydrogels to shear and compressive deformation, and, using a two-fluid model, describe it in terms of network elasticity and fluid permeation. We first introduce Darcy's law, where a solvent flows through an unperturbed network, driven by gravity. We then report measurements, using a rheometer, where we study fibrin gels by subjecting them to either shear or compression deformations, while observing the time-dependent normal force exerted by the gels. We find a typical time scale of relaxation, dictated by both the network structure and the macroscopic dimensions of the network. We summarize a recently developed theoretical framework that considers the elastic contribution of the gel and the viscous contribution of the solvent. We experimentally test this framework by varying the pore size of the fibrin gel, the time scale of deformation and the distance over which the solvent flows. We see a transition from a regime of strong viscous coupling between the network and the solvent, suppressing motion of the solvent relative to the network and effectively rendering the gel as a whole incompressible, to a regime where the solvent and network are decoupled. This occurs on a time scale that is well described by the two-fluid model, demonstrating that fluid permeability plays an important role in the mechanical properties of fibrin, both under shear and compression.

This study demonstrates how fibrin gels, along with other fibrous biological materials, are a prime example of the advantage that porous materials offer: high mechanical integrity, while retaining the capability for transport not found in uniform, solid materials. Our results demonstrate the importance of the solvent in the mechanical stability of tissues under applied stress or deformation.

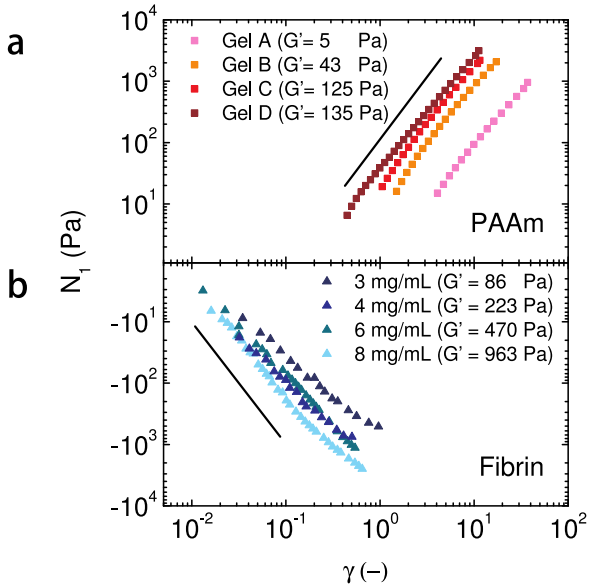

Figure 3.1: Normal stress difference $N_1 = \frac{2F}{\pi R^2}$, where F is the normal force (thrust) reported by the rheometer and R is the sample radius, as a function of the amplitude of the applied oscillatory shear strain γ for **(a)** Polyacrylamide (PAAm) gels prepared with various ratios of monomer-to-cross-linker concentrations. The line indicates a quadratic dependence of $N_1 \sim \gamma^2$, as expected from the Mooney-Rivlin model [131, 132]. In **(b)** $\frac{2F}{\pi R^2}$ is shown for fibrin gels polymerized at 22°C at various fibrinogen concentrations (in mg/ml). The line indicates a γ^2 dependence, but with negative sign. PAAm is a synthetic gel with a pore size of around 10 nm [137], while fibrin is a biopolymer gel with a pore size in the micrometer range (Chapter 2).

3.2. MODELING THE NORMAL FORCE UNDER SHEAR AND COMPRESSION

3.2.1. SHEAR DEFORMATION

When a viscoelastic gel is sheared in a cone and plate rheometer, tension tends to build up along the streamlines, giving rise to tensile circumferential (hoop) stress $\tilde{\sigma}$. Given the curved nature of these streamlines, this stress leads to inward-directed radial forces on the network. By symmetry, hoop stress and, more generally, diagonal elastic contributions to the stress tensor must be even in the applied strain, since they are independent of the direction of rotation of the rheometer. Thus, to lowest order, a quadratic dependence on shear strain γ is expected. We define this force (per unit volume) to be

$$f_r = -\frac{\tilde{\sigma}}{r} \simeq -\frac{1}{r}\tilde{A}G\gamma^2 \tag{3.2}$$

where G is the shear modulus, and the coefficient $\tilde{A} > 0$ is dimensionless.

To quantitatively model the effects of network poroelasticity in the shear rheology of polymer networks, we start from the two-fluid model [141–144] that describes a polymer gel as a biphasic system comprised of a linear elastic network immersed in a viscous and incompressible liquid. The two components are coupled by a force per unit volume, $\Gamma\left(\dot{\vec{u}} - \vec{v}\right)$, acting on the liquid and opposite to the force on the network. The equation for the net force per unit volume acting on the fluid in the non-inertial limit is

$$0 = \eta\nabla^2\vec{v} - \vec{\nabla}P - \Gamma\left(\vec{v} - \dot{\vec{u}}\right) \tag{3.3}$$

where η is the solvent viscosity and P is the pressure. The corresponding equation for the net force on the network is

$$0 = G\nabla^2\vec{u} + (G+\lambda)\vec{\nabla}\cdot(\vec{\nabla}\cdot\vec{u}) + \Gamma\left(\vec{v} - \dot{\vec{u}}\right) \tag{3.4}$$

where the shear modulus G and Lamé coefficient λ are assumed to be of the same order. The dissipative force arises from the relative motion of the solvent, which moves with velocity $\vec{v}$, and the network, which moves with velocity $\dot{\vec{u}}$. For a network with pore size ξ and a fluid with viscosity η, $\Gamma \sim \eta/\xi^2$, since the Stokes drag force on a network strand of size $\sim \xi$ moving with relative velocity $\sim v$ is $\sim \eta\xi\Delta v$ and this acts on a volume $\sim \xi^3$. Given the small polymer volume fraction ϕ of most hydrogels and biopolymer networks ($\phi \sim 10^{-3}$ for fibrin gels), the radial velocity component of the incompressible fluid effectively vanishes and the only radial motion is due to the network. This radial motion, $\dot{u}_r$, generates a radial pressure gradient in the solvent given by:

$$\nabla_r P = \Gamma\dot{u}_r = -\tilde{\sigma}/r - (K/r^2)u_r \tag{3.5}$$

for a cone-plate geometry. The net force on the network has two distinct elastic contributions. The first contribution comes from the hoop stress $\tilde{\sigma}$, which tends to drive the network radially inward (Figure 3.2): hoop stresses generated by shearing tend to drive radial contraction of the network and expulsion of the solvent, much as a twisted sponge

expels water by contracting radially. In this case, the radial component of the force per unit volume acting on the network is of the form

$$0 = -\frac{K}{r^2}u_r - \frac{1}{r}\tilde{\sigma} - \Gamma\dot{u}_r \tag{3.6}$$

which combines with Eqs. 3.2 and 3.3 to give

$$\nabla_r P = \Gamma\dot{u}_r = -\frac{K}{r^2}u_r - \frac{1}{r}\tilde{A}G\gamma^2 \tag{3.7}$$

where the strain γ is independent of r for a cone-plate geometry. Again, by symmetry, $\tilde{\sigma} \sim \gamma^2$ to lowest order, as noted above, although Eq. 3.5 is linear in u_r. The second contribution to the net force on the network comes from a restoring force that balances the radial contraction on long time scales (i.e., as $\dot{u}_r \to 0$). This restoring force originates from the gradient in the elastic shear stress $\sim G\nabla_z u_r$ that results from the axial (z) variation of u. For a cone-plate rheometer with small gap size d and small cone angle α, the restoring force $\sim G/d^2 u_r$. Thus, since $d = \tan(\alpha)r$, $K \simeq \pi^2 G/\tan(\alpha)^2$ in Eq. 3.5. We thus predict a characteristic relaxation time

$$\tau \sim \frac{\eta d^2}{G\xi^2} \tag{3.8}$$

The two-fluid model allows us to perform an even more rigorous test of the mechanism governing the normal stress response of polymer gels, since we can calculate the time-dependence of the normal stress and compare it to experiments. For symmetry reasons, the normal-stress components σ_{xx} and σ_{zz} are expected to have a leading γ^2 dependence on strain. Since the shear stress $\sigma_{xz} \simeq G\gamma$, we define $\sigma_{xx} \equiv A_x G\gamma^2$ and $\sigma_{zz} \equiv A_z G\gamma^2$. For an oscillatory strain $\gamma(t) = \gamma_0 \sin(\omega t)$, the steady state solution of the time-dependent Eq. 3.5 is:

$$N_1^{(\mathrm{app})} = -2A_z G\gamma(t)^2 + \tilde{A}G\gamma_0^2(\mathscr{A}\cos(2\omega t) + \mathscr{B}\sin(2\omega t)) \tag{3.9}$$

where

$$\mathscr{A} = -\frac{1}{8\omega\tau}\left[2\tan^{-1}\left(1+2\sqrt{\omega\tau}\right) + 2\tan^{-1}\left(1-2\sqrt{\omega\tau}\right) - \pi + 4\omega\tau\right] \tag{3.10}$$

and

$$\mathscr{B} = \frac{1}{8\omega\tau}\log\left(1+4\omega^2\tau^2\right) \tag{3.11}$$

with $\tilde{A} = A_x - A_z$ and $\tau = \Gamma R^2/K \sim \eta d^2/G\xi^2$. In the limit where $\omega\tau \gg 1$, Eq. 3.9 reduces to the well-known Mooney-Rivlin expression for incompressible materials, $N_1 = G\gamma^2$ [131, 132]. Shearing will thus increase the pressure toward the axis of the rheometer, which results in a positive contribution to the normal force. Dense hydrogels will therefore effectively behave as incompressible materials for which the normal force F is related to the normal stress difference $\sigma_{xx} - \sigma_{zz}$ by $N_1 = 2F/\pi R^2$, where R is the sample radius [145]. In the opposite limit of networks with a large pore size where $\omega\tau \ll 1$, Eq. 3.9 instead reduces to $N_1^{(\mathrm{app})} = -2A_z G\gamma^2$ as the pressure difference can relax by water efflux and in steady state the two terms on the right hand side of Eq. 3.5 cancel.

Based on prior measurements on a range of biopolymer gels in the limit of $\omega\tau \ll 1$ [14, 127, 133] as well as models of fibrous networks [14, 135, 146, 147], we anticipate $A_z \sim 1/\gamma_c$, where γ_c is the onset strain for nonlinear elasticity, which is typically $\sim 1/10$. Thus, in the limit of low frequencies, not only is $N_1^{(\mathrm{app})}$ negative, but its magnitude can actually be much larger than $\sigma_{xy}\gamma$.

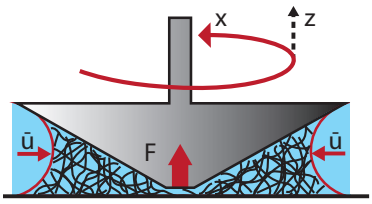

Figure 3.2: Schematic representation of the two-fluid model. A network is positioned between the top cone and bottom plate of a rheometer. Upon rotation of the cone, the network (black) is sheared and shows an inward, radial contraction relative to the solvent (blue).

INCOMPRESSIBLE LIMIT

First, we consider the case of an incompressible medium, corresponding to the limit of strong coupling $\Gamma \to \infty$ and $u_r \to 0$. Here, the network effectively inherits the incompressibility of the solvent and

$$\nabla_r P = -\frac{1}{r}\tilde{\sigma} \tag{3.12}$$

This pressure gradient will lead to a positive normal stress (thrust) contribution measured by the rheometer. Eq. 3.12 can be integrated to give

$$P(R) - P(r) = -\tilde{\sigma}\log\left(\frac{R}{r}\right) \tag{3.13}$$

where $P(R)$ is the pressure at the sample boundary, i.e., atmospheric pressure P_0. The excess pressure,

$$\Delta P = P(r) - P_0 \tag{3.14}$$

can be integrated to give a positive (upward) contribution to the thrust F

$$\int_0^R 2\pi r \Delta P \, dr = 2\pi\tilde{\sigma}\int_0^R r\log\left(\frac{R}{r}\right)dr = \frac{\pi R^2}{2}\tilde{\sigma} \tag{3.15}$$

Adding this to the direct contribution

$$-\pi R^2 \sigma_{zz} \tag{3.16}$$

from σ_{zz}, we find that the normal stress, as reported by a cone-plate rheometer

$$\sigma_N \equiv \frac{2F}{\pi R^2} \tag{3.17}$$

is given by

$$\sigma_N = N_1 = \sigma_{xx} - \sigma_{zz} \simeq (A_x - A_z)\, G\gamma^2 \tag{3.18}$$

implying that

$$\tilde{\sigma} = \sigma_{xx} + \sigma_{zz} \simeq \tilde{A} G\gamma^2 \tag{3.19}$$

where $\tilde{A} = (A_x + A_z)$. In Eq. 3.18 we have assumed not only incompressibility of the medium, but also the standard relationship between the thrust F and the first normal stress difference $N_1 \equiv \sigma_{xx} - \sigma_{zz}$ [145], valid for incompressible materials and a cone-plate rheometer. We have used this assumption to identify $\tilde{\sigma}$ in Eq. 3.12. Although this relationship between F and N_1 is a standard result for the cone-plate geometry, it is worth noting that this can change, depending on the shape of the sample/air interface, or with finite surface tension [145]. In the next section, we also show how this relationship can be violated for compressible networks, such as hydrogels. Nevertheless, because this relationship is so standard in rheology, with rheometers usually reporting the thrust F as N_1, we will use Eq. 3.17 to express the normal stress in the following sections. Importantly, however, for multi-component systems such as hydrogels, this should be considered an effective or apparent N_1, i.e., as reported by a rheometer, which may or may not be equal to the actual stress difference $N_1 = \sigma_{xx} - \sigma_{zz}$.

As noted, the various normal stress components are expected to have leading γ^2 behaviour, while the shear modulus $\sigma_{xz} \simeq G\gamma$ in the linear (shear) elastic regime. Thus, we define

$$\sigma_{xx} \equiv A_x G\gamma^2 \quad \text{and} \quad \sigma_{zz} \equiv A_z G\gamma^2 \tag{3.20}$$

For semiflexible gels, we expect $A_z \sim \frac{1}{\gamma_0}$, based on the prior low-frequency model [127, 133], where γ_0 represents the onset strain for nonlinear elasticity, which is typically of order 10% for biopolymer networks (see Chapter 4). Since σ_{xx} usually is of order but larger than σ_{zz}, we also expect that $A_z \sim \frac{1}{\gamma_0}$. Moreover, as defined, both stress components are strictly positive (tensile) and we expect that $A_x > A_z$, for $N_1 > 0$ in the incompressible limit [148]. These expectations, however, are based on the assumption of affine deformation, which is often not valid for stiff polymer gels [15, 147]. However, in Chapter 4 we show that fibrin gels do deform affinely under shear strains up to $\approx 100\%$.

COMPRESSIBLE LIMIT

In the limit of long times $t \gg \tau$ in Eq. 3.8 and low frequencies $\omega\tau \ll 1$, $\dot{u}_r \to 0$ in Eq. 3.7. Here, ΔP vanishes and the measured apparent N_1 is that of Refs. [127, 133]

$$\frac{2F}{\pi R^2} = \sigma_N = -2\sigma_{zz} = -2A_z G\gamma^2 \tag{3.21}$$

For intermediate times/frequencies, we solve Eq. 3.7 for $u_r(t)$, with $\gamma(t) = \tilde{\gamma}\sin(\omega t)$. The net elastic force per volume on a network element must be balanced by its drag through the solvent, which sets up a pressure gradient in the solvent. Importantly, in spite of the nonlinear dependence on strain, Eq. 3.21 remains a linear equation in u_r, albeit inhomogeneous. The long-time, intermediate frequency steady state (ss) solution to this is given by

$$u_r^{(\mathrm{ss})}(t) = -\frac{\tilde{A} G_0 \tilde{\gamma}^2 r \left(-K^2\cos(2t\omega) + K^2 - 2\Gamma K r^2 \omega \sin(2t\omega) + 4\Gamma^2 r^4 \omega^2\right)}{2\left(K^3 + 4\Gamma^2 K r^4 \omega^2\right)} \tag{3.22}$$

Using this and $\nabla_r P = \Gamma \dot{u}_r$ we find

$$P^{(\mathrm{ss})}(r) = \frac{\tilde{A}G_0\tilde{\gamma}^2}{8} A\left(\cos(2t\omega)\log\left(K^2 + 4\Gamma^2 r^4\omega^2\right) - 2\sin(2t\omega)\tan^{-1}\left[\frac{2\Gamma r^2\omega}{K}\right]\right) + g(t) \tag{3.23}$$

where $g(t)$ is a constant of integration with respect to r, although a function of t, which is determined by $P(R) = P_0$ as above. After a further integration of $\Delta P = P(r) - P_0$, as in Eq. 3.15, and combining with Eq. 3.16, we find the steady-state

$$\sigma_N^{(\mathrm{ss})} = -2A_z G\tilde{\gamma}^2 \sin^2(\omega t) + \tilde{A}G\tilde{\gamma}^2\left(\mathscr{A}\cos(2\omega t) + \mathscr{B}\sin(2\omega t)\right) \tag{3.24}$$

where $\mathscr{A}$ and $\mathscr{B}$ are defined in Eq. 3.10-3.11, respectively. Both of these dimensionless coefficients vanish in the low frequency or fully compressible limit, leaving only the first (axial stress) term on the right hand side of Eq. 3.24.

TRANSIENT BEHAVIOUR

In addition to the steady-state solution for $u_r(t)$, there is also a transient contribution $u_r^{(\mathrm{tr})}(t)$, which can be found by choosing a homogeneous solution of Eq. 3.7 such that $u_r(t) = u^{(\mathrm{ss})}(t) + u^{(\mathrm{tr})}(t) = 0$ at $t = 0$:

$$u^{(\mathrm{tr})}(t) = \frac{\tilde{A}G_0\tilde{\gamma}^2 r}{2K\left(1 + \frac{K^2}{4\Gamma^2 r^4\omega^2}\right)} e^{-\frac{K}{\Gamma r^2}t} \tag{3.25}$$

This transient is most relevant to the case where its characteristic relaxation time $\tau \sim \frac{\Gamma R^2}{K}$ is large compared to the period of oscillation $\sim \frac{1}{\omega}$. Thus, we neglect the second term in the denominator of Eq. 3.25 to find

$$u^{(\mathrm{tr})}(t) \simeq \frac{\tilde{A}G_0\tilde{\gamma}^2 r}{2K} e^{-\frac{K}{\Gamma r^2}t}, \tag{3.26}$$

from which we determine

$$\nabla_r P^{(\mathrm{tr})} = \Gamma \dot{u}_r \simeq -\frac{\tilde{A}G_0\tilde{\gamma}^2}{2r} e^{-\frac{K}{\Gamma r^2}t} \tag{3.27}$$

and the transient contribution to σ_N

$$\begin{aligned}\sigma_N^{(\mathrm{tr})} &\simeq \frac{1}{2}\tilde{A}G_0\tilde{\gamma}^2\left(\frac{t}{\tau}\mathrm{Ei}\left(-\frac{t}{\tau}\right) + e^{-\frac{t}{\tau}}\right) \\ &\simeq \frac{1}{2}\tilde{A}G_0\tilde{\gamma}^2 \exp\left[-1.91\left(\frac{t}{\tau}\right)^{0.78}\right]\end{aligned} \tag{3.28}$$

where $\mathrm{Ei}(x)$ is the exponential integral function. As can be seen either from $\tau \sim \frac{\eta d^2}{G\xi^2}$, which depends on the gap d, or from the time dependence of Eq. 3.27, there is no single relaxation time. Thus, $\sigma_N^{(\mathrm{tr})}$ can be well approximated by a stretched exponential response. The final approximation in Eq. 3.28 is valid to within less than 2% until the transient has decayed to less than 2% of its initial value.

The general expression for σ_N is given by the sum of Eqs. 3.24 and 3.28. For an incompressible system, Eq. 3.18 is recovered for $u_r(t) = u^{(\mathrm{ss})}(t) + u^{(\mathrm{tr})}(t)$ as $\tau \to \infty$. In the limit of low frequency and long times, the steady-state solution reduces to the fully compressible limit of Eq. 3.21.

3.2.2. UNIAXIAL COMPRESSION

When a fibrin gel is subjected to an unconfined compression, we expect an efflux of solvent due to the incompressibility of water, together with a normal force response in the direction of compression. The efflux of solvents in biphasic materials, with an elastic, solid phase and a Newtonian liquid phase, can be described by the theory of poroelasticity [113, 115]. Since the storage modulus of a fibrin gel is typically two orders of magnitude larger than its loss modulus, and the solvent is water with dissolved salts, we assume that we can use this theory to describe the behaviour of fibrin networks under compression. In particular, this theory predicts that the normal force exerted by the liquid phase decays exponentially as fluid flows out of the network [115]:

$$F_n(t) = Ae^{-(t-t_0)/\tau} + B \tag{3.29}$$

where A is the amplitude of the decay and B an offset (a residual normal force exerted by the elastic network), t_0 is the start of relaxation (and is therefore not a fitting parameter) and τ is the typical relaxation time, which scales with the square of the length of the flow path.

3.3. MATERIALS AND METHODS

3.3.1. MATERIALS

Human plasma fibrinogen (Plasminogen, von Willebrand Factor and Fibronectin depleted) and human α-thrombin were obtained in lyophilized form from Enzyme Research Laboratories (Swansea, United Kingdom). All chemicals were obtained from Sigma Aldrich (Zwijndrecht, The Netherlands). Fibrinogen (lyophilized in 20 mM sodium citrate-HCl buffer at pH 7.4) was dissolved in water at 37°C for 15 min to its original concentration (approximately 13 mg/ml) and dialysed against fibrin buffer containing 20 mM HEPES and 150 mM NaCl at a pH of 7.4 in order to remove citrate, which complexes with Ca^{2+} ions that are required for FXIII and thrombin activity. A dialysis membrane with a Molecular Weight Cut-Off (MWCO) of 10 kD was used. 50 ml of sample was dialysed against 1 L of buffer, under continuous stirring. After one hour of dialysis at room temperature, the buffer was replaced, and after another hour, the buffer was replaced again. The third dialysis step was performed at 4°C overnight. After dialysis, the fibrinogen solution was aliquotted, snap-frozen in liquid nitrogen and stored at -80°C. The monomer concentration was checked by spectrophotometric measurements of the absorbance at 280 and 320 nm using a Nanodrop 2000 spectrophotometer (Thermo Scientific) and using an extinction coefficient of 16.0 mg/(ml cm) [51] at 280 nm. The absence of absorption at 320 nm indicates that no aggregates are present. The final fibrinogen concentration was typically around 10 mg/ml. Prior to use, the fibrinogen was quickly thawed at 37°C, and then diluted and mixed with 500 mM $CaCl_2$ at room temperature to a final assembly buffer containing 20 mM HEPES, 150 mM NaCl and 5 mM $CaCl_2$ ("coarse clots"). Dense networks ("fine clots") with an average pore size of 0.08 μm were obtained in fine-clot assembly buffer (400 mM NaCl, 3.2 mM $CaCl_2$ and 50 mM Tris-HCl) at a pH of 8.5 [54].

Thrombin (lyophilized in 50 mM sodium citrate and 0.2 M NaCl) was, on ice, reconstituted in water to its original concentration (approximately 10,000 U/ml), and quickly

aliquotted, snap-frozen in liquid nitrogen and stored at -80°C. Assembly was initiated by the addition and quick mixing of 0.5 U/ml of thrombin from a 20 U/ml thrombin stock, kept on ice for a maximum of 24 hours. After addition of thrombin, the mixture was quickly transferred to a serological pipette or rheometer (Section 3.3.2) to allow *in situ* polymerization.

3.3.2. METHODS

RHEOLOGY

For the normal force experiments under shear stress, fibrinogen stock solution was directly diluted to 8 mg/ml in assembly buffer, without dialysis. Fibrin gels were allowed to polymerize *in situ* for at least 12 hours (22°C and 27°C samples) or 4 hours (37°C samples) between the prewarmed cone and plate geometry. During fibrin polymerization, solvent evaporation was prevented by adding a layer of mineral oil (Sigma Aldrich, M3516) to cover the liquid-air interface. Polyacrylamide gels were polymerized by preparing a mixture of polyacrylamide and N,N'-methylenebis(acrylamide)(Bis) followed by dilution to the desired final concentration. Polymerization was initiated by adding ammonium persulfate (0.5 μg/ml) and tetramethylethylenediamine (1 μL/ml) and gels were allowed to polymerize *in situ* between the rheometer plates at 20°C. During polymerization, we measured the linear elastic shear modulus G' of the fibrin and polyacrylamide gels by measuring the stress response to a small oscillatory shear strain with an amplitude of 0.1% and frequency of 1 Hz.

The normal stress response to an applied shear was obtained by applying Large-Amplitude Oscillatory Shear (LAOS) at a range of frequencies (0.001 Hz to 7 Hz) at a shear stress amplitude of 800 Pa using an Anton Paar rheometer (Physics MCR 302, Graz, Austria). We used a 40 mm, 2° stainless steel cone-plate geometry for all fibrin data reported in Section 3.4.1 and a 50 mm, 2° stainless steel cone-plate geometry for polyacrylamide data, and a series of stainless steel cone-plate and plate-plate geometries in additional experiments reported in Figure 3.13. We measured the time-resolved strain and normal stress response using a Tektronix DPO 3014 oscilloscope coupled to the analogue outputs of the rheometer. The characteristic normal-stress relaxation time was obtained by applying a constant shear stress (400 Pa for the 22°C and the 27°C gels, 550 Pa for the 37 °C gel, 500 Pa for the fine clot gel and a strain of 150% for PAAm). The relaxation data for PAAm were smoothed using a Savitzky-Golay filter. The PAAm-stress relaxation experiment was initiated one day after the polymerization to ensure the stability of the base line of the normal force. For the nonlinear rheology data reported in Figure 3.11 we used a Kinexus Pro+ rheometer (Malvern Instruments, Malvern, United Kingdom) with a 40 mm, 1° stainless steel cone-plate geometry.

To measure the poroelastic behaviour of fibrin gels under uniaxial compression, we use a Anton Paar rheometer (Physica MCR 501, Graz, Austria) to compress a disc-shaped fibrin network, confined between two impermeable surfaces: a stainless steel bottom plate and a steel top plate, separated by an initial gap of 1 mm. We used a steel, 20 mm or 40 mm plate-plate geometry for all fibrin data reported in Section 3.4.4.

One important assumption in the biphasic models is homogeneity in both the liquid and solid phase. However, the pore size of the porous material changes during compres-

sion. There are reports of inhomogeneities in compressed fibrin gels where a fraction of the gel collapses with increasing compressive strain [149–152], a phenomenon that was shown to be rate-dependent [153, 154]. To avoid these complications, we chose to apply small compressive strains (5% - 10%), using low strain rates (0.1%/s).

In the analysis of the time-dependent normal force, we assumed that water is incompressible at the pressures we can apply (the force transducer in the rheometer can apply normal forces up to 50 N), such that any change in the position of the upper plate has to induce a flow of solvent. To verify that during compression experiments, indeed only liquid is expelled while the network remains intact, we collected the expelled liquid and confirmed by spectrophotometric measurements of the absorbance at 280 and 320 nm that no protein was present in the expelled buffer (which simultaneously confirms that all fibrinogen polymerizes into fibrin).

PORE SIZE ANALYSIS

To characterize the pore size of the fibrin gels, we performed light scattering measurements using a spectrophotometer (Lambda35 UV/VIS Perkin Elmer, Waltham, MA, USA). Gels were polymerized in quartz cuvettes and absorbance spectra were taken over a wavelength range from 450 to 900 nm. The mass-length ratio of the fibers was obtained by fitting the spectra to a scattering model that assumes a dilute, random network of rigid cylindrical fibers [16, 52] (see Chapter 2). The average mesh size $\xi \sim \sqrt{1/\rho}$ can be estimated from the fiber length density $\rho = \frac{\mu}{c_p}$, where μ is the fiber mass-length ratio and c_p the fibrinogen concentration. In Chapter 2, we have shown that the value for μ using this light scattering model is accurate within approximately 20%.

To validate the light scattering measurements, we also performed image analysis of confocal fluorescence microscopy images of fibrin networks doped with 5 mole% AlexaFluor 488-conjugated fibrinogen (Life Technologies, Eugene, Oregon, USA). Images were obtained on a Nikon Eclipse TI confocal system with a 100x oil immersion objective (NA=1.40). Image analysis was performed with open-source software introduced in [155, 156], where the radius of the largest circle is obtained (the largest "bubble") that fits within an area enclosed by filaments. Analysis was done on 2 independently polymerized samples. A FFT bandpass filter was applied to each confocal plane, filtering out features smaller than 2 pixels and larger than 30 pixels. As fibers were typically 5 pixels in diameter (the actual radius is smaller, though the diffraction limit does not allow to optically resolve the fiber radius), this filtering step preserves their structure. Various thresholding techniques were tested: the built-in Matlab thresholding function (im2bw), Kapur's thresholding method (also known as the Maximum Entropy method) [157] and Otsu's thresholding method [158]. An overview of images with the FFT filter and thresholding applied is shown in Figure 3.3. The pore sizes obtained using analysis of turbidity spectra and image analysis are shown in Table 3.1. Although absolute values differ, the ratios between the mesh sizes measured for networks polymerized at 22°C and 27°C show a consistent picture where the pore size of the fibrin network decreases by a factor of approximately 1.2 upon an increase in the polymerization temperature. A histogram of the resulting pore size distributions is shown in Figure 3.4.

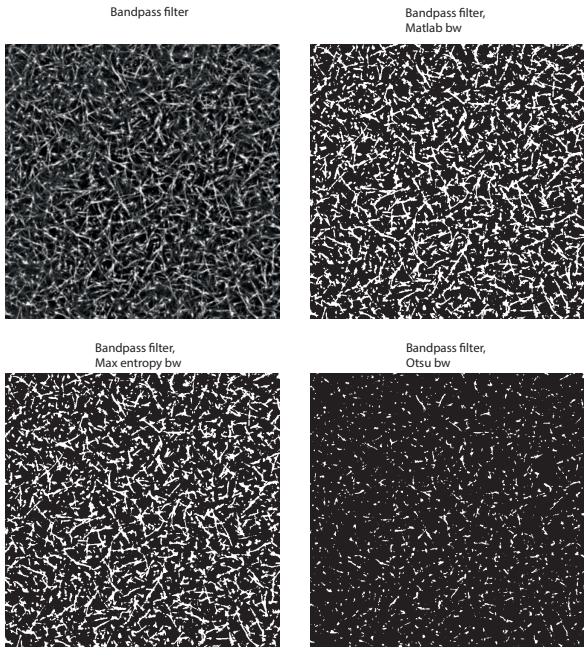

Figure 3.3: Various thresholding methods (Matlab's default thresholding function, Kapur's or Maximum Entropy method [157], Otsu's method [158]) applied on the same confocal plane of an 8 mg/ml fibrin gel polymerized at 22°C, treated with a FFT bandpass filter. Images are 40 by 40 μm.

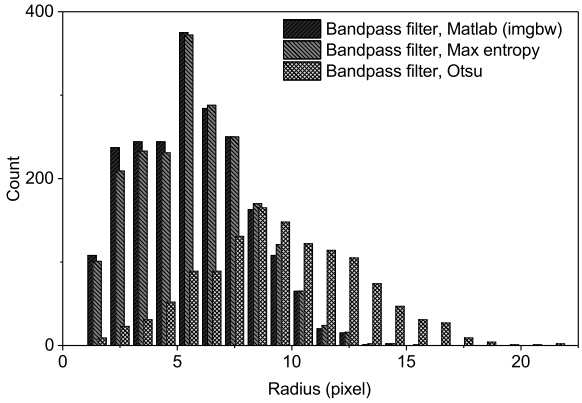

Figure 3.4: Pore size distribution resulting from bubble analysis (Ref. [155]), applied on images that are thresholded using various methods (Figure 3.3).

	22°C, pore size (μm)	27°C, pore size (μm)	Ratio
BP filter, Matlab (imgbw)	0.66 (0.00)	0.54 (0.03)	1.21
BP filter, Max. entropy [157]	0.68 (0.01)	0.60 (0.03)	1.12
BP filter, Otsu [158]	1.19 (0.10)	0.92 (0.12)	1.29
Turbidimetry	0.36 (0.01)	0.29 (0.01)	1.24

Table 3.1: Pore sizes of 8 mg/ml fibrin gels polymerized at 22°C and 27°C, obtained using bubble analysis of confocal images with various thresholding methods, and by turbidimetry. The number between brackets is the standard deviation between measurements.

LIQUID PERMEATION THROUGH UNPERTURBED FIBRIN NETWORKS

To determine the hydraulic permeability κ of fibrin gels, we use a method based on the standardized assay introduced in [139]. A 500 μl fibrin gel was polymerized in a cylindrical capillary, obtained by sawing off the ends of a plastic serological pipette. The fibrin gel has a height of approximately 1.5 cm, while the pipette is >10 cm. The inside of the pipette was roughened using a conical file, and washed using de-mineralized water to remove dust particles. During polymerization, the bottom of the pipette was sealed off using a rubber cap, while the top was sealed off using parafilm to avoid evaporation. The pipette was kept vertical to avoid a tilted meniscus at the top of the fibrin gel, and kept either at room temperature or in an oven set to the desired polymerization temperature. After the network was formed, the parafilm at the top and the rubber cap at the bottom of the pipette were removed and 2 ml of fibrin assembly buffer was gently pipetted on top of the gel and allowed to flow through. We illuminated the setup with a strip of LED-lights, with a diffuse sheet of plastic for homogeneous illumination. The setup, including capillaries, is shown in Figure 3.5a. We recorded time-lapse images of the capillaries with the gel and liquid at regular intervals using a Hamamatsu C4742-95 camera.

In Figure 3.5b, a picture of the pipette containing the fibrin gel and assembly buffer is shown. Using the image analysis software Fiji [159], an intensity profile along the length of the pipette is obtained for every frame. Plotting these profiles next to each other results in a kymograph; an example is shown in Figure 3.6a for a 2 mg/ml fibrin gel of non-dialyzed fibrinogen. We further analyse the meniscus data using a home-written Python script. Although we can already use the kymograph data to obtain the meniscus height as a function of time (the black line in Figure 3.6c), we can improve the accuracy by taking the first derivative of the intensity profile to position (Figure 3.6b), to obtain the grey line in Figure 3.6c. The advantage of using the first derivative rather than the raw data is the lower sensitivity to noise in the derivative, reducing the duration that the analysis script is stuck in a local minimum (or maximum) and thereby making the meniscus-height-versus-time curve more smooth.

Furthermore, depending on the exact position of the meniscus with respect to the camera and illumination, we track either the minimum or the maximum over time. Finally, as we now have the meniscus height in pixels as a function of time, we can convert this to a height in meters by multiplying the height in pixels with the length per millilitre[2] and dividing by the number of pixels per millilitre (the latter is obtained from Figure

[2]Note that multiplication with length per millilitre is equivalent to dividing by the cross-section of

3.5b).

The only difference between our method and the standard assay introduced in Ref. [139], is that the latter approach maintains a liquid column of on top of the gel, and rather than image analysis, the weight of the fluid flowing out of the network is measured with a balance. The advantage of a constant fluid level is the constant driving term, although technically it is more challenging to maintain. We believe our method of image analysis rather than using a balance is more accurate for gels, in particular those with a small permeability: drops fall (and add weight on the balance) in discrete numbers, which is less accurate in describing a dynamic event than a continuous decrease in a fluid level in the pipette. Furthermore, droplets still hanging on the bottom end of the pipette can partly evaporate before their mass is large enough to break off. We verified that evaporation at the top of the pipette plays no measurable role by leaving a pipette with a sealed bottom, filled with water: after 24 hours no decrease in water level was observed.

To obtain κ, we use Darcy's law [160]:

$$Q = \frac{\Delta P\, \kappa\, A}{L\, \eta} \tag{3.30}$$

where Q is the volumetric rate of liquid flow through the network in units of $[m^3/s]$, ΔP $[kg/(m\ s^2)]$ the pressure difference between the top and the bottom of the network caused by the column of liquid on top of the gel, A $[m^2]$ the cross-sectional area of the gel, L $[m]$ the length of the gel in the vertical direction and η $[kg/(m\ s)]$ the viscosity of the buffer (0.001 Pa s). Furthermore, we use that

$$Q = \frac{\Delta h\, A}{\Delta t} \tag{3.31}$$

and

$$\Delta P = \rho\ g\ h(t) \tag{3.32}$$

where ρ is the mass density of the liquid, g the gravitational constant, Δh is the change in water height in a time interval Δt, and $h(t)$ the current height of the water column on top of the gel. We then calculate the hydraulic permeability using known constants and experimentally accessible parameters

$$\kappa = \frac{\Delta h\, L\, \eta}{\Delta t\ \rho\ g\ h(t)} \tag{3.33}$$

where κ is in units of m^2. For every time point, we obtain a permeability value. We then average all values to obtain a single permeability value for an individual sample. Permeability values obtained were $6.7 * 10^{-15}$ m^2 for 8 mg/ml gels polymerized at 22°C and $6.2 * 10^{-15}$ m^2 for 27°C. Although permeability values for fibrin gels polymerized under these experimental conditions have not been reported earlier, previous experiments gave permeability values of comparable order of magnitude, with an expected tendency to lower permeability values for gels containing a higher fibrin concentration [139, 161–163].

the pipette; however, as the cross-section already falls out of the Equation 3.33, we can altogether avoid using it in this way and thereby reduce the error introduced by input parameters.

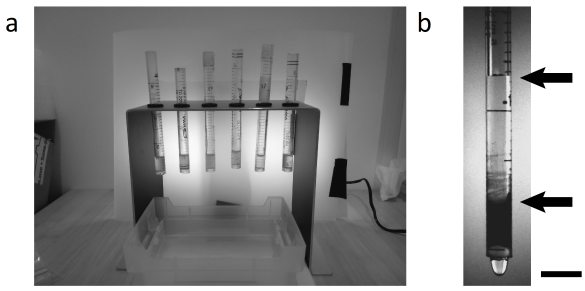

Figure 3.5: The setup for permeability measurements. **(a)** An overview of the setup used to measure permeability. Not shown is the camera that captures images of the capillaries at regular intervals. **(b)** An example of a capillary filled with a fibrin gel (bottom part) and buffer on top. The meniscus of the fluid-air interface is clearly visible and indicated by the top arrow, the fluid-gel interface is also indicated by the bottom arrow , although it is less clear due to the roughening of the pipette. The scale bar (corresponding to panel b only) is 10 mm.

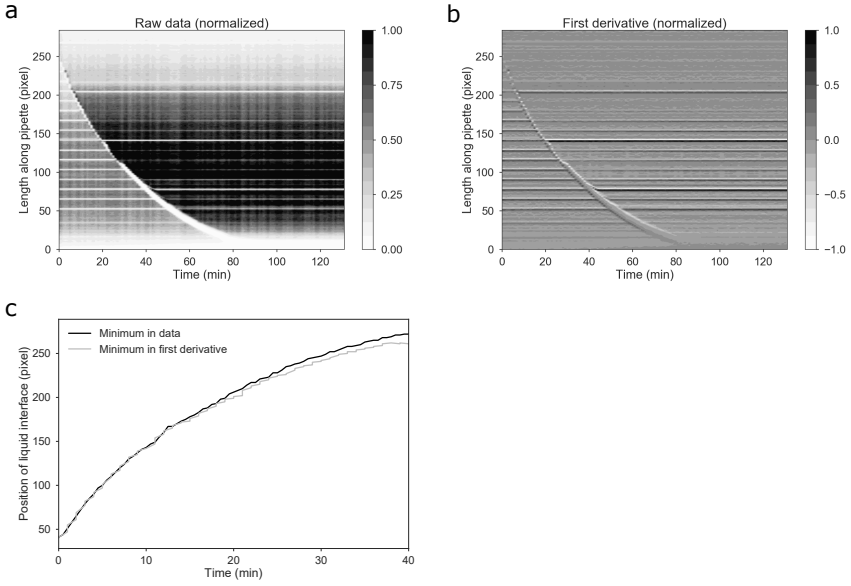

Figure 3.6: Tracking the meniscus of a liquid-air interface for a 2 mg/ml fibrin gel of non-dialyzed fibrinogen. **(a)** An intensity profile as a function of time for the liquid-air interface. The meniscus is clearly visible, gradually moving towards the gel (low values of the length along the pipette). The black markings on the pipette (see Figure 3.5b) show up as vertical stripes. **(b)** First derivative of the same intensity profile. **(c)** Tracking the minimum in intensity as a function of time corresponding to the raw data shown in panel a and the first derivative in panel b. Tracking the position of the derivative gives a more smooth meniscus position over time. Panel a and b are normalized by their maximum intensity.

3.3.3. APPLICATION OF THE BIPHASIC MODEL TO SHEARED NETWORKS

The experiments are done on fibrin samples with different mesh sizes, obtained by varying the temperature, ionic conditions and pH. To test whether the two-fluid model can explain the data, we fit the steady state normal stress data to Eq. 3.24. The free parameters in this equation are A_z and $\tilde{A}$. In this formula ω is the frequency of oscillatory shear stress or strain. The other parameters G, γ_0 and τ can all be directly obtained experimentally. The amplitude of the shear strain, γ_0 is evaluated by fitting a sinusoidal function to the recorded shear strain data. The linear shear modulus G is obtained by fitting a linear stress-strain relation to the stress-strain curves. In all cases, the relaxation time τ is obtained by fitting the normal stress relaxation curves versus time to Eq. 3.28, as shown in Figure 3.7. In Figure 3.10a, τ is plotted versus $1/(G\xi^2)$, to test the predicted scaling ξ and G. The mesh size for fibrin samples was measured (see Table 3.1 in Section 3.3.2), while for PAAm we use a mesh size of 10 nm [137] and the predicted $\tau \sim \eta d^2/G\xi^2$ using $G = 141$ Pa, $\eta = 10^{-3}$ Pa and $d \simeq 1$ mm.

3.4. RESULTS AND DISCUSSION

3.4.1. NORMAL FORCE UNDER SHEAR DEFORMATION

To study the role of porosity in the mechanical behaviour of fibrin network, we first demonstrate how we can tune the pore size of our fibrin networks by changing the temperature, ionic strength and pH during self-assembly [164]. This is shown in Figures 3.7a and b, which show fluorescence microscopy images of two fibrin gels that are assembled at the same monomer concentration of 8 mg/ml but at different temperatures. Using quantitative measurements of the fiber mass-length ratio by light scattering, we calculate average mesh sizes of 0.36 μm and 0.29 μm for these networks (see Section 3.3.2 for details).

To test the influence of pore size on the normal stress response, we subject each network to a constant shear stress and we monitor the normal stress as a function of time. Intriguingly, we find that in each case, the normal stress relaxes from an initially positive or close-to-zero value to a negative steady-state value with a rate that strongly varies with pore size. The characteristic relaxation time, τ, increases from just a few seconds to ~100 s as the pore size of fibrin decreases from 0.36 μm to 0.08 μm. For comparison, we also performed measurements on PAAm gels, which have a pore size of ~ 10 nm [137], much smaller than fibrin gels. We find that the normal stress relaxation time is more than 15 hours (Figure 3.7c). Indeed, we experimentally observe a rapid decrease of the relaxation time with increasing pore size, consistent with the predicted scaling of Eq. 3.8 (see Figure 3.10a). The data suggest that the normal stress is positive as long as the polymer network and the fluid remain viscously coupled, and switches sign to become negative when the fluid can move relative to the network. Importantly, the time scale separating these behaviours is unrelated to the time scales apparent in the linear viscoelastic response, as G' is constant and much larger than G'' over the entire frequency range (see inset of Figure 3.7c).

A key prediction of the two-fluid model is that the response of the normal stress measured in a rheology experiment should depend on the experimental time scale relative to the characteristic relaxation time, Eq. 3.8. To quantitatively test this prediction, we subject the fibrin gels to an oscillatory shear stress with frequencies between 0.001 Hz and 5 Hz, allowing us to conveniently probe a range of time scales from 0.2 to 1000 s in a single experiment. We measure the normal stress response after the system has reached steady state. We focus on fibrin gels polymerized at 27°C, which have a relaxation time $\tau \approx 12.5$ s that lies in the middle of the experimentally accessible frequency range. In steady state, the observed normal stresses are indeed negative over the entire frequency range.

The normal stress response to oscillatory shear at different frequencies is plotted for these gels in Figure 3.8 (blue squares), together with the applied shear stress (black dashed line) and the corresponding fits of the steady state oscillatory normal stress (Eq. 3.9, red line), as functions of time. The only fit parameters are A_z and $\tilde{A}$, since the shear modulus G is measured independently by a small oscillatory shear and the relaxation time τ is measured independently from the normal stress relaxation upon applying a constant shear stress ($\tau = 12.5$ s, Figure 3.7c). We observe excellent agreement between the data (symbols) and the model (solid lines) over the entire range of oscillation fre-

quencies (Figure 3.8), with fitting parameters that are insensitive to frequency (Figure 3.10b).

Perhaps the agreement between experimental data and the theoretical predictions is easier to spot in Figure 3.9a-h where the normal stress response from Figure 3.8 (blue square symbols) is plotted versus shear stress. As clearly seen in the figures, the Lissajous curves change shape as the frequency of the applied shear stress is increased. For oscillation periods longer than τ (low frequencies), the normal stress decreases with increasing shear stress, demonstrating contractile behaviour under shear. In contrast, for oscillation periods shorter than τ (high frequencies), the normal stress increases with increasing shear stress, demonstrating extensile behaviour This experiment unambiguously shows that the normal stress response of a polymer gel is governed by fluid flow, which is suppressed at higher frequencies. The normal stress response is therefore controlled by the network pore size, and is furthermore dependent on the shear modulus G and the gap size d between the cone and the plate (see Figure 3.13).

Figure 3.9i-l shows the normal stress response for a fibrin gel polymerized this time at 22°C. Although the modulus G of the gel is not significantly different from that of the 27°C gel, its mesh size is larger and hence the characteristic time scale τ is expected to be shorter (and the characteristic frequency higher). This means that if both gels are sheared at the same frequency, they are expected to show different Lissajous shapes. Indeed, the Lissajous curve of the 27°C gel sheared at $\nu = 0.01$ Hz is similar to the Lissajous curve of the 22°C gel sheared at $\nu = 0.1$ Hz. We observe excellent agreement between the data and the model over the entire range of applied oscillation frequencies both for fibrin gels polymerized at 22°C and 27°C.

Thus, we find very good agreement overall with the main predictions of our model. These predictions are, strictly speaking, derived in the low strain regime, corresponding to linear shear elasticity. We note that our experimental results in Figures 3.8 and 3.9 were measured at a strain amplitude near 20%, as indicated by the dashed line in Figure 3.11. This is a level of strain below the point at which the response becomes strongly nonlinear: the differential modulus at $\gamma \simeq 20\%$ is within approximately a factor of 2 of its linear value. In practice, it is difficult to measure the normal stress accurately at lower strains over the full frequency range we study here, since the normal stress varies quadratically with strain: at a strain level indicated by the arrow in Figure 3.11, the normal stresses would already be approximately a factor of 10 smaller, which would significantly reduce our ability to accurately probe the time dependence shown in Figure 3.9. Well within the linear regime, with an amplitude of the shear oscillation of 0.4%, the applied shear stress is 10 Pa. However, at that applied shear stress the normal force channel of our Kinexus Pro+ rheometer rheometer shows a noisy signal with an amplitude of approximately 0.001 N, which is comparable to the specified resolution of the normal force sensor of 0.001 N.

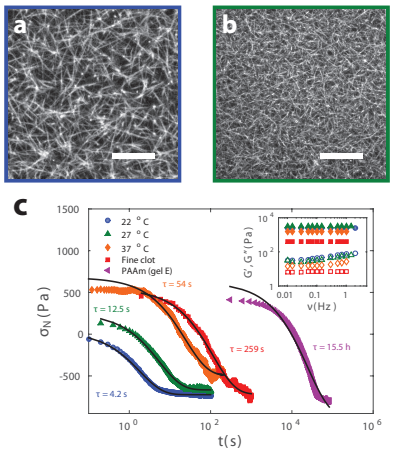

Figure 3.7: Fluorescence confocal microscopy images of fibrin networks whose pore size is tuned by polymerizing under different conditions: at 22°C **(a)** and 27°C **(b)**. The scale bars are 10 μm. The protein content is 8 mg/ml in both samples. **(c)** Normal stress σ_N, given by the apparent normal stress difference $\frac{2F}{\pi R^2}$ obtained from the rheometer thrust F, for four fibrin networks differing in pore size and a polyacrylamide gel, as a function of time after the application of a constant shear stress at $t = 0$. The stress relaxation curves are fitted to an exponential decay derived from the two-fluid model (black lines). The characteristic time for normal stress relaxation is unrelated to the viscoelastic time scale, as shown in the inset where the storage moduli (filled symbols) and the loss moduli (open symbols) of the gels are plotted.

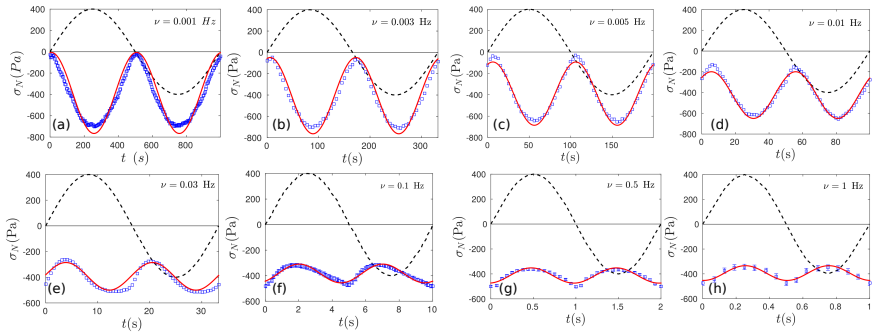

Figure 3.8: Normal stress response σ_N, given by the apparent normal stress difference $N_1^{(\mathrm{app})} = \frac{2F}{\pi R^2}$ reported by the rheometer (blue square symbols), of a fibrin gel polymerized at 27°C to an oscillating shear stress (dashed line) for different frequencies ν versus time. The fit (red line) according to Eqs. 3.9-3.11 is also shown where the fitting parameters are $2A_z$ and $\tilde{A}$. In these equations the shear modulus G is independently obtained from the rheology data. The data shown at $\nu \geq 0.1$ Hz represent averages with standard deviations obtained by averaging over 34 cycles to compensate for the low sampling frequency of the rheometer. The normal stresses are all negative since they correspond to steady-state values, obtained after initial relaxation (Figure 3.12).

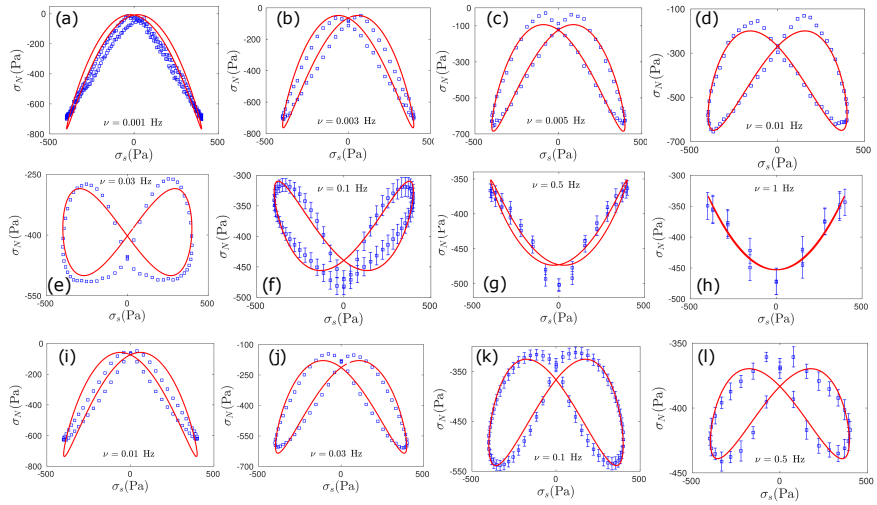

Figure 3.9: **(a)** - **(h)** Normal stress response (blue square symbols) of fibrin gels polymerized at 27°C for different shearing frequencies versus shear stress. The fit (red solid line) according to Eqs. 3.9-3.11 is also shown. The data are the same as in Figure 3.8. **(i)** - **(l)** Normal stress response (blue square symbols) of a fibrin gels polymerized at 22°C for different shear stress frequencies versus shear stress. The fit (red solid line) according to Eqs. 3.9-3.11 is also shown where the fitting parameters are $2A_z$ and $\tilde{A}$. The characteristic time τ for this gel is shorter ($\tau = 10.17$ s) than for the gel in **(a)** - **(h)**, such that similar "butterfly-shapes" are found at a higher frequency. The data shown at $\nu \geq 0.1$ Hz represent averages with standard deviations obtained by averaging over 34 cycles to compensate for the low sampling frequency of the rheometer.

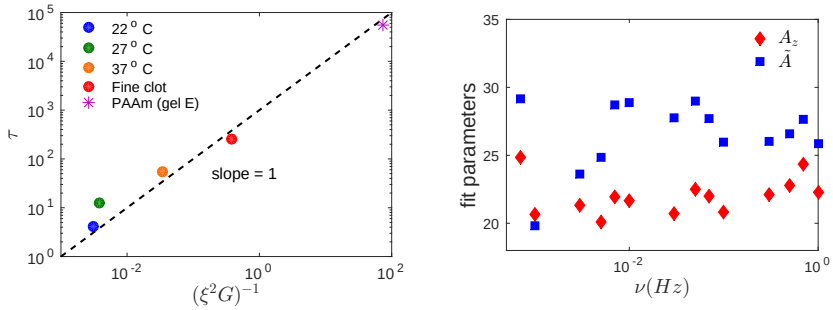

Figure 3.10: **(a)** Relaxation times for fibrin and PAAm gels obtained from the fits in Figure 3.7. These relaxation times are plotted vs $1/(G\xi^2)$ for comparison with predicted relaxation time dependence (Eq. 3.8) on ξ and G. For PAAm, we use $\xi = 10$ nm, which is consistent both with prior literature values [137] and with the estimated $\xi \sim \sqrt{\eta d^2/(G\tau)}$ using our model, together with the fit $\tau = 15.5$ h, $G = 141$ Pa, $\eta = 10^{-3}$ Pa and $d = R\tan(\alpha) = 25\tan(2°)$ mm $\simeq 1$ mm. **(b)** The fit parameters A_z and $\tilde{A}$ for the fibrin sample polymerized at 27°C as a function of frequency.

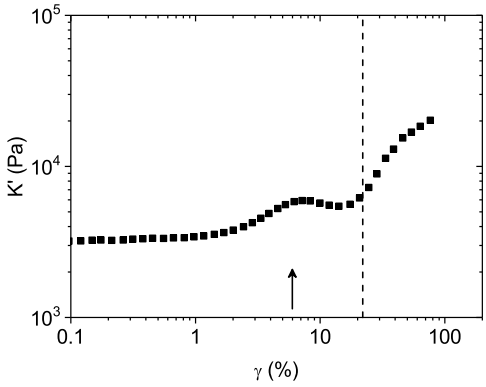

Figure 3.11: The differential storage modulus K' as a function of applied shear strain γ for a 8 mg/ml fibrin gel polymerized at 27°C. The arrow indicates the onset of nonlinearity at $\gamma_0 = 6.0\%$, calculated using $\gamma_0 = 0.61/(A_z - 0.86)$ (Ref. [165]), where A_z is obtained from Figure 3.10b. The dashed line corresponds to an applied shear stress of 800 Pa, which is the applied stress in Figures 3.8 and 3.9.

3.4.2. TRANSIENT STARTUP REGIME DURING OSCILLATORY SHEAR MEASUREMENTS

The presented two-fluid model predicts a transient response in the normal stress at the beginning of the shearing process. We test this by measuring the full time dependence of σ_N, as determined by the thrust F, according to Eq. 3.17, as shown in Figure 3.12. In Figure 3.12a, a constant shear stress is applied whereas in Figure 3.12b we show the transient normal stress response to an oscillatory shear stress. The red line shows the experimental data, the blue line is the fit using Eq. 3.28. In Figure 3.12c the data of Figure 3.12b are replotted, with σ_N as a function of shear stress instead of time. This representation allows us to have a better perspective of the initial transient behaviour found in both the experimental data and the model. Both in the case of a constant shear stress and an oscillatory shear stress, the normal stress decay is accurately described by the two-fluid model, and with comparable decay constants.

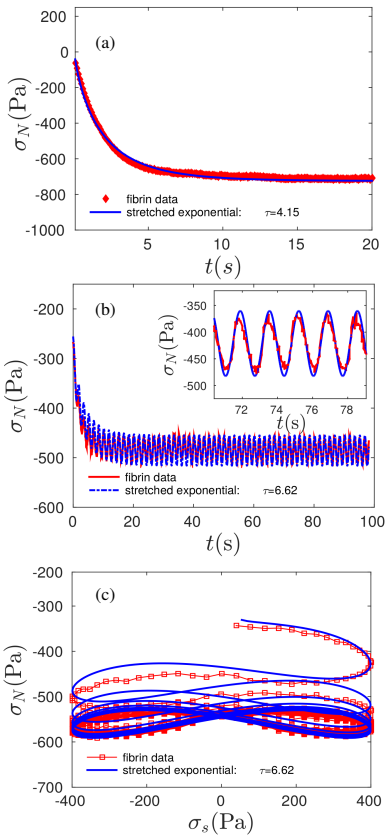

Figure 3.12: Transient normal stress data for fibrin gels polymerized at 22°C. **(a)** The red line shows the normal stress difference relaxation data versus time when a constant shear stress has been applied. The blue line is a stretched exponential fit of the data using Eq. 3.28 which yields the relaxation time τ = 4.15 s. **(b)** The red line shows the normal stress difference data versus time when an oscillatory shear stress with frequency ν = 0.3 Hz is applied. The blue line is the fit which yields the relaxation time τ = 6.62 s. The inset zooms in on the stationary response. **(c)** The same data shown in **(b)** plotted as apparent normal stress versus shear stress.

3.4.3. INFLUENCE OF RHEOMETER SHEAR CELL GEOMETRY ON THE NORMAL STRESS SIGNAL

As a further test of the validity of the two-fluid model for fibrin gels, we measure the normal stress relaxation time for different measurement geometries, using a fibrin gel of a fixed pore size (8 mg/ml, polymerized at 27°C). The dimensional analysis ($\tau \sim \frac{\eta d^2}{G\xi^2}$, Eq. 3.8) predicts a dependence of the relaxation time on the square of the gap size d. By changing the measurement geometries, we thus expect the normal force signal at a given oscillation frequency to change.

We measure for different frequencies the phase shift ϕ between the normal force signal, $N(t) = A\cos(2(2\pi\nu)t + \phi)$, and the squared shear strain, $\gamma(t)^2 = (\gamma_0 \cos((2\pi\nu)t))^2 = \frac{\gamma_0^2}{2}(1+\cos(2(2\pi\nu)t))$. We choose to compare $N(t)$ with $\gamma(t)^2$ because both quantities have the same frequency (2ν), and because of the analogy with the Mooney-Rivlin model prediction, $N = G\gamma^2$.

The phase shift as a function of frequency measured for several cone-plate (CP) geometries is shown in Figure 3.13a. We observe a marked dependence on the type of geometry, and thereby the gap size. As shown in Figure 3.13b, we can scale out these differences by rescaling the frequency axis by the characteristic relaxation time τ, where d is the gap of the rheometer, chosen at the edge for the cone-plate geometries. To test that indeed the size of the gap at the edge of the geometry is the relevant parameter and not the diameter of the geometry, we used a PP-20 system with two different gap sizes. We observe a collapse of all the curves (Figure 3.13b), showing that the gap size at the boundary (Figure 3.2) is the relevant length scale that governs the time-dependence of the normal force, in accordance with predictions from the dimensional analysis.

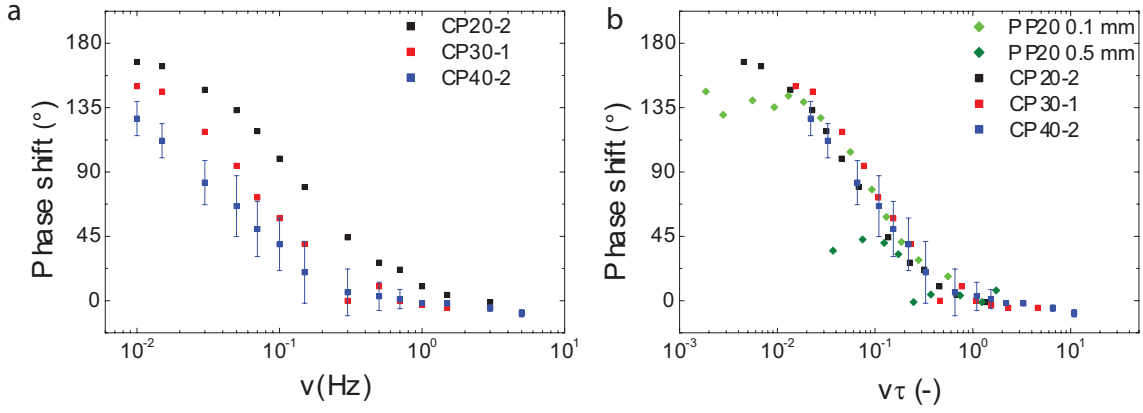

Figure 3.13: (a) Apparent phase shift between the normal stress and the shear strain for fibrin gels polymerized at 27°C as a function of the shearing frequency, for various shearing geometries. **(b)** The frequency axis is rescaled by the characteristic time $\tau \sim \eta d^2/(G\xi^2)$. Error bars on the CP40-2 data set represent the standard deviation between 6 measurements.

3.4.4. NORMAL FORCE UNDER UNIAXIAL COMPRESSION

In response to shear deformation, we observed a normal force due to solvent flow on the length scale of the gap size d of the rheometer geometry. In this Section we report measurements on fibrin gels that are compressed between two impermeable steel plates, which induces fluid flow on a larger length scale: the radius of the rheometer geometry.

An example of such a measurement is shown in Figure 3.14a, where two fully polymerized fibrin networks (2 and 4 mg/ml fibrin), polymerized under coarse clot conditions (Section 3.3.1), are compressed at a rate of 1 μm/s until 10% axial strain is reached. During the compression an increase of the normal force is observed, which relaxes to a value slightly higher than the initial normal force after the axial strain is held constant at 0.9 mm for at least one minute. Indeed, when we apply an increasing axial strain, we find that, after full relaxation, that the residual normal force increases as well, as shown in Figure 3.14b. This demonstrates the poroelastic nature of fibrin gels: a residual, static normal force originating from the elastic network, and a decaying normal force from viscous solvent flow.

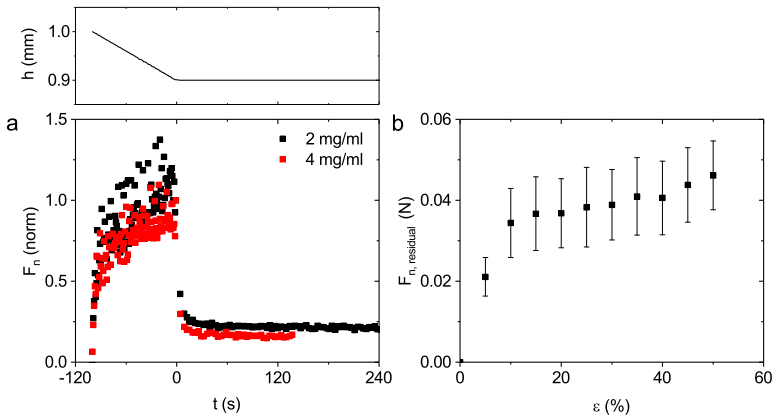

Figure 3.14: Network compression followed by normal force relaxation. **(a)** The samples are a 2 and 4 mg/ml coarse fibrin gel, polymerized at 22°C in a 40 mm plate-plate geometry. During the first 100 s, the network is compressed at a constant rate of 1 μm/s from h = 1.0 mm to 0.9 mm. Starting at t = 0 s, the sample is held at a fixed (axial) strain, and the normal force F_n, normalized to the value at t = 0 s, relaxes to a value close to the initial value. **(b)** Residual normal force with increasing compressive strain ϵ. The samples are 2 mg/ml coarse fibrin gels, polymerized at 22°C in a 40 mm plate-plate geometry. Data points were taken after full relaxation, indicated by a constant normal force. The data points shown in this graph are the average of three independent measurements; error bars represent the standard deviation.

Unfortunately the relaxation time for the 2 mg/ml fibrin gels polymerized in coarse clot assembly buffer is so fast that within the first data point (with duration 1 second) most relaxation already has taken place (Figure 3.14a). In Supplementary Figure 3.1 we show the normal force relaxation for fibrin gels polymerized in both coarse and fine assembly buffers, with a range of fibrinogen concentrations. The fibrin gels assembled in

fine clot buffers are expected to have a slower relaxation response due to their smaller pore size [166]. We chose to use gels with a protein concentration of 6 mg/ml, to slow down the relaxation mechanics while maintaining a normal force below 50 N, which is the highest force that our rheometers can apply. In Figure 3.15 the normal force relaxation is shown for gels polymerized in a 40 mm and in a 20 mm diameter plate-plate geometry. We chose to use two different geometry radii, as during compression of a biphasic material, fluid flow (poroelasticity) can be distinguished from rearrangement of the network (viscoelasticity) by considering that the former is scale-dependent, while the latter is not [167]. On long time scales (over approximately 3000 s for the PP-40 and 1000 s for the PP-20 geometries), the force resolution of the instrument, specified to be 0.01 N, limits the accuracy with which we can monitor the normal force.

When plotted on a log-lin scale (Figure 3.15a and c), we observe two regimes before the noise floor is reached, indicating that there are (at least) two typical time scales over which relaxation takes place (which is predicted in Ref. [168] for systems with a heterogeneous force distribution). We independently fitted both regimes, indicated by the bars in panels a and c. When plotted on a log-log scale (panel b and d), we observe, after a short initial adaptation period, a power law decay of the normal force over one decade in time. The fitted values of the decay times and power law exponent for both geometries are summarized in Table 3.2.

As there is a significant variability in decay times measured for different repeats between the fitted decay times t_1 and t_2 for samples polymerized in the PP-40 and PP-20 geometries, we can only make the qualitative observation that increasing the geometry radius increases both decay times. We conclude that the (macroscopic) permeation of fluid through the network is responsible for the normal stress response. However, the sample-to-sample variation is too large to distinguish between e.g. a factor 2, 2^2 or $\sqrt{2}$ between the PP-40 and the PP-20 geometries (where 2^2 is predicted in Ref. [115]), or whether the difference between t_1 and t_2 is dependent on the radius of the geometry. The two-stage decay suggests the existence of at least two decay mechanisms: one due to poroelasticity [115], and another, perhaps pressure-mediated remodeling of the gel (which has been shown to occur in previous works [169–174]).

Finally we measure the normal stress response of 8 mg/ml gels polymerized at 27°C under coarse clot conditions (Figure 3.16). This is the same gel as used in Section 3.4.1 for measurements of the normal force under shear. Although relaxation is faster than for the 6 mg/ml fibrin gels polymerized under fine clot conditions, the acquisition frequency is high enough to capture the full normal force decay, including the rapid initial relaxation. When we fit the normal force decay curve of these gels to a double exponential, we find an average decay time of 21.0 ± 1.1 s for the first exponential decay. This value for t_1 is higher than the value of $\tau = 12.5$ s we found during shear experiments. As the gels are formed under identical conditions, this indicates that fluid permeation during shear experiments is quicker, and hence has to occur on a smaller length scale (on the order of the gap size, see Eq. 3.8 and Section 3.4.3), while fluid permeation during the compression experiments occurs on the larger scale of the plate radius. Although the difference between t_1 and τ seems minor considering the difference between the geometry radius and the gap size, one has to consider that the surface area of a cylinder grows with the square of its radius, such that half of the gel's volume sits in the outer 29% of the sample.

	PP-40 (6 mg/ml fine)	PP-20 (6 mg/ml fine)	PP-40 (8 mg/ml coarse)
t_1	79 ± 37 s	29 ± 1 s	21.0 ± 1.1 s
t_2	386 ± 1 s	205 ± 45 s	136 ± 89 s
power	-1.70 ± 0.21	-1.22 ± 0.06	1.44 ± 0.34

Table 3.2: Normal force relaxation of 6 mg/ml fibrin gels polymerized under fine clot conditions in a PP-40 or PP-20 geometry, and 8 mg/ml fibrin gels polymerized in a PP-40 geometry under coarse clot conditions at 27°C, characterized either by fitting with the time-dependent decay with two exponentials with decay times t_1 and t_2, or by fitting a power law. Errors are the standard deviation from three independent samples.

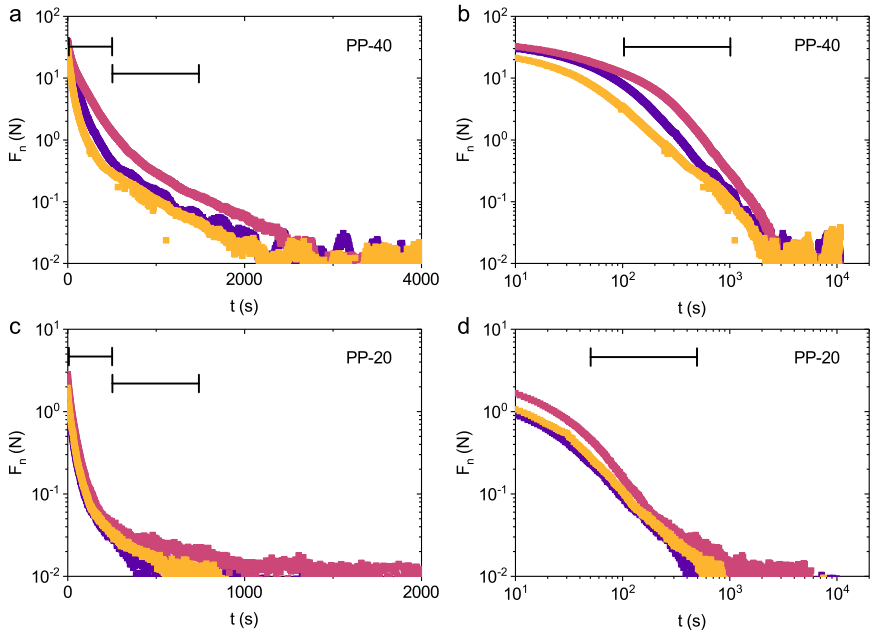

Figure 3.15: Network compression followed by normal force F_n relaxation. The samples are 6 mg/ml fine fibrin gels, polymerized at 37°C in a plate-plate-40 (PP-20) or plate-plate-20 (PP-20) geometry. Different colours mark independently prepared samples. During the first 50 s, the network is compressed at a constant rate of 1 μm/s from 1.0 mm to 0.95 mm. Starting at $t = 0$ s, the sample is held at a fixed (axial) strain and the normal force F_n, normalized to the value at $t = 0$ s, relaxes to a value close to the initial value. The relaxation in a PP-40 geometry is plotted on a lin-log scale **(a)** and on a log-log scale **(b)**. The relaxation in a PP-20 geometry is plotted on a lin-log scale **(c)** and on a log-log scale **(d)**. The fitting range of the exponential function in **(a)** and **(c)**, and the power law behaviour in **(b)** and **(d)**, is indicated by the horizontal bar.

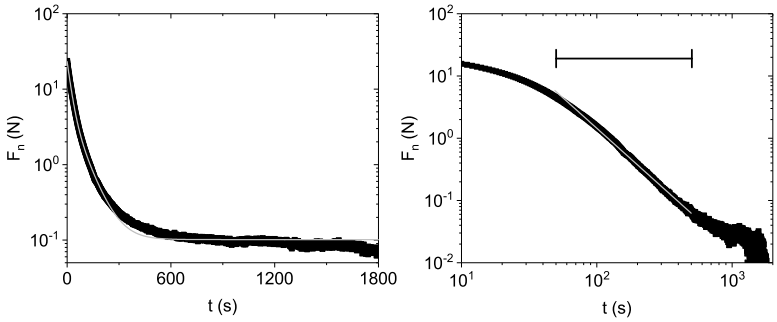

Figure 3.16: Network compression followed by normal force F_n relaxation. The sample is a 8 mg/ml coarse fibrin gel, polymerized at 27°C in a plate-plate-40 geometry. **(a)** A double exponential decay function (grey line) has been fitted to the data. For this sample, the typical decay time $t_1 = 21.7$ s, and $t_2 = 72.9$ s. **(b)** A power law fit (grey line) between $t = 50$ and $t = 500$ s (indicated by the horizontal bar) results in a power of -1.96. The interpretation of the power law decay function is currently unclear.

3.5. CONCLUSION

We showed that poroelastic effects involving interstitial fluid flow play an unexpectedly important role in the shear rheology of polymer gels. Poroelastic effects in porous media such as fluid-imbibed polymer gels are usually considered to affect only volume-changing deformations such as compression and extension [175–177]. Our experiments and theory demonstrate that the shear response of polymer gels is highly sensitive to fluid flow and network compressibility, in spite of the volume-conserving nature of simple shear deformations. Depending on the time scale of deformation and the hydrodynamic coupling of the polymer network with the surrounding solvent, polymer gels behave as either incompressible materials with a positive normal stress or compressible materials with a negative normal stress. We also demonstrated, by comparing compressive versus shear deformations on the same gels, that the typical time scale that sets whether a material is considered compressible or incompressible, depends in shear on the gap size of the rheometer geometry, while in compression on the geometry radius.

We demonstrated that the normal stress response of both synthetic and biopolymer gels is quantitatively captured by a minimal model that takes into account the biphasic nature of hydrogels. This model can explain why synthetic hydrogels exhibit shear-dilation, while biopolymer gels exhibit shear-contraction. This insight suggests a new route to tailor the sign and magnitude of the normal stresses for polymer materials by tuning the pore size, solvent viscosity, and nonlinear shear elasticity. This design principle could prove valuable in the context of materials science, since normal stresses can cause elastic instabilities that severely complicate processing [130]. In principle, the mechanism of local relative motion of solvent and network applies to any two-component gel with network and solvent. In practice, however, the relaxation time τ can become very long for small pores, making the gel effectively behave as incompressible single-component systems.

Finally, our findings highlight the important role of poroelastic effects in tissue and extracellular matrix mechanics [178], where normal stresses can become a dominant stress component, even for small strains of order 10% [133]. Related poroelastic effects in intracellular networks have previously been shown to govern the rheology of cells. However, the much smaller cellular dimensions $d \simeq 1$ μm, can be expected to limit the corresponding poroelastic relaxation time to of order 1 s, even though the mesh size is only of order 10 nm [179], which renders cells effectively compressible on time scales $\gtrsim$ 1 s.

I thank Melle Punter, Mahsa Vahabi and Henri de Cagny for a pleasant collaboration and interesting discussions on the permeability of fibrin hydrogels. I thank Hinco Schoenmaker for his help with the permeability setup.

APPENDIX

3.A. COMPRESSION OF FINE CLOT AND COARSE CLOT FIBRIN GELS AT MULTIPLE PROTEIN CONCENTRATIONS

In Supplementary Figure 3.1 we show the normal force relaxation for fibrin gels polymerized in coarse (150 mM NaCl, 20 mM HEPES and 5 mM $CaCl_2$ at a pH of 7.4) and fine (400 mM NaCl, 50 mM Tris and 3.2 mM $CaCl_2$ at a pH of 7.4) assembly buffer, for a range of fibrinogen concentrations. For the coarse clots, the decay of the normal force is so fast that most relaxation has taken place before the first data point. For fine gels with a 10 mg/ml fibrin concentration, the normal force reaches a value of 50 N, which is the highest that the rheometer can apply. In this case, the gel is not compressed to the final axial position in one go but held at an intermediate strain until the normal force has sufficiently decayed such that it can be further compressed.

We chose for our compression measurements 6 mg/ml fine clots, as the relaxation dynamics can be monitored on an experimentally accessible time scale (both the quick, initial response and the slow decay), while at the same time the maximum normal force is well below 50 N, such that even with sample-to-sample variations the 50 N limit is not reached.

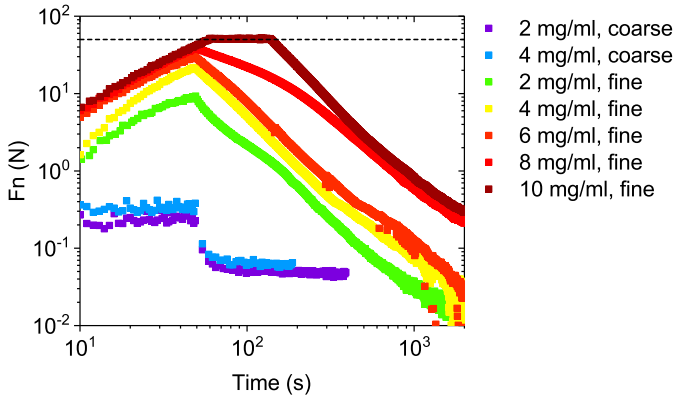

Supplementary Figure 3.1: Normal force decay after compression, for a range of fibrin concentrations (2 to 10 mg/ml), in both coarse and fine assembly buffer. The maximum normal force that the rheometer can apply (50 N) has been indicated by a dashed line.

4

CONNECTING FIBRIN'S STRUCTURE AND MECHANICS BY A MULTISCALE APPROACH

Monomers! Filaments!
Who bears the strain today?
Will one extend,
or the other align?

Nature is sharing the
responsibility.
Strong yet extensible
through its design.

Fibrin is an elastomeric protein that plays a critical role in blood clotting and wound healing by assembling into fibrillar networks that scaffold blood clots. Fibrin networks strongly stiffen when strained and are highly extensible, thus imparting an enormous mechanical resilience to blood clots. It has been difficult to pinpoint the origin of this elastomeric behaviour due to fibrin's complex structure. Here we reveal the mechanisms that underlie the mechanical resilience of fibrin networks by performing in situ X-ray scattering measurements of the changes in structure upon mechanical shearing across all relevant scales, from the network level down to the molecular packing structure of the constituent fibers. We show that the mechanical resilience of fibrin networks is caused by a hierarchy of structural responses that set in consecutively as the shear strain is increased. The networks exhibit an entropic response at small strains where fiber slack is pulled out, followed by fiber

reorientation and finally by fiber stretching mediated by stretching of the intrinsically disordered domains of the fibrinogen molecule. We measure only a slight increase of the axial periodicity, indicating that there is minimal unfolding of the ordered domains of the molecule. When the load is removed, the structural changes at the network level are fully reversible, but the molecular packing structure is changed to a more ordered structure with a smaller axial periodicity than for the virgin sample. Our findings provide a mechanistic framework to understand the strain-dependent mechanical response of blood clots, which is a prerequisite to understand the molecular basis of blood clotting disorders. Moreover, our findings identify hierarchical structuring as a powerful design principle to make resilient materials.

4.1. INTRODUCTION

IN Nature, many examples are found of elastomeric materials made of protein fibers. Prominent elastomeric proteins in the human body are the intermediate filament cytoskeleton of cells [180], elastin and fibronectin in the extracellular matrix [181, 182], and fibrin in blood clots and wounds [124]. These proteins all form filaments that can reversibly stretch up to tensile strains of around 150% and sustain strains of several hundreds of percent [183–185]. Fibrin networks are a particularly interesting example, as they also strongly stiffen under deformation, increasing their elastic modulus by two orders of magnitude before rupture [125]. This stress-stiffening response, together with the high extensibility of fibrin, provide blood clots with an enormous mechanical resilience against the shear forces exerted by flowing blood and the traction forces exerted by cells [186, 187]. Given the importance of fibrin elasticity for hemostasis [13], there has been a long-standing interest in the molecular mechanisms by which fibrin achieves its elastomeric behaviour.

The elastomeric properties of fibrin networks are believed to somehow originate from their complex hierarchical architecture (Figure 4.1a). This architecture is generated by a multi-step self-assembly process that is encoded in the molecular structure of the soluble precursor protein fibrinogen. Fibrinogen is a symmetric trinodular molecule that is 45 nm in length, made up of two sets of three polypeptide chains denoted Aα, Bβ and γ [188, 189]. The central nodule is formed by the N-terminal portions of all six chains, and is connected to the distal nodules formed by the C-terminal parts of the β- and γ-chains via α-helical coiled-coil connector regions. Near the ends of the molecule, the Aα chains expose long and flexible C-terminal regions known as the αC regions [190]. Self-assembly is initiated by the enzymatic conversion of fibrinogen to fibrin by thrombin, which unmasks 'knobs' in the central region that recognize corresponding 'holes' in the distal regions of other molecules. Knob-hole interactions drive precisely half-staggered self-assembly of monomeric fibrin into protofibrils [191]. Once the protofibrils reach a critical length, they laterally associate into fibers driven by knob-hole interactions as well as specific interactions between the flexible αC regions of adjacent protofibrils [192]. The resulting bundle-like structure is covalently bonded by enzymatic cross-linking mediated by Factor XIII (FXIII) [18]. Along their axis, fibrin fibers exhibit the same half-staggered packing periodicity as protofibrils [193–195]. But in cross-section, evidence from light and X-ray scattering suggests that protofibrils are packed in a more disordered fractal or partially crystalline array [52, 96, 196]. The fibers in turn form a random network structure that is branched and cross-linked to varying degrees depending on the self-assembly conditions [75, 197].

The complex architecture of fibrin networks covering multiple length scales provides several possible mechanisms that may contribute to fibrin elasticity. On the molecular scale, single-molecule experiments and molecular dynamics simulations have shown that fibrin monomers can lengthen substantially through forced unfolding of the coiled-coil connector regions [198, 199]. Simulations predict that stretching converts the molecular conformation of the connector regions from α-helical to β-sheet [200, 201], providing a possible mechanism to explain the nonlinear stiffening of fibers observed at large tensile strains [202]. At the fiber scale, an additional mechanism for elongation emerges as a consequence of the intrinsically disordered αC regions, which form long and flex-

ible tethers connecting the more rigid protofibrils [203]. The most direct evidence for this mechanism comes from stretching experiments on fibers assembled from fibrinogen from different animal species, showing that the fiber extensibility correlates with the length of the αC region [204]. Further evidence comes from observations of the recoil dynamics of individual fibrin fibers, which was shown to be faster than expected from a mechanism involving protein refolding [205]. Yet the relative importance of the stretching of the αC regions versus unfolding of the coiled-coil connector regions remains unknown since we lack direct measurements or simulations of secondary structure at the fiber level. On the network level, yet another mechanism by which fibrin accommodates strain emerges, coming from the alignment of fibers towards the direction of principal strain [31, 133, 206].

It is currently unknown to what extent the different levels of structure of fibrin network contribute to the overall mechanical behaviour [32]. Experimentally, the challenge is to perform in situ measurements of structural changes from the monomer to protofibril, fiber and network level in response to a macroscopic deformation. A few studies have started to address this challenge by using either vibrational spectroscopy to track the secondary structure of fibrin monomers [207, 208] or Small Angle X-ray Scattering (SAXS) to track the axial packing periodicity of the fibers [31]. These studies provided evidence that molecular unfolding occurs at macroscopic tensile strains above 100%. However, it remains unclear to what extent mechanisms such as fiber reorientation and stretching of the unstructured αC-regions contribute to the macroscopic elasticity.

Shear rheology measurements suggest that the different levels of structure each contribute at different levels of strain [16, 125]. A typical example of the strain-dependent elasticity for a reconstituted fibrin network is shown in Figure 4.1b. The elasticity shows clearly distinguishable elastic regimes with an initial linear regime followed by a multi-step stiffening response. Based on polymer network models it was proposed that increasing levels of shear strain induce a succession of distinct elastic responses. Small strains pull out thermal fluctuations of the fibers, leading to an entropic strain-stiffening response. Larger strains stretch the fiber backbone, leading to an enthalpic mechanical regime. In the enthalpic regime, the network is expected to stiffen by a combination of fiber alignment along the shear direction and nonlinear stiffening of the fibers themselves. This model can indeed quantitatively account for the stress-strain response of fibrin networks [16, 125], but relies on the assumption that the macroscopic strain is homogeneously distributed to smaller scales. Strain-field mapping experiments have shown that this affine assumption can break down in fibrous networks [35, 133]. Clearly a complete explanation of the multi-step stiffening and extensibility of fibrin networks requires direct measurements of structural changes both at the molecular and network scale.

In this Chapter we present direct measurements of the structural mechanisms that explain the elasticity of fibrin networks by *in situ* SAXS experiments on fibrin networks subject to a macroscopic shear deformation. The SAXS scattering patterns provide simultaneous access to shear-induced changes in alignment of the fibrin fibers through the anisotropy in the scattering patterns, and changes in the molecular packing structure of the fibers through the position and width of the Bragg peak corresponding to the periodic axial packing order. We independently verify the alignment measurements

by confocal microscopy of sheared fibrin networks. We show that increasing levels of shear strain induce distinct changes in elasticity that coincide with distinct structural responses at different scales. There are no observable changes in the fiber or network structure up to strains of around 25%, consistent with entropic elasticity. At 25% strain, we find the onset of fiber alignment, which coincides with the onset of a second strain-stiffening regime. We find that fiber reorientation closely follows the expected alignment for an affinely deforming network, showing that strain is uniformly distributed down to length scales of at least 50 nm. Once the strain reaches values above 100%, we observe a progressive increase of the axial packing distance, albeit much smaller than the total fiber strain. Surprisingly, when the strain is brought back to zero, the fiber orientations return back to the original state, whereas the axial packing distance slightly shrinks compared to the original state, and the axial packing order increases. We propose that mechanical stretching can remodel the packing order of the protofibrils forming a fiber, since fibers are arrays of protofibrils connected by stretchable αC-domains.

Prior molecular-scale investigations of deformed fibrin networks considered uniaxial stretching rather than shear [31, 209]. A direct comparison between measurements under shear versus uniaxial extension is difficult, since shear is a volume-conserving deformation while extension is accompanied by volume changes that will affect the degree of fiber reorientation and thereby the strain field. To test the correspondence between structural responses under shear versus tensile deformation, we also perform SAXS measurements on fibrin networks subject to uniaxial extension. We find that a strong reduction of the network volume with increasing tensile strain enhances the degree of fiber alignment compared to that observed during shear. Similar to shear, we observe a small increase of the axial packing distance, that is much smaller than the total fiber strain.

Our findings provide a mechanistic framework to understand the strain-dependent mechanical response of blood clots. Specifically, the SAXS measurements provide direct support for recent models of fibrin elasticity that propose a combination of entropic (network-scale) elasticity at small strains and enthalpic (fiber-scale) elasticity at high strains. Our measurements furthermore support proposals that fiber stretching is mainly mediated by the reversible stretching of the αC regions. Our results provide a basis for interpreting the molecular basis of hemostatic and thrombotic disorders associated with mutations in fibrinogen and abnormalities in fibrin structure [210], especially in the αC-region [211, 212]. In the context of materials science, our findings show how hierarchical structure provides a design principle to create bio-mimicking materials capable of sustaining large strains and stresses [213].

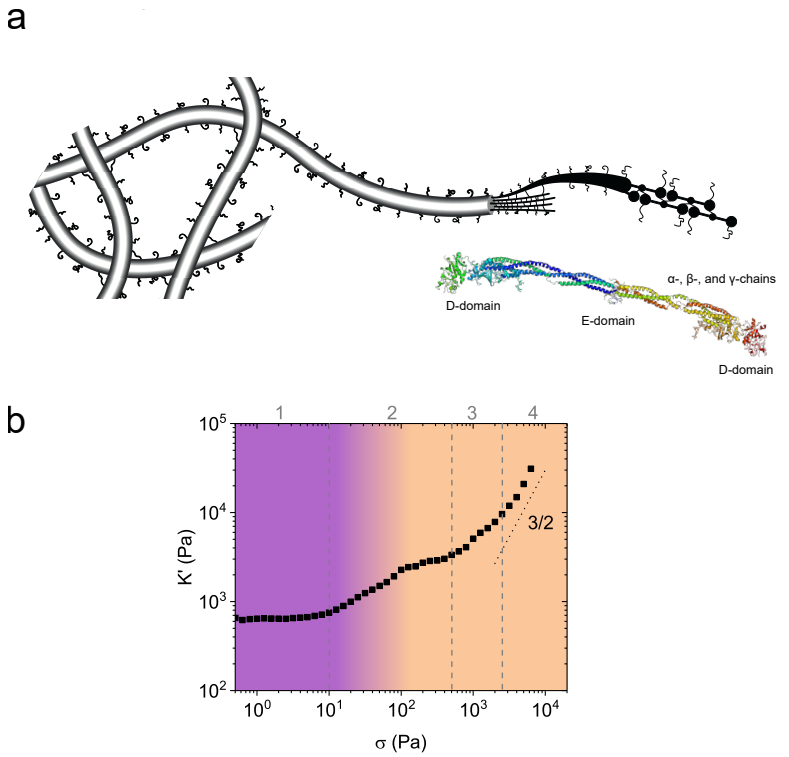

Figure 4.1: Hierarchical structure and elasticity of fibrin networks. **(a)** Schematic representation of the hierarchical structure of fibrin, progressively zooming in from the network level, to the fiber level, to the protofibril level, and ultimately the monomer level. The molecular structure of the monomer is shown in the bottom right corner, with the distal D-domains, central E-domain, and α-helical coiled-coil connector regions. The crystal structure is taken from [188]. Note that the intrinsically disordered αC-regions do not show up in the crystal structure. **(b)** Example measurement of the differential elastic modulus K' of a 4 mg/ml fibrin gel as a function of an applied shear stress σ. The entropic stretching regime is indicated by a purple background, the enthalpic regime by an orange background. Different mechanical regimes are indicated by numbers, and separated by grey dashed lines. A dotted line indicates a power law with slope 3/2, which is predicted for stretching of a semiflexible polymer chains.

4.2. BACKGROUND ON SMALL-ANGLE X-RAY SCATTERING

When we consider a ray of light incident on a crystal lattice [214–216], every plane of the lattice will reflect a tiny portion of the incident light under the same angle as the incident angle θ. The extra distance travelled by light reflected on a plane deeper in the crystal is twice (back and forth) the separation between the planes d, multiplied by the sine of the angle of incidence θ. When this factor of $2d\sin(\theta)$ equals exactly one or any integer multitude n wavelengths λ, the waves reflected on different planes will be in phase, and hence interfere constructively. This scattering condition is referred to as Bragg's law [217] and often denoted in the following form (see Figure 4.2):

$$2d\sin(\theta) = n\lambda \tag{4.1}$$

Note that $\frac{n\lambda}{2d} \leq 1$; otherwise the light will pass directly through the crystal (as the maximum value that the sine function can attain is one). Hence, with the right choice of wavelength and angle of illumination, the crystal structure can be investigated from the so-called Bragg peaks. If the scattering occurs on a monocrystalline sample, individual spots will appear at specific distances and angles with respect to the axis of the incident light beam, where the position of the spots is determined by the periodicity of the lattice in x, y and z; while the width of the spots is determined by how well-defined the crystal lattice is. On the other hand, if the crystal is not monocrystalline and all different crystal orientations are present (e.g. diffraction on a powder), a ring rather than individual spots will form around the beam axis.

Historically, X-ray scattering has been used to study the crystal structure of salts, as the X-ray wavelength and salt periodicity are both in the nanometer range, and strong scattering on the relatively heavy elements present in salts provides good signal [216]. More recently, X-ray scattering is also employed to study biological materials, despite the challenge posed by a weaker scattering signal. Some examples include scattering on polyisocyanide gels [218], a material mimicking biological hydrogels, correlating its structural and mechanical properties. On a larger scale SAXS has been used to quantify alignment in collagen [219], accessing a length scale that we also intend to use.

4.3. MATERIALS AND METHODS

4.3.1. FIBRIN POLYMERIZATION

Human plasma fibrinogen (Plasminogen, von Willebrand Factor and Fibronectin depleted) and human α-thrombin were obtained in lyophilized form from Enzyme Research Laboratories (Swansea, United Kingdom). All chemicals were obtained from Sigma Aldrich (Zwijndrecht, The Netherlands). Fibrinogen (lyophilized in 20 mM sodium citrate-HCl buffer at pH 7.4) was dissolved in water at 37°C for 15 min to its original concentration (approximately 13 mg/ml) and dialysed against fibrin buffer containing 20 mM HEPES and 150 mM NaCl at a pH of 7.4 in order to remove citrate, which complexes with Ca^{2+} ions that are required for FXIII and thrombin activity. A dialysis membrane with a Molecular Weight Cut-Off (MWCO) of 10 kD was used. 50 ml of sample was dialysed against 1 L of buffer, under continuous stirring. After one hour of dialysis at room temperature, the buffer was replaced, and after another hour, the buffer was replaced again.

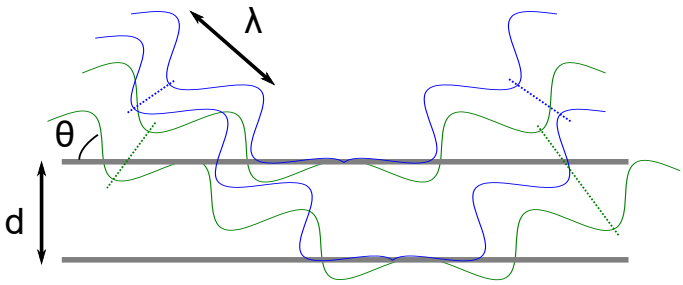

Figure 4.2: A schematic representation of Bragg scattering. When incident light with wavelength λ hits a plane in a crystal lattice, it will be partially reflected under the same angle as the angle of incidence θ. With the right combination of λ, θ and separation between planes d, there will be constructive interference as the light reflected on one plane and the next are in phase (green waves), resulting in Bragg diffraction. In case of a mismatch, there will be destructive interference (blue waves) and no Bragg diffraction.

The third dialysis step was performed at 4°C overnight. After dialysis, the fibrinogen solution was aliquotted, snap-frozen in liquid nitrogen and stored at -80°C. The monomer concentration was checked by spectrophotometric measurements of the absorbance at 280 and 320 nm using a Nanodrop 2000 spectrophotometer (Thermo Scientific) and using an extinction coefficient of 16.0 mg/(ml cm) [51] at 280 nm. The absence of absorption at 320 nm indicates that no aggregates are present. The final fibrinogen concentration was typically around 10 mg/ml. Prior to use, the fibrinogen was quickly thawed at 37°C, and then diluted and mixed with 500 mM $CaCl_2$ at room temperature to a final assembly buffer containing 20 mM HEPES, 150 mM NaCl and 5 mM $CaCl_2$ ("coarse clots"). Dense networks ("fine clots") with an average pore size of 0.08 μm were obtained in fine-clot assembly buffer (400 mM NaCl, 3.2 mM $CaCl_2$ and 50 mM Tris-HCl) at a pH of 8.5 [54].

Thrombin (lyophilized in 50 mM sodium citrate and 0.2 M NaCl) was, on ice, reconstituted in water to its original concentration (approximately 10,000 U/ml), and quickly aliquotted, snap-frozen in liquid nitrogen and stored at -80°C. Assembly was initiated by the addition and quick mixing of 0.5 U/ml of thrombin from a 20 U/ml thrombin stock, kept on ice for a maximum of 24 hours. After addition of thrombin, the mixture was quickly transferred to a custom-made Teflon mould for tensile tests or to a (confocal) rheometer, to allow *in situ* polymerization.

4.3.2. TENSILE TESTING

We performed extension tests on fibrin networks using a Deben Microtest tensile tester (Woolpit, United Kingdom), equipped with a 2N-loadcell at room temperature. After the addition of thrombin, 700 μl of the assembling fibrin network was pipetted into a custom-made Teflon mould with a dog-bone shape (39 × 6.5 mm, see Figure 4.3a). Pieces of Velcro were inserted in the polymerizing gel at both ends, to allow clamping of the gel in the tensile tester (see Figure 4.3a). The Teflon mould with the polymerizing sample

was placed in a sealed box with some wet tissue, to prevent solvent evaporation. After polymerization, the sample was gently removed by lifting the Velcro at the two ends using a pair of tweezers, and was transferred to the tensile tester. In order to monitor the strain on the gel, we added markings with graphite powder (obtained by grinding a piece of graphite), as shown in Figure 4.3b. The initial length of the fibrin was 10.0 mm, and deformation was applied at a rate of 4 mm/min, or 67 μm/s. The deformation and applied force were recorded every 0.5 s. We note that the weakest mechanical link in the system is the method by which we load the fibrin gel in the tensile tester, as rupture always occurred at the attachment site between the Velcro and the fibrin gel. Alternative methods, such as direct clamping [220] or a toroidal gel shape [221], could improve the maximum achievable strain.

The resulting force-extension curves for a 4 mg/ml fibrin gel are shown in Figure 4.4. The engineering strain is defined as $\gamma = L/L_0$, where L is the instantaneous length and L_0 the original length of the unloaded gel. Since there is some variation to the slack in the fibrin gels after clamping in the tensile tester, we used the onset of the force response to determine L_0, which is at approximately 11 mm gel length (see the inset of Figure 4.4; the initial distance between the two clamps is 10.0 mm).

We measured the volume of the fibrin gel during extension by tracking the separation of the graphite markings and the width of the gel. To this end, we positioned a Sony Cybershot DSC RX100 M3 camera above the tensile tester, and took an image every 1 mm of extension. Using manual tracking in ImageJ, we then obtained the gel's volume through multiplication of the length with the width squared. We checked the assumption that the sample width and height decreased by the same amount by placing a second camera (a Nikon D40) orthogonal to the first camera, allowing pictures to be taken from the side.

In Figure 4.5a we show an example of a 4 mg/ml fibrin gel under increasing levels of applied strain, showing the contraction of the gel in the direction orthogonal to the extension, in Figure 4.5b we show the resulting relative volumes. Indeed we observed by visual inspection of the samples that droplets of liquid formed on the surface of the gel during extension. We approximate the change in relative volume by a linear regime until a threshold strain of 18%, after which the data shows a gradual decrease. We quantify this decrease by fitting an exponential decay of the form $V(\gamma) = V_0 + Ae^{-(\gamma-\gamma_0)/\gamma_t}$, where V_0 is the residual volume, A the amplitude of the volume decrease and γ_t the typical strain where the volume decrease is $1/e$, with the constraints that the transition between the regimes is continuous, such that the sum of V_0 and A is 1, and that $\gamma_0 = 0.18$, i.e., the end of the linear regime. This provides us a functional form of the change in volume with strain, that we can use to calculate the expected nematic order parameter using Equations 4.46 and 4.50.

Figure 4.13b shows the predicted evolution of the nematic order parameter for an affinely deforming collection of rods with strain with the assumption that the system's volume changes as in Figure 4.5. The order parameter increases more rapidly than when the boundaries that are orthogonal to the direction of strain are fixed or when volume conservation is assumed, indicating that the volume of the gel decreases during extension.

Our observation of gel shrinkage in response to extension is consistent with several prior studies, although there are variations in the magnitude of the effect and the onset

strain. These variations are likely due to differences in the assembly conditions and assay geometry. One study showed a vertical contraction of 50% already upon 10% applied stretch for a gel that was stretched in the x-direction, confined in the y-direction, and was allowed to move freely in the z-direction [126]. The fibrin concentration was the same as ours but the assembly contained a higher (20 mM versus 5 mM) $CaCl_2$ concentration and a lower (0.05 U/ml versus 0.5 U/ml) thrombin concentration. Another study reported a linear decrease in sample volume until approximately 60% strain, leading to a final volumetric shrinkage by a factor 10. This study used a higher fibrinogen concentration (10 mg/ml instead of 4 mg/ml) and a higher $CaCl_2$ concentration (10 mM versus 5 mM), and the same thrombin concentration [31]. It was proposed that gel shrinkage could be due to expulsion of water from the fibers themselves upon protein unfolding and hydrophobic collapse [31, 222]. Alternatively, contraction could also be due to fiber reorientation [223].

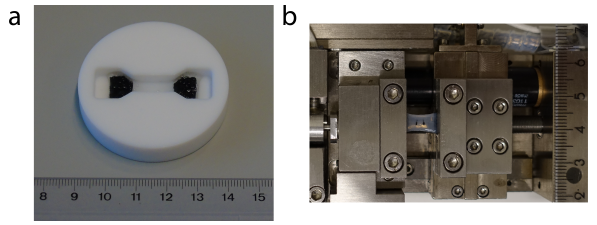

Figure 4.3: (a) A photograph of a Teflon mould filled with a sample, with pieces of Velcro (black) embedded in the gel on both ends, to enable clamping in the tensile tester. **(b)** A fibrin gel clamped in a tensile tester. Two markings have been made with graphite powder to track the deformation of the gel.

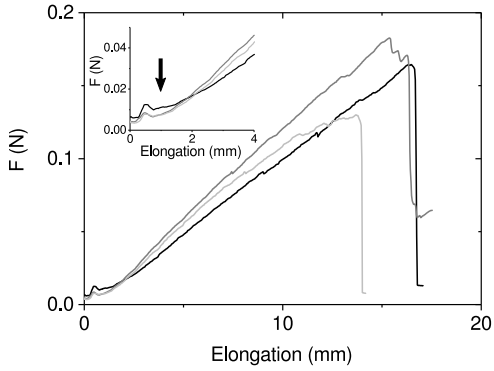

Figure 4.4: Measurements of the force F exerted by the fibrin gels as a function of imposed elongation, $L-10.0$ with 10.0 the initial separation of the clamps, on three independently prepared fibrin gels with fibrin concentrations of 4 mg/ml. Inset: a zoom-in of the initial deformation, where the force response shows that the sample extension only starts once L reaches a finite value. L_0 is indicated by the arrow.

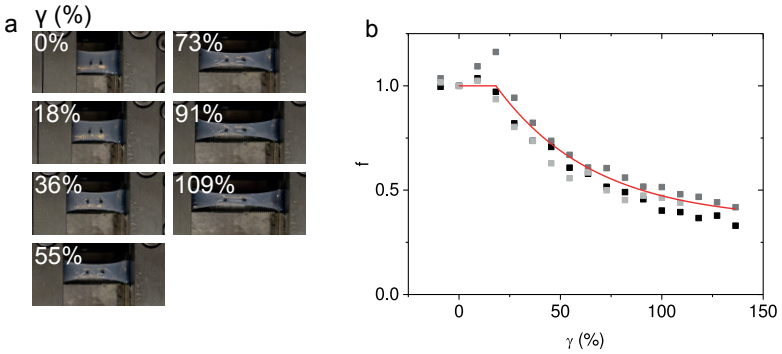

Figure 4.5: Volume change of fibrin gels during extension. **(a)** A series of photographs of a gel under increasing extensile deformations, with the gel strain $\gamma(\%)$ indicated in the corner of each photograph. **(b)** The change in relative volume f with strain γ for 3 independent data sets of 4 mg/ml fibrin gels. We fit the relative gel volume with a linear regime until 18% strain, and a regime where the gel volume exponentially decreases at higher strains. In the determination of the relative volume, a single camera was used to record the change in sample thickness for the black and dark grey squares, with the assumption in the calculation of the volume change that the sample shrank identically in width and thickness. The light grey data set was obtained with two cameras, tracking the shrinkage of both the width and the thickness. We find good agreement between the 3 data sets, indicating that the sample indeed shrinks isotropically in cross-section.

4.3.3. RHEOLOGY

Rheological experiments were performed using a Kinexus rheometer (Kinexus pro+, Malvern, United Kingdom) equipped with a 40 mm stainless steel cone-plate geometry with a 1° angle. For rheology on des-αC fibrinogen we used a 20 mm stainless steel cone-plate geometry with a 1° angle, due to the scarcity of des-αC fibrinogen (requiring 40 μl versus 300 μl of sample for a 40 mm diameter cone-plate geometry). After initiation of fibrin polymerization, we transferred the solution to the bottom plate of the rheometer and lowered the top plate. During polymerization, the temperature was kept constant at 37°C, and solvent evaporation was prevented by adding a layer of mineral oil (M3516, Sigma Aldrich) on the liquid-air interface. We checked that the oil layer did not influence the mechanical behaviour of the networks by comparing experiments in the absence and presence of an oil layer. We found insignificant differences between the mechanical response of samples with and without oil, falling within the variability between repeat measurements. Given the long duration of many of the rheology experiments, we chose to include the application of mineral oil in the protocol since it is the most robust way to prevent evaporation over long time scales.

During polymerization, we continuously measured the shear modulus, to verify that there was no solvent evaporation or other disturbances of the sample. To this end, we applied a small oscillatory shear strain with an amplitude of 0.5% and a frequency of 0.5 Hz, and measured the shear stress response. Polymerization was complete after 2 hours, as indicated by a time-independent shear modulus. We measured the mechanical response to increasing levels of stress by applying a constant shear stress, superimposed with an oscillatory shear stress with an amplitude of 0.1 times the constant shear stress and a frequency of 0.5 Hz. We then increased both the constant and oscillatory stress level, to maintain their 10-to-1 ratio, until the sample broke. As the applied oscillatory stress is small compared to the total stress on the network, we calculate the differential modulus $K = \frac{\delta\sigma}{\delta\gamma}$, with $\delta\sigma$ the applied amplitude of the oscillatory stress, and $\delta\gamma$ the measured amplitude of the oscillatory strain. We chose this prestress protocol rather than large-amplitude oscillatory measurements (LAOS) that measure $G = \frac{\Delta\sigma}{\Delta\gamma}$, as for materials with a nonlinear mechanical response, the differential elastic modulus more accurately describes the material behaviour [224, 225].

4.3.4. CONFOCAL RHEOLOGY

In order to characterize the network response to an applied shear strain, we use a home-built setup, consisting of a spinning disc confocal microscope (a Leica DM IRB inverted microscope with a 100x oil objective, a Yokogawa CSU-22 spinning disk, and a Hamamatsu EM-CCD C9100 camera) with a rheometer head (Anton Paar DSR 301) on top.

There are several design considerations for confocal rheometry [34, 89, 226–231]. We chose to use a parallel plate measurement geometry instead of a cone-plate system. Parallel plates have the advantage that the measurement is relatively insensitive to inaccuracies in the gap distance, but require careful measurement of the objective position relative to the rheometer geometry since the strain increases with radial distance from the center. We furthermore chose rotational rheometry over translating parallel plates [232, 233], because rotational rheometry can more readily access large shear strains.

A fibrin gel spiked with 10 mole% of fluorescently labelled monomers is polymerized in between a glass coverslip and a 20 mm diameter stainless-steel plate; the latter attached to the rheometer. The separation between the plate and the coverslip can be manually adjusted by a micrometer screw that lowers/lifts the rheometer head. The microscope objective is situated underneath the glass coverslip, such that the center of the objective is located half way the center and the edge of the rotating top plate. A layer of low-viscosity mineral oil (M3516, Sigma Aldrich) is applied at the sample-air interface. The polymerization is monitored by an oscillation with amplitude 0.5% and frequency 0.5 Hz. Polymerization takes place at room temperature (approx. 22°C) for at least 2 hours.

To track individual fibers in the 3D fiber matrix, we use an open source software package called SOAX [234]. In short, first small segments are detected based on a local intensity maximum and a gradient. These segments are stretched and connected to neighbouring segments, if the "energy penalty" for bending and stretching the segments permits. Finally, junctions are identified where fibers intersect. The first step in optimizing the parameters for initialization and evolution is done empirically. To fine-tune the parameters, we use the option in SOAX to systematically scan a range of parameters, where each parameter set is evaluated based on a function that penalises segments with a low signal to noise. To avoid interpolation errors during segment initialization, we set the z spacing of the confocal images during acquisition equal to the xy-spacing (0.16 μm).

The output of the software is a list of tracked filaments, with two angles θ and ϕ characterizing the orientation of each filament. With this orientation, we calculate the nematic order parameter for every image. We elaborate in Section 4.3.6 on the calculation of the order parameter.

4.3.5. SMALL ANGLE X-RAY SCATTERING

EXPERIMENTAL PROCEDURE

Small Angle X-ray Scattering (SAXS) experiments were performed at the DUBBLE BM26B beamline at the ESRF (European Synchrotron Radiation Facility) in Grenoble, France. The energy of the x-rays was 12 keV, corresponding to a wavelength of 1.0×10^{-10} m. The sample-to-detector distance was adjustable; for our experiment we choose a distance of 3 m to optimally access the relevant q-range possible with this setup.

A Pilatus 1M detector (169 mm x 179 mm active area) [235] was used to collect SAXS images. The specified beam dimensions are 300 x 300 μm. A beamstop is placed in between the sample and detector to block the unscattered X-ray beam, in order to prevent overexposure and damage of the detector. Both the beamstop and its holder can be seen in Figure 4.6a in a so-called mask image: a binary image where all pixels that are not suitable for analysis are indicated in black. As the detector used in our measurements consists of multiple panels, the space in between the panels is also visible in, and needs to be removed by the mask image. Determination of the center position of scattering images, as well as calibration of the wavevectors, was done with a sample of AgBe (silver behenate) powder (see Figure 4.6b).

Measurements of undeformed fibrin gels were performed by pipetting the assem-

bling fibrin network in a thin glass capillary (borosilicate glass capillaries with 10 μm wall thickness, Hilgenberg, Germany), using a 120 mm needle. An oven was used to maintain a 37°C environment during polymerization; the capillaries were sealed off with grease to prevent evaporation. As background for the capillary measurements we used a capillary filled with assembly buffer.

Measurements of fibrin gels under a shear deformation were performed by polymerizing the fibrin sample in a home-built polycarbonate Couette cell attached to a TA HR2 rheometer (during beamtime proposal BM26-02-797, 2016) or an Anton Paar MCR501 rheometer (during beamtime proposals BM26-02-857, 2017 and SC-4789, 2018). The rheometer's Peltier cell maintained a constant temperature (37°C) during assembly. A schematic representation of the Couette cell, as well as a picture of the Couette cell in the actual setup, is shown in Figure 4.7. The Couette is designed such that the outer wall is stationary, and the inner cylinder is attached to the rheometer spindle and rotates. During rheology experiments, a background image of the assembly buffer was taken for 60 s prior to every measurement. For the fibrin samples, the acquisition time was 45 s per strain step. No visual damage from the high-energy radiation to the sample was observed during the SAXS measurements. Figure 4.19 shows the mechanical loading protocol as used during the beamtime proposal BM26-02-857 (2017) measurements.

Measurements of a fibrin gel under an extensile deformation was performed by polymerizing the fibrin sample as described in Section 4.3.2, with two pieces of Velcro embedded in the gel on both ends. A Linkam TST350 tensile tester (Linkam Scientific Instruments, Tadworth, United Kingdom), equipped with a 20N-loadcell was placed in the beam path. After polymerization, the fibrin gel was placed in the tensile tester by clamping the Velcro at the two ends. The acquisition time was 20 s per image, at 6 positions per strain step. During analysis, the average was taken of the 6 positions per strain step. In between measurements the strain was increased, at a pulling speed of 7 μm/s. Assembly buffer was added every second strain step to prevent solvent evaporation. The background was taken by 60 s exposure of a capillary filled with assembly buffer.

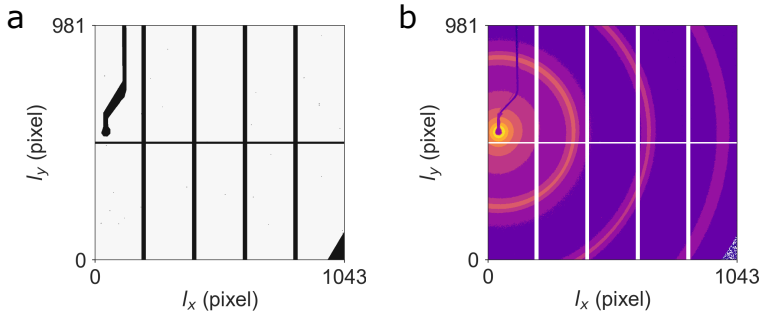

Figure 4.6: (a) The mask used to filter out the beamstop and bands in between the panels on the detector. Black pixels are removed from the scattering data during analysis. **(b)** AgBe sample used for calibration of the wavevector and determination of the center position. The first three scattering orders are clearly visible, and are used all three to determine the position of the X-ray beam and to calibrate the q-range.

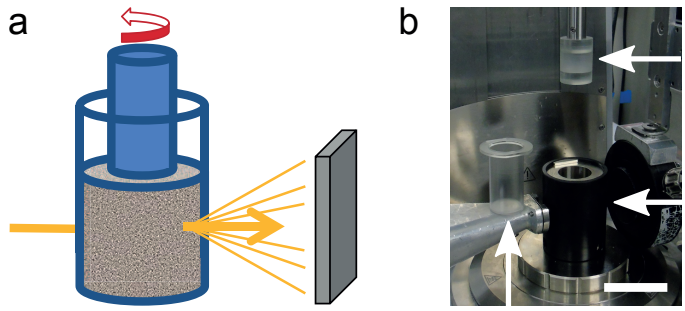

Figure 4.7: **(a)** Schematic representation of the Couette cell. A shear deformation is exerted on the sample as the inner cylinder rotates, while the outer cylinder remains stationary. The X-ray beam passes through the sample; unscattered light is stopped by the beamstop while scattered light reaches the detector. **(b)** A picture of the Couette cell at the beamline. The top right arrow indicates the inner cylinder, attached to the rheometer; the bottom left arrow indicates the outer cylinder placed next to its holder (indicated by the bottom right arrow), which is connected to the Peltier element for temperature control. The scale bar is approximately 5 cm.

SAXS ANALYSIS: PROCESSING RAW IMAGES

We wrote a customized Python program to analyse the scattering images, based on the following procedure. First, the bands in between the detector panels and the beamstop are removed by the application of a binary mask (shown in Figure 4.6a; all black pixels are removed in the scattering image). From the .poni file, a file created from the AgBe calibration image that contains meta-data of the experimental conditions, we obtained the detector pixel size, the X-ray wavelength, the sample-to-detector distance and the center of the beam on the detector (x_0, y_0). For every pixel in the scattering image, we calculated the distance $d = \sqrt{(x-x_0)^2 + (y-y_0)^2}$ and the angle $\phi = \text{atan}(\frac{y-y_0}{x-x_0})$ to the center. We subtracted the background according to Equation 4.2 (see also Supplementary Section 4.A):

$$I_s(q_x, q_y) = \frac{I_{s+bg}(q_x, q_y)}{I_{0,s+bg}} - \frac{I_{bg}(q_x, q_y)}{I_{0,bg}} * Abs \tag{4.2}$$

where $I_s(q_x, q_y)$, $I_{s+bg}(q_x, q_y)$ and $I_{bg}(q_x, q_y)$ are the scattering intensity of the fibrin sample, the (measured) sum of the fibrin and background and the (measured) background, respectively, and Abs is the difference in absorption between the sample and the background:

$$Abs = \frac{\frac{I_{0,s+bg}}{I_{0,bg}}}{\frac{monitor_{s+bg}}{monitor_{bg}}} \tag{4.3}$$

where I_0 and $monitor$ for both the sample and the background are obtained from a pin-diode integrated in the lead beamstop, and are saved in the metadata of every scattering image. To convert distances in pixels to wavenumbers (q (nm^{-1})), we use the following formula:

$$q = \frac{4\pi \sin(\frac{l * l_{pixel}}{2 l_{SD}})}{\lambda} \tag{4.4}$$

where l is a length in pixel, $l_{pixel} = 172$ μm the size of an individual pixel, l_{SD} the sample-to-detector distance (approximately 3 m) and λ the wavelength of the X-rays.

Figure 4.8 shows the scattering images of a 4 mg/ml fibrin sample without background subtraction (panel a), the measured background (panel b), and the sample with background subtracted (panel c). Clearly the scattering signal from the fibrin network is weak, requiring careful background subtraction [216].

Radial integration of the scattering intensity is performed by taking the average value of all pixels that fall in a distance bin size with a width of 1 pixel. As shown in Figure 4.8d, the background-subtracted scattering intensity of the fibrin network is approximately a factor 3 lower than the total measured intensity. At high q-values, the scattering intensity from the sample becomes nearly identical to that of the background, so small fluctuations (e.g. read-out noise) can cause the background-subtracted sample to show negative intensities in individual pixels.

Azimuthal integration is performed by averaging all pixels within a specified q-range of 47.0 nm to 102 nm, with a bin size with a width of $\theta = 2°$. The lower limit is set by the limitation that we do not want to take the Bragg peak originating from the molecular packing order into account, the upper limit is set by the lowest q-value we can access. The azimuthal integration region is shown in Figure 4.9a. We verified that using this q-range we do not include the panel boundaries in the azimuthal integration. A slice of $\theta = 40°$ is left out at the top to avoid the holder of the beamstop.

SAXS ANALYSIS: BRAGG SCATTERING PEAK

To determine the position of the Bragg-peak resulting from the periodic axial packing structure of fibrin fibers, we first need to subtract the slope of the scattered intensity that is convoluted with the Bragg peak. We consider three approaches to obtain the scattering peak:

1. Fitting the data to a function of the form

$$y(x) = \frac{1}{a * x + b} \tag{4.5}$$

   with a and b fit parameters, and subtracting the fitted curve from the data.

2. Applying a Gaussian filter with a large width on the data, subtracting it from the data that has been smoothened with a Gaussian filter with a small width.

3. Applying a filter of the derivative of a Gaussian with a large width to obtain the local slope, subtracting it from the data that has been smoothened with a Gaussian filter with a small width.

The first method, involving a fitting routine, is similar to the approach of [31] and [236], using respectively an exponential and a sixth-order polynomial; the advantage of the function in Eq. 4.5 is that only two fitting variables are involved. The clear disadvantage

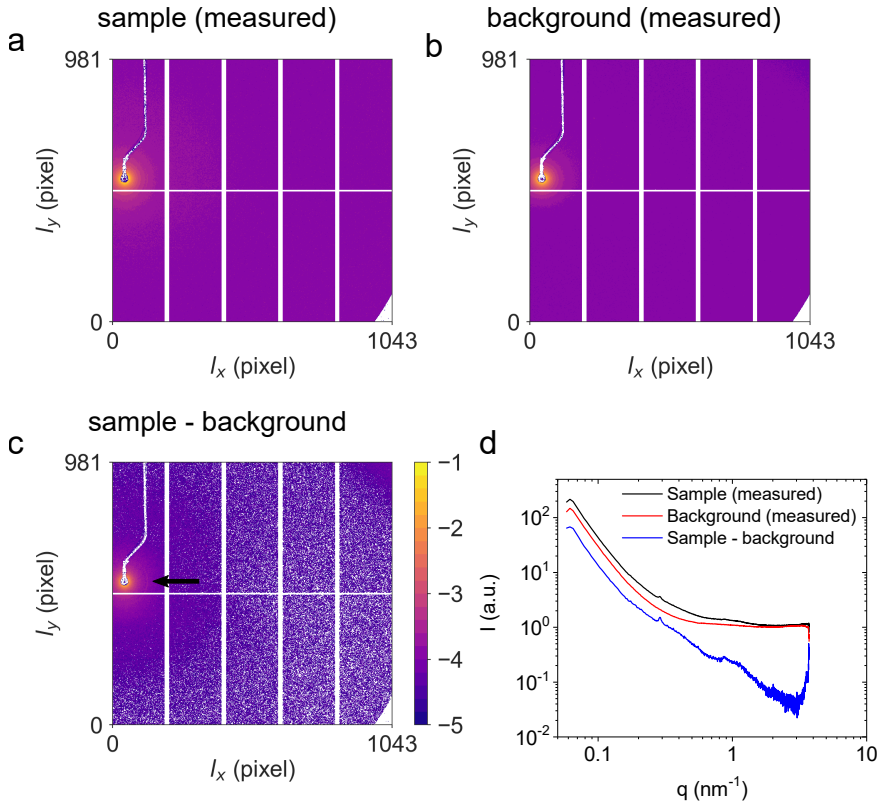

Figure 4.8: SAXS patterns. **(a)** Scattering patterns recorded for a 4 mg/ml fibrin sample, **(b)** for the buffer background, and **(c)** the background-subtracted image. After background subtraction, the first order scattering ring is (dimly) visible around the beamstop, as indicated by the black arrow. The spacings between the panels and the beamstop are visible in the images, but are removed during data processing. Data is shown on a logarithmic scale, in arbitrary units. **(d)** Radially integrated scattering intensity I as a function of wavevector q. The total scattering intensity for a a 4 mg/ml fibrin sample is shown in black, the background in red, and the background-subtracted intensity where only the scattering from the fibrin remains in blue.

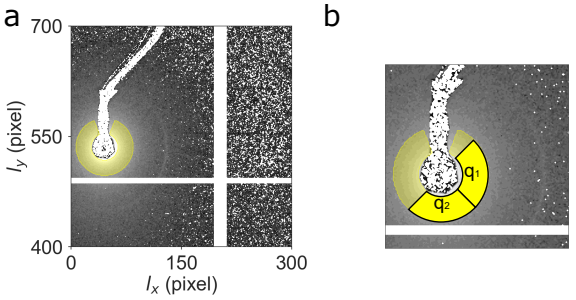

Figure 4.9: (a) The azimuthal integration area. The q-range of the yellow ring runs from 0.062 nm^{-1} nm to 0.13^{-1} nm, corresponding to distances of 102 nm to 47 nm. A segment of 40° has been left out at the top, to avoid the holder of the beamstop. The spacing between the detector panels is visible as the horizontal and vertical band. Dimly, the first scattering order of the fibrin gel is visible. **(b)** As input for the asymmetry factor (Equation 4.7), we divide the azimuthal integration area into an equal-sized horizontal quadrant q_1 and vertical quadrant q_2 and take the sum of the scattering intensities in each quadrant.

of the first method is the lack of filtering of high-frequency noise. In the second and third approach, it is essential to choose the first filtering step (basically a low-pass filter) such that the Bragg peak is not conserved, while the role of the second filtering step is to only remove high-frequency noise, without smoothing the Bragg peak. To this end, we choose a width of $\sigma = 1$ (in units of pixel width on the detector, corresponding to approximately $q = 0.0034$ nm^{-1} at this q-range) to filter out the high-frequency noise. We chose the third method over the second method as it better describes the non-Bragg scattering: the baseline of the data-subtracted Bragg peak is flat with the third filtering method, but contains a slight inclination with the second filtering method. In Figure 4.10a the raw data is shown, together with the data filtered with a Gaussian, for a 4 mg/ml fibrin sample.

The scattering peak we obtain by this method is shown in Figure 4.10b. We fit this peak to an analytical function to quantify its shape. In literature several functions are used to describe a Bragg peak: Gaussian, Lorentzian, Voight, pseudo-Voight, or Pearson VII [237]. Only in the case of a perfect lattice where broadening is only due to resolution limits, the peak is a Gaussian, whereas when sample disorder contributes, an exponentially modified Gaussian should be used [238]. However, because of low signals in our experiment, we cannot distinguish the exact shape, hence we still use a Gaussian function to characterize the peak rather than a Voight function (convolution of a Gaussian with a Lorentzian) or an exponentially modified Gaussian since the latter two have 5 rather than 4 free variables. We chose to use a Gaussian rather than Lorentzian function because of the slightly lower residual squares value of a Gaussian function. Furthermore, this has also been the function of choice in an earlier SAXS study of fibrin [31]. The Gaussian function has the form

$$y(x) = ae^{-\frac{(x-x_0)^2}{2\sigma^2}} + b \tag{4.6}$$

with a the peak height, x_0 the peak center, σ the standard deviation and b the offset. We calculate the Full Width Half Maximum (FWHM) of the scattering peak as FWHM = $2\sqrt{2log(2)}\sigma$.

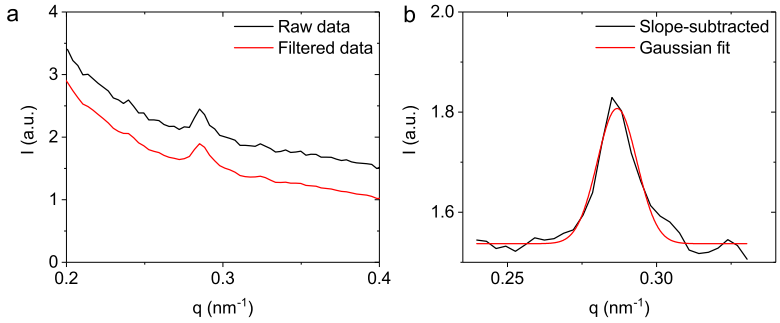

Figure 4.10: Quantitative analysis of the Bragg scattering peak. The sample is a 4 mg/ml fibrin gel under 0% applied strain. **(a)** The data (black line) is filtered with a Gaussian with a small width (red line). For clarity, the curves have been shifted along the y-axis. **(b)** Subtraction of the filtered data with the slope of the scattering curve, which was obtained by multiplying q with the derivative of a Gaussian with a large width (black line), and a fit with a Gaussian function (red line, Eq. 4.6). The fitting range runs from 24.0 nm^{-1} to 32.4 nm^{-1} and is chosen such that the Bragg scattering peak is approximately centered in the middle of the fitting range, with approximately one peak width extra on either side.

SAXS ANALYSIS: PATTERN ANISOTROPY UNDER STRAIN

Macroscopic shearing is expected to cause fiber alignment along the principal strain direction, as sketched in Figure 4.11. We apply shear by moving the inner cylinder of a Couette cell while keeping the outer cylinder stationary. The resulting strain field in the ϕ-plane, set by the spacing between the two cylinder walls, will change the projected length of the filaments both on the ϕ-plane and on the θ-plane, defined by the surfaces of the cylinders.[1] The X-ray beam passes perpendicularly through the surfaces of the Couette cell, so the scattering image captures the projection on the θ-plane.

To quantify the anisotropy from the scattering patterns we used two methods. In the first method we obtain the nematic order parameter from fitting an Orientational Distribution Function [240] to the azimuthally integrated scattered intensity as a function of ϕ (see Figure 4.12 and Section 4.3.6). In the second method we quantify the asymmetry of the scattering pattern from the ratio between the intensities of a horizontal quadrant and a vertical quadrant according to Equation 4.7:

$$A_{asym} = \frac{I_1 - I_2}{I_1 + I_2} \tag{4.7}$$

We use the same q-range in both cases (see Figure 4.9b). The first method has the advantage of permitting a quantitative comparison of shear-induced order with literature,

[1] This similar to how e.g. a collection of randomly oriented dipoles will emit light in all directions, while a set of aligned dipoles emits only in a well-defined direction [239].

while the second method has the advantage of being model-independent and being applicable to samples at low strain that lack clearly distinguishable peaks in the orientational distribution. However, the disadvantage of the first method is a large uncertainty in the fit at negligible anisotropy, and the downside of the second method is that A_{asym} is more sensitive to the background subtraction procedure than the nematic order parameter, which translates into a larger sample-to-sample variability. Even a small, isotropic deviation δ in the background intensity can result in a substantial change in the background-corrected asymmetry factor, A_{asym}:

$$A_{asym} = \frac{(I_1 + \delta) - (I_2 + \delta)}{(I_1 + \delta) + (I_2 + \delta)} = \frac{I_1 - I_2}{I_1 + I_2 + 2\delta} \approx \frac{I_1 - I_2}{2\delta} \tag{4.8}$$

which, *independently* of the difference between I_1 and I_2, will result in $|A_{asym}| \ll 1$.

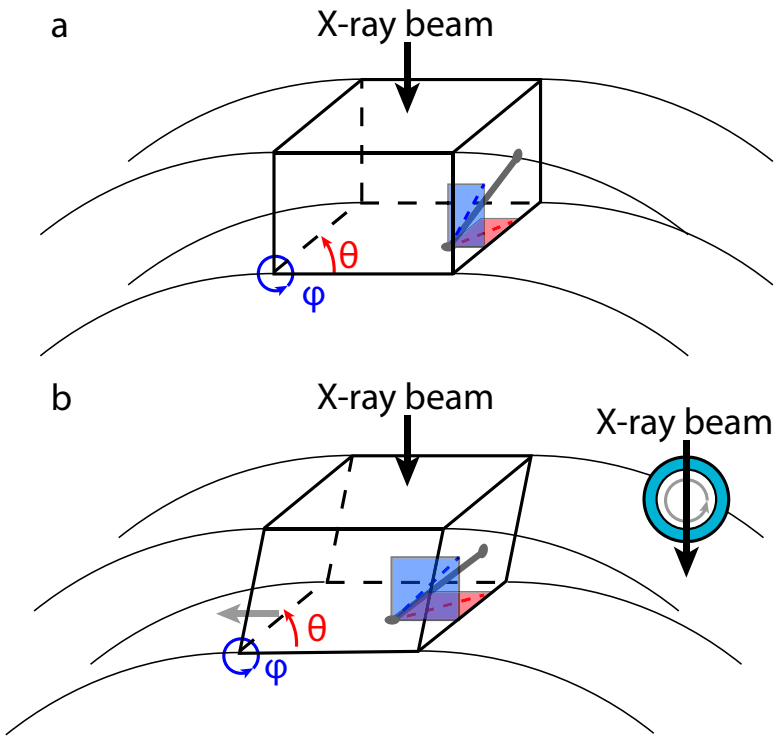

Figure 4.11: Schematic representation of the geometry of the combined SAXS-rheometry experiments and the effect of shear-induced alignment on the degree of anisotropy observed in the scattering image. **(a)** A single filament (dark grey) is sketched within an undeformed network (not shown). Its projection on the ϕ- and θ-plane is shown in blue and red, respectively. **(b)** As a shear strain (grey horizontal arrow) is applied in the ϕ-plane using a Couette cell (the inset shows a zoomed-out, top view of the Couette cell), the filament stretches and aligns to the direction of principal strain. This reorientation also affects the projected length (red dashed line) on the θ-plane, which is the plane that is imaged through X-ray scattering.

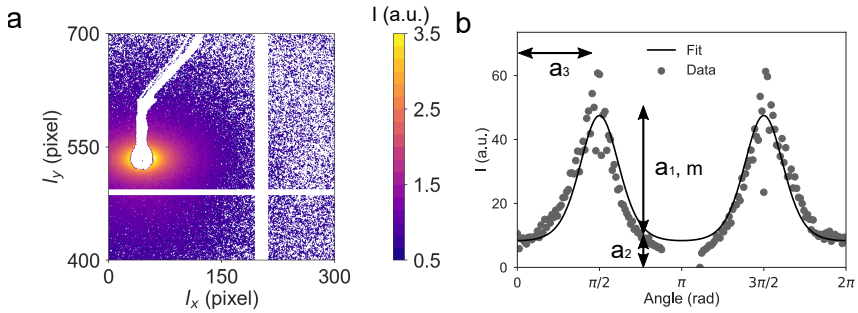

Figure 4.12: Quantifying shear-induced alignment of the fibers by fitting the azimuthally integrated scattering intensity with an ODF. **(a)** The background-subtracted scattering image for a 4 mg/ml fibrin gel under 189% applied shear strain, showing clear anisotropy. Dimly, the first scattering order appears near the center of the image. **(b)** The azimuthally integrated intensity I (symbols) together with a fit to Equation 4.20 (line), using fit parameters a_1, a_2, a_3 and m as indicated. Data shown are in arbitrary units. Data in **(a)** is shown on a logarithmic scale.

4

4.3.6. NEMATIC ORDER PARAMETER

The nematic order parameter S was calculated using an approach originally developed to quantify liquid crystal formation of semiflexible fd virus rods [241] and actin filaments [240]. We start with an expression for the Orientational Distribution Function (ODF) [240]:

$$\Phi(\theta) = Ae^{m\cos(\theta)^2} \tag{4.9}$$

where A is a normalization constant. We determine the normalization constant A by integrating $\Phi(\theta)$ over a solid angle $d\Omega$

$$\Phi(\theta) = \int_0^{2\pi}\int_0^{\pi} Ae^{m\cos(\theta)^2}\sin(\theta)d\phi d\theta \tag{4.10}$$

$$= 2\pi A\int_0^{\pi} e^{m\cos(\theta)^2}\sin(\theta)d\theta \tag{4.11}$$

$$= \frac{2\pi A}{\sqrt{m}}\int_0^{\pi} e^{(\sqrt{m}\cos(\theta))^2}(-1)d\sqrt{m}\cos(\theta) \tag{4.12}$$

$$= \frac{2\pi A}{\sqrt{m}}\int_{\sqrt{m}\cos(0)}^{\sqrt{m}\cos(\pi)} e^{x^2}(-1)dx \tag{4.13}$$

$$= \frac{2\pi^{3/2}A}{\sqrt{m}}\frac{1}{\sqrt{\pi}}\int_{\sqrt{m}}^{-\sqrt{m}} e^{x^2}(-1)dx \tag{4.14}$$

$$= \frac{2\pi^{3/2}A}{\sqrt{m}}\frac{1}{\sqrt{\pi}}\int_{-\sqrt{m}}^{\sqrt{m}} e^{x^2}dx \tag{4.15}$$

$$= \frac{2\pi^{3/2}A}{\sqrt{m}}\text{erfi}(\sqrt{m}) \tag{4.16}$$

$$= 1 \tag{4.17}$$

using the imaginary error function[2] $\mathrm{erfi}(x) = \frac{1}{\sqrt{\pi}} \int_x^x e^{-t^2} dt$, $\frac{d\cos(\theta)}{d\theta} = -\sin(\theta)$, and changing variables $d\sqrt{m}\cos\theta = dx$, changing the integration boundaries accordingly. Hence,

$$A = \frac{\sqrt{m}}{2\pi^{3/2}\mathrm{erfi}(\sqrt{m})} \tag{4.18}$$

so that

$$\Phi(\theta) = \frac{\sqrt{m}\, e^{m\cos(\theta)^2}}{2\pi^{3/2}\mathrm{erfi}(\sqrt{m})} \tag{4.19}$$

We then add the fit parameters a_1, a_2 and a_3

$$\Phi(\theta) = a_1 \frac{\sqrt{m}\, e^{m\cos(\theta - a_3)^2}}{2\pi^{3/2}\mathrm{erfi}(\sqrt{m})} + a_2 \tag{4.20}$$

We then fit Equation 4.20 to the azimuthally integrated scattering intensity (see Figure 4.12), where a_1 and m are free parameters, a_2 is set to the maximum of the lowest 10% of the intensity values and a_3 is $\pi/2$, as we expect fiber alignment in the horizontal direction (see Figure 4.7, where $\theta = 0$ corresponds to up-down alignment and $\theta = \pi/2$ to left-right alignment). To obtain the nematic order parameter S from the ODF we start with the expression used in Ref. [241], following a similar procedure as in the derivation starting at Equation 4.10, and where $\frac{3}{2}\cos^2(\theta) - \frac{1}{2}$ is used as the form factor of a single rod.

$$S = 2\pi \int_0^\pi \left(\frac{3}{2}\cos^2(\theta) - \frac{1}{2}\right) \Phi(\theta) d\cos(\theta) \tag{4.21}$$

$$= 2\pi \int_0^\pi \left(\frac{3}{2}\cos^2(\theta) - \frac{1}{2}\right) \frac{\sqrt{m} e^{m\cos(\theta)^2}}{2\pi^{3/2}\mathrm{erfi}(\sqrt{m})} d\cos(\theta) \tag{4.22}$$

$$= \frac{\sqrt{m}}{2\sqrt{\pi}\,\mathrm{erfi}(\sqrt{m})} \int_0^\pi \left(3\cos^2(\theta) - 1\right) e^{m\cos(\theta)^2} d\cos(\theta) \tag{4.23}$$

$$= \frac{1}{2\sqrt{\pi}\,\mathrm{erfi}(\sqrt{m})} \int_0^\pi \left(\frac{3}{m}(\sqrt{m}\cos(\theta))^2 - 1\right) e^{(\sqrt{m}\cos(\theta))^2} d\sqrt{m}\cos(\theta) \tag{4.24}$$

$$= \frac{1}{2\sqrt{\pi}\,\mathrm{erfi}(\sqrt{m})} \int_{-\sqrt{m}}^{\sqrt{m}} \left(\frac{3}{m}x^2 - 1\right) e^{x^2} dx \tag{4.25}$$

$$= \frac{1}{2\sqrt{\pi}\,\mathrm{erfi}(\sqrt{m})} \left(\int_{-\sqrt{m}}^{\sqrt{m}} \frac{3}{m}x^2 e^{x^2} dx - \int_{-\sqrt{m}}^{\sqrt{m}} e^{x^2} dx\right) \tag{4.26}$$

$$= \frac{1}{2\sqrt{\pi}\,\mathrm{erfi}(\sqrt{m})} \left(\int_{-\sqrt{m}}^{\sqrt{m}} \frac{3}{m}x^2 e^{x^2} dx - \sqrt{\pi}\,\mathrm{erfi}(\sqrt{m})\right) \tag{4.27}$$

[2] Despite its name, the imaginary error function is real when x is real.

To integrate $\int_{-\sqrt{m}}^{\sqrt{m}} x^2 e^{x^2}\,dx$ we use integration by parts[3] ($\int u\,dv = uv - \int v\,du$):

$$\int_{-\sqrt{m}}^{\sqrt{m}} x^2 e^{x^2}\,dx \tag{4.28}$$

$$= \frac{1}{2}\int_{-\sqrt{m}}^{\sqrt{m}} x(2xe^{x^2}\,dx) \tag{4.29}$$

$$= \frac{1}{2} x\, e^{x^2} \|_{-\sqrt{m}}^{\sqrt{m}} - \frac{1}{2}\int_{-\sqrt{m}}^{\sqrt{m}} e^{x^2}\,dx \tag{4.30}$$

$$= \sqrt{m}\, e^m - \frac{1}{2}\sqrt{\pi}\,\mathrm{erfi}(\sqrt{m}) \tag{4.31}$$

so that our expression for S finally becomes

$$S = \frac{1}{2\sqrt{\pi}\,\mathrm{erfi}(\sqrt{m})}\left(\int_{-\sqrt{m}}^{\sqrt{m}} \frac{3}{m} x^2 e^{x^2}\,dx - \sqrt{\pi}\,\mathrm{erfi}(\sqrt{m})\right) \tag{4.32}$$

$$= \frac{1}{2\sqrt{\pi}\,\mathrm{erfi}(\sqrt{m})}\left(\frac{3}{m}\sqrt{m}\,e^m - \frac{3}{2m}\sqrt{\pi}\,\mathrm{erfi}(\sqrt{m}) - \sqrt{\pi}\,\mathrm{erfi}(\sqrt{m})\right) \tag{4.33}$$

$$= 2\pi\left(\frac{3e^m}{4\sqrt{m}\pi^{3/2}\mathrm{erfi}(\sqrt{m})} - \frac{3+2m}{8m\pi}\right) \tag{4.34}$$

4.3.7. SIMULATIONS OF AFFINE DEFORMATIONS ON RANDOMLY ORIENTED RODS

To benchmark the development of shear-induced alignment in fibrin networks, we calculate the *affine* effect of deformation on an initially isotropic network using simulations of initially random ensembles of rigid, elastic rods. Each rod has a fixed initial length of $r = 1$, and is further characterized by one or two random angles, for a two or three dimensional simulation, respectively. We retrieve Cartesian coordinates $\{x, y\}$

$$x = r\cos(\phi)$$
$$y = r\sin(\phi)$$

for two dimensional systems, and $\{x, y, z\}$

$$x = r\sin(\theta)\cos(\phi)$$
$$y = r\sin(\theta)\sin(\phi)$$
$$z = r\cos(\theta)$$

for three dimensional systems. We generate a sufficiently large number of rods (100,000) to obtain a statistically significant ensemble average, and apply strain in small steps of 0.01. The deformation matrices $\mathbf{D_{s,2D}}$ and $\mathbf{D_{s,3D}}$ for simple shear in 2 and 3 dimensions, respectively, are:

$$\mathbf{D_{s,2D}} = \begin{pmatrix} 1 & \gamma \\ 0 & 1 \end{pmatrix}, \mathbf{D_{s,3D}} = \begin{pmatrix} 1 & \gamma & 0 \\ 0 & 1 & 0 \\ 0 & 0 & 1 \end{pmatrix} \tag{4.35}$$

[3] Contrary to popular believe, this *is* a useful technique!

For extension (and compression, which is extension with negative strain values), we show here the deformation matrices for two simple cases: first, extension where the total volume of the system is conserved, $\mathbf{D_{e,2D}}$ and $\mathbf{D_{e,3D}}$:

$$\mathbf{D_{e,2D}} = \begin{pmatrix} 1+\gamma & 0 \\ 0 & \frac{1}{1+\gamma} \end{pmatrix}, \mathbf{D_{e,3D}} = \begin{pmatrix} 1+\gamma & 0 & 0 \\ 0 & \frac{1}{\sqrt{1+\gamma}} & 0 \\ 0 & 0 & \frac{1}{\sqrt{1+\gamma}} \end{pmatrix} \tag{4.36}$$

such that at any strain the product of $(1+\gamma) \times \frac{1}{\sqrt{1+\gamma}} \times \frac{1}{\sqrt{1+\gamma}} = 1$; and second, extension without volume conservation, where there is only deformation in the direction of strain and no lateral expansion or compression, $\mathbf{D_{e,2D}}$ and $\mathbf{D_{e,3D}}$:

$$\mathbf{D_{e,2D}} = \begin{pmatrix} 1+\gamma & 0 \\ 0 & 1 \end{pmatrix}, \mathbf{D_{e,3D}} = \begin{pmatrix} 1+\gamma & 0 & 0 \\ 0 & 1 & 0 \\ 0 & 0 & 1 \end{pmatrix} \tag{4.37}$$

However, not all systems under extensile strain can be described by these deformation matrices. Some systems will show intermediate behaviour, potentially with a strain-dependent volume reduction (see for example Figure 4.5). The general solution for an arbitrary volume change in response to an uniaxial extensile strain γ is as follows. We first write down the volume of the system before (V) and after (V') deformation:

$$V = x * y * z \tag{4.38}$$

$$V' = x' * y' * z' \tag{4.39}$$

$$V' = x(1+\gamma) * y\frac{1}{(1+\gamma)^a} * z\frac{1}{(1+\gamma)^a} \tag{4.40}$$

$$f * V = x * y * z * (1+\gamma)^{(1-2a)} \tag{4.41}$$

where f is the relative volume change and a an arbitrary exponent. The two special (3D) cases of $a = 0.5$, and $a = 0$ correspond to the deformation matrices in Equation 4.36 and 4.37, where $a = 0.5$ leads to $1-2a = 0$ so that the volume does not change under extension (Eq. 4.36), and $a = 0$, such that $\frac{1}{(1+\gamma)^a} = 1$, so that the y and z dimensions are unaffected by extension (and hence V grows linearly with strain). The general expression for a deformation matrix under extension is:

$$\mathbf{D_{e,2D}} = \begin{pmatrix} 1+\gamma & 0 \\ 0 & (1+\gamma)^{-a} \end{pmatrix}, \mathbf{D_{e,3D}} = \begin{pmatrix} 1+\gamma & 0 & 0 \\ 0 & (1+\gamma)^{-a} & 0 \\ 0 & 0 & (1+\gamma)^{-a} \end{pmatrix} \tag{4.42}$$

We can obtain the value of a (which can depend on γ), given that we know f and γ:

$$f = (1+\gamma)^{(1-2a)} \tag{4.43}$$

$$\log f = \log(1+\gamma)^{(1-2a)} \tag{4.44}$$

$$\log f = \log(1+\gamma) - 2a\log(1+\gamma) \tag{4.45}$$

$$a = \frac{\log(1+\gamma) - \log f}{2\log(1+\gamma)} \tag{4.46}$$

After a deformation matrix is applied to a filament, we re-calculate its length and orientation. To quantify the (average) orientation in the deformed network, we calculate the nematic order parameter S [242], starting from the tensor order parameter Q:

$$\mathbf{Q} = \frac{1}{d-1} \sum d * \hat{u}_i \hat{u}_j - \delta_{i,j} \tag{4.47}$$

with d the dimensionality of the system, and $\delta_{i,j}$ the Kronecker delta function that is 1 when $i = j$ and 0 otherwise. For three dimensions[4],

$$\mathbf{Q} = \frac{1}{2} \begin{pmatrix} 3\sin(\theta)^2\cos(\phi)^2 - 1 & 3\sin(\theta)^2\cos(\phi)\sin(\phi) & 3\cos(\theta)\sin(\theta)\cos(\phi) \\ 3\sin(\theta)^2\cos(\phi)\sin(\phi) & 3\sin(\theta)^2\sin(\phi)^2 - 1 & 3\cos(\theta)\sin(\theta)\sin(\phi) \\ 3\cos(\theta)\sin(\theta)\cos(\phi) & 3\cos(\theta)\sin(\theta)\sin(\phi) & 3\cos(\theta)^2 - 1 \end{pmatrix} \tag{4.48}$$

However, this expression requires knowledge of the preferred alignment in the system, and that $\mathbf{Q}$ aligns along that direction. By quadratically summing all terms and taking the square root, we can obtain the nematic order parameter, invariant to the orientation of the strain:

$$S = \sqrt{\frac{2}{3}} \sqrt{\langle u_1 u_1\rangle^2 + \langle u_1 u_2\rangle^2 + \langle u_1 u_3\rangle^2 + \langle u_2 u_1\rangle^2 + \langle u_2 u_2\rangle^2 + \langle u_2 u_3\rangle^2 + \overline{\langle u_3 u_1\rangle^2 + \langle u_3 u_2\rangle^2 + \langle u_3 u_3\rangle^2}} \tag{4.49}$$

where a factor $\sqrt{\frac{2}{3}}$ has been added to normalize S, such that S equals zero for a perfectly isotropic system and one for a perfectly aligned system. We write Equation 4.49 out and simplify the terms:

$$S = \sqrt{\frac{2}{3}} \left(\frac{1}{4}\langle 3\sin(\theta)^2\cos(\phi)^2 - 1\rangle^2 + \frac{1}{4}\langle 3\sin(\theta)^2\sin(\phi)^2 - 1\rangle^2 + \frac{1}{4}\langle 3\cos(\theta)^2 - 1\rangle^2 + \frac{9}{2}\langle \cos(\theta)\sin(\theta)\cos(\phi)\rangle^2 + \frac{9}{2}\langle \cos(\theta)\sin(\theta)\sin(\phi)\rangle^2 + \frac{9}{2}\langle \sin(\theta)^2\cos(\phi)\sin(\phi)\rangle^2 \right) \tag{4.50}$$

From this expression for S, we can already see two properties of the nematic order parameter. First, for an isotropic distribution of α, $\langle\cos(\alpha)\rangle = 0$ and $\langle\cos(\alpha)^2\rangle = \frac{1}{2}$, such that the average of all off-diagonal terms and the sum of the average of the diagonal terms in Equation 4.48 are zero, which we expect for a system where the filament orientation is isotropic. Secondly, for a single value of θ and ϕ, Equation 4.50 equals 1, as we expect for a single filament, or a collection of filaments with identical orientation. Furthermore, for $\hat{u}_z\hat{u}_z$, we find $Q = \frac{3}{2}\cos(\theta)^2 - \frac{1}{2}$, which is the second Legendre polynomial for $\cos(\theta)$, in agreement with previous work [242, 243].

The derivation for the two-dimensional nematic order parameter is similar to its three-dimensional equivalent, yet (much) simpler, as the matrix in Equation 4.48 contains four rather than 9 terms. The final expression one obtains for S is as follows:

$$S = \sqrt{\langle 2\cos(\phi)^2 - 1\rangle^2 + \langle 2\cos(\phi)\sin(\phi)\rangle^2} \tag{4.51}$$

[4] The expression for the nematic order parameter (Eq. 4.47) is mentioned in several works [242–247], although how one exactly obtains an expression for S given a set of angles θ and ϕ is, to my knowledge, not written down. I hope the reader finds this derivation educational.

using the fact that $\langle 2\cos(\phi)^2 - 1\rangle^2$ and $\langle 2\sin(\phi)^2 - 1\rangle^2$ are identical for $0 < \phi < 2\pi$.

In Figure 4.13a the predicted order parameter is shown for 2D and 3D networks under simple shear. As we expect, the order parameter is zero in the absence of applied strain, and increases asymptotically towards one as the strain reaches (very) high values (> 500%, depending on the dimensionality). As the direction in which shear is applied should not matter for an initially isotropic network, the order parameter should be symmetric around zero strain, which is indeed observed. Furthermore, these results are in full agreement with results presented in literature [246].

Unlike shear deformations, which are intrinsically volume conserving, extensile deformations do not necessarily conserve volume. The nematic order parameter for a system with volume conservation (a Poisson ratio[5] of 0.5, typical for most simple, elastic materials), for both 2D ($\alpha = 1$) and 3D ($\alpha = 0.5$), is shown in Figure 4.13b. Unlike shear, there is no symmetry around zero strain: while shear and positive extension can (at least in theory) reach arbitrarily large values, negative extension (i.e. compression) has a maximum strain value of -1, where the system is fully flattened. This indeed leads to an order parameter of 1.0 in the case of a 2D system, and 0.5 for a 3D system, where there is still orientational freedom in the plane orthogonal to the compressive deformation. Similar to shear deformation, the order parameter approaches 1 more quickly for 2D networks than for 3D network at large, positive strains. Shrinking boundaries in the directions orthogonal to the deformation (volume conservation) lead to a more rapid approach of $S = 1$ than a system where the boundaries in the directions orthogonal to the deformation do not change: the aspect ratio, the ratio between the length (direction of strain) and the width, grows with $(1+\gamma)^2$ in a system with volume conservation, and with $1+\gamma$ in a system without volume conservation, both in 2D and 3D.

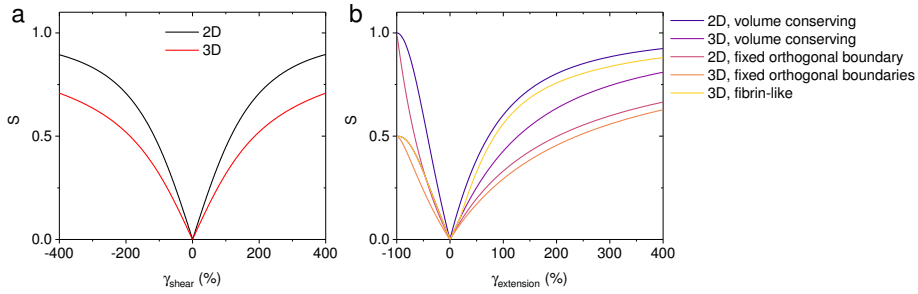

Figure 4.13: The nematic order parameter S as a function of applied strain (γ_{shear} and $\gamma_{extension}$ for shear and extension, respectively) for an ensemble of 100,000 (independent) filaments. **(a)** Networks subjected to a shear deformation, in two and three dimensions. **(b)** Networks subjected to an extension, in two and three dimensions: with volume conservation; for a system where the boundaries are fixed in the direction(s) orthogonal to the direction of strain; and for a system that changes its volume similar to a fibrin network (fibrin-like), calculated by the measured volume decrease of fibrin gels under extension, as shown in Figure 4.5.

In Figure 4.14a and b the probability function is shown for the ϕ-coordinate for a 3D

[5]Note that a Poisson ratio is only defined for an infinitesimal deformation.

system of filaments under shear and extensile deformation, both in volume-conserving conditions. At zero strain, the probability function for ϕ is flat and identical for shear and extension. As the shear angle changes with increasing strain, the peak position of the probability function shifts for increasing strain levels, and increases in intensity. On the other hand, for extension, the direction of deformation remains the same, hence we only see an increase in intensity, but no change in peak position. Finally, as we expect for the ϕ-coordinate, the probability function is periodic with a shift of π, as a filament with length (x_i, y_i) is identical to a filament with length $(-x_i, -y_i)$.[6] In Figure 4.14c and d the probability function is shown for the same systems, but now for the θ-coordinate. For θ, the probability distribution at $\gamma = 0\%$ behaves as a cosine function, with a peak developing at $\theta = \pi/2$ as strain increases, indicating alignment towards the ϕ-plane. A schematic representation of the alignment of filaments in the ϕ- and θ-direction is shown in Figure 4.11.

In Figure 4.14e and f the probability function is shown for still the same systems, but now for the length of the filaments. At zero strain, this is a single spike at $l = 1$, but as strain increases, the distribution broadens. For both shear and extension, we see that there is not only a population of filaments that is extended, but also a population of filaments that is compressed as the filaments are oriented orthogonal to the direction of strain. Interestingly, the maximum strain a filament can experience is the global strain in the case of an extension, but as the strain orientation changes during shear, some individual filaments experience a higher strain than the global shear strain. In the insets in Figure 4.14e and f, the fraction of the filament population that is under compression, extension up to 100% and extension of more than 100% is shown. Even for 300% applied shear or extensile strain, approximately 20% of the filaments are still under compression.

Finally, the reason why $P(\phi)$ in Figure 4.14 is flat while $P(\theta)$ behaves as a cosine at 0% strain, comes from the definition of solid angle $d\Omega = \sin(\theta) d\phi d\theta$. However, the choice of angle definitions is arbitrary. We can change our definition such that, for an equal distribution of filaments, θ runs from 0 to 2π, without the cosine-term[7]. This is shown in Figure 4.15. The reason for choosing this definition of angles is because this is the projection seen by the SAXS-detector.

[6] Alternative way of viewing this: rotate a stick 180° and it'll point in the same direction.

[7] This is analogous of replacing earth's North and South pole with a West pole in Ecuador and an East pole in Malaysia, with the equator now running over both artics. Earth's surface itself does not change by this transformation, only the way it is described in terms of longitude and latitude.

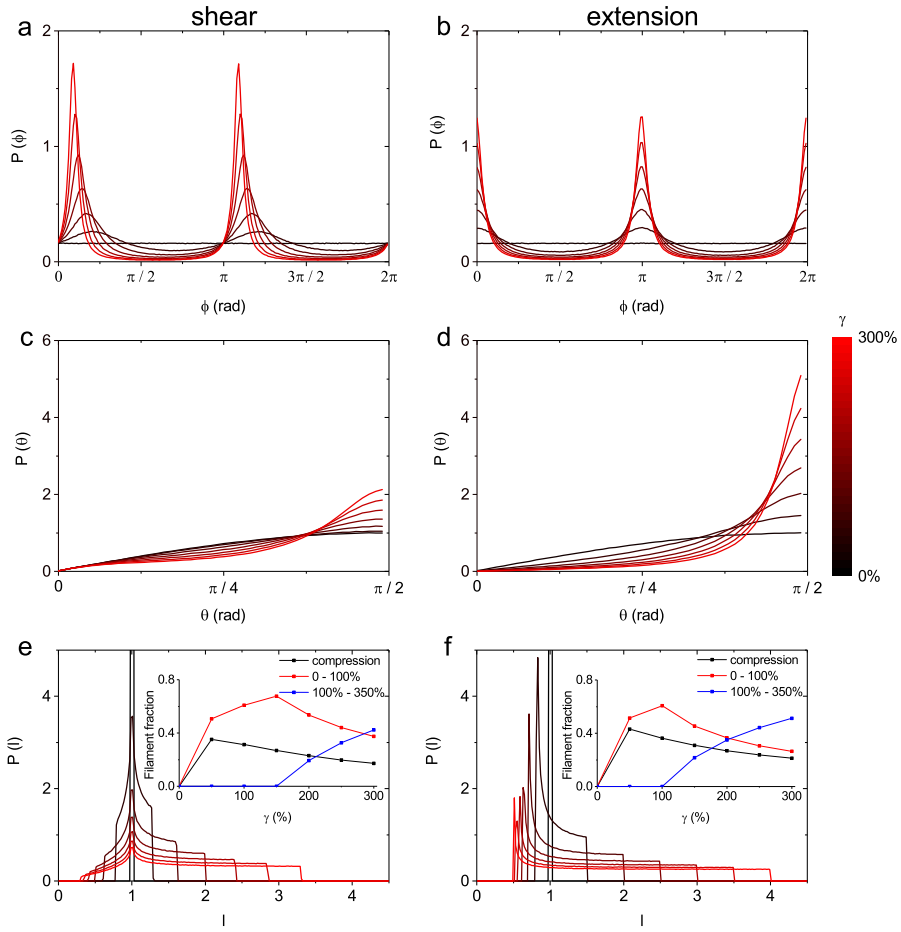

Figure 4.14: (Normalized) probability function P for the ϕ-projection of a 3D ensemble of filaments under shear **(a)** or extension deformation under volume conservation conditions deformation **(b)**, with increasing applied deformation γ. **(c)** and **(d)** show the probability function for the same networks in the θ-direction. In **(e)** and **(f)** the probability function is plotted for the filament length l. The insets in **(e)** and **(f)** show the fractional population of filaments under compression, extension up to 100% and extension higher than 100%, as a function of the applied network strain γ. Orientations of 3 million filaments were averaged to obtain these graphs.

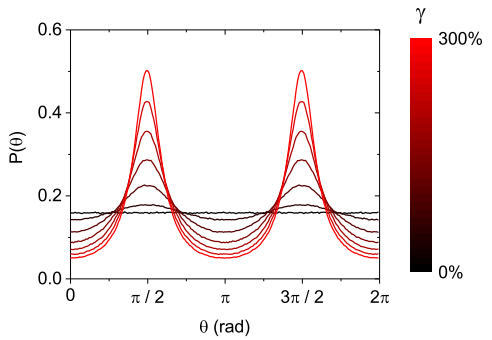

Figure 4.15: (Normalized) probability function P for the θ-projection of a 3D ensemble of filaments under shear deformation, with increasing applied deformation γ. The conventional $d\Omega = \sin(\theta)d\phi d\theta$ with $0 < \phi < 2\pi$ and $0 < \theta < \pi/2$ has been replaced by $d\Omega = \sin(\phi)d\phi d\theta$ with $0 < \phi < \pi/2$ and $0 < \theta < 2\pi$. Orientations of 3 million filaments were averaged to obtain these graphs.

4.4. RESULTS

4.4.1. STRAIN-INDUCED FIBER ALIGNMENT

In Figure 4.16 we show the background-subtracted scattering images of a 4 mg/ml fibrin gel under 0%, 100% and 300% applied strain, and 0% strain after a maximum of 300% strain had been applied. We observe a ring around the beamstop, corresponding to the first scattering order (Bragg peak). As strain increases, we observe that anisotropy develops in the scattering image, and that the Bragg peak decreases in intensity. However, both changes are reversible upon removal of the applied strain.

To quantify the change from an isotropic to a anisotropic scattering pattern, we azimuthally integrated the scattering patterns of Figure 4.16, shown in Figure 4.17a. We observe, in line with what the scattering images show, an onset of alignment around 100% applied shear strain, strong anisotropy at 300% strain, and a complete reversibility of fiber alignment back to isotropy upon return to 0% strain. In the same panel, in black lines, is the prediction from a simulation of an initially random ensemble of rigid, elastic rods, undergoing an affine shear deformation (see also Figure 4.15). For the 300% data set, the width of the curve appears to be slightly smaller than for the data, indicating a slightly lower alignment than expected based on affine deformation (see also 4.17b). However, overall, the shape of the azimuthally integrated intensity can be very well described by a model of affine deformation.

By fitting the azimuthally integrated data, we determined the nematic order parameter. The q-range where we analysed the data corresponds to spatial lengths of 49.7 nm to 102 nm. The nematic order parameter for fibrin gels under shear deformation is shown in Figure 4.17b, together with the order parameter that is calculated with a model of affine deformation. We observe that the measured and calculated order parameter agree remarkably well up to approximately 100% shear strain, indicating that the fibrin network deforms affinely up to this strain level. The non-zero order parameter at zero strain is due to the large uncertainty in the fit at zero anisotropy. Above 100% strain, the measured order parameter increases more slowly than the calculated order parameter, suggesting that non-affinity starts to play a role.

An alternative, more direct approach of quantifying anisotropy in the scattering image, that does not involve a fitting procedure, is by taking the ratio in intensity in the SAXS pattern between the direction of deformation and the direction orthogonal to deformation (Equation 4.7 and Figure 4.9b). This anisotropy factor A_{asym} is shown in Figure 4.18, together with the affine prediction for fiber orientation in the θ-plane (see Figure 4.11). We observe that A_{asym} increases more slowly with increasing strain than the nematic order parameter, yet for both, the data follow the theoretical prediction up to approximately 100% applied strain. The inset shows the asymmetry factor A_{asym} when the sample is returned to 0% strain, as a function of the maximum applied strain γ_{max}. We observe, independent of the maximum applied strain, full return to an isotropic image.

In Figure 4.17b we also show the nematic order parameter, as determined from analysis of confocal rheology. Although the order parameter does not start at zero (possibly due to finite size effects), we observe a trend, where the order parameter increases with applied strain. The order parameter increases less than what would be expected for a purely affine deformation.

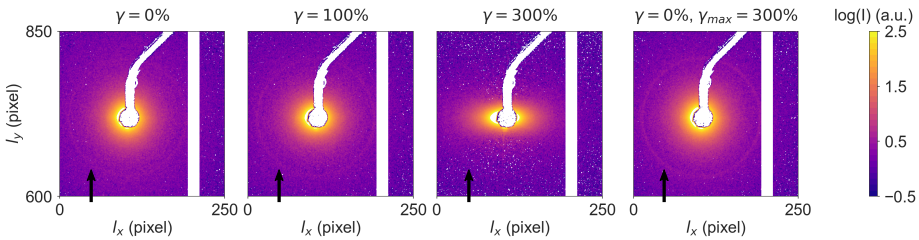

Figure 4.16: Background-subtracted scattering patterns of a 4 mg/ml fibrin gel under increasing levels of shear strain (0%, 100% and 300%), and a return to 0% after the gel has experienced a maximum strain of 300%. The white bar corresponds to the panel edge, and the white dot and thread to the beamstop and its holder. The first order scattering rings are indicated by black arrows. The ring becomes weaker from 100% to 300%, and brighter again on return to 0%, where it is even brighter than for the virgin sample.

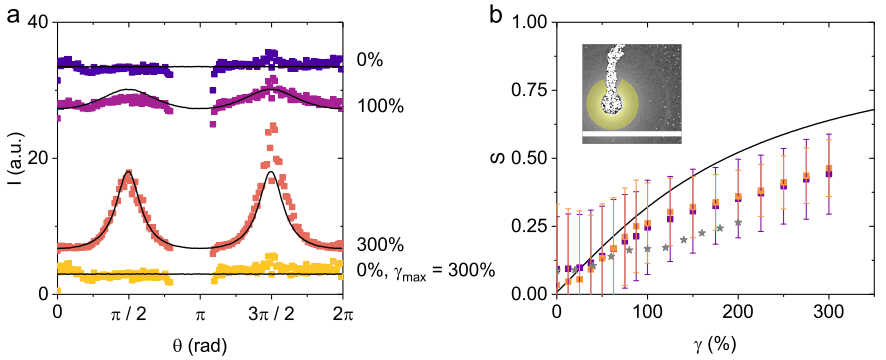

Figure 4.17: (a) Azimuthally integrated intensities of the scattering patterns shown in Figure 4.16. For clarity, the curves have been shifted along the y-axis. The anisotropy in the azimuthally integrated intensity that develops as a function of applied strain, is fully reversible upon removal of the strain. The black curves are the prediction from a simulation of an initially random ensemble of rigid, elastic rods, undergoing an affine shear deformation (Figure 4.15). The theory curves were multiplied by a manually determined factor based on the 300%-curve. For clarity, the curves have been shifted along the y-axis. **(b)** The nematic order parameter S, calculated from the azimuthally integrated scattering intensity for a q-range of 0.062 to 0.13 nm^{-1} (see inset), as a function of applied strain γ, together with the nematic order parameter in a model for affine network deformation (black line), for two independently prepared samples. The grey stars show the nematic order parameter for a 2 mg/ml fibrin gel, as determined from fiber orientation in confocal rheology.

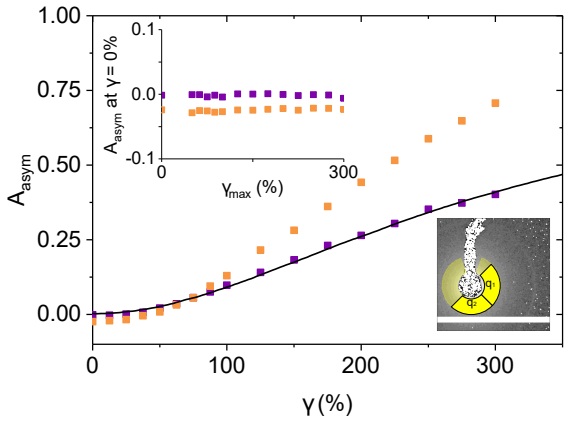

Figure 4.18: Anisotropy in scattering patterns calculated from the azimuthally integrated scattering intensity for a q-range of 0.062 to 0.13 nm^{-1}, corresponding to spatial structures of 102 to 49.7 nm (see inset bottom-right), for two independently prepared samples. The asymmetry factor A_{asym} (Equation 4.7) as a function of applied strain, together with the prediction for a model of affine deformation (black line). Inset top-left: The asymmetry factor A_{asym} when the sample is returned to 0% strain, as a function of the maximum applied strain γ_{max}, for two independent data sets.

4.4.2. STRAIN-INDUCED MONOMER LENGTHENING

To quantify the effect of network deformation on the monomer level, we perform radial integration of the scattering patterns shown in Figure 4.16. In Figure 4.20a we see a decrease in scattering intensity with increasing q, as scattering by the fractal network structure gives a power-law of the scattering intensity as a function of wave number. On top of this trend, there are two peaks visible, around $q = 0.3$ nm^{-1} and $q = 0.9$ nm^{-1}, corresponding to the first and third order Bragg diffraction, respectively, and indicated by arrows. Another arrow is placed at the q-value where we expect the fourth order peak, although it is ambiguous whether it appears in the data. At increasing strain the first order peak decreases in intensity, yet upon removal of the strain, the peak returns. The second peak is missing altogether, see Section 4.4.2.

Figure 4.21a shows in more detail how the first order scattering peak in the background-subtracted spectra develops with strain, obtained from integration in the quadrants of the scattering spectra that are oriented in the direction of strain. Overlaid on the data are curves of the data that have been convoluted with a Gaussian function, as used in the analysis of the Bragg peak (see Section 4.3.5). These spectra show a small shift towards smaller q-values, corresponding to an increase of the characteristic repeat length. Figure 4.21b shows the spectra taken at 0% applied strain, with a history of increasing maximum applied strains. These spectra show larger shift towards higher q-values, which implies a *shortening* of the real-space characteristic length compared to the original periodicity in the virgin sample.

To further quantify the monomer response to applied strain, we applied a fitting pro-

cedure to the first Bragg diffraction peak. We quantify the peak with three different parameters: the peak position q_{peak1}, which we associate with a repeat distance; the full-width half-maximum (FWHM) of the peak, which we associate with a distribution of sizes in the repeat distance; and the peak height h, which we associate with the degree of order of the periodic packing of the monomers. In Figure 4.22a, c and e, we show these three parameters for two independent measurements on 4 mg/ml fibrin gels as a function of applied strain, according to the protocol shown in Figure 4.19. The data are obtained from analysis of the quadrants of the scattering spectra that are oriented in the direction of strain, the horizontal quadrant q_1 in Figure 4.9. The value of the peak position, width and height of the virgin fibrin network is indicated by a dashed line in each figure.

We observe that the monomer length starts to increase (corresponding to a decrease in the q-value) at approximately 100% applied shear strain, and that the peak width slightly increases in the same regime, indicating a growing spread in the repeat distances, implying that not all fibrin monomers increase equally in length. The peak height decreases after this strain, indicating that there is a disruption of the spatial order.

Interestingly, we observe inelastic effects upon a return to the initial unstrained configuration. In Figure 4.22b, d and f we show the peak position, peak FWHM and peak height at 0% applied strain, as a function of the maximum strain that the sample has experienced. Although the FWHM shows no inelastic effect, the height of the peak increases and the position of the peak shifts to higher q-values with increasing maximum strain. This implies that, upon removal of the strain, the characteristic repeat length *shortens* with respect to the length of the virgin network, and that the axial packing order is enhanced by stretching and relaxation. A possible explanation for the increase in peak height is that the axial ordering of the fibrin protofibrils may be imperfect in the virgin network, but can be enhanced by mechanically working the fiber.

In Supplementary Figure 4.3 we show the position of the first scattering peak $q_{peak\,1}$ measured in the direction perpendicular to the direction of strain, as a function of the position of the first scattering peak in the direction of strain. We observe that during application of a shear strain (i.e., when we expect the peak position to shift to a lower q-value), that the monomer lengthening is stronger in the direction of strain, than orthogonal to the direction of strain. However, the shift to higher q-values after return to 0% strain is equally strong for both directions, indicating that the repeat distance of fibrin monomers is shortening equally in both directions.

In Supplementary Figure 4.5 we show the first order scattering peak position of fibrin gels measured during the 2017-beamtime session together with the peak position of a fibrin gel measured during the 2018-beamtime session. The protocol for the 2018-beamtime session did not include returns to zero strain, while the protocol for the 2017-beamtime session did (Figure 4.19). Nevertheless, the shift of the Bragg peak follows the same trend, supporting the notion that only the maximum applied strain is relevant for the shortening for the characteristic repeat length.

MISSING SCATTERING ORDERS

We find in the scattering spectra of fibrin gels at rest that the second order scattering peak (at approximately $q = 0.56$ nm^{-1}) is missing [193]. This is a so-called forbidden

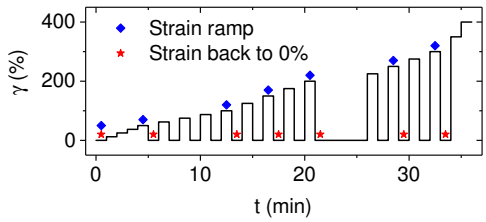

Figure 4.19: Strain protocol for shear experiments with stepwise increases in shear strain γ interspersed with intervals where the strain is brought back to zero. The blue diamonds refer to the left columns of Figures 4.21 and 4.22, while the red stars correspond to the right-hand columns.

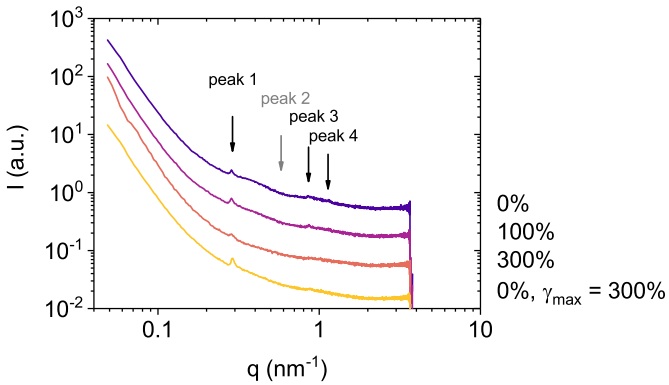

Figure 4.20: Radially integrated intensities of the scattering patterns shown in Figure 4.16. For clarity, the curves have been shifted along the y-axis. Black arrows indicate the position of the first (left), third (middle) and fourth (right) scattering order. A grey arrow indicates the position of the missing second scattering order.

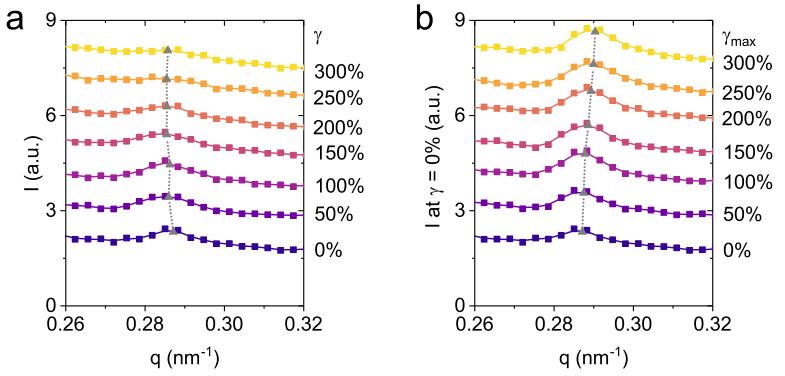

Figure 4.21: Background-subtracted, radially integrated scattering intensities I as a function of scattering vector q for a 4 mg/ml fibrin gel (dots), together with a convolution of the data with a Gaussian function with a width of $\sigma = 1$ (lines). **(a)** The scattering curves at increasing applied shear strain γ. **(b)** The scattering curves when the sample is brought back to 0% shear strain, after increasing values of the maximum applied strain γ_{max}. For clarity, the curves have been shifted along the y-axis. The grey dashed line indicates the peak position $q_{peak\,1}$, obtained from fitting the radially integrated scattering curve.

order, and arises from an effect caused by an extra scattering plane in between two scattering planes [216]. If the combination of the incident angle θ, the wavelength λ and the separation between planes d is such that the difference in path length is an odd number of wavelengths, then the difference in path length of the extra plane, located half-way the top and bottom planes, is an odd number of half wavelengths. That means the scattered light will be out of phase by half a wavelength of the bottom plane, and destructive interference occurs. If, however, the difference in path length between the top and bottom plane is an even number of wavelengths, the difference in path length of the in-between plane will be half the number of even wavelengths, which is still an integer number such that scattered light will be in phase and constructive interference still occurs.

It has been shown before [209] that when fibrin is stretched above 50% extensile strain, the lattice spacing is disrupted, and the destructive interference that suppresses the second scattering peak no longer occurs. However, in our shear measurements, we do not see the second order scattering peak appear even for shear strains up to 300%. This can potentially be attributed to the lower signal in the shear experiment, due to a low protein concentration (4 mg/ml versus 8 mg/ml), a shorter path length through the fibrin gel (1 mm in the Couette cell, versus several mm through the free-hanging gel in extensile experiments), or reduced alignment in shear experiments compared to extension (Figure 4.13a versus b).

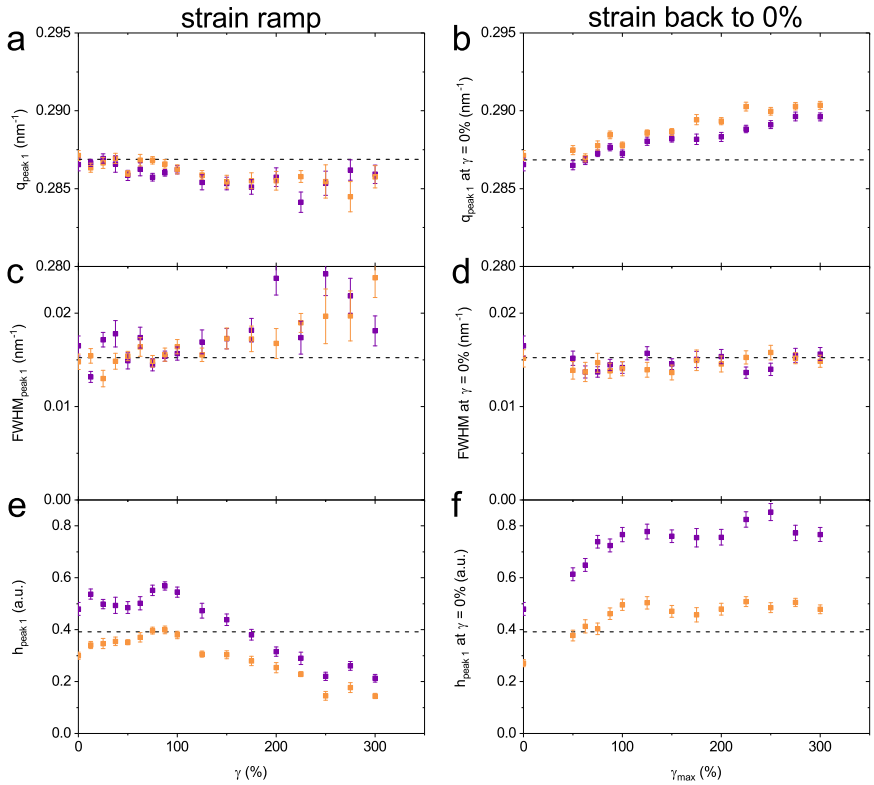

Figure 4.22: **(a)** Position of the first scattering peak $q_{peak\,1}$, as a function of applied shear strain γ. **(b)** Position of the first scattering peak when the sample is returned to 0% strain, as a function of the maximum applied strain γ_{max}. **(c)** Full-width half-maximum (FWHM) of the first scattering peak $FWHM_{peak\,1}$, as a function of applied strain. **(d)** FWHM of the first scattering peak when the sample is returned to 0% strain, as a function of the maximum applied strain. **(e)** Height of the first scattering peak $h_{peak\,1}$, as a function of applied strain. **(f)** Height of the first scattering peak when the sample is returned to 0% strain, as a function of the maximum applied strain. The dashed lines indicate the value of the peak position, FWHM and height of the virgin fibrin network, and serve as a guide to compare changes in these parameters as a function of applied strain. Error bars are obtained from the fitting routine.

4.4.3. SAXS-RESPONSE OF FIBRIN UNDER EXTENSION

In Figure 4.23 we report the nematic order parameter, the asymmetry factor and the peak position of an 8 mg/ml fibrin gel under extension, for comparison with the shear experiments. In Figure 4.23b and d we show respectively the nematic order parameter and the asymmetry factor, together with the affine prediction, assuming a decrease in volume according to Figure 4.5. We observe with increasing strain, both in S and A_{asym}, an increase in the degree of fiber alignment, even exceeding the affine prediction. This is potentially due to a stronger decrease in sample volume than what we observed in Figure 4.5, which is caused by solvent evaporation due the long duration of the SAXS experiments. The finite value of S and A_{asym} at zero strain indicates that there is already fiber alignment, likely due to mounting of the sample in the tensile tester. A_{asym} shows a decrease at increasing strain, which we attribute to the fact that the sample gets thinner and thus contains less scattering material in the cross-section of the X-ray beam. Yet the background remains identical and thereby relatively grows in strength. Consequently, Eq. 4.8 illustrates that this causes A_{asym} to decrease, irrespective of the alignment of the fibers. Since the nematic order parameter relies on the shape of the azimuthally integrated data rather than the ratio of two magnitudes, S is unaffected.

In Figure 4.23c we show the position of the first scattering peak. The data are obtained from analysis of the quadrants of the scattering spectra that are oriented in the direction of strain, the horizontal quadrant q_1 in Figure 4.9. Similar as to the shear experiments, the position of the scattering peak remains unchanged at low strain. At a slightly lower strain, approximately 90% versus 100%, we start to observe a decrease in the peak position, corresponding to an increase in the axial periodicity. At 110% extension, the highest strain we access, this corresponding increase of the axial periodicity is 0.3 nm, equal to the maximum shift we observe in shear. Unfortunately, the peak position could be determined of only a single sample, polymerized from fibrinogen that was dialysed against fibrin buffer, containing 20 mM HEPES and 150 mM NaCl at a pH of 7.4. All other samples were assembled from fibrinogen that was not dialysed, and hence contained the citrate that was present in the buffer of the supplier. As citrate complexes with Ca^{2+} ions that are required for FXIII and thrombin activity, the presence of citrate could lead to reduced protofibril-cross-linking and thereby fewer protofibrils per fiber, and hence a weaker Bragg peak signal.

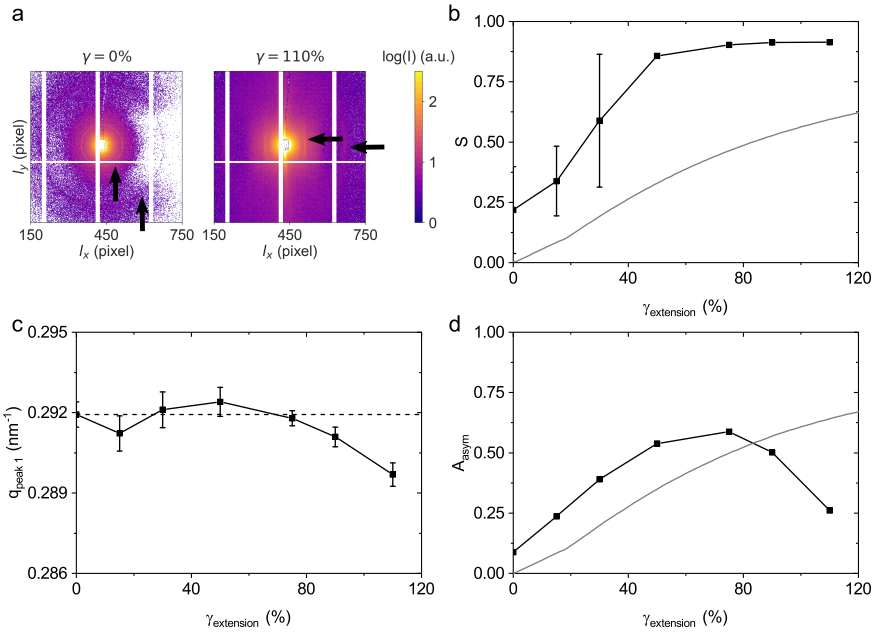

Figure 4.23: Analysis of SAXS-patterns of an 8 mg/ml fibrin gel under extensile strain. **(a)** The background-subtracted scattering patterns of a gel under 0% and 110% applied extensile strain. The first and third order scattering rings are indicated by black arrows. **(b)** The nematic order parameter S, calculated from the azimuthally integrated scattering intensity for a q-range of 0.062 to 0.13 nm^{-1}, as a function of applied extensile strain $\gamma_{extension}$, together with the nematic order parameter in a model for affine network deformation with a decrease in volume as the strain increases (grey line). **(c)** The position of the first scattering peak $q_{peak\,1}$, as a function of applied strain. The value of the peak position of the virgin fibrin network is indicated by a dashed line. Error bars are obtained from the fitting routine. **(b)** The asymmetry factor A_{asym} as a function of applied strain, together with the prediction for a model of affine deformation with a decrease in volume as the strain increases (grey line).

4.5. DISCUSSION

We started this Chapter with the question by what mechanisms fibrin obtains its elastomeric behaviour. Fibrin gels exhibit a remarkable strain-stiffening response to an applied shear that extends out to large strains on the order of 300% (Figure 4.1b). Fibrin's elastomeric behaviour has been tentatively attributed to the hierarchical structure of the fibrin gel across multiple scales [125], but it has been challenging to pinpoint the exact contribution of each scale [32, 248]. To relate the different mechanical regimes that occur at increasing strain levels to structural changes, we combined network deformation with *in situ* measurements of the structure. By combining confocal microscopy and SAXS with shear rheology, we can access all relevant structural length scales: from the molecular to the network scale. We correlated the rheological response to the following structural parameters: the nematic order parameter as a measure of shear-induced fiber alignment, and the position of the first order scattering peak as a measure of the monomeric length, with the results summarized in Figure 4.24.

In rheology measurements, we distinguish four distinct mechanical regimes (indicated in Figure 4.24). We do not observe any changes in fiber alignment or monomer elongation in the first two regimes. It has been argued, based on a quantitative comparison between the elastic modulus of fibrin networks with predictions of polymer network models, that this stiffening regime originates from the entropic resistance of the fibers to being straightened [125, 146]. Our data are consistent with this hypothesis, in the sense that no structural changes are expected on the molecular scale in case of an entropic network response. The third mechanical regime starts at around 25% shear strain and is accompanied by the onset of fiber alignment, indicated by an increase in the nematic order parameter. This regime has been interpreted in prior rheological studies as the enthalpic regime, where the origin of stiffening is the re-orientation of linearly elastic filaments in the direction of strain (Refs. [31, 133, 206] and Figure 4.14a and c). The fourth mechanical regime sets in at about 100% strain, correlating with the onset strain of elongation of the characteristic repeat length on the monomer level. In this regime, the fiber backbones are strongly stretched. Finally, typically between 200% and 300% applied shear strain, the network ruptures, indicated in the mechanical response by a sudden drop in stiffness to a vanishingly small value, in the confocal images by the disappearance of a percolating network (see Supplementary Figure 4.7), and in the SAXS patterns by a return of the nematic order parameter to values characteristic of undeformed, isotropic samples.

In summary, we observe a close correlation between the rheological response and changes in fibrin structure. Does this correlation provide a clue regarding the underlying mechanisms? To address this question, it is helpful to consider the strain level felt at the filament level, compared to the macroscopically applied strain. For a continuum elastic solid under shear, the local strain is everywhere identical and equal to the macroscopic strain. However, semiflexible polymer networks are known to be prone to non-affine behaviour [227, 249, 250], although the degree of nonaffinity is difficult to predict *a priori*. We therefore decided to measure the nematic order parameter and compare it to predictions made in the limit of an affine deformation. Any nonaffinity would be expected to delay the onset of alignment and lower the nematic order parameter compared to the affine prediction. We find that the nematic order parameter at the filament level, mea-

sured with both microscopy and SAXS, closely follows the affine prediction up to applied shear strains of 100%, while it increases less rapidly than the affine prediction at higher strains, likely because the filaments are rotationally constrained by cross-links. This observation justifies the use of an affine model to predict the elongation and orientation of the fibers that comprise our fibrin gels for the entropic and enthalpic regimes.

How much do the fibers themselves stretch? We estimate from the affine model that at an applied shear strain of 250%, the average increase in fiber length is 83% (for fibers oriented in the direction of strain, see "quadrant 1" in Figure 4.9b), which fibrin fibers can sustain without breaking [184]. As the network does not behave fully affinely at this strain level, this number is only approximate. However, experimentally we found that the Bragg peak position shifts only slightly, from approximately 0.287 nm^{-1} to 0.285 nm^{-1} at 250% applied shear strain, corresponding to an increase of only 0.3 nm, or 0.7% of the fibrin monomer length.

Under macroscopic extensile deformation, we observe from the SAXS-spectrum a similar structural response compared to fibrin gels under shear deformation. The nematic order parameter approaches unity already at strains below 100% (Figure 4.23a), indicating a strong degree of alignment due to the effect of a volume reduction. However, Figure 4.23c shows that also in extension, the increase in monomer length is minimal, approximately 0.3 nm at 110% extensile strain. At 75% applied strain, alignment of the fibers is already complete so any further elongation of the gel has to originate from fiber elongation, yet this is not reflected in a shift of the Bragg peak. What is the structural origin of this discrepancy between the large fiber strain on the one hand and the tiny monomer strain on the other hand?

In literature, the origin of the extensibility of fibrin fibers has been subject to a long-standing debate that has led to two different views on the mechanism by which fibers deform. The first view is that elongation is mediated by the unfolding of the coiled-coil connector regions within the monomer [198, 199, 251]. The second view is that the extensibility of fibers originates from the stretching of the αC-regions, either between protofibrils, or between short protofibril fragments [205, 252]. These mechanisms are sketched in Figure 4.25a-c.

As Bragg scattering occurs on periodic structures, the 1.83-fold elongation of fibrin fibers that takes place at 250% strain would lead to a shift in the position of the Bragg peak from $q_{peak\,1}$ = 0.287 nm^{-1} at rest to $q_{peak\,1}$ = 0.157 nm^{-1} (since multiplication with a factor 1.83 in real space corresponds to division with a factor 1.83 in reciprocal space) if it were completely mediated through unfolding of the structured coiled-coil regions (Figure 4.25a), in stark contrast to the final peak position $q_{peak\,1}$ = 0.285 nm^{-1} that we measure. Furthermore, molecular simulations of fibrin monomers (that lack the disordered αC-regions) predicted the unfolding of the coiled-coil regions under increasing strain, with a characteristic force-extension relation as different parts of the monomer unfold [199–201, 253]. To achieve a strain of 83%, the predicted force-extension relation dictates that a force of ~100 pN per monomer is required. To estimate the actual force experienced per protofibril at this fiber strain, we use N_p = 288 and a pore size of 1.35 μm (Chapter 2) for a 4 mg/ml fibrin gel, and a stress of 4400 Pa (obtained from the rheology files that accompanied the SAXS-data) at 250% applied shear strain. We thus estimate a force per fiber of 8.0 nN, and a force per protofibril of 28 pN. This force per protofibril

should only lead to a minimal increase in monomer length due to molecular unfolding of at most a few nm [199].

The alternative model, where the disordered αC-regions are held responsible for the elongation on the monomer level (Figure 4.25b), predicts that, even though the macroscopic strain field is (almost) directly mapped onto fibers, the characteristic repeat length does not change, since the disordered rather than the ordered structures within protofibrils deform. This is consistent with the minute shift of the position of the Bragg scattering peak we observe experimentally.

To test the validity of the αC-elongation mechanism, we make an estimation of the maximum deformation of the αC-region, to see whether the stretching of the αC-regions can accommodate the strains that fibrin fibers experience. The αC-region in human fibrinogen consists of a partially folded αC-domain of 218 amino acids long, and an unstructured αC-connector of 170 amino acids [254, 255], see Figure 4.25d. At rest, the measured length of the αC-region in fibrinogen oligomers is 45 nm to 50 nm [256], which is significantly shorter than a fully stretched αC-region (390 amino acids × 0.35 nm per amino acid ≈ 140 nm). To make a rough estimation of the maximum deformation of the αC-connector, we use a maximum length of 170 × 0.35 ≈ 60 nm, while we estimate its rest length $r_0 = a\sqrt{N}$ from a random coil of N chains of length l_p, where the persistence length l_p of the αC-connector is approximately 0.6 nm[203, 255], such that $N = \frac{60}{0.6} = 100$ and $r_0 = 6$ nm. This allows an extension per monomer of $2 \times (60 - 6) = 108$ nm from the unstructured αC-connector (the factor 2 originating from the fact that every monomer has two αC-regions), equivalent to 240% strain. This can be even higher when elongation of the full αC-region, including the αC-domain, is taken into account: $2\times(140-50) =$ 180 nm elongation per monomer, or 400% strain. Hence, αC-regions can easily accommodate the strains that fibrin fibers experience.

We find further support for this mechanism when we consider the stress dependence of the elastic modulus of the fibrin networks at high stress. In the mechanical regime above 100% applied shear strain, we find a power law with a slope of 3/2 (dotted line in Figure 4.1b), which is consistent with a model of stretching of semiflexible polymer chains [257] (such as the αC-regions). Strong support for this model in the literature comes from stretching measurements on single fibrin fibers prepared from fibrinogen from different animal sources, where the maximum extensibility was found to increase linearly with the length of the αC-region [204, 258].

The return of the fibrin network from a highly deformed state to zero strain provides further insight in the mechanism of fiber stretching. We observe a decrease in characteristic length (0.5 nm with respect to the initial length), which is difficult to reconcile with monomer unfolding, since it is unlikely that monomers would refold into a configuration that is more compact than the native state. The decrease in characteristic length does fit well in a model where the αC-regions are responsible for elongation within the fiber, since the unstructured nature of these regions allows elongation, but also shortening.

We obtain further clues from the height of the Bragg scattering peak, which is a measure of the degree of axial packing order. We observe a decrease in peak height with increasing strain, consistent with prior studies [31, 209] and indicative of increased disorder. There are two possible contributions to the observed disorder. First, the initially

random fiber orientation means that there is a broad distribution of strains experienced at the fiber level (Figure 4.14e for shear and Supplementary Figure 4.2c for extensile deformation). This phenomenon increases the distribution of characteristic lengths at high strain (calculated for an affine shear deformation in Supplementary Figure 4.4) and thereby decreases the height of the Bragg scattering peak. A second mechanism contributing to enhanced disorder at large strain comes from a model where the αC-regions between protofibril segments are stretched (Figure 4.25c), which will facilitate an additional increase in scattering disorder, as a single fiber under deformation contains multiple characteristic lengths from both the undeformed monomers and the increased protofibril-segment-distance.

Surprisingly, we observe an increase in the height of the peak upon return to 0% strain. This observation implies that the packing of the virgin, undeformed fiber is imperfect. This observation fits in an ongoing debate about the way in which protofibrils pack together to form a fibrin fiber [65, 96–101], which is strongly influenced by the assembly conditions [22, 54, 197, 259–261]. Since aggregation of protofibrils into fibrin fibers occurs at a protofibril length of around 600 nm, or 13 monomers [262, 263], imperfections in assembly will create protofibril segments rather than infinitely long protofibrils, which are essential elements in a model where αC-regions govern fiber stretching (Figure 4.25b and c).

We believe in hindsight that the SAXS spectra presented in Refs. [31, 209] of fibrin gels under extensile deformation are also in line with αC-elongation. At increasing strain, the Bragg peak was observed to disappear, yet no shift was observed in the position of the peak, in line with our measurements where the peak position shifts a maximum of 0.7%. If we assume a model of affine extensile deformation with a decrease of volume with increasing strain (Supplementary Figure 4.2), we conservatively estimate an increase in average fiber length of 12.1% at 100% extensile strain. If this strain were borne by coiled-coil unfolding, then we expect a shift in the peak position from 0.287 nm^{-1} to 0.256 nm^{-1} - a relatively small number, caused by the strong volume-reducing effect that accompanies extension, but a shift that should be clearly observed. The SAXS measurements did not observe any peak shift, suggesting that the strain is carried by elongation of the unstructured αC-regions rather than unfolding of the structured monomers.

By contrast, in experiments of bovine fibrin films under extensile strain [206, 264], the first order Bragg peak was observed to shift substantially, by an amount that corresponded to an increase in the monomer length of 6 nm. It remains to be determined whether this discrepancy with our measurements under shear and extensile deformation is due to the fibrinogen source (bovine versus human).

We get a final confirmation of the involvement of αC-stretching from nonlinear rheology experiments performed on fibrin gels formed from des-αC fibrinogen and full-length fibrinogen. In Supplementary Figure 4.6 we see at zero strain that the linear elastic modulus is higher for coarse fibrin gels than for fine and des-αC fibrin gels, originating from the relatively stiff bundles of protofibrils that comprise coarse clots. In contrast, at high shear strains the coarse and fine gels show the same rheological response. This confirms that at high shear strain the mechanical response of the network originates from the level of fibrin protofibrils, independent from the way in which they are packed. This is in agreement with earlier work [16]. Similarly to fine fibrin, the des-αC gel shows

stiffening at the same onset strain as the affine prediction for alignment (Supplementary Figure 4.6). However, a further strong stiffening response at high strain (>100%), as observed for the fine and coarse networks prepared from full length fibrinogen, is absent. Only a small stiffening response at this strain level is seen, likely originating from continuation of fiber alignment. The absence of the stiffening response at high strain in des-αC fibrin is direct evidence that stretching of the αC-regions is the structural origin of the mechanical response of fibrin gels under high shear deformations. In order to explain the nonlinear rheology experiments on different fibrin gels, we again turn to the concept that protofibrils consist of segments (Figure 4.25c). This model explains both the equal stiffening response of coarse and fine fibrin gels at high strains through the elongation of αC-regions, and the lack of stiffening in des-αC gels.

4.6. CONCLUSION

In conclusion, we applied a multi-scale approach to understand the origin of fibrin's mechanical behaviour. We demonstrated that the strain field in sheared fibrin network is nearly affine. This is consistent with indirect conclusions from earlier studies, which were based on the close correspondence between measured elastic moduli and predictions of affine network models [16, 125]. Around 25% shear strain, fibers start to significantly orient along the direction of principle strain, and at 100% applied strain, the fibers themselves are being appreciably stretched due to elongation of the connecting αC-regions. The monomeric repeat distance only barely increases, suggesting that molecular unfolding plays an insignificant role, even in networks under large shear or extensile deformations. This framework is further supported by nonlinear rheology on fibrin gels formed from full-length fibrinogen and des-αC fibrinogen, where the stiffening response at high strains observed in full-length fibrin gels is absent in des-αC fibrin gels. Interestingly, in Nature, both unfolding of ordered [265, 266] and disordered domains [267] are employed to accommodate large deformations in elastomeric materials. Fibrin monomers are in principle able to extend through both pathways; yet in this Chapter we have shown that they primarily deform through the stretching of disordered αC-regions up to shear strains of 200% to 300%. In principle fibrin fibers could stretch more, but this is pre-empted in reconstituted fibrin networks by rupture of fiber-fiber connections.

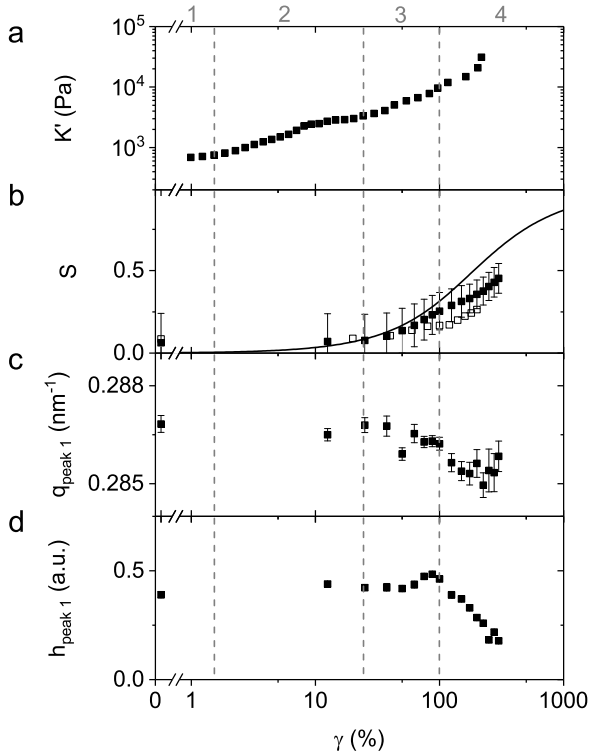

Figure 4.24: Correlation between the strain dependence of the macroscopic elastic response of fibrin networks **(a)** and the changes in fiber alignment **(b)**, and in the position **(c)** and height **(d)** of the peak characterizing the axial packing order of the fibers. The nematic order parameter shown in **(b)** shows data from SAXS (solid squares) and confocal rheology (open squares), together with the prediction for an affine model (black line). S_{SAXS}, $q_{peak\ 1}$, and the error bars in the second and third panel are the average of two measurements. The vertical lines serve as a guide to indicate distinct mechanical regimes.

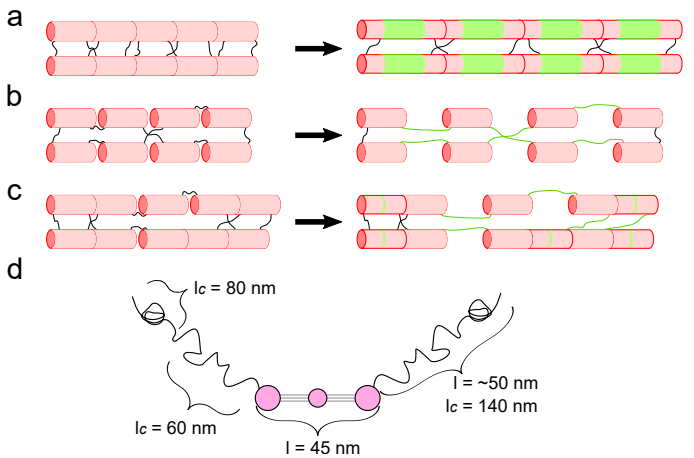

Figure 4.25: Schematic representation of three different mechanisms of fibrin fiber extension. The schematic shows the structured part of the monomer as red cylinders, connected by the αC-regions, shown as black lines. The mechanism through which strain is accommodated is **(a)** conversion of α-helices to β-sheets (green regions); **(b)** extension (indicated in green) of the αC-regions connecting fibrin monomers; and **(c)** a variant of the αC-elongation mechanism, where the protofibrils consist of a few fibrin monomers [262, 263], such that the αC-regions connecting these protofibril segments can also extend, possible accompanied with monomer unfolding. **(d)** shows a schematic representation of the fibrinogen monomer, with the end-to-end length l and contour length l_c indicated (from left to right) of the αC-domain, the αC-connector, the ordered part of the monomer and the entire αC-region. The length of the αC-region is obtained from Ref. [192], the contour length of the αC-region, domain and connector are obtained from Ref. [254], and the length of the fibrinogen monomer from Ref. [268, 269].

I gratefully acknowledge Paul Kouwer (Radboud University Nijmegen, the Netherlands) for kindly allowing us to use his TA HR2-rheometer during beamtime BM26-02-797 (2016). I also acknowledge the beamline staff, in particular Daniel Hermida Merino, of BM26 at the ESRF for their help with setting up the experiment, performing measurements and data analysis. I acknowledge Dennis K. Galanakis (Stony Brook University School of Medicine, New York, USA) for generously providing the des-αC fibrinogen used in this Chapter. For the SOAX-analysis, I thank Dimitrios Vavylonis (Lehigh University, USA) and Ting Xu (Lehigh University, USA). I thank Bela Mulder (AMOLF) for discussions on the calculation of the nematic order parameter, and finally I thank Federica Burla, Cristina Martinez Torres, Karin Jansen and Lucia Baldauf (AMOLF) for being such a wonderful team during the beamtime-sessions, and Cristina for her help in and useful discussions on analysis of SAXS-data.

APPENDIX

4.A. BACKGROUND SUBTRACTION

In Equations 4.2-4.3 we subtract the background from the SAXS-images. Although on average the intensity of all pixels with the same q-value is positive for all q-values, negative intensities occur due to random fluctuations in intensities, especially at high q-values where the measured background intensity is almost equal to the sample intensity (Figure 4.8d). These negative values can be removed by setting them to zero (orange curve in Supplementary Figure 4.1). The software provided by the beamline (black curve) uses (unintentionally) a similar threshold method, where the threshold is set to $\approx 2 \times 10^{-5}$ in arbitrary units (blue curve). The reason underlying the thresholding in the beamline software is that it cannot handle negative numbers, and handles floating numbers only with a certain precision. For strongly scattering samples the image intensity is sufficiently large such that negative or small numbers do not occur, however, in our samples we find that we need to be able to handle negative and small scattering intensities. Finally, the full overlap of the red and green curve indicates that the order in which background subtraction and radial integration is done, is not relevant for the final intensity. For the green curve, the radial integration has been performed prior to background subtraction, such that there have not been negative count values at all, as the background signal has to be always lower than the sample + background signal (see Figure 4.8d).

In this Chapter, we have chosen to not apply a threshold to our background-subtracted data. Although negative intensities are not physical, they are a result from random instrument noise rather than an underlying physical principle. When a threshold would be applied, the distribution that the noise follows will be disrupted as the weight of this distribution would be shifted, and hence, our scattering curves would receive an unknown and arbitrary offset at high q-values.

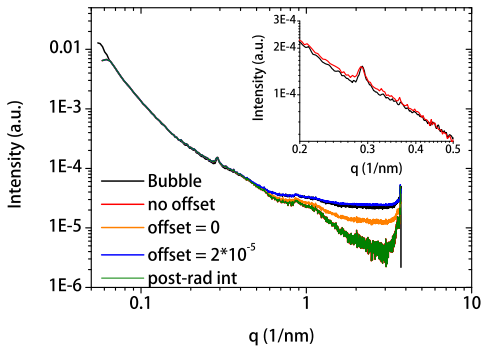

Supplementary Figure 4.1: Radially integrated intensities for SAXS on a background-subtracted, 4 mg/ml fibrin gel. The sample is a 4 mg/ml fibrin gel under 0% applied shear strain. The black curve is the background subtraction and radial integration performed by software supplied by the ESRF. The red curve is obtained by our Python-script and has no threshold applied, the orange curve has all values below 0 set to 0 and the blue curve has all values below $2 * 10^{-5}$ set to $2 * 10^{-5}$. In green the radial integration of the sample and background is performed *before* background subtraction. The inset shows a zoom-in of the first scattering peak, showing slight variations between the ESRF-software and our home-written software, possibly arising from a difference in binning step size during radial integration, or different normalization.

4.B. FILAMENT ORIENTATION AND ELONGATION WITH VOLUME-DECREASING NETWORK EXTENSION

In Supplementary Figure 4.2 we show filament orientation of an initially random ensemble of rigid, elastic rods through the probability function $P(\phi)$ and $P(\theta)$ in the ϕ and θ plane, respectively. The deformation is a 3D extensile strain, with a network volume reduction that resembles fibrin under extension (see Figure 4.5b). We see a stronger orientation than in Figure 4.14b and d, due to the shrinking of boundaries orthogonal to the direction of extension. The maximum filament strain does not change though, as that follows the maximum global strain.

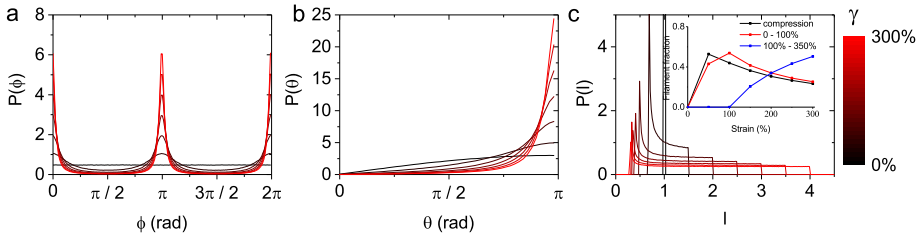

Supplementary Figure 4.2: Extension of an initially random ensemble of rigid, elastic rods, undergoing an affine deformation with fibrin-like volume reduction (see Figure 4.5b). **(a)** The probability function P for the ϕ-orientation, **(b)** the probability function P for the θ-orientation, and **(c)** the probability function P for the filament length l. The inset shows the fractional population of filaments under compression, extension up to 100% and extension higher than 100%, as a function of the applied network strain γ. Orientations of 3 million filaments were averaged to obtain these graphs.

4.C. PEAK POSITION PARALLEL AND PERPENDICULAR TO STRAIN DIRECTION

In Supplementary Figure 4.3 we show the position of the first order Bragg scattering peak for two 4 mg/ml fibrin gels, subjected to the deformation protocol shown in Figure 4.19. For every strain step, the peak positions of the corresponding SAXS-image is shown in the direction parallel and perpendicular to the direction of strain (see also Figure 4.9b). In the inset the average values are shown at intervals of $q = 0.0005$ nm^{-1}. The position of the peak of the virgin sample is indicated by a dotted line, the data points with a lower q-value correspond to deformed samples, the data points with a higher q-value correspond to samples at 0% strain with a strain history.

In Supplementary Figure 4.4a we show the predicted mean length of filaments oriented in the direction parallel and perpendicular to the direction of shear strain, in an model of affine shear deformation. The average length of all filaments lies close to the prediction for the parallel fibers, since most filaments orientate in this direction as the network strain increases. Interestingly, filaments oriented perpendicular to the direction of strain hardly change in length at all, while fibers orientated in the direction of strain strongly elongate. In Supplementary Figure 4.4b we show the inverse of the average filament length (representing q-space) in both quadrants for increasing values of the shear strain, where the rest length is normalized to $q = 0.285$ nm^{-1}, the rest length of the fibrin monomer.

As the measured relation between monomer deformation in the direction of the applied strain and the direction orthogonal to the strain (Supplementary Figure 4.3) is strongly deviating from the affine prediction (Supplementary Figure 4.4b), both in shape and in magnitude, this is another indication that the affine deformation that occurs on the fiber level is not transferred to the structured part of the fibrin monomers. Instead, the unstructured αC-regions accommodate the strain (which does not show in the Bragg scattering peak), which explains the discrepancy between the measured and predicted shift in peak position in the direction parallel and perpendicular to the shear direction.

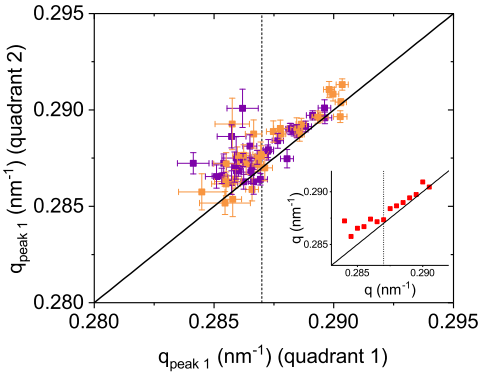

Supplementary Figure 4.3: Position of the first scattering peak in the vertical quadrant $q_{peak\,2}$ (perpendicular to the direction of shear strain), plotted as a function of the position of the first scattering peak in the horizontal quadrant (in the direction of strain), for two independent data sets. The inset shows the average of this data set, divided in bins of $q = 0.0005$ nm^{-1}. A dotted vertical line indicates the position of the first order scattering peak of the virgin, undeformed gels. The function $y(x) = x$ is shown by the black lines, indicating whether the change in peak positions in the directions parallel and perpendicular to the direction of strain is equal or not.

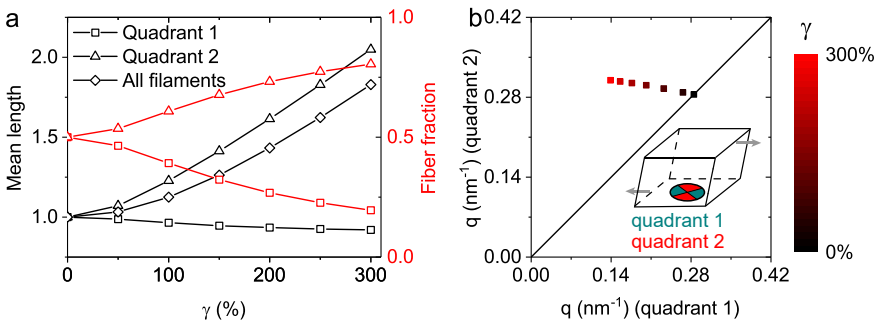

Supplementary Figure 4.4: **(a)** shows the average length of filaments in quadrant 1 and 2, and the fraction of filaments in both orientations. **(b)** shows the inverse of the average length in both quadrants, similar to Supplementary Figure 4.3. At zero strain, the average length in both directions is normalized to 0.285 nm^{-1}, and filaments are equally distributed over all orientations. The function $y(x) = x$ is shown by the black lines, indicating whether the change in peak positions in the directions parallel and perpendicular to the direction of strain is equal (when the squares follow this curve) or not.

4.D. COMPARISON OF THE PEAK POSITION OF 2017 AND 2018 BEAMLINE SESSIONS

In Supplementary Figure 4.5 we show the first order scattering peak position of fibrin gels measured during the 2017-beamtime session together with the peak position of fibrin gel measured during the 2018-beamtime session. The protocol for the 2018-beamtime session did not include returns to 0% strain while the protocol for the 2017-beamtime session did (Figure 4.19), with otherwise identical strain steps, holding times and acquisition times. As the data from both session agree well, this supports the notion that only the maximum applied strain is relevant for the shift to lower q-values, such that the returns in the protocol for the 2017-beamtime session did not affect panel a, c and e of Figure 4.22.

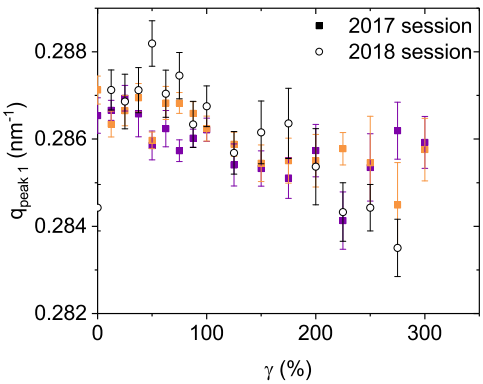

Supplementary Figure 4.5: Comparison between data acquired during the 2017-session (square symbols) and the 2018-session (open circles). Both data sets show the peak position $q_{peak\ 1}$ in units of nm^{-1} in the direction of strain ("q1" in Figure 4.9b).

4.E. NONLINEAR RHEOLOGY OF DES-αC FIBRIN NETWORKS

Based on the SAXS measurements, we hypothesize that the force-extension response of the disordered αC regions dominates the mechanical response at high deformations. To test this hypothesis, we performed nonlinear rheology on fibrin polymerized from fibrinogen monomers that lack the αC-region, and compare it with nonlinear rheology measurements on fibrin formed from full-length fibrinogen. A detailed description of the preparation of the des-αC fibrinogen solution, including an SDS-gel to confirm that indeed the Aα has a lower molecular weight than full-length fibrinogen, is given in Section 5.2.1 in Chapter 5.

We noticed that fibrin gels polymerized from des-αC fibrinogen rupture at substantially lower applied shear stresses than gels polymerized from full-length fibrinogen. We hypothesized that the earlier rupture is due to reduced adhesion of the gel to the rheometer plates (inspired by the notion that the αC-domains are involved in the interaction between fibrin and cells [270]), rather than rupture of the gel itself. To increase the adhesion between the gel and the rheometer plates, we incubated the stainless steel top and bottom plates of the rheometer for 45 minutes at 22°C with a solution of 2 mg/ml full-length fibrinogen dissolved in 150 mM NaCl, 20 mM HEPES and 5 mM $CaCl_2$. Prior to loading the des-αC fibrinogen solution onto the rheometer plate, the excess solution of full-length fibrinogen monomers was carefully absorbed with a tissue. When we compare the linear elastic modulus of the des-αC fibrin gel formed between the two fibrinogen-treated surfaces with the values for gels formed between untreated surfaces (reported in Table 5.1 in Chapter 5), we find that the surface treatment does not increase the linear elastic modulus. This indicates that no full-length fibrinogen is incorporated in the bulk material of the gel, yet it improves adhesion to the rheometer plate such that the rupture strain substantially increases.

In Supplementary Figure 4.6 we report the nonlinear elastic behaviour of a 2 mg/ml des-αC fibrin gel, together with full-length fibrin polymerized in coarse and fine fibrin buffer. We observe that the onset of the nonlinear response of the des-αC fibrin occurs at a higher shear strain (approximately 6% versus 2% for coarse gels). At high shear strains of order 100%, the des-αC fibrin gel does not show the stiffening that we observed in fibrin gels polymerized from full-length monomers. Since fibers in des-αC fibrin gels are thinner [271, 272], we performed the same nonlinear experiment on full-length fibrinogen polymerized under fine clot conditions. The onset of nonlinear behaviour of fine fibrin gels is similar to des-αC fibrin, but the fine clots show stiffening at high strain that is absent in the des-αC fibrin gel. We note that at high strain, the nonlinear elastic response of the fine and coarse networks prepared from full length fibrinogen overlap exquisitely well.

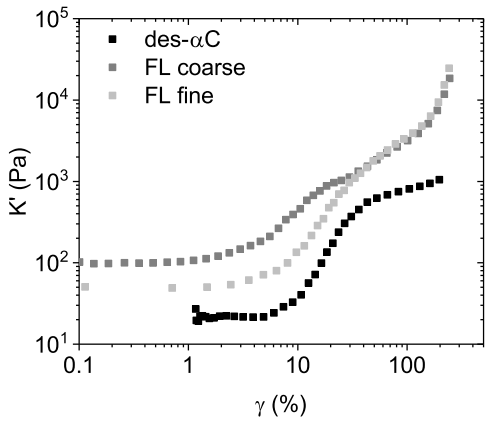

Supplementary Figure 4.6: The differential elastic modulus K' as a function of applied shear strain measured for a 2 mg/ml des-αC fibrin gel, a 2 mg/ml fibrin gel formed from full-length monomers in coarse assembly buffer ('FL coarse') and a 2 mg/ml fibrin gel formed from full-length monomers in fine assembly buffer ('FL fine'). The des-αC fibrin gel was polymerized in a cone-plate geometry that had been incubated with a full-length fibrinogen solution to increase adhesion of the sample to the surface. The other two samples were polymerized *in situ* without surface treatment.

4.F. NETWORK FAILURE IN CONFOCAL RHEOLOGY

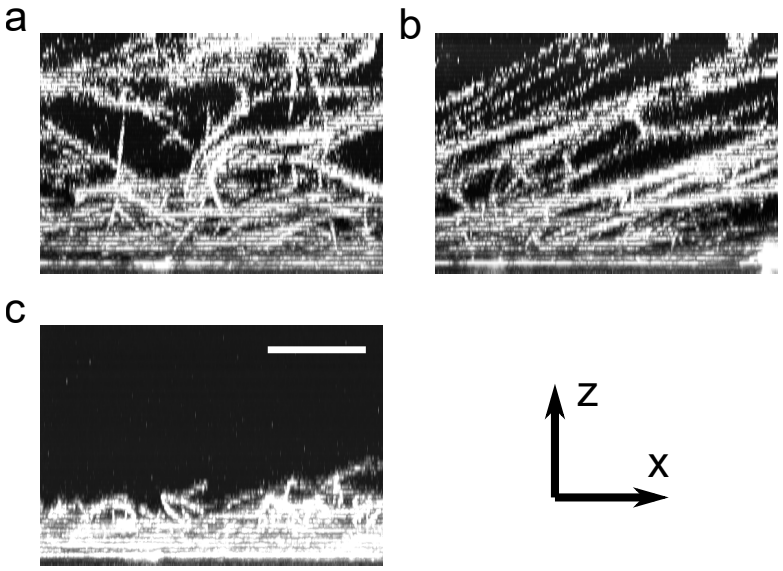

Supplementary Figure 4.7: Confocal rheology on a 1 mg/ml fibrin gel. A shear deformation is applied in the x-direction. Images are maximum intensity projections on the xz-plane with a depth in y of 50 μm. The relatively large steps in z during acquisition make the image look "liney", making this image unsuitable for further analysis with fiber tracking. This image also shows a higher protein density directly on the glass (at the bottom of the images), which is why we start imaging 10 μm away from the glass surface. **(a)** shows the network with no applied deformation, **(b)** shows the last image taken before rupture, and **(c)** shows the network after rupture. The scale bar is 20 μm.

5

FIBRIN NETWORK REMODELING UNDER CYCLIC SHEAR OR COMPRESSIVE LOADING

On command! Modify!
Networks enforce themselves!
Adding connectors, that
hardy can fail.

Striking example of
bio-technology:
Velcro scaled down to the
nano-length scale.

Fibrous networks are ideal functional materials since they provide mechanical rigidity at low weight. Here, we demonstrate that fibrous networks of the blood clotting protein fibrin undergo an irreversible increase in their mechanical rigidity in response to shear deformation and uniaxial compression, where the latter mode of deformation has the strongest effect. We explain this by noting that fiber-fiber interactions are more likely to occur when the network volume is reduced. Under compression, rigidification can be precisely controlled by the level of applied compressive strain, providing a means to program the network rigidity without having to change its composition. To identify the underlying mechanism we measure single fiber-fiber interactions using optical tweezers. We identify the αC-regions on the fibrin molecule as the molecular origin of the fiber-fiber interactions. We further develop a minimal computational model of cohesive fiber networks under compression that shows that stiffening arises due to the formation of new bonds in

the compressed state, which develop tensile stress when the network is re-expanded. The model predicts that the network stiffness after a compression cycle obeys a power-law dependence on tensile stress, which we confirm experimentally. This finding provides new insights into how biological tissues can adapt themselves independently of any cellular processes, offering new perspectives to inspire the design of reprogrammable materials.

5.1. INTRODUCTION

FIBROUS materials are ubiquitous in biology, forming the structural framework of cells and connective tissues [1]. Similar design principles are also harnessed in many man-made materials ranging from paper and textiles to light-weight composites [2]. Fibrous networks are superior functional materials, since stiff polymers and rigid fibers can form space-filling elastic networks at exceedingly low volume fractions of less than 1%, and at low connectivities where only 3 to 4 fiber segments meet at each node. This connectivity is below the Maxwell isostatic threshold for simple spring networks, which requires a connectivity of at least 6 for a mechanically stable network [23]. Fibrous materials can beat this threshold, due to the stabilizing effects of stress and the large bending resistance of fibers [24–27]. Moreover, the stiffness of fibrous networks is sensitive to the density of cross-linkers between fibers [273]. Such networks also reversibly stiffen under shear or tensile deformation, a phenomenon that has been explained by network models consisting of either semiflexible or elastic fibers [14, 25, 26, 274]. These properties in principle allow one to adjust the stiffness of fibrous networks to specific functional requirements. However, they offer only limited options for *in situ* adjustment since changing cross-link density requires making a new system for each application, while strain-stiffening is only operative as long as a mechanical strain is applied.

Nature has found intriguing ways to adapt the mechanical performance of fibrous networks in tissues in a more dynamic fashion to diverse and time-varying mechanical loading conditions. Tissues are able to actively reinforce their structure along the principal load direction. The mechanisms of mechanical reinforcement are generally thought to originate from cellular activity, involving strain-dependent fiber degradation and synthesis [275, 276]. However, recent studies suggest that biopolymer networks are inherently adaptive themselves, since they are held together by weak transient bonds [33, 277]. Cyclic shear loading has been shown to cause reinforcement for a number of biopolymer systems [172, 278–280], although softening can occur as well [35, 281]. The physical principles responsible for these varied inelastic responses are still not fully understood, although possible mechanisms include bond breaking and reformation between fibers [277, 281–284] and within fibers [35].

To test the influence of cyclic loading on the inelastic behaviour of fibrous networks, we choose fibrin as a model biopolymer (Figure 5.4c) whose elastic properties have already been extensively studied in the context of blood clotting [252]. We find that fibrin networks undergo irreversible stiffening when subject to high shear stresses. We show that we can enhance the stiffening response by applying a compressive strain, which is indeed more adept for strain-induced programming due to the volume-reducing nature of the deformation [177, 285, 286].

By directly measuring the interactions between individual fibrin fibers using optical tweezers, we identify new bond formation as a possible origin for this stiffening. We develop a minimal computational model of cohesive fiber networks to show that bond remodeling can indeed explain reinforcement of fibrin networks under compression. Moreover, this model reveals that the strong degree of stiffening we observe can arise from a surprisingly small fractional increase in network bonds, due to the pre-stressed nature of new bonds formed under compressive loading. Our model predicts a power-law dependence of the stiffening on the resulting contractile prestress, which we confirm

experimentally. The generality of the stiffening of cohesive fiber networks, together with its predictable and reproducible dependence on compression, can be used as a basis for *in situ* programming the mechanics of fibrous materials by purely mechanical means.

5.2. MATERIALS AND METHODS

5.2.1. FIBRIN NETWORK RHEOLOGY

We purchased chemicals from Sigma Aldrich (Zwijndrecht, Netherlands), human plasma fibrinogen and α-thrombin from Enzyme Research Laboratories (Swansea, United Kingdom), and fibrinogen labeled with the fluorophore Alexa488 from Life Technologies (Eugene, OR, USA). Fibrinogen lacking αC-regions [256, 287] was obtained from plasma and generously provided by Dennis K. Galanakis[1] in lyophilized form in 0.3 M $NaCl_2$, and, after dissolving, dialysed against fibrin assembly buffer. We checked its purity on a 7.5% SDS-gel, using 2.5 μg of protein per lane, staining with InstantBlue (Gentaur, Eersel, The Netherlands). Molecular masses were calibrated by running a lane with Bio-Rad Kaleidoscope Standards 161-0375. In Figure 5.1 we show the SDS-page gel of des-αC fibrinogen and fibrin, together with full-length fibrinogen and fibrin for comparison.

Rheological experiments were performed using an Anton-Paar rheometer (Physica MCR501, Graz, Austria) equipped with a 40 mm, 1°stainless steel cone plate geometry (shear experiments) or a 40 mm stainless steel parallel plate geometry to allow variation of the gap size (compression experiments). Samples were prepared by diluting fibrinogen stock solution (dialysed against a 150mM NaCl, 20mM HEPES, pH 7.4 buffer) to 2 mg/ml in an assembly buffer to obtain final concentrations of 150 mM NaCl, 20 mM HEPES and 5 mM $CaCl_2$ at a pH of 7.4. Polymerization was initiated by addition of 0.5 U/ml thrombin. Directly after mixing, we transferred the solution to the bottom plate of the rheometer and lowered the top plate to reach a gap size of 1.0 mm. During polymerization, the temperature was kept constant at 22°C, and solvent evaporation was prevented by adding a layer of mineral oil (M3516, Sigma Aldrich) on the liquid-air interface. We checked that the oil layer did not influence the mechanical behaviour of the networks.

During polymerization, we continuously measured the shear modulus, to verify that there was no evaporation or other disturbances of the sample. To this end, we applied a small oscillatory shear strain with an amplitude of 0.5% and a frequency of 0.5 Hz, and measured the shear stress response. Polymerization was complete after 10 hours as indicated by a time-independent shear modulus. For the shear experiments, we applied a constant shear stress, with a superimposed oscillation with an amplitude of 10% of the constant stress level, and a frequency of 0.5 Hz. The stress level (both the constant level and the oscillation amplitude) was logarithmically increased with 8 points per decade, which is a factor $10^{1/8} \approx 1.3335$.

Compression was achieved by lowering the top plate at a slow rate of 1 μm/s in steps of 100 μm, corresponding to strain steps of 10%. In between each compression step, we held the gap fixed for 125 s to allow the normal force to equilibrate. Figure 5.2 shows

[1] Department of Pathology, Stony Brook University School of Medicine, Stony Brook, Stony Brook, NY, USA

a typical example of the relaxation of the normal force during and after compression, which we associate with poroelastic behaviour (see Chapter 3 of this Thesis). The time scale of the relaxation process is quite fast, on the order of 13 s [288], reflecting the large (micron-scale) mesh size of the fibrin networks. We then measured the shear modulus of the equilibrated network by applying a small oscillatory shear strain (amplitude $\gamma = 0.5\%$ and oscillation frequency $\nu = 0.5$ Hz). Stepwise compression was continued until the thickness of the gel was reduced to 0.2 mm, corresponding to 20% of the original height and an axial strain of 80%. After compression, the gap was increased back to 1 mm (corresponding to an axial strain of zero) in a similar stepwise manner, and again allowing enough time for buffer to re-enter the network. We observed a residual tensile normal force (see Figure 5.4d), indicative of good adherence of the network to the rheometer plates and in line with earlier reports where high (shear) stresses were applied without requiring prior treatment of the rheometer surfaces (e.g. Ref. [125]). As a more rigorous test for strong enough plate adhesion, we also performed uniaxial extension tests in the rheometer. We found that the fibrin gels could be stretched by axial strains of at least 50%, corresponding to tensile stresses of at least 1.4 N, well above the stress levels (ca. 0.6 N) relevant throughout this work.

We verified by UV-VIS absorption measurements of the expelled buffer solution that no protein was released from the networks during compression. In some experiments cross-linking by FXIII was inhibited by the addition of D004 (Zedira, Darmstadt, Germany) to the fibrinogen solution in a 30 to 1 molar ratio prior to the addition of thrombin [289]. For the rheology experiments, data points show the average of three measurements on independently prepared fibrin gels with error bars representing the standard deviation.

5.2.2. OPTICAL TWEEZERS

Optical tweezers experiments were performed using a custom-built four-trap optical tweezers system, combined with fluorescence microscopy [293]. The sample chamber was a microfluidic flow cell with three inlets. Laminar flow conditions ensured that no mixing of the channels occurred. The first inlet contained 4.5 μm diameter spherical polystyrene beads (Spherotech, Lake Forest, IL, USA), which were trapped by a 20 W infrared ($\lambda = 1064$ nm) laser. The second inlet contained fibrin fibers, obtained by adding 0.5 U/ml thrombin to a 0.01 mg/ml fibrinogen solution where 10% of the monomers was labeled with Alexa-488. The third inlet contained just assembly buffer, which was supplemented in some experiments with the FXIII inhibitor D004. To test whether fibrin fibers are able to form bonds when brought in contact, we first trapped four beads in the bead channel, and next captured two fibrin fibers in the fibrin channel by connecting them end-to-end to a bead pair, using the ability of fibrin to strongly adhere to polystyrene beads [294]. Finally, the two fibers were moved to the buffer channel using the beads as handles and one fiber was positioned underneath the other one by defocusing the trapping lasers and oriented in a crossed configuration. All beads were then brought back to the same focal plane in order to bring the fibers in contact. To test for fiber cohesion, we moved one of the bead pairs and performed time-lapse fluorescence imaging while concurrently measuring the force response on the other bead pair using a position-sensitive diode.

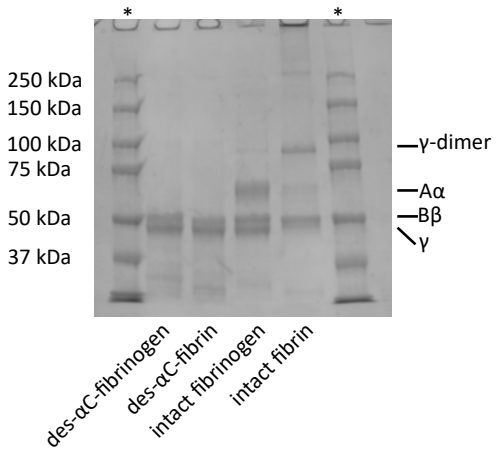

Figure 5.1: A 7.5% SDS-gel of fibrinogen and fibrin lacking αC-regions and full-length fibrinogen and fibrin. The Aα, Bβ and γ-chains are indicated; gels polymerized from des-αC-fibrinogen lack the Aα chain with a molecular mass of 64 kDa [19]. The remaining part of the α chain is poorly visible at approximately 25 kDa [290]. Upon polymerization the molecular weight changes due to the removal of fibrinopeptide A from the Aα-chain and fibrinopeptide B from the Bβ-chain [291]. Around 100 kDa, γ-dimers are visible in the intact fibrin gel [292]. Molecular weights are calibrated using a standard reference; marked with an asterisk.

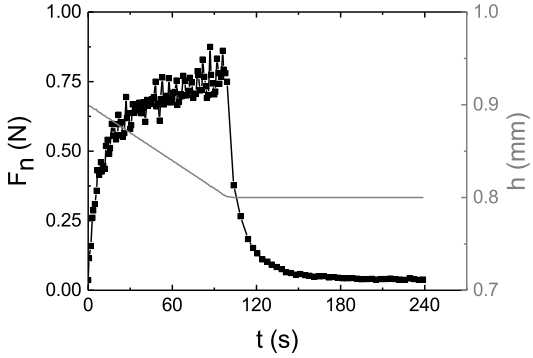

Figure 5.2: The normal (axial) force F_n, exerted by a 2 mg/ml fibrin network, equilibrates over time t, after the network underwent a stepwise compression from a height h of 0.9 mm to 0.8 mm. A small residual normal force (see Figure 5.16) corresponds to the build-up of internal normal stresses. The corresponding sample height h is shown in grey.

5.2.3. SCANNING ELECTRON MICROSCOPY

After polymerization of fibrin gels in the caps of Eppendorf tubes, the caps containing the gels were placed in a 150 mM sodium cacodylate buffer at a pH of 7.4 for 30 min per incubation step for a total of 3 steps while stirring slowly with a magnetic stirring bar, and fixated overnight in the cacodylate buffer with 2% glutaraldehyde. Afterwards, the samples were washed again in 3 steps in cacodylate buffer for 30 min. Samples were stepwise dehydrated by placing them in mixtures with an increasing ethanol content for 20 min per mixture. After full dehydration, ethanol was replaced by hexamethyldisilazane (HMDS) (first by 50% HMDS and 50% ethanol, and in the second step by 100% HMDS) and left to evaporate overnight in a fume hood. Samples were mounted on Scanning Electron Microscopy (SEM) stubs using conductive tape and coated with a 10 nm layer of gold-palladium (80/20) by sputtercoating (Leica EM ACE600). Electron microscopy was performed on a FEI Verios 460 system, with a beam voltage of 2 kV and a magnification up to 150,000×.

5.2.4. CONFOCAL MICROSCOPY

Confocal microscopy was performed on a Nikon Eclipse Ti inverted microscope equipped with a 100x oil-immersion objective (NA = 1.40). Fibrinogen labeled with Alexa Fluor 488 (Life Technologies, Bleiswijk, The Netherlands) was mixed with unlabeled fibrinogen in a 1:19 molar ratio. For des-αC-fibrinogen, this ratio was adjusted to 1:29. Samples were prepared in glass chambers made of a microscope coverslip and slide with Parafilm spacers. Polymerization occurred at room temperature for at least 12 hours.

Confocal microscopy in combination with compression was performed on a home-built setup, consisting of an Anton Paar rheometer head (DSR 301, Graz, Austria) placed on top of an inverted microscope equipped with a Yokogawa CSU-22 spinning disk confocal head, a Hamamatsu EM-CCD C9100 Digital Camera, and a 100x oil-immersion objective. The bottom plate consisted of a microscopy coverslip, while the top plate was a 20 mm stainless steel plate. The gap height was adjusted manually by moving the rheometer head up and down with a micrometer screw. The molar ratio of fluorescently labeled to unlabeled fibrinogen monomers was adjusted to 1:9, allowing shorter exposure times and reduced photobleaching.

5.2.5. SIMULATIONS

Disordered 2D lattices were generated by modifying triangular lattices with a lattice spacing of l_0 such that at each lattice vertex, one out of three passing filaments is randomly freed up [295]. This phantomization procedure sets the average connectivity (local coordination number) of the network to $z = 4$. We further diluted the network by random removal of fiber segments until the average connectivity, $\langle z \rangle$, reached a value between 3 and 4 that is typical of biopolymer networks. Biopolymer networks of fibrin, collagen and actin usually exhibit combinations of fiber branching ($z = 3$) and cross-linking ($z = 4$) [296]. This average connectivity is below the point of marginal stability for a network of Hookean springs with only stretching interactions. This isostatic connectivity is $2d_s$ where d_s is the dimensionality of the system[23]. Spring networks are floppy below this threshold, but they can be stabilised by introducing a bending rigidity or by applying

an internal or external stress [24–26, 29, 297–299]. Here, we include bending interactions in the Hamiltonian of the system to account for the finite rigidity of fibrin fibers. Thus, the filaments in the network are described by the Hamiltonian

$$H = \sum_f \left[\int \frac{\kappa}{2} \left| \frac{d\hat{t}}{ds_f} \right|^2 ds_f + \int \frac{\mu}{2} \left(\frac{dl}{ds_f} \right)^2 ds_f \right] \tag{5.1}$$

where the first term accounts for bending and the second term accounts for stretching. The summation is over all filaments in the system, $\hat{t}$ is the unit tangent along the filament and dl/ds_f is the longitudinal strain at point s_f along the fiber contour. Each fiber is assigned a bending rigidity κ and stretch modulus μ. Note that the simulations assume an athermal network, which is appropriate for rigid biopolymers such as collagen, microtubules, and actin bundles, and fibrin networks above a threshold strain of a few percent [125]. We set the dimensionless fiber rigidity, defined as $\tilde{\kappa} = \kappa/(\mu l_0^2)$ where l_0 is the lattice spacing, to 10^{-4}, a value that is appropriate for fibrin networks at the protein concentrations we are working at. The fiber rigidity is a dimensionless quantity that quantifies the relative importance of bend and stretch energy contributions and it is expected to vary approximately linearly with protein concentration assuming that the network architecture is invariant [25, 26]. Simulation results shown in Figure 5.13 have a capture radius of $d = 0.01\ l_0$; simulation results shown in Figure 5.14 have a capture radius of $d = 0.001\ l_0$. The simulation results shown in Figure 5.13 are an ensemble average of a total of ten different random networks.

5.3. RESULTS AND DISCUSSION

5.3.1. FIBRIN SHEAR AND COMPRESSION

We apply a logarithmic stress-ramp protocol on a 1 mg/ml fibrin gel, where we started at a small shear stress of 0.1 Pa, the stress was increased to a certain maximum, and decreased back to the original 0.1 Pa. In Figure 5.3 we show that the application of shear stresses up to 100 Pa is fully reversible. However, when a maximum shear stress of 1000 Pa is applied, the linear modulus increased by a factor 1.5 upon removal of the stress. During the subsequent loading cycle, the loading curve follows the same path as the previous unloading curve, indicating that stiffening is irreversible. However, there is a high onset stress for the stiffening effect as the network ruptures almost immediately after the stiffening effect was first observed (only one data point above 1000 Pa shear stress was measured).

As an alternative to shear deformation, we apply a compressive deformation. We hypothesize that we will observe a stronger response than shear deformation, as the decrease in network volume brings fibers closer to each other, increasing the likelihood of fiber-fiber interactions. We compress the fibrin networks stepwise in increments of 10% axial strain, relative to the initial state. After each compression step, we return the sample to the initial (0% axial strain) state, for a complete compression cycle. We define the compressive strain by $\epsilon = \frac{L_0 - L}{L_0}$, where L_0 is the initial sample height and L is the sample height under compression. Importantly, this definition of strain is not with respect to the relaxed state of the sample, which changes during a compression cycle. We perform

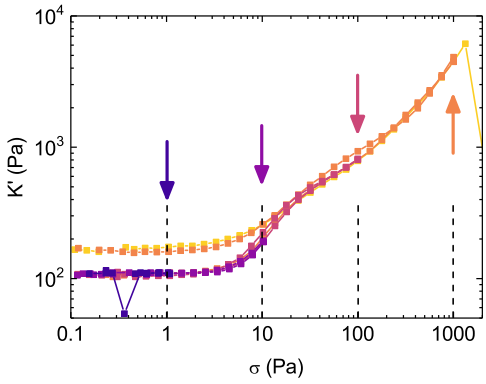

Figure 5.3: Application of increasing levels of shear stress on a 1 mg/ml fibrin network. The shear stress initially is 0.1 Pa, is then increased to the maximum as indicated by the arrows and the vertical dashed lines, and is finally decreased back to 0.1 Pa. Up to shear stresses of 100 Pa, there is full reversibility upon unloading. After the application of 1000 Pa shear stress, the network has become stiffer, as evident from the unloading curve and the next loading curve up.

each (de)compression step at a slow rate to allow for water efflux and influx (Figure 5.4e). Furthermore, we allow the network to equilibrate for at least 125 s until the normal force exerted by the network on the rheometer top plate reaches a constant level (Figure 5.2). We probe the rigidity of the network at different levels of axial strain by measuring the shear modulus with a small amplitude oscillation.

As we compress the network to increasing axial strains, the shear modulus progressively decreases (Figure 5.4a, black). This softening response is consistent with previous studies of fibrin [177, 285, 300] and actin [301] and may indicate fiber buckling [186, 300, 302–304]. Even for pure spring networks, however, extension tends to stabilize networks while compression tends to destabilize networks [305, 306]. At the highest maximum compressive strains that we apply (80%), there is a slight upturn of the modulus, possibly reflecting network densification [285, 303, 304].

When we decompress the network to its original height, we observe a strong increase in the shear modulus compared to the virgin state (Fig 5.4a), accompanied by an increased residual normal stress (Figure 5.4d; the normal stress σ_n is the measured normal force F_n divided by the rheometer plate surface area). The increase is already more than twofold when the network has experienced a compressive strain of 10% and rises to eightfold when the network has experienced a compressive strain of 80%. Importantly, the shear modulus reached after decompression is constant over time (measured for 1 hour, data not shown), so the compressive programming is irreversible.

To test whether the loading history affects the inelastic response, we also subjected networks to a single cycle of compression and decompression (Figure 5.4a, red; Figure 5.4e). The softening upon compression and stiffening upon decompression are nearly identical to the changes observed in the stepwise programming protocol, suggesting that only the maximum compressive strain that the sample has experienced is relevant, while

the subsequent strain history plays no role. This conclusion is further supported by repeating cycles of compression to 80% strain and decompression to 0% strain, where we observe that the once-programmed network switches between the same high stiffness at 0% strain and low stiffness at 80% strain in subsequent cycles (Figure 5.4b).

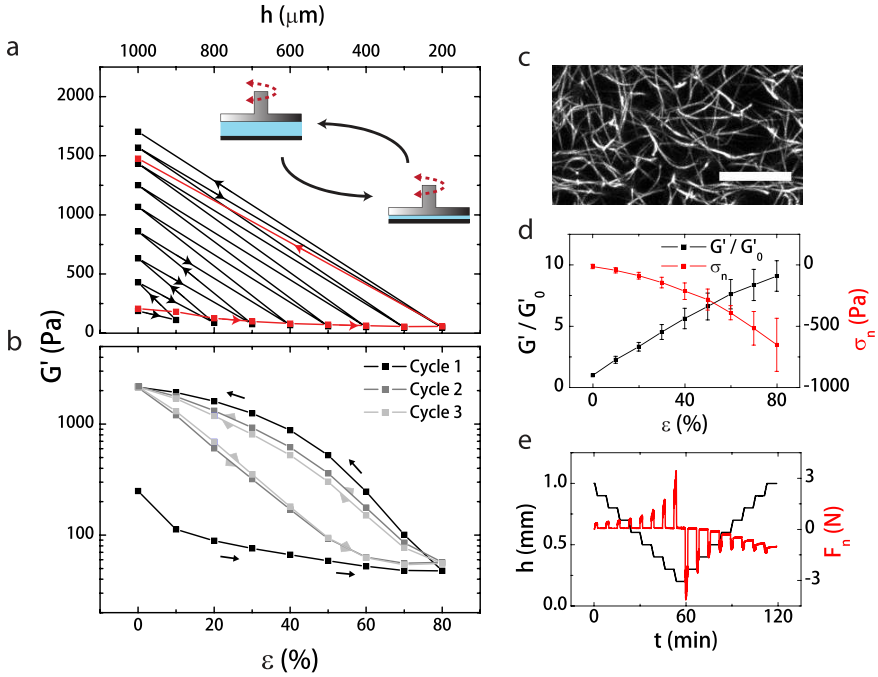

Figure 5.4: **(a)** Shear modulus G' of a fibrin network as a function of compressive strain ϵ and corresponding sample height h. The inset shows how the shear modulus is obtained by applying a small oscillatory shear strain while varying the axial strain. The black curve is obtained by cyclic loading-unloading in strain steps of 100 μm, while the red curve was obtained by directly compressing to $\epsilon = 80\%$. **(b)** Repeated compression to 80% strain and decompression, showing the first (black), second (grey) and third (light grey) cycle. **(c)** Maximum intensity projection of a stack of confocal images of a fibrin network, acquired over a depth of 10 μm; scale bar, 10 μm. **(d)** Normalized network stiffening G'/G'_0 and residual normal stress σ_n as a function of the maximum compressive strain ϵ that the network has experienced. **(e)** Gap size h and normal force F as a function of time t during a single compression-decompression cycle. Arrows indicate the sequence of the compression-decompression steps. Error bars represent standard deviations.

We repeated the compression-decompression experiment for multiple fibrinogen concentrations. In Figure 5.5a we show the results for four different initial concentration, 0.5 mg/ml, 1 mg/ml, 2 mg/ml and 4 mg/ml. The initial modulus depends strongly on the fibrin concentration, in line with earlier work revealing a close-to-quadratic dependence [125]. In all cases, the networks soften upon compression and stiffen upon decompression. In Figure 5.5b we show the ratio of the modulus of the network after compression-decompression to the modulus of the virgin network, and to the network at the highest compressive strain (80%). Strikingly, the stiffening ratio with respect to

the virgin network is highest for low concentration fibrin gels, while the stiffening factor with respect to the compressed state is highest for high concentration fibrin gels.

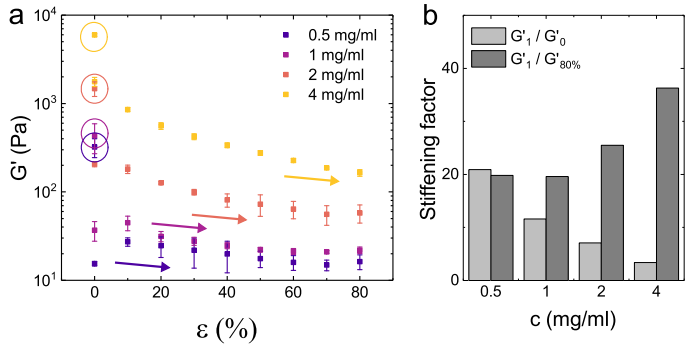

Figure 5.5: **(a)** Shear modulus G' as a function of compressive strain ϵ, for fibrin networks with varying protein concentration. Although the initial modulus strongly differs, the gels show a similar softening response upon compression and stiffening response upon decompression. Arrows indicate the sequence of the compression steps; the modulus after full decompression is encircled. Error bars represent standard deviations. **(b)** The ratio of the modulus after a compression-decompression cycle G'_1 to the modulus of the virgin network G'_0, and to the modulus of the network at the highest compressive strain (80%) $G'_{80\%}$, as a function of fibrin concentration c.

We observed that the stiffening is not completely irreversible under large applied loads. We applied a logarithmic stress-ramp protocol, similar to the cyclic shear experiment shown in Figure 5.3. The results are shown in Figure 5.6a. We observe that the loading-unloading of the shear stress was fully reversible up to stresses of 100 Pa. However, when we applied a stress of 1000 Pa, which is well into the nonlinear regime and close to the point of rupture for this particular gel, the gel became softer upon removal of the shear stress. Furthermore, by applying a new cycle of compression and decompression, the modulus of the gel can be increased again (see Figure 5.6b). Furthermore, we observe that although the linear modulus of the gel is increased eightfold, once the stress-stiffening regime is reached, the shear modulus follows the same trend as a virgin gel that has not received compressive training.

5.3.2. OPTICAL TWEEZERS

The strong and irreversible stiffening of the fibrin networks upon axial compression suggests that the structure of the network is being remodeled. A plausible hypothesis is that the fibers form additional bonds during compression, since compression increases the fiber density and thereby enhances the chance of fiber-fiber interactions. To test this hypothesis, we use a recently developed quadruple optical tweezers assay to directly probe the interaction between two individual fibrin fibers [277, 307, 308]. Using a microfluidic flow cell with separate inlets for a dilute suspension of 4.5 μm-sized polystyrene beads, a dilute solution of fluorescently labeled fibrin fibers, and assay buffer, we first capture four beads in the traps, then suspend a fibrin fiber between each bead pair, and move

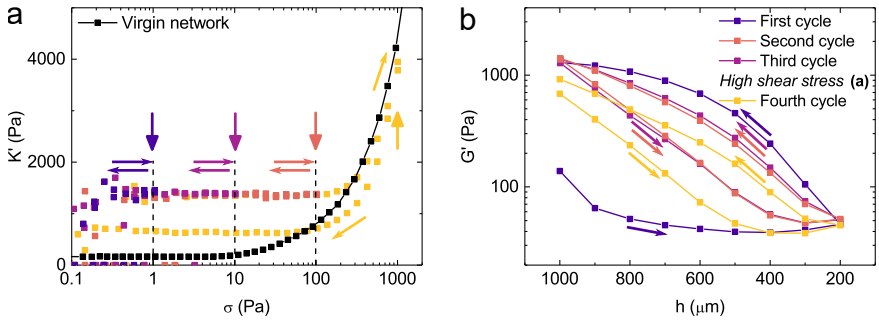

Figure 5.6: (a) Application of increasing levels of shear stress on a 2 mg/ml network that has beforehand been repeatedly compressed and decompressed (the first three cycles in panel **(b)**). The shear stress is initially 0.1 Pa, is then increased to the maximum as indicated by the arrows and the vertical dashed lines, and is finally decreased back to 0.1 Pa. After the application of 1000 Pa shear stress, the network softens. Arrows indicate the sequence of the shear steps. In black, the response to a shear stress is shown of an independently prepared fibrin network, that has not been compressed and decompressed. **(b)** A fibrin network is first subjected to three cycles of compression-decompression, then to a shear stress (panel **(a)**), and finally to a new cycle of compression and decompression. The stiffness that was lost during the application of a high shear stress is partly recovered. Arrows indicate the sequence of the compression steps.

5

the two fibers into the buffer channel. We next bring the fibers in a crossed configuration by rotating one fiber (vertical in the fluorescence images in Figure 5.7), bringing it underneath the second, horizontally oriented fiber, and finally moving it upwards into contact with the horizontal fiber. To test whether the fibers spontaneously bond, we pull on the vertical fiber. As shown in Figure 5.7, pulling on the vertical fiber causes displacement of the horizontal fiber. This observation provides clear evidence that the fibers spontaneously form bonds when brought in contact. To measure the bond strength, we monitor the force on the trapped beads. The red curve in Figure 5.7 shows the force as a function of time on the beads connecting to the horizontal, stationary fiber, while the blue curve corresponds to the vertical fiber. Each time we pull on the vertical fiber, there is a corresponding force increase on the horizontal fiber until, at a force of 259 pN, the uppermost bead is pulled out of the trap. Indeed, we observe consistently (10 independent experiments) that the bead is pulled out of the trap while the connection between the fibers remains unbroken. As the trap strength is in the range of 300-400 pN, the tweezers measurements set a lower limit on the strength of the newly formed fiber-fiber junction of 343 ± 104 pN.

5.3.3. MOLECULAR ORIGIN OF NETWORK RIGIDIFICATION

What is the molecular mechanism of new bond formation? Fibrin fibers are thick bundles of around 100 to 200 (depending on protein concentration, see Chapter 2 of this thesis) double-stranded protofibrils held together by covalent and noncovalent interactions [277]. We polymerize fibrin in the presence of FXIII, a physiologically important enzyme that stabilizes blood clots by generating covalent peptide bonds between fibrin

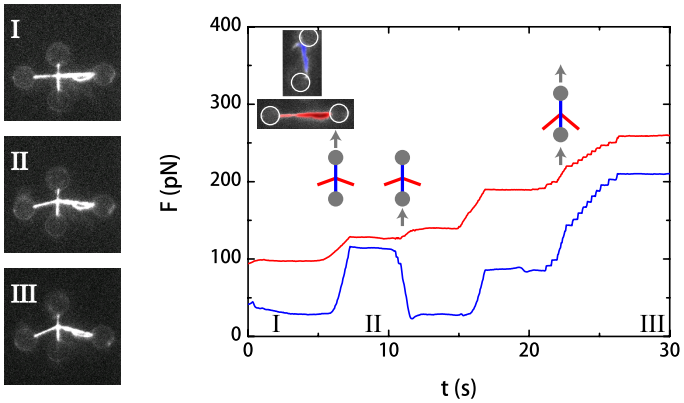

Figure 5.7: Fluorescence microscopy images (left) and force F versus time t graph (right) for a typical optical tweezers experiment. Two fibers are crossed and brought into contact using four optically trapped beads as handles. After the vertically oriented fiber (blue) is brought in contact with the horizontally oriented fiber (red) (I), there is a force response on both fibers when the upper or lower bead of the vertical bead pair is moved.

monomers [289, 309, 310]. A possible origin of the spontaneous fiber bonding could be the creation of new cross-links by fibrin-bound FXIII as the fibers are brought in contact. To test this idea, we repeated the fiber interaction measurements in the presence of the specific FXIII inhibitor D004 [289]. We again observed strong fiber-fiber cohesion (Figure 5.8) and consistent with this, we find that inhibition of FXIII cross-linking activity does not change the extent of network stiffening after compressive loading (Figure 5.9). We conclude that FXIII induced cross-linking is not responsible for bond formation.

Instead, we propose that bond formation is facilitated by noncovalent interactions, most likely mediated by the unstructured αC-regions, two long and flexible chains attached to the distal ends of each fibrin monomer [192, 311]. Specific interactions between these chains mediate lateral association of protofibrils into fibers as well as interactions between fibrin fibers [312] (see schematic in Figure 5.10). Evidence from optical tweezers experiments showed strong interactions of these chains at the single molecule level [312]. We can estimate the total strength F of a bond between two adjacent fibers mediated by the two juxtaposed brushes of αC-regions as: $F = P * f_r * \frac{d}{l_m} * \sqrt{n_p} * 2$. Single-molecule force spectroscopy showed that two αC-regions form bonds with a binding probability P of 62% and an average rupture force f_r of 34 pN [312]. The ratio $\frac{d}{l_m}$ is the fiber diameter $d \approx 100$ nm divided by the length of the fibrinogen monomer, $l_m = 45$ nm [191], and gives the number of monomers over the length of the interaction area. We multiply $\frac{d}{l_m}$ by $\sqrt{n_p}$, where n_p is the total number of protofibrils in a fiber cross-section (around 180, depending on the fibrin concentration; see Chapter 2 of this thesis), to obtain an estimate of the total number of monomers per interaction area. Finally, the factor 2 takes into account that there are two αC-regions per monomer.

This order-of-magnitude calculation predicts a binding strength of 1260 pN. Is this number large enough to make bond formation effectively irreversible even when fibrin networks are subject to a mechanical shear? To test this, we consider that for a 1% de-

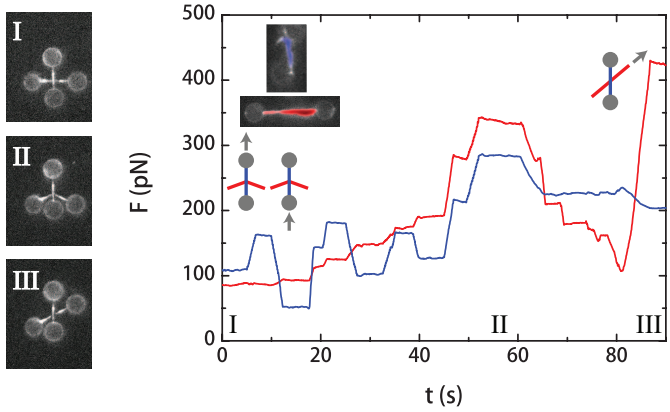

Figure 5.8: Optical tweezer measurement of the interaction between two fibrin fibers in the presence of D004, a specific inhibitor for the cross-linker FXIII. The numbers above the fluorescence images (left) correspond to time points indicated in the graph (right). The colours refer to the horizontally oriented fiber (red) and the vertically oriented fiber (blue). The fibers spontaneously form a strong (>300 pN) bond, indicating that bond formation does not require FXIII-mediated cross-linking.

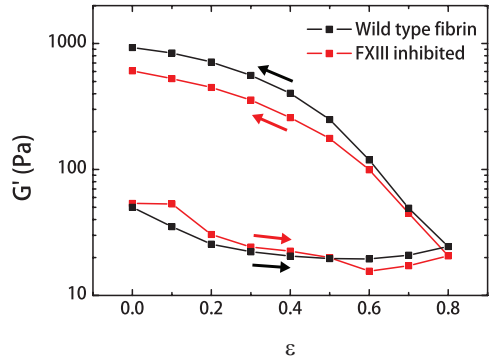

Figure 5.9: Compression and decompression of a 1 mg/ml fibrin gel, comparing cross-linked and uncross-linked networks. The black line shows the response of a control network which is cross-linked by FXIII, while the red line shows the response of a corresponding gel where FXIII-mediated cross-linking is inhibited by adding D004. The initial sample height of the FXIII-inhibited gel was 0.5 mm; in order to match the compression rate to the other experiments, where the initial height was always 1.0 mm initial, the compressive speed was adjusted to 0.5 μm/s. Arrows indicate the sequence of the compression-decompression steps.

formation of a fibrin network with shear modulus of 1700 Pa (1700 Pa being the average modulus after a compression-decompression cycle for our networks) we need to apply a 17 Pa shear stress. Per characteristic area of 1.6 μm × 1.6 μm (where 1.6 μm is an estimate of the pore size, or average area per fiber, based on [155] and Chapter 2) we find that, to a first approximation, each fiber is subjected to an average force of 44 pN. Thus, we find that the newly formed connections are much stronger than the forces applied on the fibers, hence we can consider the new connections to be irreversible.

To directly test the hypothesis that the αC-regions are responsible for fiber-fiber cohesion, we perform experiments on fibrin formed from monomers lacking the αC-region [256]. First we check the structure of these networks by taking confocal images of fibrin formed from des-αC monomers and full-length monomers, as shown in Figure 5.11a and b. While both samples have the same protein concentration (in mg/ml), the fibrin network formed from full-length monomers contains fewer fibers, indicating that individual fibers are thicker. Note that in both images fibers appear equally thick, as the fibers are thinner than the diffraction limit of light $d = 1.22 * \lambda / NA = 470$ nm, where λ is the wavelength of the emitted light and NA the numerical aperture of the objective, such that the thickness of individual fibers cannot be resolved optically.

To overcome this limitation, we performed Scanning Electron Microscopy (SEM) on specially prepared fibrin samples. Although the preparation requires the samples to be dehydrated and coated with a layer of metal for electrical conductivity, such that absolute fiber thickness cannot be obtained in this way, we observe a clear difference between the different fibrinogen species, where again the des-αC monomers produce thinner fibers (Figure 5.11c and d). Although there is lateral aggregation beyond the protofibril level, fibers remain thinner, consistent with prior SEM data on des-αC-fibrin gels [271, 272].

We next repeated the compression-decompression experiment with networks formed from fibrinogen lacking αC-regions. We observed that after polymerization, the linear storage modulus of the network was significantly lower than for full-length monomers at the same protein concentration (19.5 Pa versus 207 Pa, respectively), which is another indicator of a changed structure of individual fibrin fibers, or a reduction in fiber-fiber cross-linking. We performed the compression experiment with a 20 mm plate-plate geometry with an initial gap size of 0.5 mm, to conserve material. The speed of compression was reduced to 0.5 μm/s to match the rate of the compression experiments on gels made of full-length fibrinogen. In Table 5.1 we show the results of three measurements on fibrin gels formed from des-αC-fibrinogen, together with three measurements on fibrin gels formed from full-length fibrinogen for comparison. The stiffening effect is strongly reduced compared to full-length fibrin gels, although there is still an increase in the shear modulus from 19.5 Pa to 35.6 Pa.

There are two possible explanations for the observation that a stiffening effect is still present. As a population of the des-αC monomers has short αC-regions remaining (on average 0.8 αC-strands per monomer) [256], these might still interact and hence cause the observed stiffening. Alternatively, as the pore size of the des-αC-gels is smaller compared to that of fibrin gels formed from full-length monomers, there is a longer relaxation time for fluid efflux after compression. The modulus after the compression-decompression cycle might not be obtained in steady state (which also could explain the

large sample-to-sample variability in Table 5.1). In Figure 5.12 the normalized storage modulus is shown for a fibrin gel formed from full-length monomers and from monomers lacking the αC-regions, after decompression to the original gap size. For the des-αC-gel, the relaxation takes significantly longer and is characterized by a larger amplitude, indicating that the increase in stiffness observed after decompression is likely (at least partly) explained by pressure-induced stresses, rather than network remodeling. Note that we considered the relaxation of the shear modulus rather than the normal force. Although the normal force would have been a more direct indicator of reduced water efflux due to a higher pore size, the sensitivity of the rheometer to vertical forces was not high enough to resolve the normal force relaxation of the des-αC-gel.

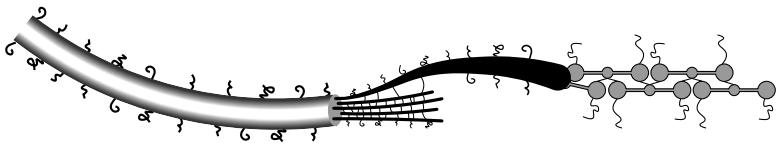

Figure 5.10: Schematic of the hierarchical organization of a fibrin fiber, with monomers (right) forming protofibrils (middle), and protofibrils forming bundles interconnected by the unstructured αC-regions (left).

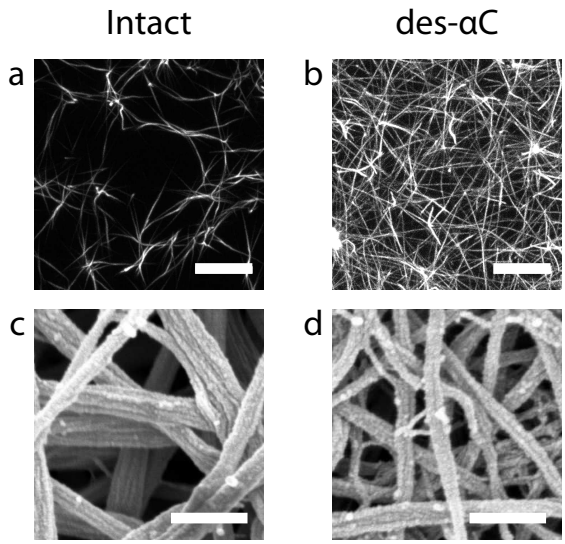

Figure 5.11: Structure of 2 mg/ml fibrin gels formed from full-length monomers (left) and des-αC fibrinogen (right). In **(a)** and **(b)** fluorescence microscopy is used to image the gels. Images are maximum intensity projections of a 20 μm z-stack with a spacing between slices of 0.5 μm. The intensity of the images is normalized to the maximum value in each image. The scale bar is 10 μm. In **(c)** and **(d)** electron microscopy is used to image the gels. The scale bar is 0.1 μm.

	Des-αC		Full-length	
	G'_0 (Pa)	G'_1 (Pa)	G'_0 (Pa)	G'_1 (Pa)
Sample 1	20.9	31.7	199	1680
Sample 2	18.5	21.3	198	1588
Sample 3	18.6	53.9	223	1161
Average	19.5 ± 1.3	35.6 ± 16.7	207 ± 14	1476 ± 277

Table 5.1: Values for the elastic modulus G' for 2 mg/ml fibrin gels formed from des-αC-fibrinogen, directly after polymerization (G'_0) and after a compression-decompression cycle (G'_1), forn des-αC and full-length fibrinogen. The error bar in the lowest row is the standard deviation obtained from the three independent measurements.

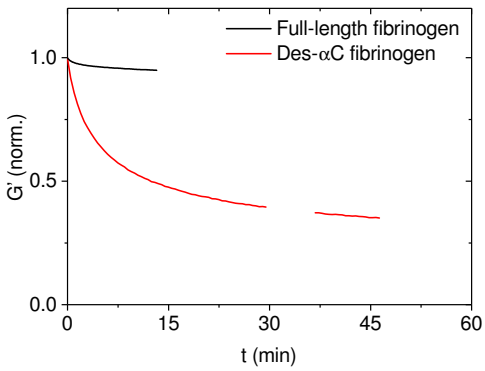

Figure 5.12: Relaxation of the storage modulus G', normalized to the value at the beginning of relaxation, as a function of time t for a fibrin gel formed from full-length monomers and from monomers lacking the αC-regions, after decompression from 80% compression to the original gap size. Both experiments were performed with a rheometer plate with a diameter of 20 mm. The acquisition during relaxation of the des-αC sample was briefly interrupted around $t = 30$ min.

5.3.4. SIMULATIONS

The observations of new bond formation suggest a mechanism for fibrin network reinforcement by compressive loading. To address this, we develop a computational network model that allows for new bond formation under deformation [295]. Fibrous networks are modeled as a 2D triangular disordered lattice with lattice spacing l_0 and dimensions of 50 $l_0 \times 50$ l_0. We perform 2D simulations for computational efficiency, which is justified by recent studies showing that subisostatic fiber networks in 2D are surprisingly predictive of 3D behaviour for the same connectivity z [25]. The average coordination number is adjusted to a physiologically relevant value of 3.4 to reflect the combination of branches and cross-links in networks such as fibrin. This is done by a combination of phantomization, a computational procedure to reduce the local connectivity of triangular networks from 6 to a maximum of 4, and dilution. Similar to the experiments, the lattices are compressed in steps of 1% from an initial axial strain of 0% to 50% and back to 0%. The fibers are modeled as elastic beams with a stretching modulus μ and bending modulus κ. We performed simulations for a fixed fiber rigidity, $\tilde{\kappa} = \kappa/\mu l_0^2 = 10^{-4}$, in the relevant range for fibrin networks. After each (de)compression step, we minimize the energy of the network and determine the normal and shear stresses from the variation of the energy with strain. Periodic, Lees-Edward boundary conditions are used to minimize boundary effects.

To allow for network remodeling, we introduce a single midpoint between adjacent network nodes and allow two midpoints to merge into one node when applied deformations force them to approach one another to within a predetermined capture radius d, which we will refer to as the remodeling distance. In our simulations we choose $d = 0.01$ l_0. Figure 5.13a illustrates a merging event in half a unit cell of the lattice. The additional bond is added at the point indicated by the grey arrows. The bend and stretch moduli for the fiber segment shown by the thick vertical line both change by a factor of 2. The capture radius d does not really correspond to a new structural parameter but primarily controls the probability of bond formation. In developing the model, we confirmed this by varying independently d and a separate binding probability, with no significant differences between these two control parameters. In our simulations we choose $d = 0.01$ l_0 to ensure sufficiently dilute new bond formation to be consistent with the degree of stiffening observed experimentally. Higher values of d increased the probability of new bond formation and were found to lead to higher levels of stiffening at lower levels of compression, although the results were otherwise qualitatively consistent with our experiments.

A typical remodeling event during the first steps of compression is highlighted in Figure 5.13b, which shows a zoomed-in section of a simulated network. A non-trivial combination of bending and stretching of individual fibers brings two midpoints to within the remodeling distance, encircled in grey. With increasing compressive strain, the simulations predict an initial softening, followed by stiffening when the axial strain reaches ca. 30% (Figure 5.13c, black circles). Upon decompression to the initial network height, the simulations reveal a strong increase of the shear modulus by a factor 140, while the density of nodes has increased by only a factor 1.32, suggesting that high levels of stiffening are possible with only a modest increase in cross-linking. We find good qualitative agreement with experiment in the dependence of both the normal stress and shear mod-

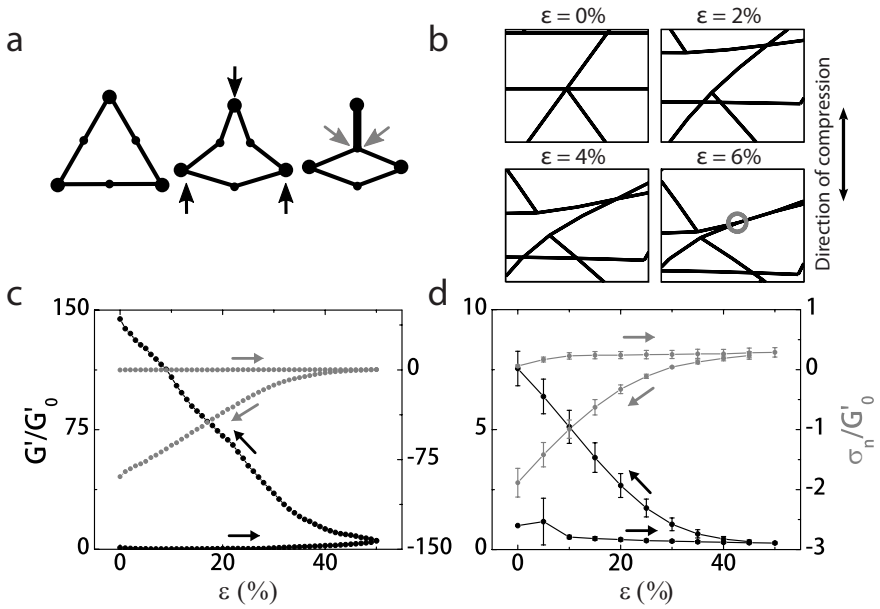

Figure 5.13: (a) Half a unit cell of our simulated fibrous lattice. Under compression (black arrows), two nodes within a remodeling distance $d = 0.01\ l_0$ merge (grey arrows). **(b)** A small section of a simulated network during compression, shown up to the moment where the first merging event occurs (encircled in grey). **(c)** Shear modulus (black) and corresponding normal stress (grey) as a function of compressive strain for a simulated network ($\tilde{\kappa} = 10^{-4}$), and **(d)** a fibrin network. Both vertical axes are normalized by the initial shear modulus. Arrows indicate the sequence of the compression-decompression steps. Error bars represent standard deviations.

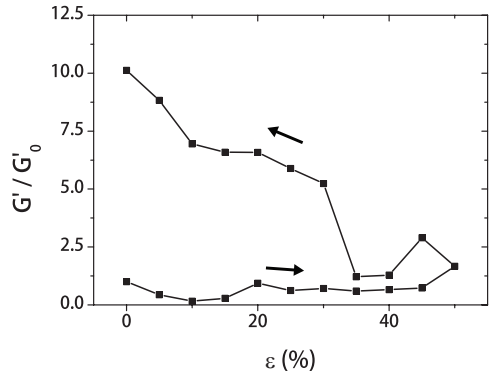

Figure 5.14: Shear modulus, normalized by the shear modulus of the virgin network, as a function of compressive strain for a simulated network ($\tilde{\kappa} = 10^{-3}$, $d = 0.001$). The stiffening is lower than in Figure 5.13 due to the lower value of the remodeling radius d. Another consequence of a low value of d is a relatively noisy signal since the number of new bonds is very small: an average increase in cross-linker density of 1.3% in two runs of the simulation. To reduce noise, we averaged all data points within 5% strain intervals. Arrows indicate the sequence of the compression-decompression steps.

ulus on compressive strain, as shown in Figure 5.13d.

The extent of stiffening observed in simulations is sensitive to the remodeling distance d: for a ten-fold decrease in d ($d = 0.001\ l_0$) the stiffening factor is ~10-fold (Figure 5.14), consistent with what we observe experimentally for fibrin networks. Importantly, this level of increase in stiffness is accompanied by only ~1.3% increase in cross-link density. To verify this, we performed confocal imaging on a network (1) at rest, (2) under compression and (3) after decompression (Figure 5.15). We indeed observe no pronounced difference between the network structure before compression and after the compression/decompression cycle, confirming the theoretical prediction that stiffening occurs with only a small increase in cross-linker density.

From the simulations, we obtain further insight into the mechanism of stiffening by considering the normal (axial) stress. New bond formation under compression is accompanied by a change in the relaxed state of the sample. After compression, the sample is returned to its initial height (Figure 5.4a schematic). As this is done, we observe the development of tensile normal stress in the decompressed network (Figure 5.13c, grey circles). Our experiments exhibit similar normal stress behaviour, as shown in Figure 5.13d. In our simulations, we can identify this tensile stress as arising from tensile forces in the decompressed network, resulting from the newly formed bonds. Thus, the residual axial stresses in the decompressed state are consistent with contractile forces acting on the initial network.

To test whether these contractile forces can account for network stiffening in our computational model, we plot in Figure 5.16 the relative increase in shear modulus against the residual normal stress for networks exposed to different levels of axial strain (open symbols). Interestingly, we find not only a strong correlation between the normal stress

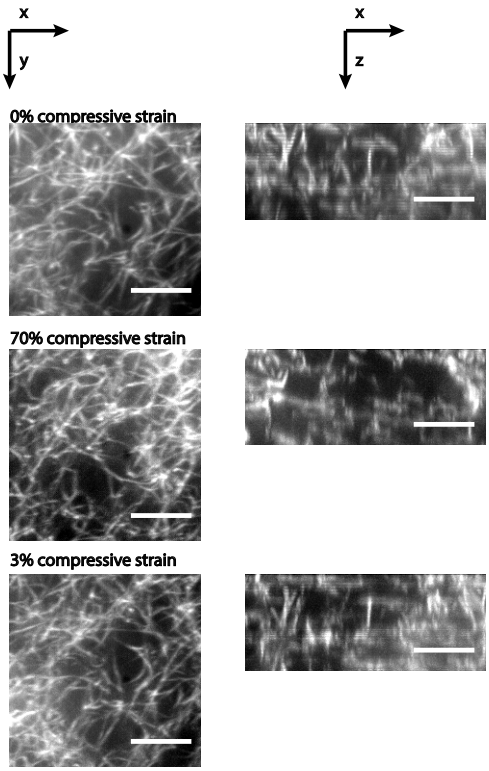

Figure 5.15: Confocal microscopy under compression. Left column: x-y projections of a confocal recording of 4 μm depth with a spacing between slices of 0.16 μm; right column: 4 μm x-z projections of a confocal recording of 4 μm depth. The applied compressive strain is indicated above the respective images. In the right column, the glass cover slip (i.e., the bottom surface, nearest to the objective) is located at the top of the projection. During decompression, a small residual strain of 3% remained, due to glass bending. We observe no pronounced change in network structure after compression-decompression, confirming that only a small fraction of new bonds is created. The scale bar is 10 μm.

and the increase in network stiffness, but this relationship is characterized by a sublinear or fractional power-law with exponent $\simeq 0.5$. Such a fractional power-law dependence is also observed in our experiments (filled symbols). Importantly, since both axes have been normalized by the initial linear shear modulus before compression, which can be independently determined in simulation as well as experiment, this provides a direct quantitative comparison between our experiments and our computational model: there are no adjustable parameters in this plot. While there is a small systematic difference between the simulations and experiments, both show a clear and consistent sublinear behaviour with exponent $\simeq 0.5-0.6$.

The simulations demonstrate the role of the new bonds formed by compressive training is not simply to provide new network constraints. Rather, the new bonds cause stiffening because they provide contractile forces. It is well-known from previous theoretical work that fibrous networks are highly nonlinear in their elastic response [1, 2, 15, 135, 313], so even dilute contractile force centers in the network can result in a significant change in the macroscopic network response. In prior work, this effect was demonstrated for the case of active contractile centers provided by molecular motors [29, 295]. Here we show a new mechanism by which the same effect can occur in a purely passive system without motors. Network compression effectively creates contractile centers since new bonds that are formed in the strained state get extended when the network is decompressed. Specifically, it was recently predicted that randomly distributed contractile forces in subisostatic networks such as ours can result in a sublinear increase in G' with contractile stress [29]. While that work aimed to address stiffening by molecular motors, an increase in $G' \sim \sigma^y$ with contractile stress σ was found, with exponents y ranging from $0.6-0.8$ depending on network connectivity z. For $z \simeq 3.4$, comparable to what we expect for fibrin networks, $y \simeq 0.6$ was found, which is consistent with a fit to our experimental results in Figure 5.16.

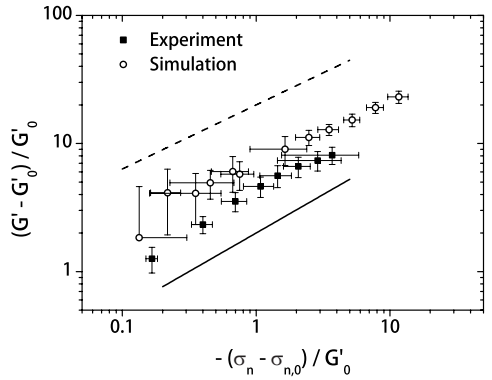

Figure 5.16: Relative increase in the shear modulus with normal stress for a fibrin gel (black squares) and a simulated network with $\tilde{\kappa} = 10^{-4}$ (open circles) trained by compressing to different levels of axial strain (up to 80% and 50%, respectively). The initial network parameters (G'_0, $\sigma_{n,0}$) are subtracted, and the data are normalized by dividing by G'_0. We find power-law scaling with a slope between 0.6 (black line) and 0.5 (dashed line), only to guide the eye. Error bars represent standard deviations.

5.4. CONCLUSIONS

We find that networks of cohesive fibers stiffen under cyclic shear or compressive loading and that this can be understood by the formation of new bonds between fibers while the network is deformed, which generate contractile forces upon network unloading. Compressive deformation appears to be a particularly effective way to reinforce networks compared to tensile and shear loading [277, 314, 315], perhaps due to increased contacts formed when fibers buckle under compression. We identified the αC-regions on the fibrin monomer as the structural component responsible for the strong fiber-fiber cohesion. Our computational model shows that the rigidity of fibrous networks can be tuned over a wide range as a consequence of the inherent sensitivity of the stiffness of fibrous networks to mechanical stress. This behaviour provides a powerful way to program fibrous networks and tune their stiffness to diverse mechanical loading requirements. We expect this finding to be transferable to both tissue scaffolding proteins like collagen [281], and to cell scaffolding proteins like actin, which forms fiber bonds via cross-linking proteins [316]. In the latter case, remodeling emerges from redistribution of diffusible cross-linkers rather than from the formation of contacts between intrinsically cohesive fibers [278].

Since our minimal model shows that the only ingredient needed to achieve programmable mechanics is fibers that are stiff and cohesive, this bioinspired design principle can be readily carried over to synthetic self-reinforcing materials using any of a wide range of available synthetic fibers, including carbon nanotubes and cellulose nanofibrils [317–319].

I gratefully acknowledge Dennis K. Galanakis (Stony Brook University School of Medicine, New York, USA) for generously providing the des-αC fibrinogen used in this Chapter. I thank Marjolein Kuit-Vinkenoog and Jeffrey den Haan (AMOLF) for their help with SDS-page, Andries Lof (AMOLF) for his help with SEM-imaging, Gijs Wuite and Erwin Peterman for the hospitality at the VU, and Andreas Biebricher for help with the four-trap optical tweezers setup. I thank Nicholas Kurniawan for joining the four-trap optical tweezers experiments, which required us to spend weeks in the basement of the VU. For the design and contruction of the confocal rheometer I thank Marnix Verweij, Federica Burla and the AMOLF workshop, and Martin van Hecke for loaning the rheometer head. Finally I thank Mahsa Vahabi, Luka Liebrand and Fred MacKintosh for discussions and contributing to the theoretical modeling.

6

DESIGNING AND BUILDING A LIGHT SHEET MICROSCOPE

Hey, is your setup slow?
And does your dye bleach fast?
Those are confocal
microscopy's feat.

Now try detection with
orthogonality!
Take all your z-stacks
in just a heart's beat.

In recent years, the inelastic mechanical behaviour of biopolymer networks has sparked widespread interest, in addition to the elastic behaviour of these networks. To uncover the structural changes in the network that underlie the inelastic mechanical behaviour, long time-lapse imaging needs to be performed, in conjunction with mechanical deformation. Conventional (confocal) fluorescence microscopy has a relatively high rate of photobleaching, limiting the possibility to capture a dynamic structural response to a (mechanical) stimulus. In this Chapter we overcome this fundamental limit of confocal microscopy by designing and building a light sheet microscope. In addition to reduced photobleaching, we also achieve high acquisition rates of 25 frames/s while taking a 3D stack, allowing both high frame rates and long time series. Finally, to study the structural response of the network to strain, we include a tensile tester in our microscope design.

6.1. INTRODUCTION

THE elastic properties of biological fibrous materials have been widely studied over the past decades, both by experiment and theory. Recently, there has been a growing recognition that biological materials also exhibit inelastic behaviour, which is crucial for their function. For example, inelasticity of the cytoskeleton plays a role in mechanosensing [320], force exertion [321], cell shape change [322] and cell division [323], while inelasticity of the extracellular matrix influences e.g. cell spreading and differentiation [324–326]. To experimentally capture the dynamics of these inelastic processes, one needs to perform long time-lapse imaging at a high acquisition rate. Using conventional confocal fluorescence microscopy, high-frequency imaging poses a challenge: as this technique is based on the detection of a single illuminated point, imaging a 3D volume in high resolution requires scanning many individual points, which results in a relatively long acquisition time. Furthermore, although every point is illuminated by the focused laser beam only once, there is a much weaker, but continuous illumination from the out-of-focus light, causing photobleaching of fluorophores while discarding the fluorescent signal. This limits the total number of frames that can be acquired.

An alternative to confocal fluorescence microscopy is Selective Plane Illumination Microscopy (SPIM). Although the first use of this technique dates back to 1903 in the field of granular matter [327], it was not further developed until in the past decade the technique was adopted by the developmental biology community [328, 329]. The principle of this technique is that instead of illumination of a single point, an entire plane is illuminated. Detection of the fluorescence light is performed orthogonal to the plane of illumination with a regular CMOS camera (see Figure 6.1a). Subsequent scanning in order to obtain a 3D image needs only to be performed in one direction. This has two imminent advantages, namely that every acquisition step captures the fluorescence of an entire plane rather than a point, reducing acquisition time, and as the light sheet is focused, there is no out-of-focus luminescence, reducing the number of photons every fluorophore receives and thereby the rate of photobleaching.

However, the principle of orthogonal excitation and detection also has drawbacks. Firstly, the fact that two objectives are needed that face the sample orthogonally poses a geometrical challenge. High-numerical aperture (NA), high-magnification objectives tend to have a short working distance and a low inclination (<45°). This poses two possible problems: the objectives will get in each other's way, and the working distance may become too short. This is sketched in Figure 6.1b, with a combination of two objectives suitable for light sheet microscopy. There are setups with orthogonal illumination and detection using a single objective [330–334], although each of these setups have their individual drawbacks. The second consideration is the finite thickness of the light sheet. The light sheet can be created in multiple ways. The simplest is a so-called Gaussian sheet profile. This is obtained by using cylindrical lenses that focus light in only one direction, reducing a bundle's dimension in that direction but not orthogonally. Afterwards, the illumination objective focuses the sheet on the sample, reaching a sheet thickness (thinness) d_s that is maintained over a length l_s given by [329]:

$$d_s = \frac{2\lambda}{\pi \mathrm{NA}^2} \tag{6.1}$$

and

$$l_s = \frac{2\lambda}{\pi \mathrm{NA}} \tag{6.2}$$

with λ the wavelength of the illumination light and NA the numerical aperture of the objective. Hence, there is a trade-off between the thinness of the sheet, and the length over which this is maintained, which is determined by the objective. For comparison, the axial resolution in confocal microscopy is given by the height of the point-spread function [87]:

$$\text{Axial resolution} = \frac{0.88\lambda}{n - \sqrt{n^2 - \mathrm{NA}^2}} \tag{6.3}$$

which is smaller than d_s for any objective[1], where n is the refractive index of the immersion medium. An alternative is the Airy sheet, which is created by modulating a Gaussian sheet with a spatial light modulator (SLM) [335] or using conical lenses [336]. Although with comparable objectives, the waist of an Airy sheet is thicker than a Gaussian sheet, it maintains its thickness over a longer length. Also in a Bessel sheet profile, which can also be created with a SLM [335], or conical lenses [337], the sheet is thicker than an Gaussian sheet, yet the profile is maintained over a longer distance.

Here we report the design and development of a SPIM microscope based on the OpenSPIM initiative [338]. We specifically aim to image turbid fibrin gels, which poses a challenge that we overcome by illumination from two sides [339]. We adapt the design in order to combine it with a tensile tester, to enable *in situ* imaging of the effect of mechanical deformation on the network structure, imaging both the fast, elastic and the slow, inelastic response. We chose to use two objectives for illumination and detection, since a single objective imposes strong limitations on the sample holder. Furthermore, we kept the optical path simple by using a Gaussian sheet instead of an Airy or Bessel sheet profile since the high optical density of the sample does not allow imaging deep into the sample, eliminating the need for a sheet with a profile that is maintained over a long distance.

[1] An objective with a NA of at least $0.95 \times n$ would be required to match the light-sheet thickness to the height of a point-spread function, which, according to Eq 6.2, would be maintained over only a short distance.

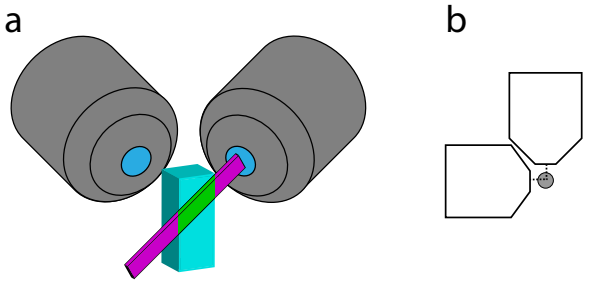

Figure 6.1: (a) A schematic representation of the principles of light sheet microscopy (Selective Plane Illumination Microscopy). The objective on the right sends a focused light sheet (magenta) into the sample (cyan block), which induces fluorescence (green) in a 2D plane in the sample. This is detected by the second objective (left). **(b)** An illustration of the requirements posed to objectives in a light sheet setup. The working distance of the objectives is illustrated by the dashed line, the grey circle represents a top view of the sample.

6.2. MATERIALS AND METHODS

6.2.1. SETUP DESIGN

Our design is based on the open-source OpenSPIM initiative [338]. The website provides a detailed description of the components needed to design a light sheet microscope, and also instructions on how to assemble the components into a working setup. The design of the setup is shown in Figure 6.2, both as top view and side view. Our main adaptation is the use of two-sided illumination [339], and a sample clamp in the xy-plane (both shown in Figure 6.3a). As the sample clamp limits the access to the sample for the detection objective, we perform orthogonal detection by placing the detection objective underneath the sample, by drilling a hole in both the optical board and the sample cell.

In Figure 6.2 the optical elements in the setup are annotated, and discussed below. The laser beam **(1)** is split by a beamsplitter **(2)** into two identical paths. First, two lenses (with focal length $f = 25.0$ mm and $f = 50.0$ mm, **(3)** & **(4)**) expand the collimated laser beam. Next is a mechanical slit with adjustable width (0 to 6 mm, with a graduation of 10 μm per division on the micrometer screw **(5)**) that cuts off the top and bottom part of the expanded beam. Using a cylindrical lens ($f = 50.0$ mm **(6)**), we create light sheets with a Gaussian beam profile. The cylindrical lens focuses the sheet only in the vertical direction, such that the sheet remains unfocused in the horizontal plane. Another lens ($f = 50.0$ mm **(4)**) is used to make a collimated sheet fall onto the back focal plane of the illumination objective (10× magnification). As our samples are water-based, we designed a sample chamber that holds the sample in an aqueous environment. The illuminated slice in the sample is in the focus of a 40× detection objective. The fluorescence light that is captured by the detection objective is then focused by a lens ($f = 200.0$ mm **(9)**) onto the detector **(11)**, first passing through a 500 nm longpass filter **(10)** to remove any scattered laser light.

The components used in the setup are as follows:

- **Illumination** is provided by a MLD Cobolt 488nm 60mW laser (Laser 2000, Vinkeveen, the Netherlands) **(1)**
- **Objectives** are two Nikon MRH07120 CFI Plan Fluor 10x W (illumination) and a Nikon MRD07420 CFI Apo 40x W NIR (detection), where the "W" indicates "water dipping" (Nikon instruments Europe, Amsterdam, the Netherlands)
- **z-stage** MCL Nano-ZL100 (Mad City Labs, Kloten, Switzerland) **(7)**
- **xy-stage** MCL XY-Microstage (Mad City Labs, Kloten, Switzerland) **(8)**
- **Camera** Hamamatsu Orca Flash 4.0 with an extension kit (commercially available from Hamamatsu) that enables acquisition of full-frame images at a frame rate of 100 Hz (Hamamatsu Photonics, Almere, the Netherlands) **(11)**
- **Sample cell** is milled from a block of poly(methyl methacrylate) (PMMA), and is shown in Figure 6.3. Three holes have been drilled in the sample cell: two at the side for the illumination objectives, and one in the bottom for the detection objective. Rubber rings are used to seal the holes and prevent leaking of the sample cell.
- **Tensile tester** Deben Microtest 200N Tensile stage with a 2N loadcell with a force resolution of 1 mN, and a total travel distance of 20 mm (Deben, Suffolk, United Kingdom). The tensile tester is shown in Figure 6.4, together with the adapter to mount it on the z-stage.

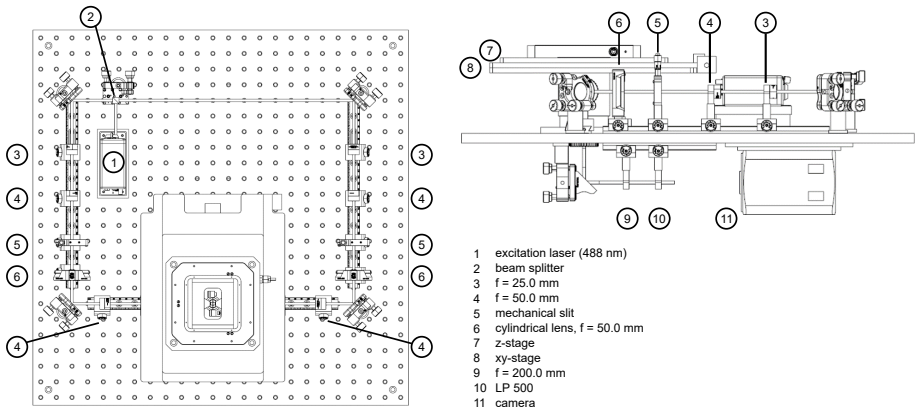

Figure 6.2: A drawing of the design of the light sheet microscope, showing both the top view (left) and the side view (right). The optical component annotated in the drawing are discussed in the text. The dimensions of the breadboard are 62.5 × 62.5 cm.

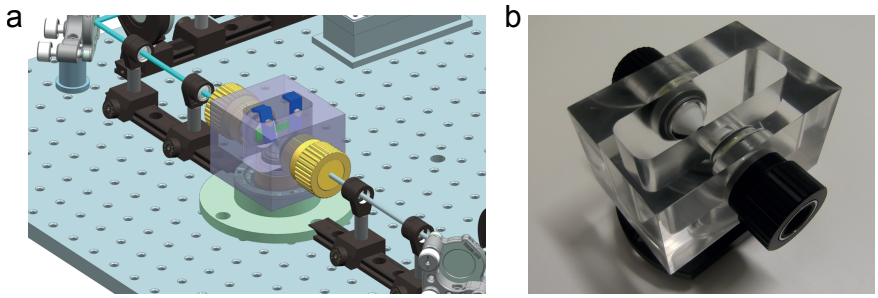

Figure 6.3: (a) A drawing of the sample cell with two-sided illumination, without the xy-stage and z-stage that would normally cover it. The sample clamps are shown in blue, and the sample itself in dark green. A hole is drilled in the light green plateau underneath, containing the detection objective. **(b)** A photograph of the sample cell, with the two illumination objectives inserted.

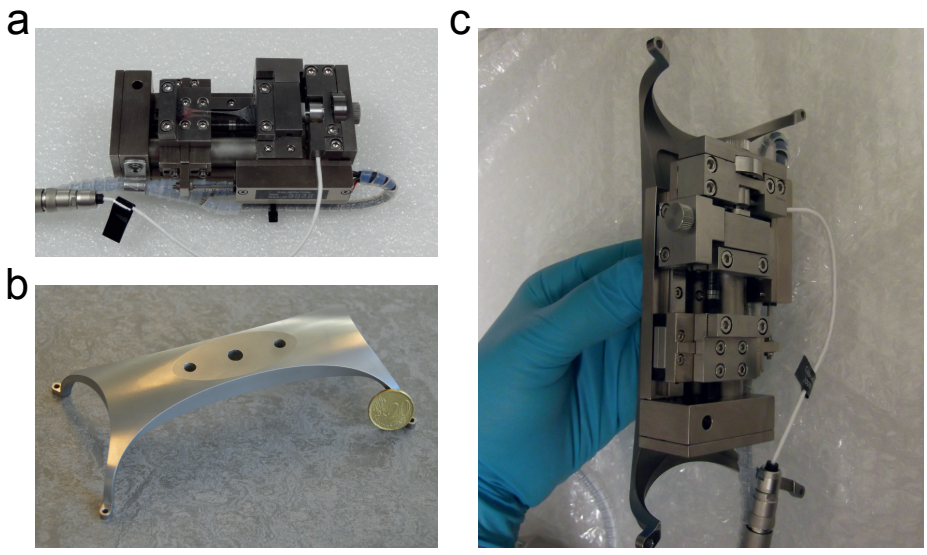

Figure 6.4: (a) The tensile tester with a fibrin gel clamped on two ends, **(b)** the adapter that holds the tensile stage on top of the z-stage, and **(c)** the tensile tester attached to the adapter.

6.2.2. ELECTRICAL CIRCUIT

In order to acquire three-dimensional images, image acquisition needs to be alternated by movement of the sample through the light sheet. The timing of this process is orchestrated by the camera. The camera sends a Start Of Frame-signal to the NI-DAQ board (National Instruments, Woerden, the Netherlands). The NI-DAQ-board sends an analogue signal to the z-stage to move to the vertical position where the first image will be taken. Although the real-time position of the z-stage is recorded, this signal is not used to determine when the image acquisition should start. Instead, 35 ms after the signal is sent to the z-stage, a signal is sent to the laser to turn on. The response time for the laser power to build up is specified to be shorter than 300 ns, which can be considered instantaneous in our experiment. At this moment, all pixels of the camera are exposed (the camera works with a rolling shutter), for a duration specified by the user (typically around 10 ms). At the end of the exposure, a signal is sent to the laser to turn off, the camera chip is read out, and a new Start Of Frame-signal is generated.

The communication between the user and the electronic components of the setup is mediated by home-written acquisition software, written in C#. It allows the user to set the acquisition time per frame, the number of steps in z and the step size for the acquisition of 3D images, as well as the laser power and the position of the xy-stage.

When setting a new position of the piezo stage, there is an instantaneous response of the driving voltage, but a delay is observed in the actual position of the stage, originating from the inertia of the stage and the sample holder. The stage thus acts as a damped spring, and hence we can use the input signal to optimize the time with which the stage positions reaches its set position. We chose to overshoot (damping less than critical damping) as this brings the stage earlier near the set position, even though there is some ringing in the position afterwards. For optimal performance, we tuned the piezo with a 770 g load (sample holder) and a 1 μm step to have a maximum of 5% overshoot: we reach in 10.5 ms the set point within a 5% accuracy. An example of the driving voltage and the actual stage position is shown in Figure 6.5 for a series of 1 μm steps in z. Furthermore, we chose to operate the z-stage in closed-loop mode since this mode has lower drift and allows the position of the z-stage to be recorded, at the expense of a slower system compared to open-loop mode.

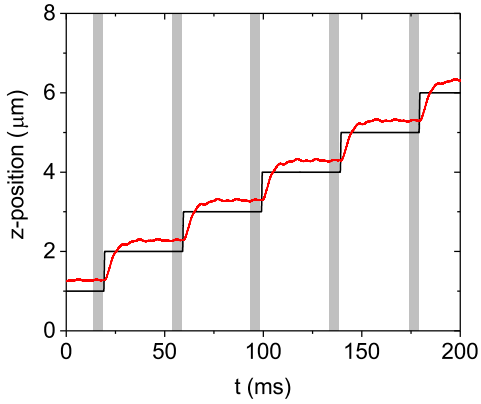

Figure 6.5: z-position of the sample stage, both the input signal (black) and the reported position of the piezo stage (red). A protocol is applied where every 40 ms a 1 μm step in z is applied. For this experiment, the exposure time of the camera is 5 ms (the grey areas), while the time for the sample stage to reach its new position is 35 ms.

6.2.3. SAMPLE PREPARATION

Human plasma fibrinogen (Plasminogen, von Willebrand Factor and Fibronectin depleted) and human α-thrombin were obtained in lyophilized form from Enzyme Research Laboratories (Swansea, United Kingdom), and fibrinogen labeled with the fluorophore Alexa488 from Life Technologies (Eugene, OR, USA). All chemicals were obtained from Sigma Aldrich (Zwijndrecht, The Netherlands). Fibrinogen (lyophilized in 20 mM sodium citrate-HCl buffer at pH 7.4) was dissolved in water at 37°C for 15 min to its original concentration (approximately 13 mg/ml) and dialysed against fibrin buffer containing 20 mM HEPES and 150 mM NaCl at a pH of 7.4 in order to remove citrate, which complexes with Ca^{2+} ions that are required for FXIII and thrombin activity. A dialysis membrane with a Molecular Weight Cut-Off (MWCO) of 10 kD was used. 50 ml of sample was dialysed against 1 L of buffer, under continuous stirring. After one hour of dialysis at room temperature, the buffer was replaced, and after another hour, the buffer was replaced again. The third dialysis step was performed at 4°C overnight. After dialysis, the fibrinogen solution was aliquotted, snap-frozen in liquid nitrogen and stored at -80°C. The monomer concentration was checked by spectrophotometric measurements of the absorbance at 280 and 320 nm using a Nanodrop 2000 spectrophotometer (Thermo Scientific) and using an extinction coefficient of 16.0 mg/(ml cm) [51] at 280 nm. The absence of absorption at 320 nm indicates that no aggregates are present. The final fibrinogen concentration was typically around 10 mg/ml. Prior to use, the fibrinogen was quickly thawed at 37°C, and then diluted and mixed with 500 mM $CaCl_2$ at room temperature to a final assembly buffer containing 20 mM HEPES, 150 mM NaCl and 5 mM $CaCl_2$ ("coarse clots").

Thrombin (lyophilized in 50 mM sodium citrate and 0.2 M NaCl) was, on ice, reconstituted in water to its original concentration (approximately 10,000 U/ml), and quickly

aliquotted, snap-frozen in liquid nitrogen and stored at -80°C. Assembly was initiated by the addition and quick mixing of 0.5 U/ml of thrombin from a 20 U/ml thrombin stock, kept on ice for a maximum of 24 hours. After addition of thrombin, the mixture was quickly transferred by pipetting into a custom-made Teflon mould with pieces of Velcro at both ends to clamp the gel (Figure 6.6), to allow *in situ* polymerization overnight at room temperature, in a moist environment to prevent evaporation.

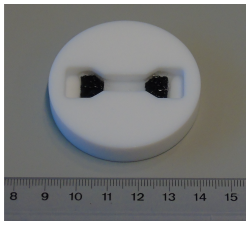

Figure 6.6: A photograph of a Teflon mould filled with a sample, with pieces of Velcro (black) embedded in the gel on both ends, to enable clamping in the sample holder.

6.3. RESULTS

First we determine the height of the light sheet by imaging a glass cube (a beamsplitter) that is held under an angle of 45° in the light sheet. The reflected light is captured by the camera. We draw a line profile through both reflections, and fit the intensity peaks with Gaussian functions (Figure 6.7). Since we hold the glass cube under an angle of 45°, we need to multiply the fitted width of the Gaussian by $\sqrt{1/2}$. We thus find a sheet height of 6.2 ± 1.0 μm.

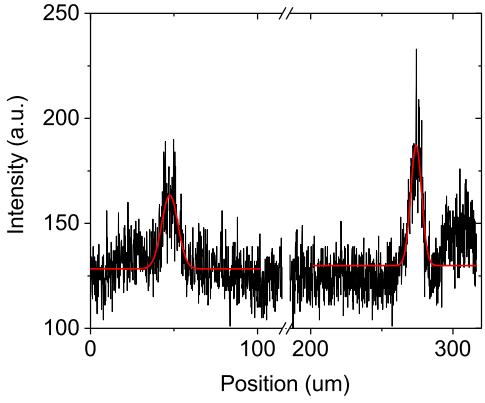

Figure 6.7: A cube of glass, held under an angle of 45°, was imaged from both sides with light sheets. The reflections on both sides of the cube were imaged, and a line profile (black) is shown here. The intensity peaks caused by the reflections are fitted with Gaussian functions (red).

Figure 6.8 shows a single slice from a z-stack of a 2 mg/ml fibrin gel, fluorescently labeled in a 1/10 molar ratio with labeled fibrinogen monomers. In this image, illumination is from the left side only. As a consequence, the illumination sheet is scattered once it reaches the right side of the image, which results in a large volume of the sample that is fluorescently excited, removing any detailed structure. Hence, when imaging turbid materials, either two-sided illumination should be used, or thin samples, such that scattering of the sheet can be neglected over the width of the sample.

In Figure 6.9a we show an image of a 2 mg/ml, fluorescently labeled fibrin gel, imaged from both the left and the right side. We used a filament tracking software to track the fibrin fibers in this image [234]. In Figure 6.9b we show the same image overlaid with the tracked filaments. Using the tracked filaments, we calculate the two-dimensional nematic order parameter (Eq. 4.51), and find a value of 0.08. This lies close to the expected value of zero for a network of completely randomly orientated filaments, that we expect for an undeformed network.

In Figure 6.10a we use a 3D-stack of xy-slices to reconstruct the xz-plane. We observe that close to the surface of the gel (at the bottom of Figure 6.10), individual fibers can be distinguished, even though the resolution in z is worse than in xy. However, deeper into the sample the image becomes more blurred, since the fluorescence light has to travel a longer distance through the turbid gel. Moreover, the difference in resolution in xy and z hinders fiber tracking and network skeletonization.

Finally, in Figure 6.11a and b we show images of a 2 mg/ml, fluorescently labeled fibrin gel, under 50% and 100% applied tensile strain, respectively. Unlike Figure 6.9a, individual fibers are no longer visible, but instead, we see a relatively homogeneous fluorescent signal, suggestive of a collapse of the network. There are indeed two strong indications of network collapse. Firstly, the network has become thinner, indicating the expulsion of water. Secondly, the density of aggregates of fluorescent material is much higher than for the unstrained gel. Both observations indicate that the volume of the fibrin gel strongly decreased with increasing tensile strain, in line with the data presented in Figure 4.5. In addition, we now learn that the solvent expulsion also occurs in an aqueous environment. The effect could be rate-dependent [340], although we did not test multiple rates.

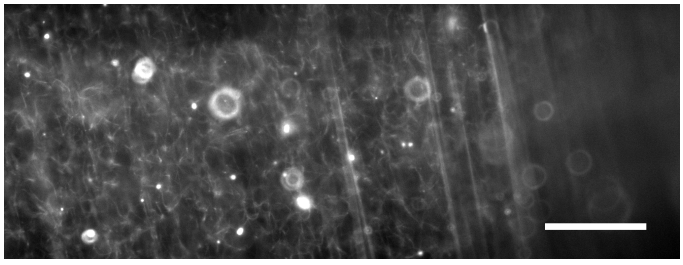

Figure 6.8: SPIM image of a 2 mg/ml fibrin gel, polymerized using fibrinogen mixed with fluorescently labeled fibrinogen in a 9:1 ratio. Illumination is from a single side (left), with 5 ms exposure. Some aggregates of fluorescently labeled fibrinogen are visible as bright spots, as well as broader circles from out-of-focus aggregates. The scale bar is 50 μm.

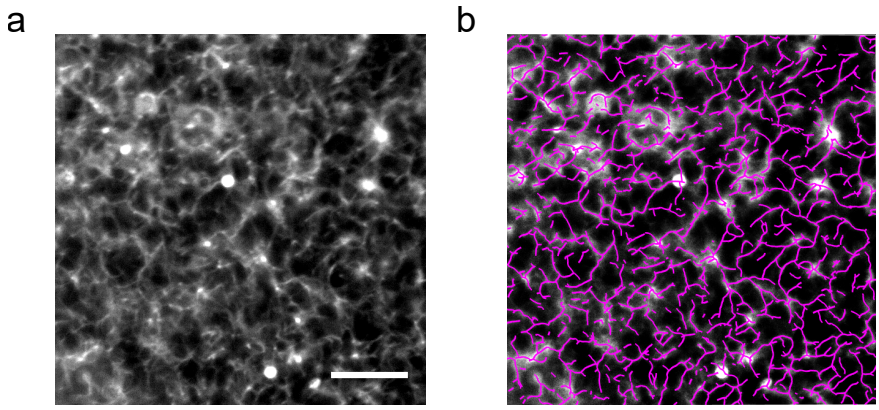

Figure 6.9: SPIM image of a 2 mg/ml fibrin gel, polymerized using fibrinogen mixed with fluorescently labeled fibrinogen in a 19:1 ratio. Illumination is from both sides, with 5 ms exposure. Some aggregates of fluorescently labeled fibrinogen are visible as bright spots. The scale bar is 20 μm. **(a)** shows a single slice of the microscopy image, while **(b)** shows the image overlaid with filaments tracked with SOAX [234]. From the coordinates of the tracked filaments in this image we calculated the nematic order parameter, which was found to be 0.08.

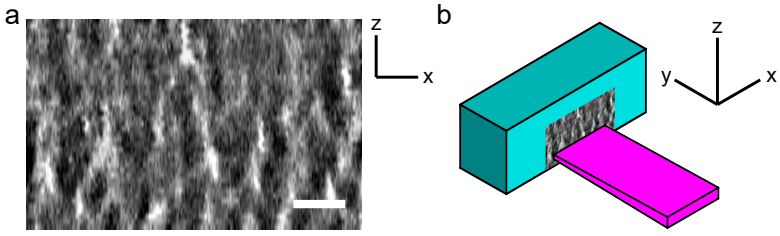

Figure 6.10: **(a)** The xz-plane of an unstretched 2 mg/ml fibrin gel, reconstructed from a SPIM 3D stack of xy-slices. The depth in z was 40 μm with a 1 μm step size, starting just above the boundary of the gel (see cartoon on the right). The contour of some filaments seems to be a wave, which is due to the fact that the setup is not standing on a damped surface. The scale bar is 10 μm. **(b)** A sketch of the geometry of the sample and the light sheet. The detection objective is positioned underneath the sample. The bottom of the gel is at $z = 0$ μm, the top of the gel (also being the upper side in **(a)**) is 40 μm deep in the sample.

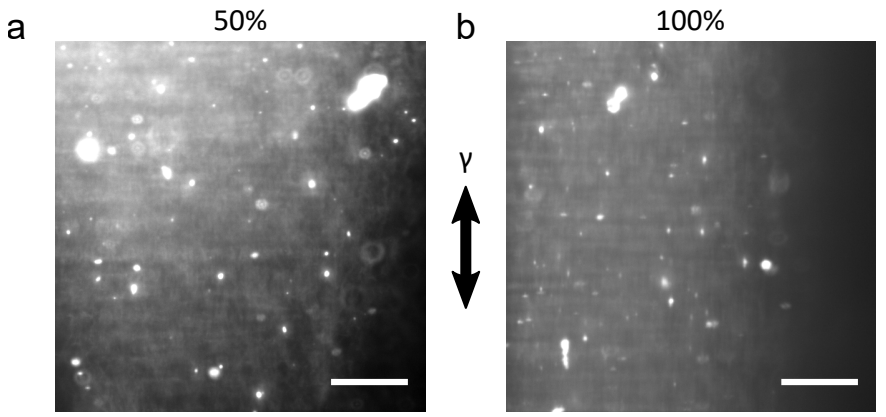

Figure 6.11: Single slices of a SPIM image of a 2 mg/ml fibrin gel, polymerized using fibrinogen mixed with fluorescently labeled fibrinogen in a 29:1 ratio. Illumination is from both sides. The scale bar is 20 μm. **(a)** shows the gel under 50% extensile strain, **(b)** shows the gel under 100% extensile strain. The direction of strain is indicated by an arrow. In both cases, the fibers that comprise the network seem to have collapsed to a structure with a very high density, such that individual fibers are no longer visible.

6.4. CONCLUSION AND OUTLOOK

In this Chapter we reported the design and development of a fluorescence light sheet microscope. We combined the setup with a tensile tester, to enable *in situ* imaging of the effect of mechanical deformation on the network structure. By using two-sided illumination, we were able to illuminate the sample without substantial scattering of the sheet. We were able to identify individual filaments in a fibrin gel using filament tracking software, demonstrating that light sheet microscopy can provide images with sufficient quality to allow quantitative image analysis.

In this Chapter we focused on the design of the setup and the instantaneous response of the fibrin network to deformation. In future work, the capability of this setup to perform long-term imaging in conjunction with mechanical deformation can be used. This extends both to the inelastic response of the fibrin network itself [174, 277, 281] and also to the effect of fibrin degrading proteins [341–345], especially since their activity is presumed to be dependent on the strain of the network [276, 346]. Moreover, since the sample resides in an aqueous environment with little photobleaching, the setup is also suitable to study cell-matrix interactions [300, 347, 348].

The work presented in this Chapter was made possible thanks to the technical support of several departments at AMOLF. In particular I thank Marko Kamp for discussions and help with the optical components and aligning the setup, Marco Konijnenburg and Marco Seynen for designing the acquisition software, Erik Clay and Duncan Verheijde for their work on connecting all electronic hardware and designing a triggering system, Dirk-Jan Spaanderman for designing the setup based on our specifications and the existing blueprints, and the workshop for creating all custom-made parts.

7

SUMMARY AND OUTLOOK

Physics! Biology!
What have we learned today?
Just read the summary;
that will just do.

Although this project was
Machiavellian
I have enjoyed it,
I hope you got through!

In this Chapter I summarize the main results of this Thesis. I also give a short outlook of follow-up research, based on pilot experiments performed during my PhD, that are not included in a more complete form in this Thesis.

7.1. SUMMARY

THE focus of this Thesis was on the mechanical and structural properties of fibrous materials found in nature. Specifically, we focused on fibrin, the main structural component of a blood clot: a biological material that is essential for survival, since it stops the flow of blood through a vascular breach. Its mechanical rigidity originates from a network of fibrin fibers, which assemble through an enzymatic cascade from monomers into protofibrils, fibers and finally the macroscopic network. Interestingly, this network performs its function at a low protein density, yet it is able to withstand large stresses and deformations without rupture. So far, the origin for this remarkable mechanical behaviour has been poorly understood. Until now, our understanding of the mechanical behaviour of fibrin gels was based on models of semiflexible filaments, ignoring the internal structure of the fibrin fibers and their ability to engage in (non-covalent) interactions, as well as ignoring the solvent that permeates the network.

In this Thesis, we asked the question how the complex structure of fibrin and its constituent fibers, protofibrils and monomers relate to the network's complex mechanical properties. To answer this question, we first implemented three existing light scattering models [51–53], to obtain quantitative information on the fiber radius and fiber mass density. We improved these models by including the contribution of wavelength dispersion of the refractive index of the solvent and the differential refractive index. We also implemented the use of a power spectral density analysis to obtain from confocal microscopy images the network's fractal dimension, which is an input parameter in an advanced light scattering model that takes the network structure into account. The light scattering analysis we developed allows us to quantify the structural properties of fibrin fibers, which is a prerequisite to interpret mechanical data. The analysis is also useful for a much broader class of fibrous networks.

We then considered three different, unaddressed mechanical aspects of the fibrin gel: (1) the role of the solvent and its coupling to the fiber network on the mechanical properties of the fibrin gel; (2) changes in structure at different length scales that occur when fibrin networks are exposed to mechanical deformation; and (3) remodeling of the fibrin network through fiber-fiber interactions.

Starting at the macroscopic length scale of the fibrin clot, we demonstrated that the fibrin network and the solvent are coupled on short time scales, set by the elastic modulus and the pore size of the fibrin gel, the viscosity of the solvent, and the macroscopic dimensions of the gel, rendering the network effectively incompressible. Yet on long time scales, the network and solvent are decoupled, such that deformation of the network can occur without solvent movement. Using a combination of experiments and theory, we demonstrated the two-fluid character of the fibrin gel during compression of the network, and also during shear, which is intrinsically a volume-conserving mode of deformation. Under shear deformation, we observed that the direction of the normal stress in response to applied shear stresses is either positive or negative, depending on the coupling between network and solvent. Our findings resolve an apparent paradox between biopolymer networks and synthetic networks, where the former exhibit a negative normal stress and the latter a positive normal stress in response to a shear stress. We demonstrated that both classes of materials are capable of exerting both positive and negative normal stresses, if probed on the right time scale.

So far, the fibrin network was still considered a uniform elastic material, without any hierarchical structure in its constituents. We demonstrated, using a combination of *in situ* microscopy and X-ray scattering, that to understand the full mechanical response of fibrin networks to shear deformation, the orienting effect that shear has on rod-like particles is not sufficient. At small strains of a few percent, before this orienting effect starts to play a role, the stretching of entropic undulations in the fibrin fibers causes network stiffening. At large strains, the mechanical response of the network is dominated by stretching of the fibers themselves, which we showed is facilitated by the stretching of the unstructured αC-regions of the monomer, rather than unfolding of the coiled-coil regions, an idea that dominates the current opinion in literature.

Next, we showed that the constituent fibers that form the network can form new bonds with each other when brought in close contact, in particular during compression of the network. We demonstrated that the αC-regions that are attached to both ends of the fibrin molecule, can interact with the αC-regions of monomers in adjacent fibers. The bonds that are formed this way require a high force to be disrupted, such that these bonds are stressed but not broken when an initially compressed network is brought back to its original configuration. This built-in stress is in turn responsible for an increase of the network stiffness, which can be finely tuned by controlling the amount of applied compression.

Finally, we presented the development of a fluorescence light sheet microscope in combination with a device that can stretch fibrin gels, to enable *in situ* imaging of the effect of mechanical deformation on the network structure, allowing both the fast, elastic response and the slow, inelastic response to be captured.

In conclusion, this research provides a better understanding of the structure-function relation of fibrin networks, which is essential for understanding fibrin's role in hemostasis, thrombosis, and wound healing. We have demonstrated that the mechanical behaviour of fibrin networks originates not only from an assembly of ideal, semiflexible polymers, but rather from a set of hierarchically ordered filaments that can stretch, but also interact with each other, and that is surrounded by an incompressible solvent that couples to the network and grants it high rigidity on short time scales. Moreover, this research also provides new handholds in the directed search and design of materials with specific mechanical properties. In a broader context, this Thesis illustrates how Nature adopts an extensive toolbox of physical principles to optimally perform in the challenging environment we call Life.

7.2. OUTLOOK

The results reported in this thesis not only answer questions, they also raise new questions. For instance, the observation in Chapter 3 that fluid permeation plays a key role in the mechanical response of the fibrin gel raises the question whether the (linear) response in shear differs from compression, due to the fact that the former mode of deformation is volume-conserving, while the latter is not. Furthermore, in Chapter 4 our rheological results suggest that strain-stiffening is simultaneously affected by fiber alignment and by changes in molecular packing of the fibers. Is it possible to disentangle these effects by measuring the stress-strain response of individual fibers? In this Section we show, using a combination of shear and extensional rheology, that the linear shear and extension moduli strongly differ for fibrin gels, due to the induced solvent flow in extensional rheology. We also show optical tweezers measurements on single fibrin fibers to determine their elastic and inelastic mechanical behaviour.

7.2.1. AXIAL AND SHEAR SUPERPOSITION RHEOLOGY

In Chapter 3 we have shown that the coupling between the fibrin network and the solvent plays a crucial role in the time-dependent mechanical behaviour of a fibrin network under applied load. Since water is incompressible and is, by far, the main component of the fibrin network, the whole network is effectively rendered incompressible on time scales shorter than the typical time for solvent efflux, while the network is compressible if solvent is able to flow out on the time scale of deformation. We have shown that the typical time scale differs for shear and compressive deformation, since the distance differs over which the fluid flow takes place. In this Section we will report simultaneously performed axial and shear rheology on a fibrin gel. This allows us to demonstrate on a single sample that the elastic moduli in shear and extension strongly differ, as a result of the different time scales associated with shear and axial deformations. This is analogous to the difference in shear and elongation viscosity, which is a factor 3 for Newtonian fluids, while for non-Newtonian fluids this factor deviates from 3 and becomes rate-dependent [349].

The principle of orthogonal superposition has been demonstrated before in a Couette geometry [350]. In this case the inner cylinder of the Couette cell simultaneously rotated and moved in the axial direction. However, both movements give rise to a shear deformation. Here we will use a Kinexus Pro+ rheometer (Malvern Instruments, Malvern, United Kingdom) with a 40 mm plate-plate geometry. This instrument and its controlling software allow the user to directly control the motor in both shear and axial directions with sufficient time resolution to apply sinusoidal deformations, thereby allowing orthogonal superposition of shear and extensional rheology.

The rSpace software that controls the Kinexus rheometer works, for almost all tests, with predefined test types (e.g. oscillations, stress ramps, frequency sweeps). However, the software is also equipped with a script-based environment that provides direct control of the rotational and axial motor, and provides as output the unadjusted response from the rheometer sensors (torque, shear displacement, axial position, normal force and temperature) at a rate of 5 kHz. This enables the use of complex, unconventional protocols such as the superposition measurement mentioned above, as well as analysis of the raw data, without analysis and averaging over cycles by a “black box” that is the

controller software[1].

We polymerized a 2 mg/ml fibrin gel with an initial sample height of 1 mm at a temperature of 22°C. We performed axial and shear oscillations with a small amplitude of 5 μm and 0.1%, respectively, at various frequencies and degrees of axial compression. We fitted the resulting normal stress and shear stress signals to a sinusoidal function, and calculated the resulting storage and loss moduli by dividing respectively the amplitude of the in-phase and out-of-phase stress response by the strain amplitude. In Figure 7.1a we show the elastic shear modulus at various frequencies and degrees of axial compression. At constant gap height, the elastic shear modulus is frequency-independent, in agreement with earlier studies [125]. During compression, we see that the elastic shear modulus decreases, in agreement with the compression-softening we observed in Chapter 5.

In Figure 7.1b we show the elastic axial modulus at various frequencies and degrees of axial compression. Since this is no longer a volume-conserving measurement, solvent flow is induced on the scale of the sample diameter, which dominates the normal stress response and thereby the measured modulus: the axial modulus is two orders of magnitude larger than the shear modulus. The axial modulus is also no longer frequency independent at a constant gap height, since the frequency of the deformation sets how much solvent flow can occur. However, since the network elasticity plays only a very minute role in the axial stiffness, we observe that the axial modulus is independent of the degree of compression. This measurement directly demonstrates the role of the solvent on the mechanical properties of hydrogels such as the fibrin network, supporting the message we conveyed in Chapter 3.

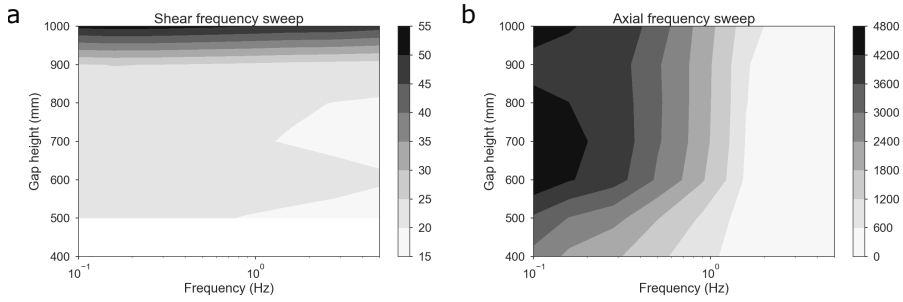

Figure 7.1: (a) Shear and **(b)** axial elastic modulus in units of Pascal (Pa) of a 2 mg/ml fibrin network polymerized at 22°C, at various frequencies and degrees of axial compression.

7.2.2. SINGLE-FIBER STRETCHING EXPERIMENTS

In Chapter 4 we showed how complex it is to deconvolve the contributions of different structural elements of fibrin networks to the macroscopic mechanical response to

[1]There is a good reason why this degree of user control is not commonplace. By directly controlling the motors, the user can unintentionally, yet easily, damage the delicate components of the instrument.

a shear deformation. It is always necessary to assume a specific model to disentangle the single fiber response from the network-level response. For instance, in Chapter 4 we had to assume an affine network deformation to infer the fiber-level strain. Clearly it would be advantageous if one could measure the mechanical response of fibers individually, also for modeling of network-level response [351–353]. With the advent of optical tweezers, this is now possible, as we demonstrate below.

In this Section we report measurements on the elastic and inelastic response of single fibrin fibers, using optical tweezers. So far, studies on single fibrin fibers have relied on the use of atomic force microscopy and spectroscopy [96, 107, 184, 354, 355], where fibers tend to be exposed to air. By using a microfluidic flow cell, we study the filaments in an aqueous environment, which is particularly relevant for fibrin filaments since they tend to be highly hydrated.

Our microfluidic flow cell is sketched in Figure 7.2. It consists of three independent inlets, where laminar flow conditions ensure that no mixing of the channels occurs. The first inlet contained 4.5 μm diameter spherical polystyrene beads (Spherotech, Lake Forest, IL, USA), which were trapped by a 20 W infrared laser (λ = 1064 nm). The second inlet contained fibrin fibers, obtained by adding 0.5 U/ml thrombin to a 0.01 mg/ml fibrinogen solution where 10% of the monomers was labeled with Alexa-488, incubating for 15 minutes at 37°C after addition of thrombin. In Figure 7.3 we show confocal microscopy images for a range of protein concentrations, demonstrating that at concentrations above 0.01 mg/ml, aggregates of fibrin fibers are formed instead of single fibers. The third inlet contained just assembly buffer. We first trapped two beads in the bead channel, and then captured a fibrin fiber in the fibrin channel by connecting them end-to-end to a bead pair, using the ability of fibrin to strongly adhere to polystyrene beads [294]. Finally, the fiber was moved to the buffer channel using the beads as handles. This procedure is schematically shown in Figure 7.2.

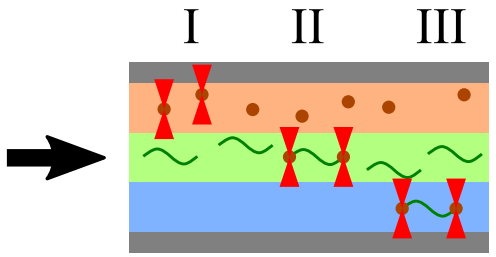

Figure 7.2: Schematic representation of the microfluidic flow cell used for optical tweezer experiments and the stepwise procedure to catch and stretch fibrin fibers. The top channel contains a suspension of 4.5 μm beads, the middle channel a suspension of fibrin fibers, while the lower channel only contains the assembly buffer. The direction of flow is indicated by the black arrow. During the first step of the experiment (I), a pair of beads is caught in the top channel. This bead pair is moved to the middle channel where a fibrin fiber attaches (II). In the bottom channel the stretching experiment is performed (III), without any disturbance from other beads or filaments.

We applied a series of loading and unloading steps, as shown in Figure 7.4a, to test both the elastic and inelastic properties of single fibrin fibers. The elastic properties

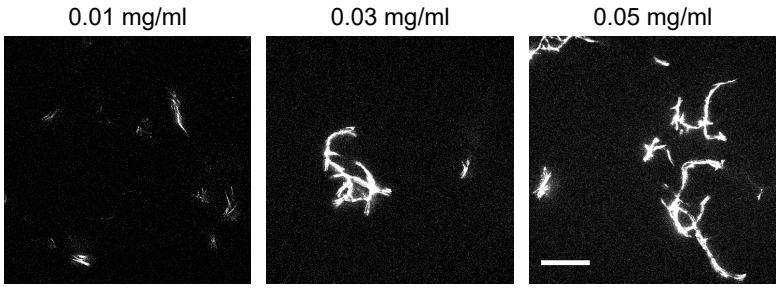

Figure 7.3: Maximum intensity projection of a confocal z-stack of fibrin fibers at increasing protein concentration. Since there is no percolating network, dangling ends and loose fibers are free to diffuse around. This appears as multiple filaments close together, yet it actually is a single filament showing up slightly displaced in multiple frames. The depth of the stacks is 25 μm, the scale bar is 10 μm.

of the fiber were probed by moving the beads apart with a velocity of approximately 0.2 μm/s until a force of 300 pN was reached. The fiber was then held at a constant bead separation to measure force relaxation. The beads were then moved back towards each other, to measure changes in the rest length of the filament. This cycle of loading-unloading was repeated for a total of three times.

By subtracting the diameter of the bead (4.5 μm) from the center-to-center distance of the optical traps we obtain the filament length l. We calculate the filament strain by dividing by the initial length, $\gamma = l/l_0$. We plot the data as a force-extension curve, shown in Figure 7.4b. Here we observe, supported by the fluorescence images, that there is an initial regime where the beads rotate and the fiber straightens, without extending, as indicated by an absence of a force response. Afterwards, the filament actually stretches, which is accompanied by an increase in the force. We fit the latter regime with a linear function (this is the linear regime; the nonlinear regime is way beyond the forces we apply [184]). We determine the onset of this regime by the minimum strain where the r-squared value of the linear fit still exceeds 0.95. A single exponential function was used to fit the force decay during the strain clamp, to determine the relaxation of the filament at high forces (Figure 7.4c).

Since we used the same ratio of unlabeled to labeled fibrinogen monomers, the same laser power and the same imaging settings throughout our experiments, we compare the fluorescence intensity of the fibers per unit length, measured directly after capture of the fiber to avoid effects of photobleaching. An example is shown in Figure 7.4d, where a box of height 20 pixels and a width depending on the fiber length is drawn to obtain fluorescence intensity per unit of filament length. In Figure 7.5a we show the fluorescence intensity per unit of fiber length versus the slope of the loading curve for 11 fibers. We observe a correlation, which we expected since a thick fiber contains more fluorescently labeled monomers, and is expected to be stiffer than a thin fiber.

Furthermore, we note that in Figure 7.4d the fluorescence intensity of the fiber is inhomogeneously distributed. This implies, assuming that the labeled and unlabeled monomers are well mixed, that this fiber is not equally thick along its length; a fea-

ture we observed for most filaments. Consequently, during elasticity measurements, the thinnest part stretches most and the thickest part least, whereas in the calculations we assumed one effective modulus.

We then performed a series of experiments to test the influence of Factor XIII (FXIII), a cross-linking agent that covalently bonds protofibrils in fibrin fibers [18], on the mechanical properties of single fibers. In Figure 7.5b we show the slope of 11 fibers polymerized from wild-type fibrinogen, and 23 fibers from fibrinogen than was depleted of FXIII. In Figure 7.5c and d we show the relaxation time and the relaxation amplitude of 9 fibers polymerized from wild-type fibrinogen, and 20 fibers from fibrinogen that was depleted of FXIII. We could not observe a difference in filament stiffness for wild-type fibrin fibers and FXIII-depleted fibers, due to a large spread in the data within these groups. Similarly, we find a spread in the relaxation time of the force exerted by the fiber under high strain (Figure 7.5c), yet here there is a clear difference with the fibers formed from FXIII-depleted fibrinogen. These show a longer relaxation compared to the fibers formed from wild type fibrinogen, and also slightly stronger relaxation (Figure 7.5d), although here the difference is again smaller than the standard deviation within the data sets. We hypothesize that the more inelastic behaviour of the FXIII-depleted samples reflects the lack of covalent bonds between protofibrils, giving rise to more (and, apparently, also longer) relaxation.

In Figure 7.6a we show the effect of multiple strain cycles on the rest length of the fiber. After the first cycle, the rest length increased by $15\% \pm 9.4$ (average of 9 fibers) in a cross-linked fibrin fiber. This may potentially reflect imperfect packing of protofibrils, which is reorganized when a strain is applied to the fiber. This would be in agreement with Chapter 4, where we hypothesized that annealing occurs of the packing of protofibrils by stretching imposed by a macroscopic shear deformation, since we observed an increase in the axial packing order (measured by the height of the Bragg diffraction peak) for strained compared to unstrained networks. The subsequent cycle of loading-unloading causes no further change in the rest length, which indicates that it is indeed plastic behaviour we observe, and not viscous.

Finally, in Figure 7.6b and c we apply a load for longer times (25 and 45 minutes) in respectively a force- and strain-controlled experiment. Here we observe in FXIII-cross-linked fibers that their rest length increases by 41%, or that 16% of the applied force is dissipated. Interestingly, after an initial decay (as reported in Figure 7.5c), there seems to be a continuous, linear increase in length with time, or decrease in force, both commencing after approximately 600 s. The notion that a constant slope is observed, rules out that we are dealing with a relaxation process. Instead, this is in agreement with a process of unbinding and rebinding of cross-linkers [356]. On the molecular scale, sliding of protofibrils within the fiber might be the origin of fiber elongation and force dissipation. However, the presence of FXIII, introducing covalent cross-links, makes this an unlikely scenario since the unbinding force would be enormous, thus making the rate of unbinding essentially zero on experimentally accessible time scales.

The plastic elongation poses a paradox: we and others do not observe plastic deformation by macroscopic rheology on (FXIII-cross-linked) fibrin networks, although we demonstrated here that single fibers deform plastically. We can understand this with the results of a recent study (Ref. [340]), demonstrating that plastic elongation of colla-

gen fibers does not necessarily lead to plastic deformation on the network scale, since, as the bending rigidity of fibers is lower than the stretching rigidity, un-elongated fibers overcome the resistance of the plastically elongated fibers and restore the network to its original state.

In conclusion, we have shown that we can use optical tweezers to manipulate single fibrin fibers, and we applied a protocol that tested both the elastic and the inelastic properties of the fibers. We measured fibers cross-linked with FXIII, and depleted of FXIII. However, due to large fiber-to-fiber variations we could not quantitatively test hypotheses on the influence of FXIII on the mechanics of single fibrin fibers, and due to fiber inhomogeneities, we could not quantify single-fiber properties, e.g. by fitting the force-extension curve with a worm-like chain model [357]. Although this is a promising technique, future experiments should use a different method to obtain single fibrin fibers that are more uniform in structure, for instance by quenching of the polymerization reaction at higher protein concentrations, or by lysis of a fully formed fibrin network.

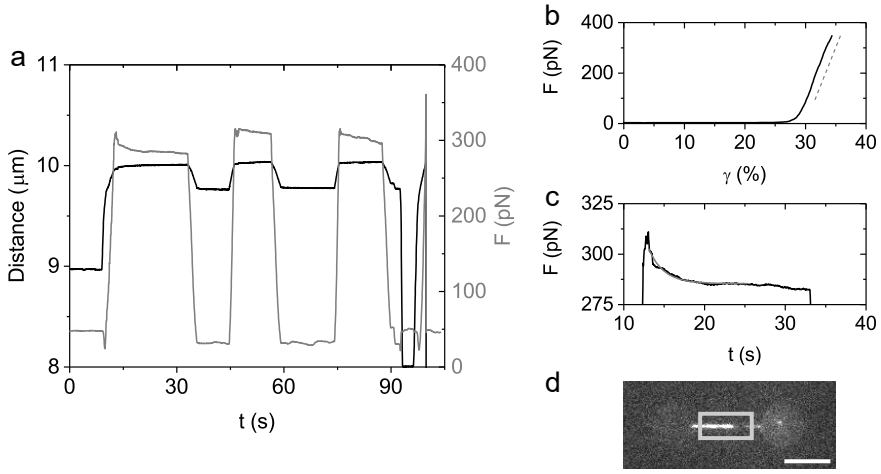

Figure 7.4: (a) Distance-controlled protocol to measure the elasticity of single fibers. First a strain is applied until a load of 300 pN is reached. This strain is held to measure force relaxation, after which the strain is removed and held at the initial force for 10 s. The loading protocol is then repeated for a total of three times. **(b)** Force as a function of fiber strain, from which the linear elasticity (grey dashed line) is obtained. **(c)** Force exerted by a fiber as a function of time, fitted with an exponential decay function (grey). **(d)** A fluorescence image of the fiber suspended between two beads. A box is shown with a height of 20 pixels, used to calculate the fluorescence intensity per unit of fiber length. The scale bar is 5 μm.

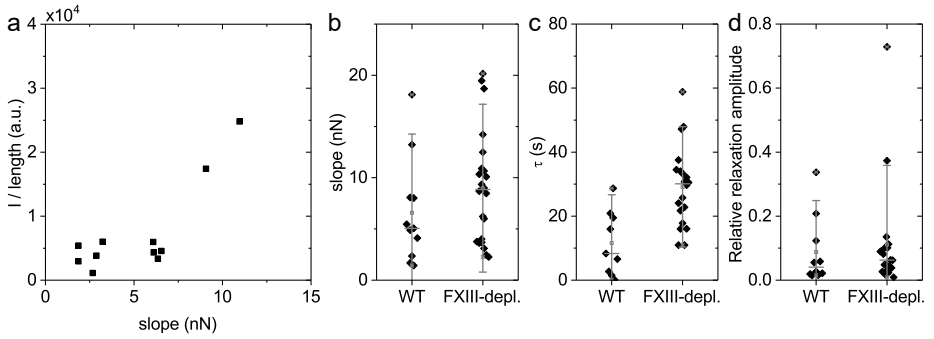

Figure 7.5: **(a)** The fluorescence intensity I per unit of fiber length as a function of the slope of the loading curve, **(b)** the slope of the loading curve for 11 fibers polymerized from wild-type (WT) fibrinogen, and 23 fibers from fibrinogen than was depleted of FXIII (FXIII-depl.), **(c)** the relaxation time τ of 9 fibers polymerized from wild-type fibrinogen, and 20 fibers from fibrinogen than was depleted of FXIII, and **(d)** the corresponding amplitude of the force decay. Grey bars in the box plots indicate the mean value and the standard deviation.

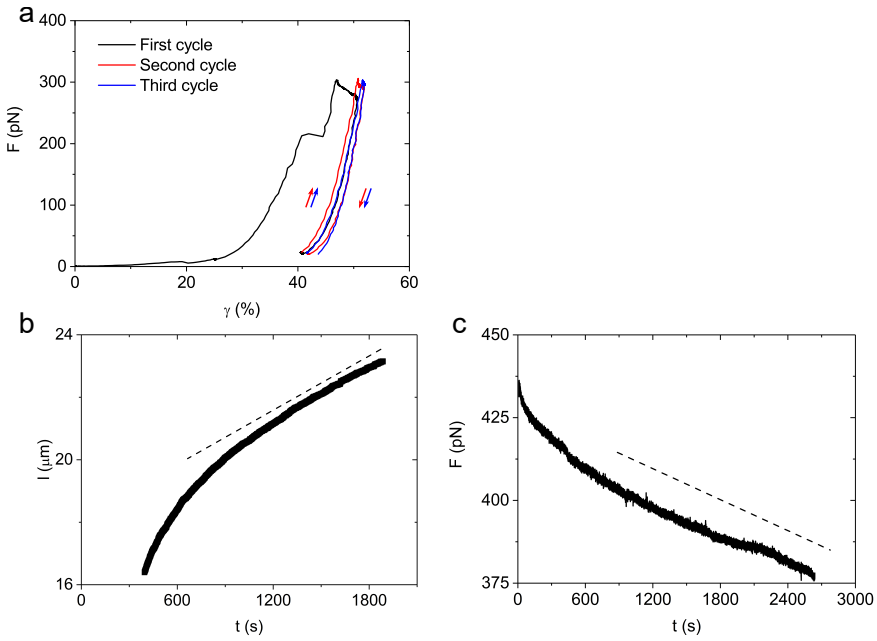

Figure 7.6: Relaxation of a fibrin fiber, **(a)** in a cyclic loading-unloading experiment (with different colours indicating subsequent cycles), **(b)** in a force-controlled experiment (with 500 pN applied load), elongating from approximately 16.4 μm to 23.2 μm, and **(c)** in a distance-controlled experiment, where the force decays from 436 pN to 377 pN. Two dashed lines indicate linear time-dependent behaviour.

I thank Gijs Wuite and Erwin Peterman for the hospitality at the VU, and Andreas Biebricher for help with the two-trap optical tweezers setup. I thank Nicholas Kurniawan and Cristina Martinez Torres (AMOLF) for joining the two-trap optical tweezers experiments. I thank Adrian Hill (Malvern, United Kingdom) for discussions and his help in achieving axial and shear superposition rheology. I thank Jaap Koopman and Jos Grimbergen (Fibriant, the Netherlands) for generously providing the FXIII-depleted fibrinogen used in this Chapter.

SAMENVATTING

HEt onderwerp van dit proefschrift was het onderzoeken van de structuur en de mechanische eigenschappen van fiberachtige materialen. In het bijzonder wordt fibrine onderzocht: een eiwit-netwerk dat stevigheid geeft aan bloedstolsels. Hoewel we ze zoveel mogelijk proberen te mijden, zijn bloedstolsels wel essentieel in ons leven: zodra een bloedvat beschadigt, vormt een bloedstolsel een beschermende laag die verder bloedverlies voorkomt, en ook de eerste stap is in het herstel. De fibrine-netwerken zelf bestaan uit fibers, die op hun beurt ontstaan zijn uit een kettingreactie waarbij uit fibrinogeen-monomeren eerst zogenaamde protofibrillen worden gevormd, die op hun beurt de dikkere fibers vormen waaruit het netwerk is opgebouwd. Het netwerk heeft de interessante eigenschappen dat het zijn functie vervult bij een heel lage concentratie van eiwit, grote krachten en vervormingen kan weerstaan zonder kapot te gaan, en steviger wordt als het sterk vervormd wordt.

Tot dusver is niet goed begrepen hoe fibrine aan deze opmerkelijke eigenschappen komt. Modellen die het mechanische gedrag beschrijven, zijn gebaseerd op elastische filamenten, en gaan voorbij aan de vloeistof die tussen de fibers in zit, de interne structuur van de fibers, en de mogelijkheid van fibers om interacties aan te gaan met andere fibers.

In dit proefschrift staat de vraag centraal hoe de complexe structuur van fibrine (en van de fibers, protofibrillen en monomeren) in verband staat tot de complexe mechanica van fibrine. Om deze vraag te beantwoorden, implementeren we in hoofdstuk 2 eerst drie bestaande modellen [51–53], waarmee, met lichtverstrooiingsexperimenten op fibrine, de straal en de massa-dichtheid van de fibers kunnen worden bepaald. We breiden deze modellen uit met een correctie voor de golflengte-afhankelijkheid van de brekingsindex van water en de differentiële brekingsindex van het eiwit. We maken gebruik van een 'power spectral density'-analyse om de fractale dimensie van het netwerk te bepalen. De fractale dimensie is een parameter in één van de verstrooiingsmodellen, waardoor ook de structuur van het netwerk in beschouwing wordt genomen. Met de analyse van de verstrooiingsspectra krijgen we informatie over de structuur van de fibrine-fibers, wat een vereiste is om het mechanische gedrag te interpreteren. Deze analyse kan ook gebruikt worden voor andere materialen die uit fibers bestaan.

Daarna beschouwen we drie verschillende mechanische aspecten van de fibrine-gel: (1) de rol die vloeistof speelt in de mechanische eigenschappen van de gel, en de koppeling tussen het netwerk en de vloeistof; (2) veranderingen die optreden op verschillende lengteschalen wanneer het fibrine-netwerk wordt vervormd, en (3) het herstructureren van het netwerk door fiber-fiber interacties.

Beginnend bij de grootste schaal, van het macroscopische stolsel, laten we in hoofdstuk 3 zien dat het netwerk en de vloeistof aan elkaar gekoppeld zijn op een korte tijdschaal, die wordt bepaald door de elastische modulus van de gel, de poriegrootte van het netwerk, de viscositeit van de vloeistof, en de afmetingen van de gel. Wanneer het

netwerk en de vloeistof gekoppeld zijn, is hun geheel niet te comprimeren; pas op langere tijdschalen, waarbij de vloeistof en het netwerk ten opzichte van elkaar kunnen bewegen, kan het netwerk vervormd worden. Met een combinatie van theorie en experimenten laten we zien dat de fibrine-gel zich inderdaad gedraagt als een materiaal dat uit een vloeibare en een vaste component bestaat, zowel tijdens compressie als tijdens een afschuifvervorming. Bij de afschuifvervorming zien we dat de richting van de normaalkracht die de gel uitoefent zowel positief als negatief kan zijn, afhankelijk van de mate van koppeling tussen de vloeistof en het netwerk. Deze resultaten lossen een paradox op tussen netwerken van biopolymeren en netwerken van synthetische materialen, waarbij tot nu toe werd aangenomen dat de eerstgenoemde een negatieve normaalkracht hebben, en de synthetische materialen een positieve normaalkracht. Wij laten zien dat beide klassen in staat zijn om zowel positieve als negatieve normaalkrachten uit te oefenen, zolang maar op de juiste tijdsschaal gemeten wordt.

Tot dusver hebben we de fibrine-gel nog beschouwd als een uniform, elastisch materiaal. In hoofdstuk 4 combineren we optische microscopie en röntgenverstrooiing met uitrek- en afschuifvervormingen van een fibrine-netwerk, om het mechanische gedrag van fibrine te begrijpen bij verschillende maten van vervorming. We laten zien dat het oriënteren van de fibers die het netwerk vormen, niet genoeg is om het mechanische gedrag te begrijpen. Bij kleine vervormingen, voordat oriëntatie van fibers een rol gaat spelen, worden entropische fluctuaties uit de fibers getrokken, wat tot een grotere stijfheid van het netwerk leidt. Bij grote vervormingen wordt de mechanische respons van het netwerk bepaald door uitrekking van de fibrine-fibers zelf. We laten zien dat de oorsprong hiervan ligt in het uitrekken van de αC-domeinen van het fibrine-monomeer, in plaats van het ontvouwen van de gestructureerde delen van het monomeer, wat tot nu toe werd aangenomen.

Vervolgens laten we in hoofdstuk 5 zien dat de fibers die het fibrine-netwerk vormen, nieuwe verbindingen met elkaar aan kunnen gaan wanneer ze met elkaar in contact worden gebracht. Dit speelt vooral een rol bij compressie van het netwerk, wanneer fibers dichter bij elkaar komen. We laten zien dat de αC-domeinen die aan beide uiteindes van het monomeer zitten, een verbinding aan kunnen gaan met αC-domeinen die vastzitten aan monomeren op nabijgelegen fibers. De verbinding die op deze manier wordt gevormd kan grote krachten weerstaan, zodat, wanneer het netwerk weer naar zijn originele vorm wordt teruggebracht, de nieuwe verbindingen onder spanning komen te staan, maar niet breken. De spanning die op deze manier in het netwerk wordt ingebouwd zorgt voor een verstijving van het netwerk, die bovendien nauwkeurig te controleren is door de mate van compressie aan te passen.

Tenslotte presenteren we in hoofdstuk 6 de ontwikkeling van een *light sheet* microscoop, een fluorescentiemicroscoop die met een brede, platte (2D) laserstraal werkt in plaats van de meer gebruikelijke (1D) laserstraal. Deze microscoop combineren we met een apparaat dat fibrine kan uitrekken. Hiermee kunnen we het effect van uitrekking op de structuur van het netwerk meten, zowel de korte, elastische respons als de langzamere, inelastische respons.

Samenvattend laat het onderzoek in dit proefschrift zien hoe de structuur en de functie van het fibrine-netwerk met elkaar in verband staan. Dit is essentieel om de rol van fibrine te begrijpen in bijvoorbeeld hemostase, trombose en wondgenezing. We hebben

laten zien dat de mechanische eigenschappen van het fibrine-netwerk niet komen van een set perfecte, homogene staafjes, maar van filamenten met een duidelijke, hiërarchische opbouw, die kunnen uitrekken maar ook onderling interacties aan kunnen gaan, en omgeven worden door vloeistof die, op korte tijdschaal, aan het netwerk gekoppeld is om het een grote stevigheid te geven. Deze principes kunnen worden gebruikt om nieuwe materialen te ontwerpen, met specifieke mechanische eigenschappen. In een bredere context laat dit proefschrift zien hoe de natuur over een uitgebreid arsenaal aan natuurkundige principes beschikt om ons optimaal te laten functioneren in de complexe en uitdagende omstandigheden die het leven ons biedt.

ABOUT THE AUTHOR

CURRICULUM VITAE

Bart Vos was born in Purmerend, the Netherlands, in 1991. Inspired by his physics teacher at high school, and motivated by a desire to learn about the physical principles that describe our world, Bart started his bachelor studies at the University of Amsterdam in Physics and Astronomy in 2008, followed by a master Physics, in the track Advanced Matter and Energy Physics, in 2011. For his master thesis he joined the Resonant Nanophotonics group at AMOLF, under the supervision of Femius Koenderink, for a project that combined microscopy and nanofabrication with analytical and numerical calculations.

He did his PhD in the Biological Soft Matter group, staying at AMOLF. Since the field of biophysics is an inherently complex field, that more often than not relies on complementary techniques, Bart was able to apply his experience in different fields of physics (since radial integration of the back-focal plane of a microscope objective and radial integration of a SAXS pattern is practically indistinguishable), and extend both his experimental and analytical toolbox. This wide and interdisciplinary range of experimental and analytical tools was challenging, yet also the appeal to start with this specific project.

PUBLICATIONS RELATED TO THIS THESIS

- M. Vahabi, **B.E. Vos**, H.C.G. de Cagny, D. Bonn, G.H. Koenderink, and F.C. MacKintosh, *Normal stresses in semiflexible polymer hydrogels*, Physical Review E (2017). Editor's Choice

- **B.E. Vos**, L.C. Liebrand, M. Vahabi, A. Biebricher, G.J.L. Wuite, E.J.G. Peterman, N.A. Kurniawan, F.C. MacKintosh, and G.H. Koenderink, *Programming the mechanics of cohesive fiber networks by compression*, Soft Matter (2017). Journal cover

- H.C.G. de Cagny*, **B.E. Vos***, M. Vahabi*, N.A. Kurniawan, M. Doi, G.H. Koenderink, F.C. MacKintosh, and D. Bonn, *Porosity governs normal stresses in polymer gels*, Physical Review Letters (2016).

- **B. E. Vos**, C. Martinez-Torres, F. Burla, and G.H. Koenderink, *Connecting fibrin's structure and mechanics by a multiscale approach*, manuscript in preparation.

OTHER PUBLICATIONS

- B. Dutta, **B.E. Vos**, Y.L.A. Rezus, G.H. Koenderink, and H.J. Bakker, *Observation of Ultrafast Vibrational Energy Transfer in Fibrinogen and Fibrin Fibers*, The Journal of Physical Chemistry B, 2018.

- Y. Bachour, L. Oei, A. van der Veen, **B.E. Vos**, S. Heulekom, A. Louis, M.J.P.F. Ritt, F.B. Niessen, P. Koken, and H.A.H. Winters, *The influence of radiotherapy on the mechanical properties of silicone breast implants*, Plastic and Reconstructive Surgery Global Open, 2018.

- N.A. Kurniawan, T.H.S. van Kempen, S. Sonneveld, T.T. Rosalina, **B.E. Vos**, K.A. Jansen, G.W.M. Peters, F.N. van de Vosse, and G.H. Koenderink, *Buffers Strongly Modulate Fibrin Self-Assembly into Fibrous Networks*, Langmuir (2017).

- K.A. Leonidakis, P. Bhattacharya, J. Patterson, **B.E. Vos**, G.H. Koenderink, J. Vermant, D. Lambrechts, M. Roeffaers, and H. Van Oosterwyck, *Fibrin structural and diffusional analysis suggests that fibers are permeable to solute transport*, Acta Biomaterialia (2017).

- N.A. Kurniawan, **B.E. Vos**, A. Biebricher, G.J.L. Wuite, E.J.G. Peterman, and G.H. Koenderink, *Fibrin Networks Support Recurring Mechanical Loads by Adapting their Structure across Multiple Scales*, Biophysical Journal (2016).

- T. Xu, C. Langouras, M. Adeli-Koudehi, **B.E. Vos**, N. Wang, G.H. Koenderink, X. Huang, and D. Vavylonis, *Automated Tracking of Biopolymer Growth and Network Deformation with TSOAX*, manuscript submitted.

- K.A. Jansen, A. Zhmurov, **B.E. Vos**, G. Portale, D.H. Merino, R.I. Litvinov, V. Tutwiler, N.A. Kurniawan, W. Bras, J.W. Weisel, V. Barsegov, and G.H. Koenderink, *Molecular packing structure of fibrin fibers resolved by X-ray scattering and molecular modeling*, manuscript in preparation.

ACKNOWLEDGEMENTS

It seems an eternity since I walked into the office of Gijsje for the first time, to express my interest in an PhD position in her group. Now, five years later, I express my sincere gratitude for the opportunity she offered me, to explore the wonderful world of Biological Soft Matter. It was a remarkable journey where I was constantly challenged to learn, to think critically and to push my boundaries. During this period, Gijsje showed herself to be an involved, committed and patient supervisor, which as much enthusiasm for a project as myself. Gijsje, I consider it a privilege and an honour to have had your supervision during the past years.

I thank all students, PhD's and postdocs at AMOLF, for their support, the useful discussions, and for listening to the many talks on nonlinear rheology. In particular, I thank the wonderful members of Team Fibrin: Nicholas, Cristina, Biplab, Tatjana, Karin, Federica, Miriam, Stijn, Mick and Ilva, and all other fellow members of the Biological Soft Matter group: Florian, Adeline, Viktoria, Galja, Anders, Jeanette, Feng, Corianne, Maga, Stef, Aditya, Agata, Celine, Yuval, Lennard, Lucia, Marjolein, Jeffrey, Tjado, Shayla, Cees, Liza, Sven, Jasmijn, Faisal, Philippine, Faranaaz, Rouquaya, Ruben, Alexandra, Merel, George and Sophie.

Viktoria, without you I would never have appreciated all the good that Bonn brought forth. Anders, I'm glad to have found someone with an equal passion for rheology (or better, nonlinear rheology!) and baking. Galja, I cherish our discussions on the important aspects of life. Nicholas, you have my admiration as an excellent experimentalist, programmer, and father, and I am very glad to have had your guidance at the beginning of my PhD. Simone, your cheerfulness and kindness seem to be without end. My fellow office mates, Marjolein, Marko, Yuval, Jacopo and Lennard, it was a delight to share over four years of good humour, fruit and cookies (although "sharing" is perhaps not the right word), and exchange our rather different tastes in music. I will truly miss you. Federica, thank you for your generous smiles and optimism, and the good conversations we had. Cristina, thank you for sharing your passion for Mexican food (and how to not confuse it with Tex-Mex!), Fourier transformations and Côte du Rhône. Ich danke auch alle Leuten auf AMOLF, mit denen ich Deutsch gesprochen habe. Es war ein gute und ganz angenehme Übung. And I thank all my colleagues at AMOLF without whom doing a PhD here would have been a terribly dull job.

My scientific work at AMOLF would have been nearly impossible without the excellent support I have received. For this, I thank all AMOLF staff. In particular Hinko, your ability to make everything from nothing is phenomenal. Marko, thanks for the many times you managed to solve my optical problems. Marco, thanks for writing and supporting a beautiful acquisition software. Dirk-Jan and Ricardo, thanks for the both beautiful and functional designs you made. Ik wil ook de mensen van de werkplaats van AMOLF bedanken, die keer op keer klaarstonden om prachtige werkstukken af te leveren. Juliette, Marjo en Ad, bedankt voor jullie dagelijkse vrolijke begroetingen, goede

gesprekken en meeting rooms die jullie voor mij hebben geboekt. Wiebe, bedankt voor het altijd fixen van mijn ICT-vraagstukken! Tatiana, André, Angela, Arnelli, Fabienne en Sebastiaan, bedankt voor jullie gezelligheid als ik weer eens in het magazijn was, en het verwerken van alle orderformulieren die ik bij jullie heb gebracht. I also thank Femius Koenderink for offering me a position in the Resonant Nanophotonics group, which not only brought me in contact with AMOLF, but also gave me a flying start in terms of working with optical setups and coding complex equations.

I thank Linda and Marjolein for their help in materializing my idea for a cover into the beautiful work of art that it became.

Ik ben ook veel mensen buiten AMOLF dankbaar voor jullie aanwezigheid, gezelschap, inspiratie en interesse. Jullie hebben, wellicht zonder het te weten, mij enorm geholpen om dit boekje tot stand te laten komen. De Rome-crew: Alexander, Koen, Manon, Nikè en Pelle, ik kijk nu al uit naar het volgende jubileum. Pelle en Nikè, het was een genoegen om met jullie de tempels van Ankor te bezoeken, zonsverduisteringen mee te maken, op Franse campings te vertoeven, alsmede om jullie als buren te hebben. Helen, al ruim een half leven delen we een passie voor vrijwel al het mooie in het leven: (alt)hobo's, duinwandelingen, optica & akoestiek, geen dag zonder Bach, drs P., en culinaire avonturen. Mogen er nog vele volgen!

Als laatste wil ik mijn familie bedanken voor jullie steun tijdens mijn PhD. Lieve Hans, Madeleen, Heleen en Jeroen, opa en oma, vanuit het diepst van mijn hart heel hartelijk bedankt. Zonder jullie was ik niet de persoon die ik nu ben.

BIBLIOGRAPHY

[1] R. H. Pritchard, Y. Y. Shery Huang, and E. M. Terentjev, *Mechanics of biological networks: from the cell cytoskeleton to connective tissue,* Soft Matter **10**, 1864 (2014).

[2] R. C. Picu, *Mechanics of random fiber networks - a review,* Soft Matter **7**, 6768 (2011).

[3] R. J. Ellis and A. P. Minton, *Join the crowd,* Nature **425**, 27 (2003).

[4] I. Golding and E. C. Cox, *Physical Nature of Bacterial Cytoplasm,* Physical Review Letters **96**, 098102 (2006).

[5] F. Huber, A. Boire, M. P. López, and G. H. Koenderink, *Cytoskeletal crosstalk: when three different personalities team up,* Current Opinion in Cell Biology **32**, 39 (2015).

[6] S. Mostowy and P. Cossart, *Septins: the fourth component of the cytoskeleton,* Nature Reviews Molecular Cell Biology **13**, 183 (2012).

[7] V. R. Sherman, W. Yang, and M. A. Meyers, *The materials science of collagen,* Journal of the Mechanical Behavior of Biomedical Materials **52**, 22 (2015).

[8] C. Du, F. Z. Cui, W. Zhang, Q. L. Feng, X. D. Zhu, and K. De Groot, *Formation of calcium phosphate/collagen composites through mineralization of collagen matrix,* Journal of Biomedical Materials Research **50**, 518 (2000).

[9] K. Farbod, M. R. Nejadnik, J. A. Jansen, and S. C. Leeuwenburgh, *Interactions Between Inorganic and Organic Phases in Bone Tissue as a Source of Inspiration for Design of Novel Nanocomposites,* Tissue Engineering Part B: Reviews **20**, 173 (2014).

[10] Y. Liu, S. Liu, D. Luo, Z. Xue, X. Yang, L. Gu, Y. Zhou, and T. Wang, *Hierarchically Staggered Nanostructure of Mineralized Collagen as a Bone-Grafting Scaffold,* Advanced Materials **28**, 8740 (2016).

[11] J. M. Forrester, *Malpighi's De polypo cordis: An annotated translation,* Medical History **39**, 477 (1995).

[12] R. a. S. Ariëns, *Fibrin(ogen) and thrombotic disease,* Journal of Thrombosis and Haemostasis **11**, 294 (2013).

[13] S. Xu, Z. Xu, O. V. Kim, R. I. Litvinov, J. W. Weisel, and M. Alber, *Model predictions of deformation, embolization and permeability of partially obstructive blood clots under variable shear flow,* Journal of The Royal Society Interface **14**, 20170441 (2017).

[14] C. Storm, J. J. Pastore, F. C. MacKintosh, T. C. Lubensky, and P. A. Janmey, *Nonlinear elasticity in biological gels,* Nature **435**, 191 (2005).

[15] C. P. Broedersz and F. C. MacKintosh, *Modeling semiflexible polymer networks,* Reviews of Modern Physics **86**, 995 (2014).

[16] I. K. Piechocka, K. A. Jansen, C. P. Broedersz, N. A. Kurniawan, F. C. MacKintosh, and G. H. Koenderink, *Multi-scale strain-stiffening of semiflexible bundle networks.* Soft matter **12**, 2145 (2016).

[17] M. Mosesson, K. Siebenlist, J. Hainfeld, and J. Wall, *The Covalent Structure of Factor XIIIa Crosslinked Fibrinogen Fibrils,* Journal of Structural Biology **115**, 88 (1995).

[18] L. Lorand, *Factor XIII: structure, activation, and interactions with fibrinogen and fibrin,* Annals of the New York Academy of Sciences **936**, 291 (2001).

[19] N. A. Kurniawan, J. Grimbergen, J. Koopman, and G. H. Koenderink, *Factor XIII stiffens fibrin clots by causing fiber compaction,* Journal of Thrombosis and Haemostasis **12**, 1687 (2014).

[20] E. L. Hethershaw, A. L. Cilia La Corte, C. Duval, M. Ali, P. J. Grant, R. A. S. Ariëns, and H. Philippou, *The effect of blood coagulation factor XIII on fibrin clot structure and fibrinolysis,* Journal of Thrombosis and Haemostasis **12**, 197 (2014).

[21] D. Rijken, S. Abdul, J. Malfliet, F. Leebeek, and S. Uitte de Willige, *Compaction of fibrin clots reveals the antifibrinolytic effect of factor XIII,* Journal of Thrombosis and Haemostasis , 1453 (2016).

[22] N. A. Kurniawan, T. H. S. van Kempen, S. Sonneveld, T. T. Rosalina, B. E. Vos, K. A. Jansen, G. W. M. Peters, F. N. van de Vosse, and G. H. Koenderink, *Buffers Strongly Modulate Fibrin Self-Assembly into Fibrous Networks,* Langmuir **33**, 6342 (2017).

[23] J. Maxwell, *On the calculation of the equilibrium and stiffness of frames,* Philosophical Magazine **27**, 294 (1864).

[24] C. P. Broedersz, X. Mao, T. C. Lubensky, and F. C. MacKintosh, *Criticality and isostaticity in fibre networks,* Nature Physics **7**, 983 (2011).

[25] A. Sharma, A. J. Licup, K. A. Jansen, R. Rens, M. Sheinman, G. H. Koenderink, and F. C. MacKintosh, *Strain-controlled criticality governs the nonlinear mechanics of fibre networks,* Nature Physics , 3 (2016).

[26] A. J. Licup, S. Münster, A. Sharma, M. Sheinman, L. M. Jawerth, B. Fabry, D. A. Weitz, and F. C. MacKintosh, *Stress controls the mechanics of collagen networks,* Proceedings of the National Academy of Sciences **112**, 201504258 (2015).

[27] A. J. Licup, A. Sharma, and F. C. MacKintosh, *Elastic regimes of subisostatic athermal fiber networks,* Physical Review E **93**, 012407 (2016).

[28] M. Dennison, M. Sheinman, C. Storm, and F. C. MacKintosh, *Fluctuation-Stabilized Marginal Networks and Anomalous Entropic Elasticity,* Physical Review Letters **111**, 095503 (2013).

[29] M. Sheinman, C. P. Broedersz, and F. C. MacKintosh, *Actively Stressed Marginal Networks,* Physical Review Letters **109**, 238101 (2012).

[30] D. Hexner, A. J. Liu, and S. R. Nagel, *Role of local response in manipulating the elastic properties of disordered solids by bond removal,* Soft Matter **14**, 312 (2018).

[31] A. E. X. Brown, R. I. Litvinov, D. E. Discher, P. K. Purohit, and J. W. Weisel, *Multiscale mechanics of fibrin polymer: gel stretching with protein unfolding and loss of water,* Science **325**, 741 (2009).

[32] M. Guthold and S. S. Cho, *Fibrinogen unfolding mechanisms are not too much of a stretch,* Structure **19**, 1536 (2011).

[33] M. Gralka and K. Kroy, *Inelastic mechanics: A unifying principle in biomechanics,* Biochimica et Biophysica Acta **1853**, 3025 (2015).

[34] S. Münster, L. M. Jawerth, B. Fabry, and D. A. Weitz, *Structure and mechanics of fibrin clots formed under mechanical perturbation,* Journal of Thrombosis and Haemostasis **11**, 557 (2013).

[35] S. Munster, L. M. Jawerth, B. A. Leslie, J. I. Weitz, B. Fabry, and D. A. Weitz, *Strain history dependence of the nonlinear stress response of fibrin and collagen networks,* Proceedings of the National Academy of Sciences **110**, 12197 (2013).

[36] O. V. Kim, R. I. Litvinov, M. S. Alber, and J. W. Weisel, *Quantitative structural mechanobiology of platelet-driven blood clot contraction,* Nature Communications **8**, 1274 (2017).

[37] V. Tutwiler, H. Wang, R. I. Litvinov, J. W. Weisel, and V. B. Shenoy, *Interplay of Platelet Contractility and Elasticity of Fibrin/Erythrocytes in Blood Clot Retraction,* Biophysical Journal **112**, 714 (2017).

[38] V. Tutwiler, R. I. Litvinov, A. P. Lozhkin, A. D. Peshkova, T. Lebedeva, F. I. Ataullakhanov, K. L. Spiller, D. B. Cines, and J. W. Weisel, *Kinetics and mechanics of clot contraction are governed by the molecular and cellular composition of the blood,* Blood **127**, 149 (2016).

[39] S. Zhu, Y. Lu, T. Sinno, and S. L. Diamond, *Dynamics of Thrombin Generation and Flux from Clots during Whole Human Blood Flow over Collagen/Tissue Factor Surfaces,* Journal of Biological Chemistry **291**, 23027 (2016).

[40] H. Polzer, *Versvormen. Leesbaar handboek* (2000) p. 198.

[41] C. F. Bohren and D. F. Huffman, *Absorption and Scattering of Light by Small Particles* (John Wiley & Sons, Inc., 1983).

[42] H. C. van de Hulst, *Light scattering by small particles* (Dover Publications, Inc., 1957).

[43] M. Kerker, *The scattering of light and other electromagnetic radiation* (Academic Press, 1969).

[44] P. Doty and R. F. Steiner, *Light scattering and spectrophotometry of colloidal solutions,* The Journal of Chemical Physics **18**, 1211 (1950).

[45] J. Jansen, C. de Kruif, and A. Vrij, *Attractions in sterically stabilized silica dispersions,* Journal of Colloid and Interface Science **114**, 481 (1986).

[46] P. Debye, D. Woermann, and B. Chu, *Critical Opalescence of Polystyrene in Cyclohexane Transmission Measurements,* The Journal of Chemical Physics **36**, 851 (1962).

[47] N. Dutta, S. Egorov, and D. Green, *Quantification of nanoparticle interactions in pure solvents and a concentrated PDMS solution as a function of solvent quality,* Langmuir **29**, 9991 (2013).

[48] D. H. Melik and H. S. Fogler, *Turbidimetric determination of particle size distributions of colloidal systems,* Journal of Colloid and Interface Science **92**, 161 (1983).

[49] F. H. Silver and D. E. Birk, *Kinetic Analysis of Collagen Fibrillogenesis: I. Use of Turbidity-Time Data,* Collagen and Related Research **3**, 393 (1983).

[50] P. Dalgaard, T. Ross, L. Kamperman, K. Neumeyer, and T. A. McMeekin, *Estimation of bacterial growth rates from turbidimetric and viable count data,* International Journal of Food Microbiology **23**, 391 (1994).

[51] M. E. Carr and J. Hermans, *Size and Density of Fibrin Fibers from Turbidity,* Macromolecules **11**, 46 (1978).

[52] C. Yeromonahos, B. Polack, and F. Caton, *Nanostructure of the Fibrin Clot,* Biophysical Journal **99**, 2018 (2010).

[53] F. Ferri, G. R. Calegari, M. Molteni, B. Cardinali, D. Magatti, and M. Rocco, *Size and Density of Fibers in Fibrin and Other Filamentous Networks from Turbidimetry: Beyond a Revisited Carr-Hermans Method, Accounting for Fractality and Porosity,* Macromolecules **48**, 5423 (2015).

[54] M. D. Bale, M. F. Müller, and J. D. Ferry, *Effects of fibrinogen-binding tetrapeptides on mechanical properties of fine fibrin clots.* Proceedings of the National Academy of Sciences of the United States of America **82**, 1410 (1985).

[55] G. V. Schulz and H. A. Ende, *Über einige thermodynamische Eigenschaften von Fibrinogenlösungen auf Grund der Lichtstreuungsmethode,* Zeitschrift für Physikalische Chemie **36**, 82 (1963).

[56] S. Motte and L. J. Kaufman, *Strain stiffening in collagen I networks,* Biopolymers **99**, 35 (2013).

[57] D. E. Tsentalovich, R. J. Headrick, F. Mirri, J. Hao, N. Behabtu, C. C. Young, and M. Pasquali, *Influence of Carbon Nanotube Characteristics on Macroscopic Fiber Properties,* ACS Applied Materials & Interfaces **9**, 36189 (2017).

[58] *Lambda 25, 35, 45 User's Guide*, PerkinElmer Inc.

[59] D. Magatti, M. Molteni, B. Cardinali, M. Rocco, and F. Ferri, *Modeling of Fibrin Gels Based on Confocal Microscopy and Light-Scattering Data,* Biophysical Journal **104**, 1151 (2013).

[60] J. J. M. Reesinck and R. W. R. Dee, *Blue Clouds,* Madjalah Ilmu Alam **109**, 212 (1953).

[61] J. W. S. Rayleigh, *XXXIV. On the transmission of light through an atmosphere containing small particles in suspension, and on the origin of the blue of the sky,* Philosophical Magazine Series 5 **47**, 375 (1899).

[62] P. W. Barber and D.-S. Wang, *Rayleigh-Gans-Debye applicability to scattering by nonspherical particles,* Applied Optics **17**, 797 (1978).

[63] U. Apfel, K. D. Hörner, and M. Ballauff, *Precise Analysis of the Turbidity Spectra of a Concentrated Latex,* Langmuir **11**, 3401 (1995).

[64] F. Li, R. Schafer, C.-T. Hwang, C. E. Tanner, and S. T. Ruggiero, *High-precision sizing of nanoparticles by laser transmission spectroscopy.* Applied optics **49**, 6602 (2010).

[65] F. Ferri, M. Greco, G. Arcovito, F. Bassi, M. De Spirito, E. Paganini, and M. Rocco, *Growth kinetics and structure of fibrin gels,* Physical Review E **63**, 031401 (2001).

[66] C. M. Sorensen, C. Oh, P. W. Schmidt, and T. P. Rieker, *Scaling description of the structure factor of fractal soot composites,* Physical Review E **58**, 4666 (1998).

[67] M. T. Sheldon, J. van de Groep, A. M. Brown, A. Polman, and H. A. Atwater, *Plasmoelectric potentials in metal nanostructures,* Science **346**, 828 (2014).

[68] F. Neubrech, A. Pucci, T. W. Cornelius, S. Karim, A. García-Etxarri, and J. Aizpurua, *Resonant Plasmonic and Vibrational Coupling in a Tailored Nanoantenna for Infrared Detection,* Physical Review Letters **101**, 157403 (2008).

[69] M. B. Rhodes and R. S. Stein, *Scattering of Light from Assemblies of Oriented Rods,* Journal of Polymer Science **7**, 1539 (1969).

[70] M. C. A. Donkersloot, J. H. Gouda, J. J. van Aartsen, and W. Prins, *Polymer gel structure elucidation by means of light scattering and photo-elasticity,* Recueil des Travaux Chimiques des Pays-Bas **86**, 321 (1967).

[71] E. F. Casassa, *Light Scattering from Very Long Rod- Like Particles and an Application to Polymerized Fibrinogen,* The Journal of Chemical Physics , 10 (1955).

[72] G. R. Palmer, O. G. Fritz, and F. R. Hallett, *Quasielastic light-scattering studies on human fibrinogen and fibrin. I. Fibrinogen,* Biopolymers **18**, 1659 (1979).

[73] G. R. Palmer and O. G. Fritz, *Quasielastic light scattering studies on human fibrinogen and fibrin. II. Fibrin polymerization,* Biopolymers **18**, 1659 (1979).

[74] C. Yeromonahos, *Nanostructure des fibres de fibrine*, Ph.D. thesis (2011).

[75] T. C. Baradet, J. C. Haselgrove, and J. W. Weisel, *Three-dimensional reconstruction of fibrin clot networks from stereoscopic intermediate voltage electron microscope images and analysis of branching,* Biophysical Journal **68**, 1551 (1995).

[76] N. Badiei, A. M. Sowedan, D. J. Curtis, M. R. Brown, M. J. Lawrence, A. I. Campbell, A. Sabra, P. Evans, J. W. Weisel, I. N. Chernysh, C. Nagaswami, P. R. Williams, and K. Hawkins, *Effects of unidirectional flow shear stresses on the formation, fractal microstructure and rigidity of incipient whole blood clots and fibrin gels,* Clinical Hemorheology and Microcirculation **60**, 451 (2015).

[77] A. J. Holder, N. Badiei, K. Hawkins, C. Wright, P. R. Williams, and D. J. Curtis, *Control of collagen gel mechanical properties through manipulation of gelation conditions near the sol–gel transition,* Soft Matter **14**, 574 (2018).

[78] F. Ferri, G. Re Calegari, M. Molteni, B. Cardinali, D. Magatti, and M. Rocco, *Correction to Size and Density of Fibers in Fibrin and Other Filamentous Networks from Turbidimetry: Beyond a Revisited Carr-Hermans Method, Accounting for Fractality and Porosity,* Macromolecules **50**, 1759 (2017).

[79] M. Papi, G. Arcovito, M. De Spirito, G. Amiconi, A. Bellelli, and G. Boumis, *Simultaneous static and dynamic light scattering approach to the characterization of the different fibrin gel structures occurring by changing chloride concentration,* Applied Physics Letters **86**, 183901 (2005).

[80] B. Cox and J. Wang, *Fractal surfaces: Measurement and applications in the earth sciences,* Fractals **1**, 87 (1993).

[81] R. Lopes and N. Betrouni, *Fractal and multifractal analysis: A review,* Medical Image Analysis **13**, 634 (2009).

[82] A. Arnéodo, N. Decoster, and S. Roux, *A wavelet-based method for multifractal image analysis. I. Methodology and test applications on isotropic and anisotropic random rough surfaces,* The European Physical Journal B **15**, 567 (2000).

[83] A. Takahashi, R. Kita, T. Shinozaki, K. Kubota, and M. Kaibara, *Real space observation of three-dimensional network structure of hydrated fibrin gel,* Colloid and Polymer Science **281**, 832 (2003).

[84] R. Gannavarpu, B. Bhaduri, K. Tangella, and G. Popescu, *Spatiotemporal Characterization of a Fibrin Clot Using Quantitative Phase Imaging,* PLoS ONE **9**, e111381 (2014).

[85] N. Sarkar and B. Chaudhuri, *An efficient differential box-counting approach to compute fractal dimension of image,* IEEE Transactions on Systems, Man, and Cybernetics **24**, 115 (1994).

[86] C. Hochman-Mendez, M. Cantini, D. Moratal, M. Salmeron-Sanchez, and T. Coelho-Sampaio, *A Fractal Nature for Polymerized Laminin,* PLoS ONE **9**, e109388 (2014).

[87] R. W. Cole, T. Jinadasa, and C. M. Brown, *Measuring and interpreting point spread functions to determine confocal microscope resolution and ensure quality control,* Nature Protocols **6**, 1929 (2011).

[88] T. G. Dewey, *Fractals in Molecular Biophysics* (Oxford University Press, 1997).

[89] K.-H. Tran-Ba, D. J. Lee, J. Zhu, K. Paeng, and L. J. Kaufman, *Confocal Rheology Probes the Structure and Mechanics of Collagen through the Sol-Gel Transition,* Biophysical Journal **113**, 1882 (2017).

[90] K.-H. Tran-Ba, D. J. Lee, J. Zhu, K. Paeng, and L. J. Kaufman, *Confocal Rheology Probes the Structure and Mechanics of Collagen through the Sol-Gel Transition - Supplementary Information,* Biophysical Journal **113**, 1 (2017).

[91] M. Manno and M. U. Palma, *Fractal Morphogenesis and Interacting Processes in Gelation,* Physical Review Letters **79**, 4286 (1997).

[92] R. H. Abou-Saleh, S. D. Connell, R. Harrand, R. A. Ajjan, M. W. Mosesson, D. A. M. Smith, P. J. Grant, and R. A. Ariëns, *Nanoscale Probing Reveals that Reduced Stiffness of Clots from Fibrinogen Lacking 42 N-Terminal Bβ-Chain Residues Is Due to the Formation of Abnormal Oligomers,* Biophysical Journal **96**, 2415 (2009).

[93] S. Baker, J. Sigley, C. C. Helms, J. Stitzel, J. Berry, K. Bonin, and M. Guthold, *The mechanical properties of dry, electrospun fibrinogen fibers,* Materials Science and Engineering C **32**, 215 (2012).

[94] P. Allan, S. Uitte de Willige, R. H. Abou-Saleh, S. D. Connell, and R. A. S. Ariëns, *Evidence that fibrinogen γ' directly interferes with protofibril growth: implications for fibrin structure and clot stiffness.* Journal of thrombosis and haemostasis : JTH **10**, 1072 (2012).

[95] M. Mosesson, J. Hainfeld, J. Wall, and R. Haschemeyer, *Identification and mass analysis of human fibrinogen molecules and their domains by scanning transmission electron microscopy,* Journal of Molecular Biology **153**, 695 (1981).

[96] M. Guthold, W. Liu, B. Stephens, S. T. Lord, R. R. Hantgan, D. a. Erie, R. M. Taylor, and R. Superfine, *Visualization and mechanical manipulations of individual fibrin fibers suggest that fiber cross section has fractal dimension 1.3.* Biophysical journal **87**, 4226 (2004).

[97] E. B. Hunziker, P. W. Straub, and a. Haeberli, *Molecular morphology of fibrin monomers and early oligomers during fibrin polymerization.* Journal of ultrastructure and molecular structure research **98**, 60 (1988).

[98] M. Rocco, M. Molteni, M. Ponassi, G. Giachi, M. Frediani, A. Koutsioubas, A. Profumo, D. Trevarin, B. Cardinali, P. Vachette, F. Ferri, and J. Pérez, *A Comprehensive Mechanism of Fibrin Network Formation Involving Early Branching and Delayed Single- to Double-Strand Transition from Coupled Time-Resolved X-ray/Light-Scattering Detection,* Journal of the American Chemical Society **136**, 5376 (2014).

[99] M. Rocco and J. W. Weisel, *Exposed: the elusive αC regions in fibrinogen, fibrin protofibrils and fibers,* Journal of Thrombosis and Haemostasis **13**, 567 (2015).

[100] J. W. Weisel and R. I. Litvinov, *Mechanisms of fibrin polymerization and clinical implications,* Blood **121**, 1712 (2013).

[101] M. W. Mosesson, J. P. DiOrio, K. R. Siebenlist, J. S. Wall, and J. F. Hainfeld, *Evidence for a second type of fibril branch point in fibrin polymer networks, the trimolecular junction.* Blood **82**, 1517 (1993).

[102] M. M. Domingues, F. L. Macrae, C. Duval, H. R. McPherson, K. I. Bridge, R. A. Ajjan, V. C. Ridger, S. D. Connell, H. Philippou, and R. A. S. Ariëns, *Thrombin and fibrinogen γ' impact clot structure by marked effects on intrafibrillar structure and protofibril packing,* Blood **127**, 487 (2016).

[103] C. Duval and R. A. Ariëns, *Fibrinogen splice variation and cross-linking: Effects on fibrin structure/function and role of fibrinogen γ' as thrombomobulin II,* Matrix Biology **60-61**, 8 (2017).

[104] A. Casini, M. Neerman-Arbez, R. A. Ariëns, and P. de Moerloose, *Dysfibrinogenemia: from molecular anomalies to clinical manifestations and management.* Journal of thrombosis and haemostasis : JTH **13**, 909 (2015).

[105] K. I. Bridge, H. Philippou, and R. A. S. Ariëns, *Clot properties and cardiovascular disease,* Thrombosis and Haemostasis **112**, 901 (2014).

[106] W. Li, J. Sigley, M. Pieters, C. C. Helms, C. Nagaswami, J. W. Weisel, and M. Guthold, *Fibrin Fiber Stiffness Is Strongly Affected by Fiber Diameter, but Not by Fibrinogen Glycation,* Biophysical Journal **110**, 1400 (2016).

[107] W. Li, J. Sigley, S. R. Baker, C. C. Helms, M. T. Kinney, M. Pieters, P. H. Brubaker, R. Cubcciotti, and M. Guthold, *Nonuniform Internal Structure of Fibrin Fibers: Protein Density and Bond Density Strongly Decrease with Increasing Diameter,* BioMed Research International **2017**, 1 (2017).

[108] G. A. Shah, I. A. Ferguson, T. Z. Dhall, and D. P. Dhall, *Polydispersion in the diameter of fibers in fibrin networks: consequences on the measurement of mass-length ratio by permeability and turbidity.* Biopolymers **21**, 1037 (1982).

[109] D. A. Head, A. J. Levine, and F. C. MacKintosh, *Distinct regimes of elastic response and deformation modes of cross-linked cytoskeletal and semiflexible polymer networks,* Physical Review E **68**, 061907 (2003).

[110] N. R. Lang, S. Münster, C. Metzner, P. Krauss, S. Schürmann, J. Lange, K. E. Aifantis, O. Friedrich, and B. Fabry, *Estimating the 3D Pore Size Distribution of Biopolymer Networks from Directionally Biased Data,* Biophysical Journal **105**, 1967 (2013).

[111] J. Wilhelm and E. Frey, *Elasticity of Stiff Polymer Networks,* Physical Review Letters **91**, 108103 (2003).

[112] H. Valtin, *"Drink at least eight glasses of water a day." Really? Is there scientific evidence for "8 × 8"?* American Journal of Physiology-Regulatory, Integrative and Comparative Physiology **283**, R993 (2002).

[113] M. A. Biot, *General Theory of Three-Dimensional Consolidation,* Journal of Applied Physics **12**, 155 (1941).

[114] R. de Boer, *Highlights in the Historical Development of the Porous Media Theory: Toward a Consistent Macroscopic Theory,* Applied Mechanics Reviews **49**, 201 (1996).

[115] M. Doi, *Gel Dynamics,* Journal of the Physical Society of Japan **78**, 052001 (2009).

[116] L. Cardoso, S. P. Fritton, G. Gailani, M. Benalla, and S. C. Cowin, *Advances in assessment of bone porosity, permeability and interstitial fluid flow,* Journal of Biomechanics **46**, 253 (2013).

[117] S. C. Cowin, *Bone poroelasticity,* Journal of Biomechanics **32**, 217 (1999).

[118] M. A. Swartz and M. E. Fleury, *Interstitial Flow and Its Effects in Soft Tissues,* Annual Review of Biomedical Engineering **9**, 229 (2007).

[119] W. Wilson, C. C. van Donkelaar, and J. M. Huyghe, *A comparison between mechano-electrochemical and biphasic swelling theories for soft hydrated tissues.* Journal of biomechanical engineering **127**, 158 (2005).

[120] S. P. Fritton and S. Weinbaum, *Fluid and Solute Transport in Bone: Flow-Induced Mechanotransduction,* Annual Review of Fluid Mechanics **41**, 347 (2009).

[121] M. A. Soltz and G. A. Ateshian, *Experimental verification and theoretical prediction of cartilage interstitial fluid pressurization at an impermeable contact interface in confined compression,* Journal of Biomechanics **31**, 927 (1998).

[122] V. C. Mow, S. C. Kuei, W. M. Lai, and C. G. Armstrong, *Biphasic Creep and Stress Relaxation of Articular Cartilage in Compression: Theory and Experiments,* Journal of Biomechanical Engineering **102**, 73 (1980).

[123] B. Cohen, W. M. Lai, and V. C. Mow, *A Transversely Isotropic Biphasic Model for Unconfined Compression of Growth Plate and Chondroepiphysis,* Journal of Biomechanical Engineering **120**, 491 (1998).

[124] M. W. Mosesson, K. R. Siebenlist, and D. A. Meh, *The structure and biological features of fibrinogen and fibrin,* Annals New York Academy of Sciences **936**, 11 (2001).

[125] I. K. Piechocka, R. G. Bacabac, M. Potters, F. C. Mackintosh, and G. H. Koenderink, *Structural hierarchy governs fibrin gel mechanics,* Biophysical journal **98**, 2281 (2010).

[126] J. Steinwachs, C. Metzner, K. Skodzek, N. Lang, I. Thievessen, C. Mark, S. Münster, K. E. Aifantis, and B. Fabry, *Three-dimensional force microscopy of cells in biopolymer networks,* Nature Methods **13**, 171 (2016).

[127] P. A. Janmey, M. E. McCormick, S. Rammensee, J. L. Leight, P. C. Georges, and F. C. MacKintosh, *Negative normal stress in semiflexible biopolymer gels,* Nature Materials **6**, 48 (2007).

[128] J. H. Poynting, *On Pressure Perpendicular to the Shear Planes in Finite Pure Shears, and on the Lengthening of Loaded Wires When Twisted,* Proceedings of the Royal Society A: Mathematical, Physical and Engineering Sciences **82**, 546 (1909).

[129] O. Reynolds, *On the dilatancy of media composed of rigid particles in contact. With experimental illustrations.* Philosophical Magazine Series 5 **20**, 469 (1885).

[130] R. G. Larson, *The Structure and Rheology of Complex Fluids.* (Oxford University Press, USA, 1998) p. 688.

[131] M. Mooney, *A theory of large elastic deformation,* Journal of Applied Physics **11**, 582 (1940).

[132] R. S. Rivlin, *Large Elastic Deformations of Isotropic Materials. IV. Further Developments of the General Theory,* Philosophical Transactions of the Royal Society A: Mathematical, Physical and Engineering Sciences **241**, 379 (1948).

[133] H. Kang, Q. Wen, P. a. Janmey, J. X. Tang, E. Conti, and F. C. MacKintosh, *Nonlinear Elasticity of Stiff Filament Networks: Strain Stiffening, Negative Normal Stress, and Filament Alignment in Fibrin Gels,* The Journal of Physical Chemistry B **113**, 3799 (2009).

[134] C. O. Horgan and J. G. Murphy, *Reverse Poynting Effects in the Torsion of Soft Biomaterials,* Journal of Elasticity **118**, 127 (2015).

[135] E. Conti and F. C. MacKintosh, *Cross-Linked Networks of Stiff Filaments Exhibit Negative Normal Stress,* Physical Review Letters **102**, 088102 (2009).

[136] B. P. Tighe, *Shear dilatancy in marginal solids,* Granular Matter **16**, 203 (2014).

[137] M. Tombs, *The interpretation of gel electrophoresis,* Analytical Biochemistry **13**, 121 (1965).

[138] M. Okada, B. Blomback, M. D. Chang, and B. Horowitz, *Fibronectin and fibrin gel structure,* Journal of Biological Chemistry **260**, 1811 (1985).

[139] M. Pieters, a. Undas, R. Marchi, M. P. M. De Maat, J. W. Weisel, and R. a. S. Ariëns, *An international study on the standardization of fibrin clot permeability measurement: methodological considerations and implications for healthy control values,* Journal of Thrombosis and Haemostasis **10**, 2179 (2012).

[140] N. R. R. Lang, S. Münster, C. Metzner, P. Krauss, S. Schürmann, J. Lange, K. E. E. Aifantis, O. Friedrich, and B. Fabry, *Estimating the 3D pore size distribution of biopolymer networks from directionally biased data Supplementary Information,* Biophysical journal **105**, 1 (2013).

[141] F. Brochard and P. G. de Gennes, *Dynamical Scaling for Polymers in Theta Solvents,* Macromolecules **10**, 1157 (1977).

[142] S. T. Milner, *Dynamical theory of concentration fluctuations in polymer solutions under shear,* Physical Review E **48**, 3674 (1993).

[143] F. Gittes, B. Schnurr, P. D. Olmsted, F. C. MacKintosh, and C. F. Schmidt, *Microscopic viscoelasticity: Shear moduli of soft materials determined from thermal fluctuations,* Phys. Rev. Lett. **79**, 3286 (1997).

[144] A. J. Levine and T. C. Lubensky, *One- and Two-Particle Microrheology,* Physical Review Letters **85**, 1774 (2000).

[145] D. C. Venerus, *Free surface effects on normal stress measurements in cone and plate flow,* Applied Rheology **17**, 1 (2007).

[146] F. C. MacKintosh, J. Käs, and P. A. Janmey, *Elasticity of Semiflexible Biopolymer Networks,* Physical Review Letters **75**, 4425 (1995).

[147] C. Heussinger, B. Schaefer, and E. Frey, *Nonaffine rubber elasticity for stiff polymer networks,* Physical Review E **76**, 031906 (2007).

[148] A. S. Lodge and J. Meissner, *On the use of instantaneous strains, superposed on shear and elongational flows of polymeric liquids, to test the Gaussian network hypothesis and to estimate the segment concentration and its variation during flow,* Rheologica Acta **11**, 351 (1972).

[149] G. W. Greene, B. Zappone, B. Zhao, O. Söderman, D. Topgaard, G. Rata, and J. N. Israelachvili, *Changes in pore morphology and fluid transport in compressed articular cartilage and the implications for joint lubrication,* Biomaterials **29**, 4455 (2008).

[150] G. W. Greene, B. Zappone, O. Söderman, D. Topgaard, G. Rata, H. Zeng, and J. N. Israelachvili, *Anisotropic dynamic changes in the pore network structure, fluid diffusion and fluid flow in articular cartilage under compression,* Biomaterials **31**, 3117 (2010).

[151] W. Wintz, R. Everaers, and U. Seifert, *Mesh collapse in two-dimensional elastic networks under compression,* Journal de Physique I **7**, 1097 (1997).

[152] O. V. Kim, X. Liang, R. I. Litvinov, J. W. Weisel, M. S. Alber, and P. K. Purohit, *Foam-like compression behavior of fibrin networks,* Biomechanics and Modeling in Mechanobiology **15**, 213 (2016).

[153] P. L. Chandran and V. H. Barocas, *Microstructural mechanics of collagen gels in confined compression: poroelasticity, viscoelasticity, and collapse,* Journal of biomechanical engineering **126**, 152 (2004).

[154] C. Ghnatios, C. H. Mathis, R. Simic, N. D. Spencer, and F. Chinesta, *Modeling soft, permeable matter with the proper generalized decomposition (PGD) approach, and verification by means of nanoindentation.* Soft matter **13**, 4482 (2017).

[155] S. Münster and B. Fabry, *A Simplified Implementation of the Bubble Analysis of Biopolymer Network Pores,* Biophysical Journal **104**, 2774 (2013).

[156] M. Molteni, D. Magatti, B. Cardinali, M. Rocco, and F. Ferri, *Fast two-dimensional bubble analysis of biopolymer filamentous networks pore size from confocal microscopy thin data stacks.* Biophysical journal **104**, 1160 (2013).

[157] J. Kapur, P. Sahoo, and A. Wong, *A new method for gray-level picture thresholding using the entropy of the histogram,* Computer Vision, Graphics, and Image Processing **29**, 273 (1985).

[158] N. Otsu, *A Threshold Selection Method from Gray-Level Histograms,* IEEE Transactions on Systems, Man, and Cybernetics **9**, 62 (1979).

[159] J. Schindelin, I. Arganda-Carreras, E. Frise, V. Kaynig, M. Longair, T. Pietzsch, S. Preibisch, C. Rueden, S. Saalfeld, B. Schmid, J.-Y. Tinevez, D. J. White, V. Hartenstein, K. Eliceiri, P. Tomancak, and A. Cardona, *Fiji: an open-source platform for biological-image analysis,* Nature Methods **9**, 676 (2012).

[160] H. Darcy, *Les Fontaines Publiques de la Ville de Dijon*, edited by V. Dalmont (Paris, 1856).

[161] M. Ząbczyk, A. Piłat, M. Awsiuk, and A. Undas, *An automated method for fibrin clot permeability assessment,* Blood Coagulation & Fibrinolysis **26**, 104 (2015).

[162] B. Blombäck, K. Carlsson, B. Hessel, A. Liljeborg, R. Procyk, and N. Aslund, *Native fibrin gel networks observed by 3D microscopy, permeation and turbidity.* Biochimica et biophysica acta **997**, 96 (1989).

[163] C. L. Chiu, V. Hecht, H. Duong, B. Wu, and B. Tawil, *Permeability of three-dimensional fibrin constructs corresponds to fibrinogen and thrombin concentrations.* BioResearch open access **1**, 34 (2012).

[164] C. Nunes and M. Roedersheimer, *Effect of microgravity, temperature, and concentration on fibrin and collagen assembly.* Microgravity science and technology **8**, 125 (1995).

[165] M. Vahabi, B. E. Vos, H. C. G. de Cagny, D. Bonn, G. H. Koenderink, and F. C. MacKintosh, *Normal stresses in semiflexible polymer hydrogels,* Physical Review E **97**, 032418 (2018).

[166] V. M. Starov and V. G. Zhdanov, *Effective viscosity and permeability of porous media,* Colloids and Surfaces A: Physicochemical and Engineering Aspects **192**, 363 (2001).

[167] D. G. T. Strange, T. L. Fletcher, K. Tonsomboon, H. Brawn, X. Zhao, and M. L. Oyen, *Separating poroviscoelastic deformation mechanisms in hydrogels,* Applied Physics Letters **102**, 031913 (2013).

[168] R. Adhikari and D. E. Makarov, *Mechanochemical Kinetics in Elastomeric Polymer Networks: Heterogeneity of Local Forces Results in Nonexponential Kinetics,* The Journal of Physical Chemistry B **121**, 2359 (2017).

[169] B. E. Vos, L. C. Liebrand, M. Vahabi, A. Biebricher, G. J. L. Wuite, E. J. G. Peterman, N. A. Kurniawan, F. C. MacKintosh, and G. H. Koenderink, *Programming the mechanics of cohesive fiber networks by compression,* Soft Matter **13**, 8886 (2017).

[170] A. Abhilash, B. M. Baker, B. Trappmann, C. S. Chen, and V. B. Shenoy, *Remodeling of Fibrous Extracellular Matrices by Contractile Cells: Predictions from Discrete Fiber Network Simulations,* Biophysical Journal **107**, 1829 (2014).

[171] R. Malik, P. I. Lelkes, and E. Cukierman, *Biomechanical and biochemical remodeling of stromal extracellular matrix in cancer,* Trends in Biotechnology **33**, 230 (2015).

[172] M. Knight, T. Toyoda, D. Lee, and D. Bader, *Mechanical compression and hydrostatic pressure induce reversible changes in actin cytoskeletal organisation in chondrocytes in agarose,* Journal of Biomechanics **39**, 1547 (2006).

[173] X. Zhao, N. Huebsch, D. J. Mooney, and Z. Suo, *Stress-relaxation behavior in gels with ionic and covalent crosslinks,* Journal of Applied Physics **107**, 1 (2010).

[174] J. Noailly, H. Van Oosterwyck, W. Wilson, T. M. Quinn, and K. Ito, *A poroviscoelastic description of fibrin gels,* Journal of Biomechanics **41**, 3265 (2008).

[175] M. A. Biot, *Theory of deformation of a porous viscoelastic anisotropic solid,* Journal of Applied Physics **27**, 459 (1956).

[176] L. Casares, R. Vincent, D. Zalvidea, N. Campillo, D. Navajas, M. Arroyo, and X. Trepat, *Hydraulic fracture during epithelial stretching,* Nature Materials **14**, 343 (2015).

[177] A. S. G. van Oosten, M. Vahabi, A. J. Licup, A. Sharma, P. A. Galie, F. C. MacKintosh, and P. A. Janmey, *Uncoupling shear and uniaxial elastic moduli of semiflexible biopolymer networks: compression-softening and stretch-stiffening,* Scientific Reports **6**, 294 (2016).

[178] S.-M. Lien, L.-Y. Ko, and T.-J. Huang, *Effect of pore size on ECM secretion and cell growth in gelatin scaffold for articular cartilage tissue engineering,* Acta Biomaterialia **5**, 670 (2009).

[179] E. Moeendarbary, L. Valon, M. Fritzsche, A. R. Harris, D. a. Moulding, A. J. Thrasher, E. Stride, L. Mahadevan, and G. T. Charras, *The cytoplasm of living cells behaves as a poroelastic material,* Nature materials **12**, 253 (2013).

[180] J. Block, H. Witt, A. Candelli, E. J. G. Peterman, G. J. L. Wuite, A. Janshoff, and S. Köster, *Nonlinear Loading-Rate-Dependent Force Response of Individual Vimentin Intermediate Filaments to Applied Strain,* Physical Review Letters **118**, 048101 (2017).

[181] S. G. Wise, G. C. Yeo, M. A. Hiob, J. Rnjak-Kovacina, D. L. Kaplan, M. K. Ng, and A. S. Weiss, *Tropoelastin: A versatile, bioactive assembly module,* Acta Biomaterialia **10**, 1532 (2014).

[182] M. J. Bradshaw and M. L. Smith, *Contribution of unfolding and intermolecular architecture to fibronectin fiber extensibility,* Biophysical Journal **101**, 1740 (2011).

[183] M. Guthold, W. Liu, E. A. Sparks, L. M. Jawerth, L. Peng, M. Falvo, R. Superfine, R. R. Hantgan, and S. T. Lord, *A Comparison of the Mechanical and Structural Properties of Fibrin Fibers with Other Protein Fibers,* Cell Biochemistry and Biophysics **49**, 165 (2007).

[184] W. Liu, C. R. Carlisle, E. a. Sparks, and M. Guthold, *The mechanical properties of single fibrin fibers,* Journal of Thrombosis and Haemostasis **8**, 1030 (2010).

[185] A. S. Tatham and P. R. Shewry, *Elastomeric proteins: biological roles, structures and mechanisms,* Trends in Biochemical Sciences **25**, 567 (2000).

[186] O. V. Kim, R. I. Litvinov, M. S. Alber, and J. W. Weisel, *Quantitative structural mechanobiology of platelet-driven blood clot contraction,* Nature Communications **8**, 1274 (2017).

[187] L. F. Brass and S. L. Diamond, *Transport physics and biorheology in the setting of hemostasis and thrombosis,* Journal of Thrombosis and Haemostasis **14**, 906 (2016).

[188] J. M. Kollman, L. Pandi, M. R. Sawaya, M. Riley, and R. F. Doolittle, *Crystal Structure of Human Fibrinogen,* Biochemistry **48**, 3877 (2009).

[189] Z. Yang, J. M. Kollman, L. Pandi, and R. F. Doolittle, *Crystal Structure of Native Chicken Fibrinogen at 2.7 Å Resolution,* Biochemistry **40**, 12515 (2001).

[190] J. W. Weisel and L. Medved, *The Structure and Function of the αC Domains of Fibrinogen,* Annals of the New York Academy of Sciences **936**, 312 (2006).

[191] W. E. Fowler, R. R. Hantgan, J. Hermans, and H. P. Erickson, *Structure of the fibrin protofibril.* Proceedings of the National Academy of Sciences **78**, 4872 (1981).

[192] A. D. Protopopova, N. A. Barinov, E. G. Zavyalova, A. M. Kopylov, V. I. Sergienko, and D. V. Klinov, *Visualization of fibrinogen αC regions and their arrangement during fibrin network formation by high-resolution AFM,* Journal of Thrombosis and Haemostasis **13**, 570 (2015).

[193] L. Stryer, C. Cohen, and R. Langridge, *Axial period of fibrinogen and fibrin.* Nature **197**, 793 (1963).

[194] J. W. Weisel, *The electron microscope band pattern of human fibrin: Various stains, lateral order, and carbohydrate localization,* Journal of Ultrastructure and Molecular Structure Research **96**, 176 (1986).

[195] J. W. Weisel, *Fibrin assembly. Lateral aggregation and the role of the two pairs of fibrinopeptides,* Biophysical Journal **50**, 1079 (1986).

[196] G. Caracciolo, M. De Spirito, A. C. Castellano, D. Pozzi, G. Amiconi, A. De Pascalis, R. Caminiti, and G. Arcovito, *Protofibrils within fibrin fibres are packed together in a regular array.* Thrombosis and haemostasis **89**, 632 (2003).

[197] E. Di Stasio, C. Nagaswami, J. W. Weisel, and E. Di Cera, *Cl- Regulates the Structure of the Fibrin Clot,* Biophysical Journal **75**, 1973 (1998).

[198] A. E. X. Brown, R. I. Litvinov, D. E. Discher, and J. W. Weisel, *Forced unfolding of coiled-coils in fibrinogen by single-molecule AFM.* Biophysical journal **92**, L39 (2007).

[199] A. Zhmurov, A. E. X. Brown, R. I. Litvinov, R. I. Dima, J. W. Weisel, and V. Barsegov, *Mechanism of fibrin(ogen) forced unfolding,* Structure **19**, 1615 (2011).

[200] A. Zhmurov, O. Kononova, R. I. Litvinov, R. I. Dima, V. Barsegov, and J. W. Weisel, *Mechanical Transition from α-Helical Coiled Coils to β-Sheets in Fibrin(ogen),* Journal of the American Chemical Society **134**, 20396 (2012).

[201] K. A. Minin, A. Zhmurov, K. A. Marx, P. K. Purohit, and V. Barsegov, *Dynamic Transition from α-Helices to β-Sheets in Polypeptide Coiled-Coil Motifs,* Journal of the American Chemical Society **139**, 16168 (2017).

[202] Z. Qin and M. J. Buehler, *Molecular dynamics simulation of the α-helix to β-sheet transition in coiled protein filaments: evidence for a critical filament length scale.* Physical review letters **104**, 198304 (2010).

[203] J. R. Houser, N. E. Hudson, L. Ping, E. T. O'Brien, R. Superfine, S. T. Lord, and M. R. Falvo, *Evidence that αC Region Is Origin of Low Modulus, High Extensibility, and Strain Stiffening in Fibrin Fibers,* Biophysical Journal **99**, 3038 (2010).

[204] M. R. Falvo, D. Millard, E. T. O'Brien, R. Superfine, and S. T. Lord, *Length of tandem repeats in fibrin's αC region correlates with fiber extensibility,* Journal of Thrombosis and Haemostasis **6**, 1991 (2008).

[205] N. E. Hudson, F. Ding, I. Bucay, E. T. O'Brien, O. V. Gorkun, R. Superfine, S. T. Lord, N. V. Dokholyan, and M. R. Falvo, *Submillisecond Elastic Recoil Reveals Molecular Origins of Fibrin Fiber Mechanics,* Biophysical Journal **104**, 2671 (2013).

[206] F. J. Roska, J. D. Ferry, J. S. Lin, and J. W. Anderegg, *Studies of fibrin film. II. Small-angle x-ray scattering,* Biopolymers **21**, 1833 (1982).

[207] F. Fleissner, M. Bonn, and S. H. Parekh, *Microscale spatial heterogeneity of protein structural transitions in fibrin matrices,* Science Advances **2**, e1501778 (2016).

[208] R. I. Litvinov, D. a. Faizullin, Y. F. Zuev, and J. W. Weisel, *The α-helix to β-sheet transition in stretched and compressed hydrated fibrin clots.* Biophysical journal **103**, 1020 (2012).

[209] K. A. Jansen, *ECM Mechanics and Implications for Cellular Mechanosensing*, Ph.D. thesis (2016).

[210] R. Tran, D. R. Myers, J. Ciciliano, E. L. Trybus Hardy, Y. Sakurai, B. Ahn, Y. Qiu, R. G. Mannino, M. E. Fay, and W. a. Lam, *Biomechanics of haemostasis and thrombosis in health and disease: from the macro- to molecular scale,* Journal of Cellular and Molecular Medicine **17**, 579 (2013).

[211] J. P. Collet, J. L. Woodhead, J. Soria, C. Soria, M. Mirshahi, J. P. Caen, and J. W. Weisel, *Fibrinogen Dusart: electron microscopy of molecules, fibers and clots, and viscoelastic properties of clots,* Biophysical Journal **70**, 500 (1996).

[212] J. Koopman, F. Haverkate, J. Grimbergen, S. T. Lord, M. W. Mosesson, J. P. DiOrio, K. S. Siebenlist, C. Legrand, J. Soria, and C. Soria, *Molecular basis for fibrinogen Dusart (A alpha 554 Arg–>Cys) and its association with abnormal fibrin polymerization and thrombophilia.* The Journal of clinical investigation **91**, 1637 (1993).

[213] B. Aghaei-Ghareh-Bolagh, S. M. Mithieux, and A. S. Weiss, *Elastic proteins and elastomeric protein alloys,* Current Opinion in Biotechnology **39**, 56 (2016).

[214] J. Hook and H. Hall, *Solid State Physics, second edition* (Wiley, 1991) p. 496.

[215] R. Turton, *The Physics of Solids* (Oxford University Press, 2000).

[216] H. Rosenberg, *The Solid State, third edition* (Oxford Science Publications, 1988).

[217] W. Bragg, *The diffraction of short electromagnetic waves by a crystal,* Proceedings of the Cambridge Philosophical Society **17**, 43 (1913).

[218] M. Jaspers, A. C. H. Pape, I. K. Voets, A. E. Rowan, G. Portale, and P. H. J. Kouwer, *Bundle Formation in Biomimetic Hydrogels,* Biomacromolecules **17**, 2642 (2016).

[219] J. Zhang, Y. Sun, Y. Zhao, B. Wei, C. Xu, L. He, C. L. P. Oliveira, and H. Wang, *Centrifugation-induced fibrous orientation in fish-sourced collagen matrices,* Soft Matter **13**, 9220 (2017).

[220] M. Nierenberger, G. Fargier, S. Ahzi, and Y. Rémond, *Evolution of the three-dimensional collagen structure in vascular walls during deformation: an in situ mechanical testing under multiphoton microscopy observation,* Biomechanics and Modeling in Mechanobiology **14**, 693 (2015).

[221] S. Meghezi, F. Couet, P. Chevallier, and D. Mantovani, *Effects of a Pseudophysiological Environment on the Elastic and Viscoelastic Properties of Collagen Gels,* International Journal of Biomaterials **2012**, 1 (2012).

[222] A. E. Ehret, K. Bircher, A. Stracuzzi, V. Marina, M. Zündel, and E. Mazza, *Inverse poroelasticity as a fundamental mechanism in biomechanics and mechanobiology,* Nature Communications **8**, 1002 (2017).

[223] H. E. Amuasi, C. Heussinger, R. L. C. Vink, and A. Zippelius, *Nonlinear and heterogeneous elasticity of multiply-crosslinked biopolymer networks,* New Journal of Physics **17**, 083035 (2015).

[224] M. R. B. Mermet-Guyennet, J. Gianfelice de Castro, M. Habibi, N. Martzel, M. M. Denn, and D. Bonn, *LAOS: The strain softening/strain hardening paradox,* Journal of Rheology **59**, 21 (2015).

[225] C. P. Broedersz, K. E. Kasza, L. M. Jawerth, S. Münster, D. a. Weitz, and F. C. MacKintosh, *Measurement of nonlinear rheology of cross-linked biopolymer gels,* Soft Matter **6**, 4120 (2010).

[226] K. Sato, I. Kunita, Y. Takikawa, D. Takeuchi, Y. Tanaka, T. Nakagaki, and H. Orihara, *Direct observation of orientation distributions of actin filaments in a solution undergoing shear banding,* Soft Matter **13**, 2708 (2017).

[227] A. Basu, Q. Wen, X. Mao, T. C. Lubensky, P. A. Janmey, and A. G. Yodh, *Nonaffine Displacements in Flexible Polymer Networks,* Macromolecules **44**, 1671 (2011).

[228] R. Besseling, L. Isa, E. R. Weeks, and W. C. K. Poon, *Quantitative imaging of colloidal flows.* Advances in colloid and interface science **146**, 1 (2009).

[229] S. K. Dutta, A. Mbi, R. C. Arevalo, and D. L. Blair, *Development of a confocal rheometer for soft and biological materials.* The Review of scientific instruments **84**, 063702 (2013).

[230] N. Koumakis, E. Moghimi, R. Besseling, W. C. K. Poon, J. F. Brady, and G. Petekidis, *Tuning colloidal gels by shear,* Soft Matter **11**, 4640 (2015).

[231] S. Aime, L. Ramos, J. M. Fromental, G. Prévot, R. Jelinek, and L. Cipelletti, *A stress-controlled shear cell for small-angle light scattering and microscopy,* Review of Scientific Instruments **87**, 123907 (2016).

[232] X. Cheng, J. H. McCoy, J. N. Israelachvili, and I. Cohen, *Imaging the microscopic structure of shear thinning and thickening colloidal suspensions.* Science (New York, N.Y.) **333**, 1276 (2011).

[233] J.-B. Boitte, C. Vizcaïno, L. Benyahia, J.-M. Herry, C. Michon, and M. Hayert, *A novel rheo-optical device for studying complex fluids in a double shear plate geometry.* The Review of scientific instruments **84**, 013709 (2013).

[234] T. Xu, D. Vavylonis, F.-C. Tsai, G. H. Koenderink, W. Nie, E. Yusuf, I-Ju Lee, J.-Q. Wu, and X. Huang, *SOAX: a software for quantification of 3D biopolymer networks.* Scientific reports **5**, 9081 (2015).

[235] C. Broennimann, E. F. Eikenberry, B. Henrich, R. Horisberger, G. Huelsen, E. Pohl, B. Schmitt, C. Schulze-Briese, M. Suzuki, T. Tomizaki, H. Toyokawa, and A. Wagner, *The PILATUS 1M detector,* Journal of Synchrotron Radiation **13**, 120 (2006).

[236] M. Missori, M. Papi, G. Maulucci, G. Arcovito, G. Boumis, A. Bellelli, G. Amiconi, and M. De Spirito, *Cl- and F- anions regulate the architecture of protofibrils in fibrin gel,* European Biophysics Journal **39**, 1001 (2010).

[237] J. I. Langford and D. Louër, *Powder diffraction,* Reports on Progress in Physics **59**, 131 (1996).

[238] B. Hammouda, *Are Bragg Peaks Gaussian?* Journal of Research of the National Institute of Standards and Technology **119**, 15 (2014).

[239] B. E. Vos, *High collection efficiency substrate by coupling to plasmonic antennas in a stratified medium*, Master thesis, University of Amsterdam (2013).

[240] E. Helfer, P. Panine, M.-F. Carlier, and P. Davidson, *The Interplay between Viscoelastic and Thermodynamic Properties Determines the Birefringence of F-Actin Gels,* Biophysical Journal **89**, 543 (2005).

[241] K. R. Purdy, Z. Dogic, S. Fraden, A. Rühm, L. Lurio, and S. G. J. Mochrie, *Measuring the nematic order of suspensions of colloidal fd virus by x-ray diffraction and optical birefringence.* Physical review. E, Statistical, nonlinear, and soft matter physics **67**, 031708 (2003).

[242] M. P. Allen, G. T. Evans, D. Frenkel, and B. M. Mulder, *Hard Convex Body Fluids,* in *Advances in chemical*, Vol. 86 (John Wiley & Sons, Inc., 1993) pp. 1–166.

[243] T. N. Shendruk and J. M. Yeomans, *Multi-particle collision dynamics algorithm for nematic fluids,* Soft Matter **11**, 5101 (2015).

[244] D. Mukhija and M. J. Solomon, *Nematic order in suspensions of colloidal rods by application of a centrifugal field,* Soft Matter **7**, 540 (2011).

[245] S. V. Savenko and M. Dijkstra, *Sedimentation and multiphase equilibria in suspensions of colloidal hard rods,* Physical Review E **70**, 051401 (2004).

[246] M. Lämmel, E. Jaschinski, R. Merkel, and K. Kroy, *Microstructure of Sheared Entangled Solutions of Semiflexible Polymers,* Polymers **8**, 353 (2016).

[247] J. Feng, H. Levine, X. Mao, and L. M. Sander, *Alignment and nonlinear elasticity in biopolymer gels,* Physical Review E - Statistical, Nonlinear, and Soft Matter Physics **91**, 1 (2015).

[248] M. R. Falvo, O. V. Gorkun, and S. T. Lord, *The molecular origins of the mechanical properties of fibrin,* Biophysical Chemistry **152**, 15 (2010).

[249] Q. Wen, A. Basu, P. A. Janmey, and A. G. Yodh, *Non-affine deformations in polymer hydrogels,* Soft Matter **8**, 8039 (2012).

[250] H. Hatami-Marbini and R. C. Picu, *Scaling of nonaffine deformation in random semiflexible fiber networks,* Physical Review E **77**, 062103 (2008).

[251] P. K. Purohit, R. I. Litvinov, A. E. Brown, D. E. Discher, and J. W. Weisel, *Protein unfolding accounts for the unusual mechanical behavior of fibrin networks,* Acta Biomaterialia **7**, 2374 (2011).

[252] M. W. Mosesson, *Fibrinogen and fibrin structure and functions,* Journal of Thrombosis and Haemostasis **3**, 1894 (2005).

[253] B. B. Lim, E. H. Lee, M. Sotomayor, and K. Schulten, *Molecular Basis of Fibrin Clot Elasticity,* Structure **16**, 449 (2008).

[254] G. Tsurupa, L. Tsonev, and L. Medved, *Structural organization of the fibrin(ogen) alpha C-domain.* Biochemistry **41**, 6449 (2002).

[255] R. D. Averett, B. Menn, E. H. Lee, C. C. Helms, T. Barker, and M. Guthold, *A Modular Fibrinogen Model that Captures the Stress-Strain Behavior of Fibrin Fibers,* Biophysical Journal **103**, 1537 (2012).

[256] A. D. Protopopova, R. I. Litvinov, D. K. Galanakis, C. Nagaswami, N. A. Barinov, A. R. Mukhitov, D. V. Klinov, and J. W. Weisel, *Morphometric characterization of fibrinogen's αC regions and their role in fibrin self-assembly and molecular organization,* Nanoscale **9**, 13707 (2017).

[257] Y.-C. Lin, N. Y. Yao, C. P. Broedersz, H. Herrmann, F. C. MacKintosh, and D. A. Weitz, *Origins of Elasticity in Intermediate Filament Networks,* Physical Review Letters **104**, 058101 (2010).

[258] L. Ping, L. Huang, B. Cardinali, A. Profumo, O. V. Gorkun, and S. T. Lord, *Substitution of the Human αC Region with the Analogous Chicken Domain Generates a Fibrinogen with Severely Impaired Lateral Aggregation: Fibrin Monomers Assemble into Protofibrils but Protofibrils Do Not Assemble into Fibers,* Biochemistry **50**, 9066 (2011).

[259] C. Nair, G. Shah, and D. Dhall, *Effect of temperature, ph and ionic strength and composition on fibrin network structure and its development,* Thrombosis Research **42**, 809 (1986).

[260] M. Carr, D. Gabriel, and J. McDONAGH, *Influence of Ca2+ on the structure of reptilase-derived and thrombin-derived fibrin gels.* Biochem. J **239**, 513 (1986).

[261] S. J. Henderson, J. Xia, H. Wu, A. R. Stafford, B. A. Leslie, J. C. Fredenburgh, D. A. Weitz, and J. I. Weitz, *Zinc promotes clot stability by accelerating clot formation and modifying fibrin structure,* Thrombosis and Haemostasis **115**, 533 (2015).

[262] R. Hantgan and J. Hermans, *Assembly of fibrin. A light scattering study.* Journal of Biological Chemistry **254**, 11272 (1979).

[263] R. Hantgan, W. Fowler, H. Erickson, and J. Hermans, *Fibrin assembly: a comparison of electron microscopic and light scattering results.* Thrombosis and haemostasis **44**, 119 (1980).

[264] M. F. Müller, J. D. Ferry, and J. S. Lin, *Small-angle x-ray scattering studies of fibrin film: Comparisons of fine and coarse films prepared with thrombin and ancrod,* Biopolymers **28**, 1011 (1989).

[265] F. Berkemeier, M. Bertz, S. Xiao, N. Pinotsis, M. Wilmanns, F. Grater, and M. Rief, *Fast-folding α-helices as reversible strain absorbers in the muscle protein myomesin,* Proceedings of the National Academy of Sciences **108**, 14139 (2011).

[266] C. Guo, J. Zhang, X. Wang, A. T. Nguyen, X. Y. Liu, and D. L. Kaplan, *Comparative Study of Strain-Dependent Structural Changes of Silkworm Silks: Insight into the Structural Origin of Strain-Stiffening,* Small **13**, 1702266 (2017).

[267] M. Rief, M. Gautel, F. Oesterhelt, J. M. Fernandez, and H. E. Gaub, *Reversible unfolding of individual titin immunoglobulin domains by AFM,* Science **276**, 1109 (1997).

[268] C. E. Hall and H. S. Slayter, *The Fibrinogen Molecule: Its Size, Shape, and Mode of Polymerization,* The Journal of Cell Biology **5**, 11 (1959).

[269] R. F. Doolittle, *Fibrinogen and Fibrin,* Annual Review of Biochemistry **53**, 195 (1984).

[270] A. M. Belkin, G. Tsurupa, E. Zemskov, Y. Veklich, J. W. Weisel, and L. Medved, *Transglutaminase-mediated oligomerization of the fibrin(ogen) alphaC domains promotes integrin-dependent cell adhesion and signaling.* Blood **105**, 3561 (2005).

[271] O. V. Gorkun, Y. I. Veklich, L. V. Medved', A. H. Henschen, and J. W. Weisel, *Role of the αC Domains of Fibrin in Clot Formation,* Biochemistry **33**, 6986 (1994).

[272] J. P. Collet, J. L. Moen, Y. I. Veklich, O. V. Gorkun, S. T. Lord, G. Montalescot, and J. W. Weisel, *The αC domains of fibrinogen affect the structure of the fibrin clot, its physical properties, and its susceptibility to fibrinolysis,* Blood **106**, 3824 (2005).

[273] M. L. Gardel, J. Shin, F. C. MacKintosh, L. Mahadevan, P. Matsudaira, and D. A. Weitz, *Elastic Behavior of Cross-Linked and Bundled Actin Networks,* Science **304**, 1301 (2004).

[274] M. Bouzid and E. Del Gado, *Network Topology in Soft Gels: Hardening and Softening Materials,* Langmuir **34**, 773 (2018).

[275] A. Dittmore, J. Silver, S. K. Sarkar, B. Marmer, G. I. Goldberg, and K. C. Neuman, *Internal strain drives spontaneous periodic buckling in collagen and regulates remodeling,* Proceedings of the National Academy of Sciences **113**, 201523228 (2016).

[276] A. D. Araújo, A. Majumdar, H. Parameswaran, E. Yi, J. L. Spencer, M. A. Nugent, and B. Suki, *Dynamics of enzymatic digestion of elastic fibers and networks under tension.* Proceedings of the National Academy of Sciences of the United States of America **108**, 9414 (2011).

[277] N. A. Kurniawan, B. E. Vos, A. Biebricher, G. J. Wuite, E. J. Peterman, and G. H. Koenderink, *Fibrin Networks Support Recurring Mechanical Loads by Adapting their Structure across Multiple Scales,* Biophysical Journal **111**, 1026 (2016).

[278] K. M. Schmoller, P. Fernández, R. C. Arevalo, D. L. Blair, and A. R. Bausch, *Cyclic hardening in bundled actin networks.* Nature communications **1**, 134 (2010).

[279] H. López-Menéndez and J. F. Rodríguez, *Microstructural model for cyclic hardening in F-actin networks crosslinked by α-actinin,* Journal of the Mechanics and Physics of Solids **91**, 28 (2016).

[280] P. Fernández and A. Ott, *Single Cell Mechanics: Stress Stiffening and Kinematic Hardening,* Physical Review Letters **100**, 238102 (2008).

[281] S. Nam, K. H. Hu, M. J. Butte, and O. Chaudhuri, *Strain-enhanced stress relaxation impacts nonlinear elasticity in collagen gels,* Proceedings of the National Academy of Sciences **113**, 201523906 (2016).

[282] L. Wolff, P. Fernandez, and K. Kroy, *Inelastic mechanics of sticky biopolymer networks,* New Journal of Physics **12**, 053024 (2010).

[283] H. Wang and S. C. Heilshorn, *Adaptable Hydrogel Networks with Reversible Linkages for Tissue Engineering,* Advanced Materials **27**, 3717 (2015).

[284] D. Poquillon, B. Viguier, and E. Andrieu, *Experimental data about mechanical behaviour during compression tests for various matted fibres,* Journal of Materials Science **40**, 5963 (2005).

[285] O. V. Kim, R. I. Litvinov, J. W. Weisel, and M. S. Alber, *Structural basis for the nonlinear mechanics of fibrin networks under compression,* Biomaterials **35**, 6739 (2014).

[286] M. G. Haugh, S. D. Thorpe, T. Vinardell, C. T. Buckley, and D. J. Kelly, *The application of plastic compression to modulate fibrin hydrogel mechanical properties,* Journal of the Mechanical Behavior of Biomedical Materials **16**, 66 (2012).

[287] Y. F. Zuev, R. I. Litvinov, A. E. Sitnitsky, B. Z. Idiyatullin, D. R. Bakirova, D. K. Galanakis, A. Zhmurov, V. Barsegov, and J. W. Weisel, *Conformational Flexibility and Self-Association of Fibrinogen in Concentrated Solutions,* The Journal of Physical Chemistry B **121**, 7833 (2017).

[288] H. C. G. de Cagny, B. E. Vos, M. Vahabi, N. A. Kurniawan, M. Doi, G. H. Koenderink, F. C. MacKintosh, and D. Bonn, *Porosity Governs Normal Stresses in Polymer Gels,* Physical Review Letters **117**, 217802 (2016).

[289] N. A. Kurniawan, J. Grimbergen, J. Koopman, and G. H. Koenderink, *Factor XIII stiffens fibrin clots by causing fiber compaction,* Journal of Thrombosis and Haemostasis **12**, 1687 (2014).

[290] J. B. Walker and M. E. Nesheim, *The Molecular Weights, Mass Distribution, Chain Composition, and Structure of Soluble Fibrin Degradation Products Released from a Fibrin Clot Perfused with Plasmin,* Journal of Biological Chemistry **274**, 5201 (1999).

[291] M. a. Rozenfel'd, V. B. Leonova, and M. I. Biryukova, *The effect of "aging" of fibrinogen molecule on the structure and properties of fibrin gel,* Biology Bulletin **34**, 323 (2007).

[292] I. K. Piechocka, N. A. Kurniawan, J. Grimbergen, J. Koopman, and G. H. Koenderink, *Recombinant fibrinogen reveals the differential roles of α- and γ-chain cross-linking and molecular heterogeneity in fibrin clot strain-stiffening,* Journal of Thrombosis and Haemostasis **15**, 938 (2017).

[293] I. Brouwer, G. A. King, I. Heller, A. S. Biebricher, E. J. G. Peterman, and G. J. L. Wuite, *Probing DNA–DNA Interactions with a Combination of Quadruple-Trap Optical Tweezers and Microfluidics,* in *Optical Tweezers, Methods and Protocols*, edited by G. A. (Humana Press, 2017) pp. 275–293.

[294] P. Żeliszewska, A. Bratek-Skicki, Z. Adamczyk, and M. Cieśla, *Human Fibrinogen Adsorption on Positively Charged Latex Particles,* Langmuir **30**, 11165 (2014).

[295] C. P. Broedersz and F. C. MacKintosh, *Molecular motors stiffen non-affine semiflexible polymer networks,* Soft Matter **7**, 3186 (2011).

[296] S. B. Lindström, D. A. Vader, A. Kulachenko, and D. A. Weitz, *Biopolymer network geometries: Characterization, regeneration, and elastic properties,* Physical Review E **82**, 051905 (2010).

[297] J. Wilhelm and E. Frey, *Elasticity of stiff polymer networks,* Physical review letters **91**, 108103 (2003).

[298] S. Alexander, *Amorphous solids: their structure, lattice dynamics and elasticity,* Physics reports **296**, 65 (1998).

[299] M. Dennison, M. Sheinman, C. Storm, and F. C. MacKintosh, *Fluctuation-stabilized marginal networks and anomalous entropic elasticity,* Phys. Rev. Lett. **111**, 095503 (2013).

[300] P. Rosakis, J. Notbohm, and G. Ravichandran, *A model for compression-weakening materials and the elastic fields due to contractile cells,* Journal of the Mechanics and Physics of Solids **85**, 16 (2015).

[301] O. Chaudhuri, S. H. Parekh, and D. A. Fletcher, *Reversible stress softening of actin networks,* Nature **445**, 295 (2007).

[302] L. D. Landau and E. M. Lifshitz, *Theory of Elasticity* (Pergamon Press, 1986).

[303] K. John, D. Caillerie, P. Peyla, A. Raoult, and C. Misbah, *Nonlinear elasticity of cross-linked networks,* Physical Review E **87**, 042721 (2013).

[304] X. Xu and S. A. Safran, *Compressive elasticity of polydisperse biopolymer gels,* Physical Review E **95**, 052415 (2017).

[305] S. Alexander, *Amorphous solids: their structure, lattice dynamics and elasticity,* Physics Reports **296**, 65 (1998).

[306] M. Sheinman, C. P. Broedersz, and F. C. MacKintosh, *Nonlinear effective-medium theory of disordered spring networks,* Physical Review E **85**, 1 (2012).

[307] N. Laurens, R. P. C. Driessen, I. Heller, D. Vorselen, M. C. Noom, F. J. H. Hol, M. F. White, R. T. Dame, and G. J. L. Wuite, *Alba shapes the archaeal genome using a delicate balance of bridging and stiffening the DNA.* Nature communications **3**, 1328 (2012).

[308] J. van Mameren, M. Modesti, R. Kanaar, C. Wyman, E. J. G. Peterman, and G. J. L. Wuite, *Counting RAD51 proteins disassembling from nucleoprotein filaments under tension,* Nature **457**, 745 (2009).

[309] R. A. S. Ariëns, *Role of factor XIII in fibrin clot formation and effects of genetic polymorphisms,* Blood **100**, 743 (2002).

[310] C. Duval, P. Allan, S. D. A. Connell, V. C. Ridger, H. Philippou, and R. A. S. Ariëns, *Roles of fibrin α- and γ-chain specific cross-linking by FXIIIa in fibrin structure and function,* Thrombosis and Haemostasis **111**, 842 (2014).

[311] J. Koo, M. H. Rafailovich, L. Medved, G. Tsurupa, B. J. Kudryk, Y. Liu, and D. K. Galanakis, *Evaluation of fibrinogen self-assembly: role of its αC region,* Journal of Thrombosis and Haemostasis **8**, 2727 (2010).

[312] R. I. Litvinov, S. Yakovlev, G. Tsurupa, O. V. Gorkun, L. Medved, and J. W. Weisel, *Direct Evidence for Specific Interactions of the Fibrinogen αC-Domains with the Central E Region and with Each Other,* Biochemistry **46**, 9133 (2007).

[313] P. R. Onck, T. Koeman, T. Van Dillen, and E. Van Der Giessen, *Alternative explanation of stiffening in cross-linked semiflexible networks,* Physical Review Letters **95**, 19 (2005).

[314] M. E. Susilo, J. A. Paten, E. A. Sander, T. D. Nguyen, and J. W. Ruberti, *Collagen network strengthening following cyclic tensile loading.* Interface focus **6**, 20150088 (2016).

[315] U. Cheema, C. B. Chuo, P. Sarathchandra, S. N. Nazhat, and R. A. Brown, *Engineering functional collagen scaffolds: Cyclical loading increases material strength and fibril aggregation,* Advanced Functional Materials **17**, 2426 (2007).

[316] K. E. Kasza, A. C. Rowat, J. Liu, T. E. Angelini, C. P. Brangwynne, G. H. Koenderink, and D. A. Weitz, *The cell as a material,* Current Opinion in Cell Biology **19**, 101 (2007).

[317] V. A. Davis, A. N. G. Parra-Vasquez, M. J. Green, P. K. Rai, N. Behabtu, V. Prieto, R. D. Booker, J. Schmidt, E. Kesselman, W. Zhou, H. Fan, W. W. Adams, R. H. Hauge, J. E. Fischer, Y. Cohen, Y. Talmon, R. E. Smalley, and M. Pasquali, *True solutions of single-walled carbon nanotubes for assembly into macroscopic materials,* Nature Nanotechnology **4**, 830 (2009).

[318] R. T. Olsson, M. A. S. Azizi Samir, G. Salazar-Alvarez, L. Belova, V. Ström, L. A. Berglund, O. Ikkala, J. Nogués, and U. W. Gedde, *Making flexible magnetic aerogels and stiff magnetic nanopaper using cellulose nanofibrils as templates,* Nature Nanotechnology **5**, 584 (2010).

[319] R. C. Picu and A. Sengab, *Structural evolution and stability of non-crosslinked fiber networks with inter-fiber adhesion,* Soft Matter **14**, 2254 (2018).

[320] M. Gupta, B. R. Sarangi, J. Deschamps, Y. Nematbakhsh, A. Callan-Jones, F. Margadant, R.-M. Mège, C. T. Lim, R. Voituriez, and B. Ladoux, *Adaptive rheology and ordering of cell cytoskeleton govern matrix rigidity sensing,* Nature Communications **6**, 7525 (2015).

[321] D. Oelz, B. Rubinstein, and A. Mogilner, *A Combination of Actin Treadmilling and Cross-Linking Drives Contraction of Random Actomyosin Arrays,* Biophysical Journal **109**, 1818 (2015).

[322] G. Salbreux, G. Charras, and E. Paluch, *Actin cortex mechanics and cellular morphogenesis,* Trends in Cell Biology **22**, 536 (2012).

[323] O. M. Lancaster and B. Baum, *Shaping up to divide: Coordinating actin and microtubule cytoskeletal remodelling during mitosis,* Seminars in Cell & Developmental Biology **34**, 109 (2014).

[324] S. Nam, J. Lee, D. G. Brownfield, and O. Chaudhuri, *Viscoplasticity Enables Mechanical Remodeling of Matrix by Cells,* Biophysical Journal **111**, 2296 (2016).

[325] O. Chaudhuri, L. Gu, M. Darnell, D. Klumpers, S. a. Bencherif, J. C. Weaver, N. Huebsch, and D. J. Mooney, *Substrate stress relaxation regulates cell spreading,* Nature Communications **6**, 1 (2015).

[326] O. Chaudhuri, L. Gu, D. Klumpers, M. Darnell, S. A. Bencherif, J. C. Weaver, N. Huebsch, H.-P. Lee, E. Lippens, G. N. Duda, and D. J. Mooney, *Hydrogels with tunable stress relaxation regulate stem cell fate and activity.* Nature materials **advance on** (2015), 10.1038/nmat4489.

[327] H. Siedentopf and R. Zsigmondy, *Über Sichtbarmachung und Grössenbestimmung ultramikroskopischer Teilchen, mit besonderer Anwendung auf Goldrubingläser,* Annalen der Physik **10**, 1 (1903).

[328] P. A. Santi, *Light Sheet Fluorescence Microscopy,* Journal of Histochemistry & Cytochemistry **59**, 129 (2011).

[329] R. M. Power and J. Huisken, *A guide to light-sheet fluorescence microscopy for multiscale imaging,* Nature Methods **14**, 360 (2017).

[330] M. Plöschner, V. Kollárová, Z. Dostál, J. Nylk, T. Barton-Owen, D. E. K. Ferrier, R. Chmelík, K. Dholakia, and T. Čižmár, *Multimode fibre: Light-sheet microscopy at the tip of a needle,* Scientific Reports **5**, 18050 (2015).

[331] M. B. M. Meddens, S. Liu, P. S. Finnegan, T. L. Edwards, C. D. James, and K. A. Lidke, *Single objective light-sheet microscopy for high-speed whole-cell 3D super-resolution,* Biomedical Optics Express **7**, 2219 (2016).

[332] R. Galland, G. Grenci, A. Aravind, V. Viasnoff, V. Studer, and J.-B. Sibarita, *3D high- and super-resolution imaging using single-objective SPIM,* Nature Methods **12**, 641 (2015).

[333] E. Zagato, T. Brans, S. Verstuyft, D. van Thourhout, J. Missinne, G. van Steenberge, J. Demeester, S. De Smedt, K. Remaut, K. Neyts, and K. Braeckmans, *Microfabricated devices for single objective single plane illumination microscopy (SoSPIM),* Optics Express **25**, 1732 (2017).

[334] M. B. Sikkel, S. Kumar, V. Maioli, C. Rowlands, F. Gordon, S. E. Harding, A. R. Lyon, K. T. MacLeod, and C. Dunsby, *High speed sCMOS-based oblique plane microscopy applied to the study of calcium dynamics in cardiac myocytes,* Journal of Biophotonics **9**, 311 (2016).

[335] T. Vettenburg, H. I. C. Dalgarno, J. Nylk, C. Coll-Lladó, D. E. K. Ferrier, T. Čižmár, F. J. Gunn-Moore, and K. Dholakia, *Light-sheet microscopy using an Airy beam,* Nature Methods **11**, 541 (2014).

[336] D. G. Papazoglou, S. Suntsov, D. Abdollahpour, and S. Tzortzakis, *Tunable intense Airy beams and tailored femtosecond laser filaments,* Physical Review A **81**, 061807 (2010).

[337] D. McGloin and K. Dholakia, *Bessel beams: Diffraction in a new light,* Contemporary Physics **46**, 15 (2005).

[338] *OpenSPIM Wiki*, `http://openspim.org/` .

[339] H.-U. Dodt, U. Leischner, A. Schierloh, N. Jährling, C. P. Mauch, K. Deininger, J. M. Deussing, M. Eder, W. Zieglgänsberger, and K. Becker, *Ultramicroscopy: three-dimensional visualization of neuronal networks in the whole mouse brain,* Nature Methods **4**, 331 (2007).

[340] E. Ban, J. M. Franklin, S. Nam, L. R. Smith, H. Wang, R. G. Wells, O. Chaudhuri, J. T. Liphardt, and V. B. Shenoy, *Mechanisms of Plastic Deformation in Collagen Networks Induced by Cellular Forces,* Biophysical Journal **114**, 450 (2018).

[341] M. Hoylaerts, D. C. Rijken, H. R. Lijnen, and D. Collen, *Kinetics of the activation of plasminogen by human tissue plasminogen activator. Role of fibrin.* The Journal of biological chemistry **257**, 2912 (1982).

[342] D. A. Gabriel, K. Muga, and E. M. Boothroyd, *The effect of fibrin structure on fibrinolysis,* The Journal of biological chemistry **267**, 24259 (1992).

[343] J. P. Collet, D. Park, C. Lesty, J. Soria, C. Soria, G. Montalescot, and J. W. Weisel, *Influence of Fibrin Network Conformation and Fibrin Fiber Diameter on Fibrinolysis Speed: Dynamic and Structural Approaches by Confocal Microscopy,* Arteriosclerosis, Thrombosis, and Vascular Biology **20**, 1354 (2000).

[344] N. J. Mutch, R. Engel, S. U. D. Willige, H. Philippou, and R. A. S. Arie, *Polyphosphate modifies the fibrin network and down-regulates fibrinolysis by attenuating binding of tPA and plasminogen to fibrin,* Thrombosis and Hemostasis **115**, 3980 (2010).

[345] E. Komorowicz, N. Balázs, Z. Varga, L. Szabó, A. Bóta, and K. Kolev, *Hyaluronic acid decreases the mechanical stability, but increases the lytic resistance of fibrin matrices,* Matrix Biology (2016), 10.1016/j.matbio.2016.12.008.

[346] A. S. Adhikari, A. H. Mekhdjian, and A. R. Dunn, *Strain tunes proteolytic degradation and diffusive transport in fibrin networks,* Biomacromolecules **13**, 499 (2012).

[347] W. G. Jerome, S. Handt, and R. R. Hantgan, *Endothelial Cells Organize Fibrin Clots into Structures That Are More Resistant to Lysis,* Microscopy and Microanalysis **11**, 268 (2005).

[348] K. A. Jansen, R. G. Bacabac, I. K. Piechocka, and G. H. Koenderink, *Cells Actively Stiffen Fibrin Networks by Generating Contractile Stress,* Biophysical Journal **105**, 2240 (2013).

[349] B. E. Vos, *Determining the elongation and shear viscosity for a number of complex fluids,* Bachelor thesis, University of Amsterdam (2011).

[350] J. Vermant, P. Moldenaers, J. Mewis, M. Ellis, and R. Garritano, *Orthogonal superposition measurements using a rheometer equipped with a force rebalanced transducer,* Review Of Scientific Instruments **68**, 4090 (1997).

[351] J.-M. Y. Carrillo, F. C. MacKintosh, and A. V. Dobrynin, *Nonlinear Elasticity: From Single Chain to Networks and Gels,* Macromolecules **46**, 3679 (2013).

[352] O. A. Saleh, *Perspective: Single polymer mechanics across the force regimes,* The Journal of Chemical Physics **142**, 194902 (2015).

[353] K. Kroy and E. Frey, *Force-Extension Relation and Plateau Modulus for Wormlike Chains,* Physical Review Letters **77**, 306 (1996).

[354] C. R. Carlisle, C. Coulais, M. Namboothiry, D. L. Carroll, R. R. Hantgan, and M. Guthold, *The mechanical properties of individual, electrospun fibrinogen fibers,* Biomaterials **30**, 1205 (2009).

[355] W. Liu, L. M. Jawerth, E. A. Sparks, M. R. Falvo, R. R. Hantgan, R. Superfine, S. T. Lord, and M. Guthold, *Fibrin fibers have extraordinary extensibility and elasticity.* Science **313**, 634 (2006).

[356] C. P. Broedersz, M. Depken, N. Y. Yao, M. R. Pollak, D. A. Weitz, and F. C. MacKintosh, *Cross-Link-Governed Dynamics of Biopolymer Networks,* Physical Review Letters **105**, 238101 (2010).

[357] C. Bustamante, J. Marko, E. Siggia, and S. Smith, *Entropic elasticity of lambda-phage DNA,* Science **265**, 1599 (1994).